

**Measurement of the Production Cross-Section of
 J/ψ Mesons Decaying into Electron-Positron Pairs
in Proton-Proton Interactions at a Collision
Energy of 10 TeV, using a detailed Simulation of
the ATLAS Detector at the CERN LHC**

THÈSE

présentée à la Faculté des sciences de l'Université de Genève
pour obtenir le grade de Docteur ès sciences, mention physique

par

Andrée Robichaud-Véronneau

Canada

Thèse N° 4268



**UNIVERSITÉ
DE GENÈVE**

FACULTÉ DES SCIENCES

**Doctorat ès sciences
Mention physique**

Thèse de *Madame Andrée ROBICHAUD-VÉRONNEAU*

intitulée :

**" Measurement of the Production Cross-Section of
 J/ψ Mesons Decaying into Electron-Positron Pairs in
Proton-Proton Interactions at a Collision Energy of
10 TeV, using a detailed Simulation of
the ATLAS Detector at the CERN LHC "**

La Faculté des sciences, sur le préavis de Messieurs A. G. CLARK, professeur ordinaire et directeur de thèse (Département de physique nucléaire et corpusculaire), M. POHL, professeur ordinaire (Département de physique nucléaire et corpusculaire), X. WU, docteur (Département de physique nucléaire et corpusculaire) et Madame P. WELLS, docteure (Département de physique, Organisation européenne pour la recherche nucléaire – CERN, Genève, Suisse), autorise l'impression de la présente thèse, sans exprimer d'opinion sur les propositions qui y sont énoncées.

Genève, le 25 novembre 2010

Thèse - 4268 -


Le Doyen, Jean-Marc TRISCONE

N.B. - La thèse doit porter la déclaration précédente et remplir les conditions énumérées dans les "Informations relatives aux thèses de doctorat à l'Université de Genève".

*Hâtez-vous lentement, et sans perdre courage,
Vingt fois sur le métier remettez votre ouvrage,
Polissez-le sans cesse, et le repolissez,
Ajoutez quelquefois, et souvent effacez.*

- Nicolas Boileau-Despréaux, *L'Art poétique*, 1674

Acknowledgments

Nothing ever gets done by a person alone, even for those who tend to ignore the influence and help gathered along the way. During the five years of my PhD, I met fantastic people who participated, directly or indirectly, to the quality of this work and for that, I would like to thank them. I apologise in advance to all the people I might forget in the following: if my memory is somewhat imperfect, your influence on me and my work lives on.

First and foremost, I am indebted to my supervisor, Prof. Allan G. Clark, for giving me the opportunity to join the DPNC group and for his constant support. Along the years, I have worked closely with various post-docs, to whom I owe so much. Thanks to Bettina, for all that you've taught me; it was so easy to work with you. Merci Régis, ton court séjour dans notre groupe, et dans notre bureau, fut des plus agréables, et ce, malgré les longues soirées passées à écrire la FSM. A special thanks goes to Gabi, for your endless patience, countless hours and dedication in the completion of this thesis. Thanks also to my numerous office mates, who were always willing to be disturbed by questions and for a good laughter: Didier, Will and Moritz. Thanks to Szymon for bearing with my constant emails about computing. Et Yann, merci pour les conversations informatiques et les fous rires de "geek", ainsi que pour les heures consacrées à des projets de toutes sortes. Of course, thanks to all my colleagues from the DPNC, for all the good times shared, in no particular order: Anna, Sofia, Chiara, Mercedes, Raphaël, Nicolax, Sébastien, Filipe, Rikard, Till, Elina, Valerio, Francesca, Andrew, Alison, Paul, Kilian, Marc, Clemencia, Jose, Sergio, Snežana, Oystein, Gauthier.

A good part of my PhD was spent working with the SCT collaboration and I am grateful to them for the welcoming attitude and the help provided during these exciting years of detector development and commissioning. Special thanks to Heinz

and Pippa for the support and the help. Thanks Anna for showing me the ropes of DCS when I arrived and being so available, even years after. Thanks Sandra for being so kind and welcoming. Thanks to Ewa, Peter and Bjarte, a.k.a. the MoPS crew, for being so patient with a rookie DCS person and for the fruitful collaboration that ensued. Thanks to Richard and Nils, who even from Uppsala, managed to be helpful in times of need. Thanks to Richard Apsimon, Lewis and all the end-cap teams, from Liverpool and NIKHEF, for allowing me to have access to the detector you cared for and loved so much. Thanks to Forrest for keeping it *cool* in all meanings of the word. Thanks also to Heidi, Pamela, Luca, Saverio, and many others from the ID community for the exchange of ideas. A special thanks to Jovan, for agreeing to take over my task to allow me to do some physics, although simulated.

For these recent years, I shifted focus towards electron reconstruction and met there a very valuable crowd. Thanks to the e/gamma group and the J/ψ enthusiasts for the feedback and help, in particular to Tanya Hryn'Ova, Frédéric Derue, Daniel Froidevaux, Else Lytken, Andrew Nelson, Darren Price, Vato Kartvelishvili, and James Catmore. A special thanks to Evelyn for being so helpful at times of need.

I wouldn't be there if it wasn't for the constant support of my dear friends. Thanks to Bilge, for your invaluable contribution in Turkish coffee and so much more. Merci pour tout Thomas, qui eut cru que nos chemins se croiseraient aussi longtemps! Marie, Rafal, Sylvie, David, Hugo, Geneviève, JR, Lorraine, Mathieu, vous êtes de Québécois formidables et si facile à apprécier... A final thanks to all the folks I met in summer schools around the world, I shall meet you again many times I hope!

Merci à mon père de m'avoir donné le plus beau des héritages et à ma famille d'être aussi *éclatée*. *In fine*, Olivier, pour les sacrifices que tu as dû faire, pour les moments de solitude que tu as subis, mais encore et surtout pour ta foi inébranlable en mes capacités dans les moments les plus difficiles, je te rends le plus grand des mercis. Avec toi à mes côtés, rien n'est impossible.

Abstract

The production of J/ψ mesons decaying into electron-positron pairs was studied in simulated proton-proton collisions at 10 TeV using the ATLAS detector at the LHC. The event simulation was performed using the Colour Octet Model for J/ψ meson hadroproduction, tuned on previous measurements from the Tevatron. The Colour Octet Model correctly describes the J/ψ cross-section at the Tevatron but fails to predict the J/ψ polarisation. New measurements of J/ψ production need to be performed in order to test the available theoretical models. The p - p collisions delivered by the LHC and recorded by the ATLAS detector will provide data to perform these measurements. Using the silicon and gaseous tracking detectors, combined with electron identification capabilities of the Transition Radiation Tracker, electrons from J/ψ decay can be measured in the ATLAS detector. In this thesis, a J/ψ cross-section measurement in the electron channel was determined to be feasible, by obtaining the prompt ($pp \rightarrow J/\psi \rightarrow e^+e^-$) and non-prompt ($b\bar{b} \rightarrow J/\psi \rightarrow e^+e^-$) cross-sections simultaneously. The expected precision of the measurement of the total production cross-sections for $p_T^{J/\psi} > 10$ GeV was evaluated to be $\sigma_p = 85 \pm 4$ (stat.) ± 14 (syst.) ± 9 (theo.) nb and $\sigma_{np} = 20 \pm 1$ (stat.) ± 4 (syst.) ± 2 (theo.) nb. The differential p_T cross-sections were also studied.

Résumé

La production du méson J/ψ dans les collisions proton-proton au LHC a été étudiée dans cette thèse. Une simulation du détecteur ATLAS a été utilisée pour produire des collisions avec une énergie de centre de masse de 10 TeV. Ces données ont ensuite servi à la mise au point d'une méthode pour évaluer la section efficace du J/ψ se désintégrant en une paire électron-positron.

Plusieurs modèles théoriques existent pour décrire la production hadronique du J/ψ . Deux d'entre eux sont présentés ici: le modèle de singulet de couleur (CSM) et le modèle d'octet de couleur (COM). Les prédictions calculées à partir de ces deux modèles ont été comparées aux données issues de collisions proton-antiproton produites avec l'accélérateur Tevatron au Fermilab. Le CSM s'est révélé incapable de décrire complètement la section efficace du J/ψ . Les contributions supplémentaires admises dans le cadre théorique du COM ont permis d'obtenir un bon accord entre la prédiction et les mesures de la section efficace. Le COM n'est pas parvenu à prédire adéquatement la polarisation du J/ψ telle que mesurée par les détecteurs du Tevatron. Il s'avère donc nécessaire de continuer à mesurer les paramètres du J/ψ aux nouvelles énergies rendues désormais possibles par le LHC afin de contribuer à l'amélioration de notre compréhension des mécanismes de production hadronique du J/ψ . Deux types de production du J/ψ sont possibles: la production subite, provenant du vertex primaire, et la production non-subite, provenant de la désintégration de mésons B .

Afin de procéder à cette mesure, il faut étudier la reconstruction des objets électromagnétiques, en particulier les électrons, à l'aide du détecteur ATLAS. Les électrons déposent leur énergie dans le calorimètre à argon liquide et, contrairement aux photons qui sont électriquement neutres, laissent une trace dans le trajectographe, au silicium (SCT) et gazeux (TRT). Le TRT permet également l'identification des électrons par rapport aux hadrons grâce à sa détection de la radiation de transition.

Le calorimètre électromagnétique à argon liquide, pour sa part, est segmenté en trois couches radiales, ce qui permet d'étudier la forme des gerbes électromagnétiques. Des coupures sont appliquées sur des variables calorimétriques et relatives aux traces, choisies pour leur pouvoir de réjection hadronique. De plus, il existe trois algorithmes de reconstruction des électrons: originant de l'amas d'énergie (conçu pour les électrons avec une énergie de plus de 5 GeV), originant de la trace (conçu pour les électrons avec une énergie de moins de 5 GeV) ou encore se spécialisant dans les sections du détecteur à grande pseudorapidité. Dans les travaux présentés ici, une étude de la reconstruction des électrons à basse énergie (moins de 5 GeV) a été réalisée. Deux aspects ont été scrutés en détails: la duplication d'amas et la superposition des algorithmes de reconstruction. Dans le premier cas, une modification des paramètres utilisés pour trouver les amas a permis d'en réduire considérablement l'incidence. Dans le deuxième cas, les observations permettent de conclure que l'utilisation de l'algorithme de reconstruction originant des amas d'énergie était suffisante pour observer la désintégration du J/ψ .

À l'aide des échantillons d'événements simulés pour le signal subit et non-subit, ainsi que pour les principales sources de bruit de fond, qui sont les saveurs lourdes (b et c), la production de Drell-Yan et la production de QCD, aussi appelée biais minimal, on mesure la section efficace de production du J/ψ . Une sélection stricte est mise au point afin d'obtenir un sous-échantillon d'événements hautement riche en électrons issus de désintégrations du J/ψ . Si la sélection retient plus d'une paire d'électrons par événement, la plus énergétique est choisie. Cette sélection est effectuée à l'aide de coupures sur l'énergie transverse, la pseudorapidité, la qualité de l'ajustement des paires de traces électroniques de charges opposées au même vertex, la distance angulaire entre les deux électrons, la masse invariante, l'identification des électrons et le système de déclenchement. Une fois cette sélection appliquée, la principale source de bruit de fond résiduelle vient de la production de saveur lourde b . Le bruit de fond résiduel est ensuite soustrait en utilisant des bandes latérales symétriques autour de la masse connue du J/ψ (3.096 GeV). On attribue un poids négatif aux événements situés dans les bandes latérales afin de compenser pour les événements de bruit de fond de la région centrale. Avec le résultat de la soustraction du bruit de fond, on évalue le nombre d'événements de signal total (somme du signal subit et non-subit) ainsi que le ratio \mathcal{R} entre le signal non-subit et subit. La quantité \mathcal{R} est obtenue en ajustant une fonction sélectionnée sur mesure à la distribution du temps propre du J/ψ , un des paramètres de la fonction étant \mathcal{R} .

Les efficacités sont également obtenues pour la sélection décrite précédemment, en fonction de la quantité de mouvement transverse, de la pseudorapidité et de l'angle polaire. À l'aide de ces résultats, les sections efficaces du signal subit et non-subit sont obtenues simultanément. Pour une quantité de mouvement transverse supérieure à 10 GeV, elles sont estimées à 85 ± 4 (stat.) ± 14 (syst.) ± 9 (theo.) nb pour le

signal subit et 20 ± 1 (stat.) ± 4 (syst.) ± 2 (theo.) nb pour le signal non-subit. Les principales sources d'erreurs systématiques sont l'identification des électrons grâce à la radiation de transition, la soustraction du bruit de fond ainsi que le modèle théorique. On conclut que la mesure de la section efficace de la désintégration du J/ψ en paire d'électrons est réalisable avec le détecteur ATLAS et devrait être obtenue avec les données acquises durant l'année 2010 avec une énergie de centre de masse de 7 TeV.

Contents

Acknowledgments	i
Abstract	iii
Résumé	iv
1 Introduction	1
2 Theoretical Introduction	3
2.1 The Standard Model	3
2.1.1 Electroweak interactions	4
2.1.2 Quantum Chromodynamics	6
2.2 J/ψ discovery - the November Revolution	7
2.3 J/ψ production at hadron colliders	10
2.3.1 J/ψ production types	11
2.3.2 Colour Singlet Model	11
2.3.3 Colour Octet Model	14
3 The ATLAS Experiment at the LHC	17
3.1 The Large Hadron Collider	17
3.1.1 The CERN accelerator complex	18
3.1.2 The LHC ring	19
3.2 The ATLAS Detector	21
3.2.1 The Inner Detector	23
3.2.2 The Liquid Argon Calorimeter	27

3.2.3	The Tile Calorimeter	29
3.2.4	The Muon Spectrometer	30
3.3	Luminosity measurement	31
3.4	Data Acquisition and Trigger System	32
3.5	Detector Control System	35
3.6	Event Data Model	35
4	The Detector Control System	38
4.1	The ATLAS DCS	38
4.1.1	JCOP framework	40
4.1.2	Finite State Machine	40
4.2	The SemiConductor Tracker DCS	41
4.2.1	Power Supply DCS	42
4.2.2	Environmental DCS	42
4.2.3	Interlock	45
4.3	The Inner Detector DCS	46
4.3.1	Cooling DCS	46
4.3.2	Environmental DCS	46
4.4	SCT DCS Operations	47
4.4.1	SCT DCS FSM	47
4.4.2	Safety actions	49
4.4.3	Data archiving	50
4.5	SCT DCS Performance	51
5	SCT Commissioning and Performance	57
5.1	The SCT module	58
5.2	SCT calibration	59
5.3	Cosmic Rays on the surface	59
5.3.1	Barrel Reception tests	60
5.3.2	EC Reception tests	60
5.3.3	Combined Testing	61
5.4	Cosmic rays in the ATLAS cavern	62
5.5	Readiness for LHC data-taking	64
6	Electron reconstruction	66
6.1	Charged particle tracking	67
6.2	Electromagnetic Clustering	68
6.2.1	Sliding Window	68
6.2.2	Duplicate Clusters	70
6.3	Reconstruction algorithms	72
6.3.1	Cluster-seeded electrons	72

6.3.2	Track-seeded electrons	74
6.3.3	Forward electrons	75
6.4	Electron Identification	75
6.5	Overlap between cluster- and track-seeded algorithms	78
6.6	Performance for low p_T electrons	81
6.6.1	Four-momentum reconstruction	84
6.7	Trigger selection for electrons	86
7	J/ψ Cross-Section Analysis	89
7.1	Monte-Carlo simulation	89
7.1.1	Signal sample	90
7.1.2	Background samples	93
7.1.3	Detector simulation	95
7.2	Event selection	96
7.2.1	Trigger cuts	97
7.2.2	Offline cuts	97
7.3	Simulation studies	104
7.3.1	Effect of the minimum bias filter	104
7.3.2	Effect of event weights for prompt signal	107
7.3.3	Study of the kinematic cuts in PYTHIA	108
7.3.4	Background composition and shape	112
7.4	Cross-Section Calculation	118
7.4.1	Efficiency estimation	118
7.4.2	Invariant mass fit	127
7.4.3	Background subtraction	128
7.4.4	Prompt and non-prompt fraction estimation	131
7.4.5	Total fiducial prompt and non-prompt J/ψ cross-sections . . .	135
7.4.6	Differential prompt and non-prompt J/ψ cross-sections	136
8	Evaluation of systematic uncertainties	142
8.1	Luminosity	143
8.2	Efficiency	143
8.2.1	Identification efficiency	143
8.2.2	Cut variation	144
8.3	Number of events estimation	147
8.4	Non-prompt-to-prompt ratio	148
8.5	Acceptance	149
8.6	Combined systematic error and final result	151
9	Conclusion and Outlook	154

Glossary	157
Bibliography	160
A Event weights and scaling	172
B Normalised cross-section derivation	176
C Offline selection cuts	179
D Transverse Decay Length	181

List of Figures

2.1	Feynman diagrams of K^+ decays	8
2.2	J/ψ production in e^+e^- collisions.	9
2.3	The charmonium spectrum	10
2.4	Feynman diagrams for J/ψ production	12
2.5	Prompt and direct production cross-section for J/ψ in CDF Run I . .	13
2.6	Direct cross-section for J/ψ in CDF Run I compared to the COM . .	15
2.7	Polarisation α in CDF Run II compared to COM	16
3.1	The LHC injection complex	18
3.2	Layout of the LHC ring	20
3.3	The ATLAS detector	22
3.4	Layout of the Inner Detector barrel	24
3.5	Layout of the Inner Detector with end-caps	25
3.6	Momentum resolution and material distribution in the ID as a function of η	27
3.7	EM Calorimeter accordion geometry	28
3.8	Calorimeter layout in ATLAS	29
3.9	The Muon Spectrometer of ATLAS	30
3.10	Forward detectors for ATLAS	32
3.11	Trigger flow diagram	33
3.12	Expected cross-sections at the LHC, compared to Tevatron	34
3.13	Data flow diagram for data and MC	36
3.14	Tier structure of the ATLAS computing grid	37
4.1	The global ATLAS DCS architecture	39

4.2	The BBIM backplanes	44
4.3	The PS FSM structure	48
4.4	The ENV FSM structure	49
4.5	The SCT barrel temperature uniformity	52
4.6	Evaporative cooling cycle	53
4.7	Hybrid temperature fluctuations and back-pressure	53
4.8	A view of all SCT temperatures for a cooling cycle	54
4.9	Module hybrid temperature distribution	54
4.10	Relative humidity from Xeritron sensors	55
4.11	Dew point and monitored temperature comparison	56
4.12	Module and cooling pipe temperature during incident	56
5.1	The SCT module	58
5.2	Cosmic ray track in the ID barrel	62
5.3	The ID barrel in its final position inside ATLAS	63
5.4	Noise Occupancy for the SCT barrel modules in 2007	63
5.5	The SCT Noise Occupancy in 2008 cosmic ray data	65
5.6	Silicon hit efficiency in 2008 cosmic ray data	65
6.1	Distance between cluster seed positions η_0 and ϕ_0 for duplicate clusters	71
6.2	Energy ratio distribution between 5×5 and 3×7 clusters	73
6.3	Duplicate rate for J/ψ clusters	73
6.4	Author distributions of electron objects in J/ψ events for all identification cuts	80
6.5	Author distributions of electron objects in $Z \rightarrow e^+e^-$ events for all identification cuts	81
6.6	Author distributions of electron objects in J/ψ events with modified preselection cuts	82
6.7	Identification efficiency for electrons from J/ψ	83
6.8	Calorimetric and track information combination for electron objects .	84
6.9	Four-momentum reconstruction checks for electrons from J/ψ	85
6.10	L1 EM algorithm diagrams	87
7.1	MultiLepton filter efficiency as a function of the PYTHIA sub-process code	92
7.2	ΔR between EF trigger and offline electron objects for the signal samples.	99
7.3	Transverse energy distributions before and after reconstruction for electrons from prompt and non-prompt J/ψ decays.	102
7.4	Difference between the J/ψ p_T and the generator level p_T	103
7.5	Leading electron reconstructed transverse energy comparison between filtered and unfiltered minimum bias events	106

7.6	Electron reconstructed transverse energy comparison between filtered and unfiltered minimum bias events after event selection	106
7.7	Electron reconstructed transverse energy distribution for the reduced event selection.	107
7.8	Invariant mass comparison for prompt J/ψ events before and after event reweighting	108
7.9	Shape comparison plots using the simplified electron pair selection with loose identification cuts for different \hat{p}_\perp values.	111
7.10	Invariant mass distribution after the loose event selection for backgrounds.	115
7.11	Invariant mass distribution after reconstruction for the unfiltered minimum bias sample	115
7.12	Correlations between the reconstructed angular distance and the mass of electron pairs for unfiltered minimum bias.	116
7.13	Correlations between reconstructed kinematical variables for filtered minimum bias.	116
7.14	Invariant mass comparison between the opposite-sign (black) and the same-sign (red) selection for backgrounds.	117
7.15	Selection efficiency as a function of the generator level p_T for the prompt and non-prompt signal sample.	120
7.16	Ratio of non-prompt-to-prompt selection efficiency as a function of the generator level p_T	121
7.17	Energy shift for electrons from prompt and non-prompt J/ψ decays.	122
7.18	Rejection of individual electron identification cuts for electrons from prompt and non-prompt J/ψ	123
7.19	Selection efficiency as a function of the generator level η for the prompt and non-prompt signal sample.	124
7.20	Selection efficiency as a function of the generator level ϕ for the prompt and non-prompt signal sample.	125
7.21	Trigger efficiencies after reconstruction.	126
7.22	Trigger efficiencies after event selection.	127
7.23	Fitted invariant mass distribution with signal shape for inclusive J/ψ production.	128
7.24	Sideband background subtraction mass range and linearity.	129
7.25	Dielectron reconstructed distributions for the background contributions after sideband subtraction	130
7.26	Pseudo-proper time distribution for all the samples.	132
7.27	Invariant mass distribution with signal shape after τ_0 cut without background subtraction.	132
7.28	Fitted pseudo-proper time distribution for the signal samples.	133

7.29	Fitted pseudo-proper time distribution for all samples.	134
7.30	Inclusive number of J/ψ events and corrected \mathcal{R} values in reconstructed p_T bins.	136
7.31	p_T distributions before and after unfolding.	137
7.32	MultiLepton filter efficiency as a function of the generator level J/ψ p_T	138
7.33	Differential prompt and non-prompt production cross-sections as a function of the generator level J/ψ p_T	140
8.1	Distribution for R_η on real 2010 collision data compared to simulation.	145
8.2	Distribution for E_{ratio} on real 2010 collision data compared to simulation.	145
8.3	Distribution for $w_{\eta 2}$ on real 2010 collision data compared to simulation.	146
8.4	Distribution for w_{tot} on real 2010 collision data compared to simulation.	146
8.5	Distribution for f_{hTR} on real 2010 collision data compared to simulation.	147
8.6	Fit to the background shape in the invariant mass window.	149
8.7	Comparison between $\hat{p}_\perp > 1$ GeV and $\hat{p}_\perp > 3$ GeV samples as a function of the generator level p_T	150
8.8	Differential prompt and non-prompt production cross-sections as a function of the generator level J/ψ p_T	152
9.1	Dielectron invariant mass in the J/ψ mass range using 77.8 nb ⁻¹ of 2010 LHC data.	156
D.1	Transverse decay length diagram	181

List of Tables

2.1	The particle spectrum of the Standard Model	4
2.2	Charmonium characteristics	10
2.3	J/ψ production types.	11
3.1	Beam parameters for the LHC	21
3.2	Performance goals for the ATLAS detector	23
4.1	The number of environmental sensors and their physical distribution .	43
6.1	Sliding Window parameters, before and after optimisation.	70
6.2	Bin definitions in η and E_T for identification cuts.	76
6.3	Track-seeded preselection cuts before and after modification.	82
6.4	Reconstruction and identification performance for J/ψ electrons . . .	83
6.5	L1 & L2 thresholds used for the trigger chain e5_medium.	86
7.1	Parameters of the PYTHIA generator used for the production of the prompt J/ψ sample.	90
7.2	Definition of the PYTHIA generator sub-process codes used for prompt J/ψ production.	91
7.3	Event weights and fractions for the prompt J/ψ sample	93
7.4	Parameters of the PYTHIA generator used for the production of the low-mass Drell-Yan sample.	93
7.5	Parameters of the PYTHIA generator used for the production of the minimum bias sample.	94
7.6	Parameters of the PYTHIA generator (and PythiaB interface) used for the production of the heavy flavour samples.	95

7.7	Cross-section information about all samples used in this analysis . . .	96
7.8	Selection efficiencies for individual cuts on all samples	101
7.9	NoETCut and NoETCut+dR selections used for the minimum bias filter bias study.	105
7.10	Event weights and fractions for the prompt signal sample generated with $\hat{p}_\perp > 1$ GeV	109
7.11	Expected signal rates for prompt J/ψ signal	110
7.12	Absolute electron efficiencies per production channel	110
7.13	Predefined particles types and origins used by the EgammaMCTruth- Classifier tool and their description.	113
7.14	Truth classification for background samples before event selection. . .	113
7.15	Truth classification for background samples after tight event selection.	114
7.16	Expected yields of signal events for $\int \mathcal{L} dt = 5 \text{ pb}^{-1}$	130
7.17	Expected yields of signal events for $\int \mathcal{L} dt = 5 \text{ pb}^{-1}$ after τ_0 cut. . . .	131
7.18	Results summary for the cross-section calculation.	135
7.19	Differential prompt and non-prompt J/ψ production cross-sections re- sults.	139
7.20	Results summary in p_T bins for the cross-section calculation.	141
8.1	Efficiency variations for the electron identification cuts.	144
8.2	Offline selection cut systematic uncertainties.	148
8.3	Differential prompt and non-prompt J/ψ production cross-section re- sults, with systematic uncertainties.	153
B.1	Generator level quantities used for the normalised cross-section calcu- lation.	177

CHAPTER 1

Introduction

The study of the fundamental constituents of our universe, or *particle physics*, has a longstanding history. Born with the Greeks and the idea that matter is composed of indivisible elementary particles, or *atoms*, it truly acquired momentum in the 19th and 20th centuries with the successive discoveries of the constituents of the atom and the advent of the underlying theories of matter and forces, used to build the model that encompasses our current understanding of the universe, the Standard Model. With extraordinary accuracy and rewarded by several Nobel prizes, the Standard Model has successfully predicted the particle physics discoveries of the 20th century.

One of the discoveries that established the concept of quarks as components of matter was the J/ψ meson. Composed of a charm-anti-charm quark pair, it appeared first in lepton collisions in the 1970's. It was later on observed at hadron colliders, such as the ISR at CERN and Tevatron at Fermilab. Although a lot of work has been accomplished to understand its physical properties, the theoretical description of its hadroproduction is still not complete to this day. Several concurrent models have been developed and tested against data and no single one could describe the observations perfectly.

At CERN, the world's most powerful particle physics accelerator, the Large Hadron Collider (LHC) is starting its operation, colliding bunches of protons at a center of mass energy of 7 TeV. This new hadron collider allows us to explore a new energy regime and sets the stage for potentially exciting discoveries. In order to look for these new phenomena, it is crucial that we rediscover the existing spectrum of particle physics. Moreover, we can take the opportunity to peek at some of the remaining questions of the Standard Model. The J/ψ hadroproduction is one of them, and we need new data and new measurements to fulfill our understanding of the matter.

The LHC could achieve this task. From the previous hadron collider measurements, we know we can observe the J/ψ meson in one of its leptonic decay channels, using a muon-anti-muon pair as the decay product. In this thesis, we study the feasibility of a J/ψ production cross-section measurement using electrons and positrons with the ATLAS detector. By doing this, we aim at providing a cross-check of the measurement performed using muons and anti-muons. Furthermore, the electrons and positrons originating from J/ψ decays provide an excellent calibration signal for the energy regime below 10 GeV. It is also one of the earliest physics measurement that can be performed with the LHC data.

In the following work, we determine that such a cross-section measurement can be performed using the ATLAS detector, given the many challenges that this measurement poses. A method for calculating the prompt and the non-prompt J/ψ cross-sections, using the inclusive number of events, i.e. from both prompt and non-prompt contributions, and the fitted ratio of the non-prompt-to-prompt components, is validated. A value is obtained for the differential p_T and total cross-section at a center of mass energy of 10 TeV, where the total value is considered for $p_T > 10$ GeV. The systematic uncertainty is significant (around 20%) and needs to be controlled by adjusting cut values on sensitive variables, especially for the electron identification.

To lead to the final cross-section estimation, a theoretical introduction is presented, describing the Standard Model and outlining our current understanding of the hadroproduction of J/ψ mesons. The ATLAS detector is described, focusing on the detector elements which are important for measuring and identifying electrons. As tracking is a key component of the electron reconstruction, the main tracking device of the ATLAS detector, the SemiConductor Tracker (SCT), is described in detail, followed by a review of the Detector Control System for the SCT, which I contributed to develop for 2 years. A synopsis of the electron reconstruction and identification methods, together with results of studies aimed specifically at low p_T electrons, is provided. Finally, the cross-section measurement method and the various studies performed on the simulated data are presented and the estimation of the systematic uncertainty is given.

CHAPTER 2

Theoretical Introduction

*Charm is a product of the
unexpected.*

- José Martí

During the 20th century, particle physics was built upon the interplay between insightful experimental discoveries and successful theoretical predictions; the J/ψ meson, which is the subject of the work presented in this thesis, is no exception. In the following, a short introduction to the theoretical foundation of particle physics is presented together with a review of the J/ψ meson history and present issues.

2.1 The Standard Model

Particle physics is the study of the elementary constituents and interactions of nature. It relies on two major concepts, matter and forces, which are accurately described by quantum fields. Known constituents of matter are spin- $1/2$ particles called *fermions* since they obey Fermi statistics. Fermions are subdivided into *quarks*, which carry colour charge (see §2.1.2 for more) and *leptons*, which do not. Force mediators carry integer spin and are called *bosons* since they obey Bose-Einstein statistics. A relativistic quantum field theory built upon the non-Abelian gauge symmetry $SU(3) \times SU(2) \times U(1)$, the Standard Model of particle physics [1], describes the dynamics of the fundamental fields. In Table 2.1, the particle spectrum, which is used as an input to the Standard Model, is shown with the associated quantum numbers [2].

Hypercharge	Charge	Spin	Fermions	Bosons	Spin	Charge	Hypercharge
-1	0 -1	$\frac{1}{2}$	Leptons	W^\pm Z, γ	1	± 1 0	0
			$\nu_e \quad \nu_\mu \quad \nu_\tau$ $e \quad \mu \quad \tau$				
$+\frac{1}{3}$	$+\frac{2}{3}$ $-\frac{1}{3}$	$\frac{1}{2}$	Quarks	$g (8)$	1	0	0
			$u \quad c \quad t$ $d \quad s \quad b$				
				H	0	0	-1

Table 2.1: The particle spectrum of the Standard Model. The weak hypercharge $Y = 2(Q - T_3)$ is given here.

The fermions are arranged according to their quantum numbers. Shown horizontally in Table 2.1, the *up-type* quarks (with electric charge of $+\frac{2}{3}$) and *down-type* (with electric charge of $-\frac{1}{3}$), as well as *charged* and *neutral* leptons are all composed of three members, which are distinguishable by their different mass. The vertical arrangement in Table 2.1 describes the classification of fermions in *generations*, or *families*. One generation is composed of two quarks, one up-type and one down-type quark, and 2 leptons, one charged and one neutral. Three generations of particles are used in the Standard Model, with increasing mass going from the first (u, d, e, ν_e) to the third generation (t, b, τ, ν_τ). This mass hierarchy allows for decays from higher to lower generations, while the first generation particles are stable. Each particle has a corresponding *antiparticle*, with the same mass but opposite quantum charges, such as electric charge, baryon number, lepton number, flavour charges and weak isospin. Particles with neutral quantum charges are their own antiparticle. In Table 2.1, the particle and antiparticle are shown only for the W boson.

The Lagrangian of the Standard Model is shown in Eq. 2.1. The two first terms are described in §2.1.1 and the last one, in §2.1.2 below.

$$\mathcal{L}_{SM} = \mathcal{L}_{EW} + \mathcal{L}_{Higgs} + \mathcal{L}_{strong} \quad (2.1)$$

2.1.1 Electroweak interactions

Electromagnetism is the study of electrically charged particles and of the force they exert on each other through a field. It is described by Maxwell's equations which unified two known physics phenomena: electricity and magnetism. Its description using Quantum Electrodynamics (QED) was the first great success of quantum field theory and more specifically, of local gauge field theory. The latter is defined as a field theory in which the Lagrangian is invariant under local gauge transformations, that is

a phase transformation of a field at every space-time point. QED is the simplest gauge theory one can build, since it is Abelian and one-dimensional, but carries principles that are used throughout the Standard Model [3].

In QED, the local gauge invariant Lagrangian is written as shown in Eq. 2.2, where ψ is the bispinor field of the electron, A^μ is the photon field and the photon field tensor $F^{\mu\nu} \equiv \partial^\mu A^\nu - \partial^\nu A^\mu$.

$$\mathcal{L}_{QED} = \bar{\psi}(i\gamma_\mu D^\mu - m)\psi - \frac{1}{4}F^{\mu\nu}F_{\mu\nu} \quad (2.2)$$

D^μ is called the *covariant derivative* and is defined as $D^\mu \equiv \partial^\mu + ieA^\mu$. The Dirac matrices, γ_μ , are the spin and charge operators acting on ψ and m is the electron mass. $\bar{\psi}$ is the Dirac adjoint field of ψ , defined as $\bar{\psi} \equiv \psi^\dagger \gamma_0$. The QED Lagrangian is invariant under local gauge transformations of the U(1) group, i.e. $\psi \rightarrow e^{ie\theta}\psi$ and $A^\mu \rightarrow A^\mu + \partial^\mu \theta$, and it has only one corresponding gauge coupling e , the electric charge.

The weak force, as its name states, is the weakest of all known forces of nature. It is mainly characterised by its unique capacity of changing the flavour of quarks involved in a reaction, hence explaining radioactivity. QED and weak interactions can be unified using an unbroken $SU(2)_L \times U(1)_Y$ theory. Here, L means that the $SU(2)$ gauge symmetry applies to the left-handed fermion fields only, thus expressing the chiral nature of the fermions, which was observed in the asymmetry of beta decays for Cobalt-60 [4]. The quantum number associated to the weak force, the weak isospin T , is conserved. The independent $U(1)_Y$ symmetry introduces the conservation of the *hypercharge* Y for all chiralities. Eq. 2.3 shows the Lagrangian of the electroweak sector of the Standard Model, where the isotriplet W_i ($i=1,2,3$) is the massless gauge field for the adjoint representation of $SU(2)_L$, defined in Eq. 2.4, the isosinglet B is the massless gauge field in $U(1)_Y$, defined in Eq. 2.5 and the covariant derivative D^μ is defined in Eq. 2.6. The two electroweak coupling parameters, g_w for $SU(2)$ and g'_w for $U(1)$, determine the strength of the interactions.

$$\mathcal{L}_{EW} = \bar{\psi}i\gamma_\mu D^\mu\psi - \frac{1}{4}W_i^{\mu\nu}W_{\mu\nu}^i - \frac{1}{4}B^{\mu\nu}B_{\mu\nu} \quad (2.3)$$

$$W_i^{\mu\nu} = \partial^\mu W_i^\nu - \partial^\nu W_i^\mu - g_w \epsilon_{ijk} W^{j\mu} W^{k\nu} \quad (2.4)$$

$$B^{\mu\nu} = \partial^\mu B^\nu - \partial^\nu B^\mu \quad (2.5)$$

$$D^\mu = \partial^\mu + ig_w W_i^\mu T^i + \frac{ig'_w}{2} B^\mu Y \quad (2.6)$$

The $SU(2)_L \times U(1)_Y$ symmetry is not observed in nature for our energies ($\sim 10^{-13}$ GeV) since, at energies around 246 GeV, it undergoes a spontaneous symmetry breaking. Terms are added to the Standard Model Lagrangian as shown in

Eq. 2.7. The potential in \mathcal{L}_Φ is minimised by a non-zero value of the Φ field, called v , the vacuum expectation value or *v.e.v.*, defined in Eq. 2.8, where $H(x)$ is a real field. This procedure is called the *Higgs mechanism*. It allows to write physically distinct mass eigenstates as linear combinations of the unbroken $SU(2)_L \times U(1)_Y$ massless fields.

$$\mathcal{L}_\Phi = |D_\mu \Phi|^2 - \lambda(\Phi^\dagger \Phi - \mu^2/2\lambda)^2 - \sum_n g_n \phi^0 \bar{\psi}_n \psi_n \quad (2.7)$$

$$\Phi = \begin{pmatrix} \phi^+ \\ \phi^0 \end{pmatrix} = \begin{pmatrix} 0 \\ \frac{1}{\sqrt{2}}(v + H(x)) \end{pmatrix} \quad (2.8)$$

The real and positive constants of the Higgs potential are chosen such that $v^2 = \frac{\mu^2}{\lambda}$. In order to give masses to all particles of the Standard Model, Yukawa interaction terms with the Φ field are introduced by the last term of Eq. 2.7 for each of the fermions (leptons, quarks). In the case of quarks, the presence of non-diagonal terms in the Lagrangian arising from these Yukawa interactions will give rise to flavour mixing.

2.1.2 Quantum Chromodynamics

In addition to electroweak interactions, the Standard Model requires a theory of strong interactions, as observed in nature. Quantum Chromodynamics can play this role, as a successor to the simpler Quark-Parton model. It is an $SU(3)$ local non-Abelian gauge theory. It introduces a new quantum number, *colour*, which forms a triplet for each quark flavour (red, green and blue) and transforms under the $SU(3)$ gauge group. Colour is needed to build baryonic bound states (e.g. $\Omega^-(sss)$) which would otherwise violate Fermi-Dirac statistics [5].

The Lagrangian of QCD is shown in Eq. 2.9. It shares similarities with Eq. 2.2.

$$\mathcal{L}_{strong} = \bar{\psi}_j (i\gamma_\mu D_{jk}^\mu - M_{jk}) \psi_k - \frac{1}{4} F_a^{\mu\nu} F_{\mu\nu}^a \quad (2.9)$$

$$D_{jk}^\mu = \delta_{jk} \partial^\mu + ig(T^a)_{jk} G_a^\mu \quad (2.10)$$

$$F_a^{\mu\nu} = \partial^\mu G_a^\nu - \partial^\nu G_a^\mu - g f_a^{bc} G_b^\mu G_c^\nu \quad (2.11)$$

The indices $a, b, c \in [1, 8]$ and $j, k \in [1, 3]$ represent the colour respectively for gluon and quark fields. The QCD coupling constant is defined as $\alpha_s \equiv g^2/4\pi$, using the coupling parameter g from Eq. 2.11. M_{jk} is the quark mass matrix, D_{jk}^μ is the covariant derivative acting on quark fields (Eq. 2.10), G_a^μ are the gluon fields and $F_a^{\mu\nu}$ is the gluon field tensor (Eq. 2.11). T^a are the $SU(3)$ generators, which are also

known as the eight Gell-Mann matrices and f_a^{bc} are the structure constants of SU(3) which are defined as $[T_a, T_b] = if_{abc}T^c$. Only colour singlet states exist in nature so meson constituents are of the same colour, $q_a\bar{q}^a$, while baryon constituents are totally anti-symmetric in colour, $\epsilon^{abc}q_aq_bq_c$.

The dynamics of quarks and gluons are different from electroweak interactions since they cannot be observed as free particles. This property of QCD is called *confinement*, since the quarks and gluons are said to be confined inside bound states. It originates from the particular running of the coupling constant α_s . Like in QED, the coupling constant for QCD depends on the energy scale. For electrons, the charge is said to be screened by vacuum polarisations and so the coupling constant α_{em} increases with energy (decreases with distance). In the case of strong interactions, the value of the coupling constant α_s has the inverse behaviour, i.e. it decreases with energy (increases with distance). The vacuum here can be seen as a paramagnetic medium for colour, hence having an antiscreening effect for colour charges. This is typical of a non-Abelian theory, where the bosons (here the gluons) carry charge (colour) and can have self-interactions. The particular running of α_s is described by the perturbative expansion of its β function, as shown in Eq. 2.12, where n_f is the number of light flavours; the first order coefficient of the expansion is negative for $n_f \leq 16$.

$$\beta(\alpha_s) = \mu^2 \frac{d\alpha_s}{d\mu^2} = -\alpha_s \left(\left(11 - \frac{2}{3}n_f \right) \frac{\alpha_s}{4\pi} + \dots \right) \quad (2.12)$$

This property of QCD is called *asymptotic freedom* [6]. Due to this, it is possible to calculate expectations of QCD using perturbation theory at high energies (which is possible at all scales in QED), leading to very precise predictions. The non-perturbative QCD regime is less well understood.

2.2 J/ψ discovery - the November Revolution

In the 1960s, a plethora of new bound states were discovered, leading to the so-called *particle zoo*. The Standard Model described above, which is the most successful attempt at explaining the composition and interactions of these particles, was still being elaborated and only three flavours of quarks (u, d, s) were known. Using only these, the Cabibbo theory of weak interactions [7] was successful at explaining decays involving a change in strangeness¹ $\Delta S = 1$ in charged currents. However, the corresponding neutral current decays, better known as Flavour Changing Neutral Currents (FCNC), predicted by the Cabibbo theory, were never observed. A stringent upper

¹*Strangeness* is a quantum number attributed to a bound state based on its number of strange quarks.

limit on them was determined, as shown in Eq. 2.13. The Feynman diagram of the FCNC decay of K^+ , so called since it is mediated through a Z exchange, is shown in Fig. 2.1(a), while its counterpart, the flavour changing charged current, is shown in Fig. 2.1(b).

$$\frac{K^+(u\bar{s}) \rightarrow \pi^+(u\bar{d}) + \nu + \bar{\nu}}{K^+(u\bar{s}) \rightarrow \pi^0(d\bar{d} - u\bar{u}) + \mu^+ + \nu_\mu} \leq 10^{-5} \quad (2.13)$$

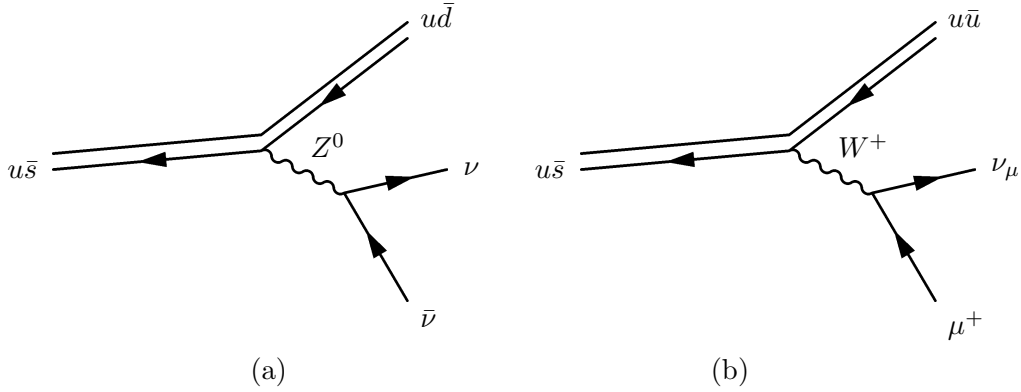


Figure 2.1: Feynman diagrams of K^+ decays: (a) FCNC (b) Flavour changing charged current.

In 1970, Glashow, Iliopoulos and Maiani introduced a new quark, the charm quark c , with charge $+\frac{2}{3}$, hence creating two symmetric doublets of quarks. With this addition to the theory, the contribution from strangeness-changing neutral weak currents could be cancelled, in agreement with its non-observation. This is known as the GIM mechanism [8]. Together with the addition of a quark to the theory, the three authors also predicted the existence of charmed particles which would have escaped detection up to then due to their high mass (~ 2 GeV) and their short lifetime.

In November 1974, this prediction was verified by experiment with the discovery of a new, very narrow, resonance with a mass of 3.1 GeV decaying to a lepton pair, hence establishing the existence of the charm quark. This discovery was special as it came so suddenly, on top of being performed simultaneously by two groups in different facilities. At Brookhaven National Laboratory, the Alternating Gradient Synchrotron (AGS) was used by Samuel C.C. Ting and his MIT colleagues to send 28 GeV protons on a beryllium target [9]. At Stanford Linear Accelerator Center (SLAC), Burton Richter and his team used the SPEAR e^+e^- collider [10]. Each facility observed a peak in the e^+e^- invariant mass distribution for the corresponding reaction:

$$\begin{aligned}
(\text{SLAC}) \quad & e^+e^- \rightarrow \psi \rightarrow e^+e^- \\
(\text{BNL}) \quad & p + Be \rightarrow J + X \rightarrow e^+e^- + X
\end{aligned}$$

The observation was quickly confirmed by the Frascati group [11] in e^+e^- annihilation. The first charmed meson gets its composite name from its simultaneous observation by two groups which named it differently (J for the MIT team and ψ by the SLAC team). Paying respect to all of its discoverers, this member of the charmonium family was called J/ψ . In the same year, another resonant state of the same nature, but with slightly higher mass, was observed by Richter's group [12], this time being called ψ' or $\psi(2S)$.

The shape of the resonance curve in [10] was characteristic of two interfering amplitudes: direct production and production via an intermediate photon, shown in Fig. 2.2. This interference established that the new particle must have the same quantum numbers as the photon, as shown in Table 2.2. Furthermore, its leptonic decay indicated that the new resonance must be a meson and its narrow width excluded the known flavours. It was then postulated that the new J/ψ particle must be a $c\bar{c}$ meson. The isospin assignment could be established after measurements of the hadronic decays $J/\psi \rightarrow \rho\pi$.

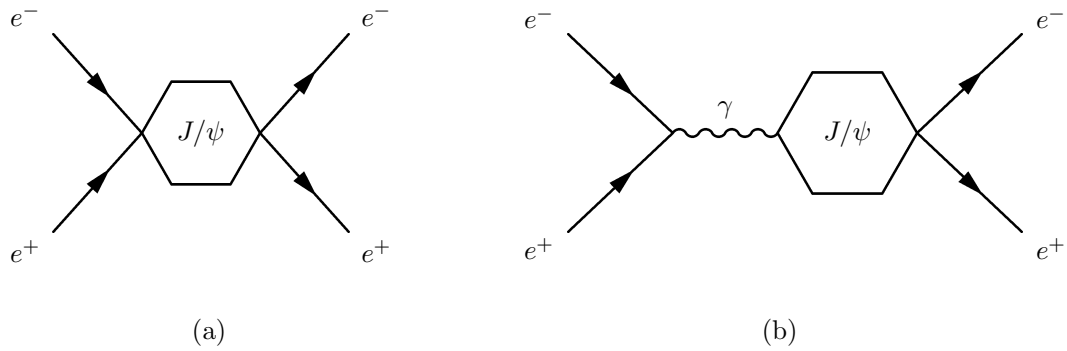


Figure 2.2: J/ψ production diagrams showing the interference with a photon intermediate state in e^+e^- : (a) direct J/ψ production and (b) J/ψ production via an intermediate state.

As two states with the same quark composition were discovered, it became clear that they were forming a whole family of excited states, similar to the positronium

State	Mass (MeV)	Γ (keV)	J^{PC}	I^G	Branching ratios
$J/\psi = \psi(1S)$	3096.916 ± 0.011	93.2 ± 2.1	1^{--}	0^-	hadrons $87.7 \pm 0.5\%$ e^+e^- $5.94 \pm 0.06\%$ $\mu^+\mu^-$ $5.93 \pm 0.06\%$
χ_{c0}	3414.75 ± 0.31	10500 ± 800	0^{++}	0^+	$\gamma J/\psi$ $1.28 \pm 0.11\%$
χ_{c1}	3510.66 ± 0.07	880 ± 50	1^{++}	0^+	$\gamma J/\psi$ $36.0 \pm 1.9\%$
χ_{c2}	3556.20 ± 0.31	1950 ± 130	2^{++}	0^+	$\gamma J/\psi$ $20.0 \pm 1.0\%$
$\psi' = \psi(2S)$	3686.093 ± 0.034	286 ± 16	1^{--}	0^-	$J/\psi X$ $57.4 \pm 0.9\%$

Table 2.2: Charmonium characteristics [13]. The list of decays is not exhaustive: only the decays related to J/ψ are listed. Γ is the decay width of the short-lived particle.

spectrum. These states are known under the name of charmonium (in analogy to positronium) and their full spectrum is shown in Fig. 2.3.

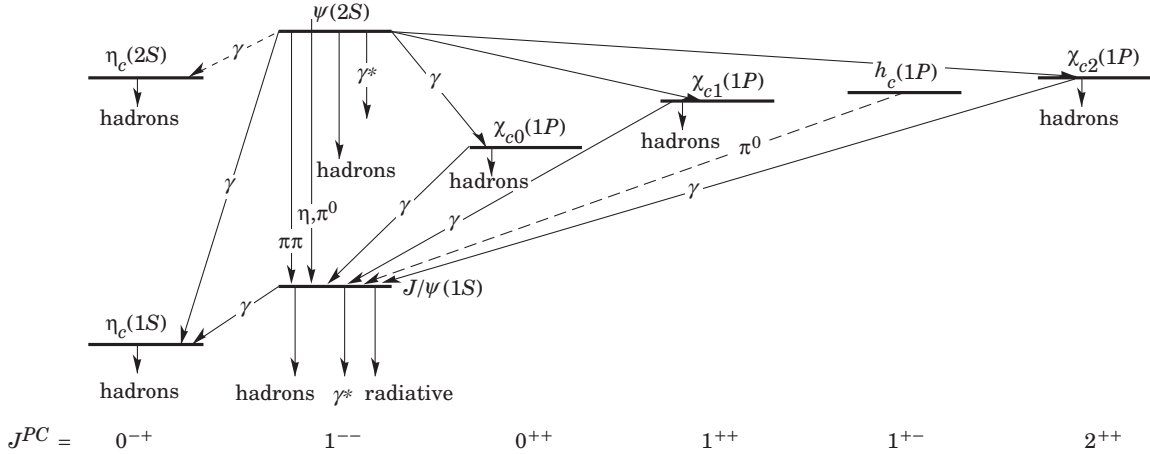


Figure 2.3: The charmonium spectrum [13].

2.3 J/ψ production at hadron colliders

Following its discovery, the J/ψ meson was observed and measured in various other facilities, in particular in hadron colliders like the ISR at CERN, RHIC and the Tevatron. Many models have been elaborated to understand its production mechanism, but none was successful at fitting the data completely; in particular the polarisation

is still not understood. A short review of the latest data and models is presented below, based on previous work [14].

2.3.1 J/ψ production types

Before discussing experimental results and theoretical models, the distinction between the different production types of charmonium needs to be established. *Prompt* production is defined as any process producing a J/ψ coming from the primary vertex. This is then subdivided into *direct* production, where the J/ψ is coming directly from the primary interaction, and *indirect* production, where the J/ψ is the decay product of a higher charmonium state. For indirect J/ψ production, the excited charmonium states² can be ψ' and $\chi_{c(0,1,2)}$. We then define *non-prompt* production as J/ψ coming from the decay of a B meson, detected by the presence of a secondary vertex in the event. It can also be included in the *indirect* contribution, depending on the author. Table 2.3 summarises the production types.

Main type	$c\bar{c}$ pair production	charmonium production	charmonium decay	Specific type
Prompt	$p\bar{p} \rightarrow c\bar{c} + X$	$c\bar{c} \rightarrow J/\psi$	—	Direct
		$c\bar{c} \rightarrow \chi_c$ $c\bar{c} \rightarrow \psi'$	$\chi_c \rightarrow J/\psi + \gamma$ $\psi' \rightarrow J/\psi + X$	—
Non-prompt	$p\bar{p} \rightarrow b\bar{c} + X$ $b\bar{c} \rightarrow c\bar{c} + \ell^- + \bar{\nu}_\ell$ etc	$c\bar{c} \rightarrow J/\psi$ $c\bar{c} \rightarrow \chi_c$	— $\chi_c \rightarrow J/\psi + \gamma$	—

Table 2.3: J/ψ production types.

2.3.2 Colour Singlet Model

In the early 90's, a few models were elaborated to explain the production of J/ψ in hadron collisions. We concentrate on two of them, the Colour Singlet Model (CSM) here and the Colour Octet Model (COM) in §2.3.3.

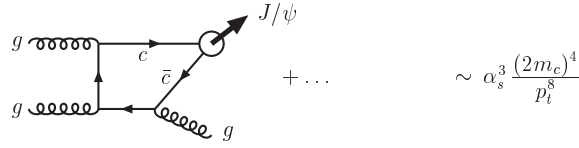
The CSM was developed to describe the production of charmonium and bottomonium. It uses the factorisation theorem³ to divide the heavy meson production

² h_c decay to J/ψ was not observed so far.

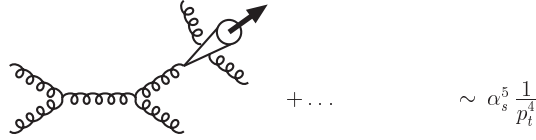
³The QCD factorisation theorem allows to separate the cross-section of a process in two parts: the short distance one, called *perturbative*, and the long distance one, called *non-perturbative* [15].

in a perturbative step, the production of two on-shell heavy quarks, and a non-perturbative one, the soft binding of the quark pair into a meson. The static approximation, which states that the quarks are at rest in the meson frame during the formation of the bound state, is used for the non-perturbative step. The assumption that the colour is unchanged during the whole process (the J/ψ is a colour singlet state) lead to the name of the model. The main contribution to the charmonium production is through gluon fusion as can be seen in Fig. 2.4(a). This contribution increases as the collider energies get higher and should be so at the LHC.

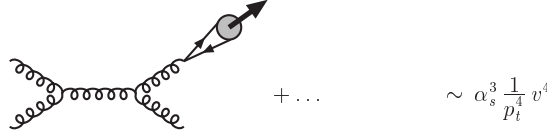
(a) leading-order colour-singlet: $g + g \rightarrow c\bar{c}[^3S_1^{(1)}] + g$



(b) colour-singlet fragmentation: $g + g \rightarrow [c\bar{c}[^3S_1^{(1)}] + gg] + g$



(c) colour-octet fragmentation: $g + g \rightarrow c\bar{c}[^3S_1^{(8)}] + g$

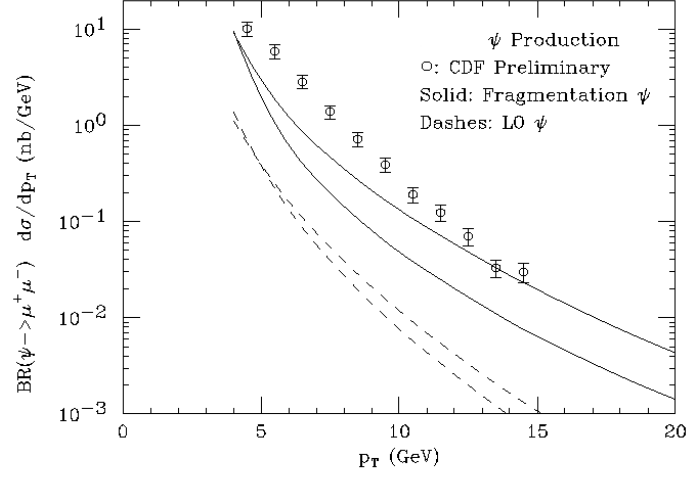


(d) colour-octet t -channel gluon exchange: $g + g \rightarrow c\bar{c}[^1S_0^{(8)}, ^3P_J^{(8)}] + g$

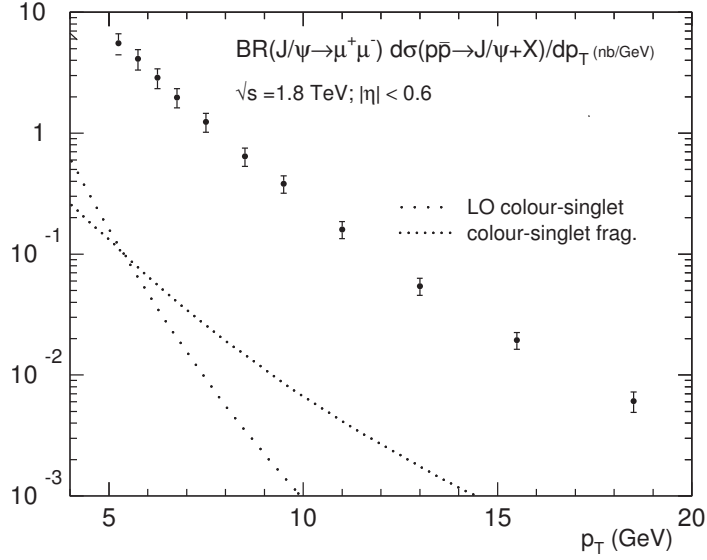


Figure 2.4: Feynman diagrams of the different contributions to J/ψ production in hadron collisions [16].

This model had some success, but failed to fit accurately the prompt cross-section for J/ψ (see Fig. 2.5(a)) and ψ' , measured in CDF Run I [17]. In the latter case, the discrepancy was even larger and was known as the ψ' *anomaly*. A contribution from gluon fragmentation was added to the CSM in an attempt to solve this problem, but this lead to a bigger discrepancy in the direct cross-section for J/ψ measured in CDF Run I [18], as can be seen from Fig. 2.5(b).



(a)



(b)

Figure 2.5: (a) Prompt and (b) direct cross-section for J/ψ in CDF Run I [17, 18] compared to CSM predictions [14].

2.3.3 Colour Octet Model

Together with the observed cross-section discrepancies, the CSM had to deal with a more fundamental theoretical problem: the appearances of infrared divergencies in the cross-section and decay rate for P -wave quarkonium (χ_c and h_c) at Leading Order (LO). These were regulated by introducing a cut-off on the binding energy of the bound state, but they were an indication that the theory was incomplete.

Given the shortcomings of the CSM, there was a need to define a model in which the previously mentioned discrepancies would disappear. One possible way to improve the CSM is by using the Non-Relativistic QCD framework (NRQCD), an effective field theory which treats the quark-antiquark pair as non-relativistic. This is essentially using the static approximation of the CSM and pushing it further by considering the contribution of higher Fock states [19] in the quarkonium wave function expansion. These new states were introduced originally to naturally cancel the infrared divergencies mentioned above. The NRQCD framework contribution to the CSM introduced sums over colours in the effective Lagrangian, hence allowing new coloured contributions to the production, as can be seen in Fig. 2.4. The new model thus created is logically called Colour Octet Model (COM) since the quark and antiquark produced by the hard-scatter can be in a colour octet state. They can then evolve into a quarkonium state (which is a colour singlet state) by the emission of soft gluons. In this model, the production cross-section for J/ψ at hadron colliders is given by Eq. 2.14, where $ij \in \{gg, gq, q\bar{q}\}$, $f_{i/p}$ and $f_{j/p}$ are the parton density functions for the colliding particles. The cross-section is a sum over all possible colour and angular momentum states of $Q\bar{Q}$, denoted by n , which factors into a short-distance coefficient $d\hat{\sigma}$ and a long-distance matrix element $\langle \mathcal{O}^{J/\psi}[n] \rangle$. The exponent of the m_c factor, L_n , is the orbital angular momentum for the given state of $Q\bar{Q}$, which is 0 for S -wave states and 1 for P -wave states.

$$d\sigma(pp \rightarrow J/\psi + X) = \sum_{i,j} \int dx_1 dx_2 f_{i/p}(x_1) f_{j/p}(x_2) \times \sum_n d\hat{\sigma}(i + j \rightarrow Q\bar{Q}[n] + X) \frac{\langle \mathcal{O}^{J/\psi}[n] \rangle}{m_c^{2L_n}} \quad (2.14)$$

The CSM contributions (for LO and fragmentation) are shown in Fig. 2.4(a)-(b) and the added contribution for the COM are shown in Fig. 2.4(c)-(d). In the LO diagram of Fig. 2.4(a), it is indicated on the right-hand side that the parton differential cross-section $d\sigma/dp_t^2$ goes as $1/p_t^8$. This cannot hold at higher transverse momentum $p_t \gg 2m_c$, where the fragmentation contribution (from gluon splitting into $c\bar{c}$) becomes dominant as it scales like $1/p_t^4$. An example of fragmentation diagram

from quarkonium production is shown in Fig. 2.4(b). The new contributions of the COM that are believed to be dominant at the Tevatron energies are the fragmentation diagrams, like the one shown in Fig. 2.4(c). At $p_t \sim 2m_c$, other contributions from the COM become significant and one of them is the t -channel gluon exchange shown in Fig. 2.4(d). The new contributions scale as v^4 , where v is the heavy quark velocity.

The COM was tested against experimental data and obtained a great success at describing the direct cross-section for J/ψ , as can be seen from Fig. 2.6, where the COM matrix elements are fitted to the data. The new octet contribution, which is greater than the CSM one by an order of magnitude, brings the prediction on top of the data for $d\sigma/dp_t$. The CDF collaboration also measured the J/ψ polarisation. The J/ψ is a spin-1 massive particle, hence having three polarisations. To achieve this measurement, the angular distribution of the decay products (in this case, muons) was used. The quantity θ is defined as the angle between the μ^+ direction in the J/ψ rest frame and the J/ψ direction in the lab frame. The distribution $I(\cos\theta)$ can be expressed as Eq. 2.15. The polarisation parameter, α , is then given by Eq. 2.16.

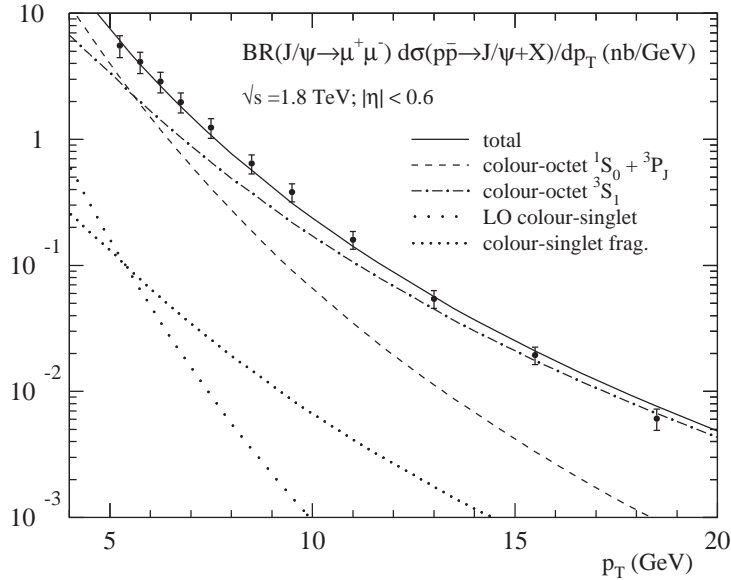


Figure 2.6: Direct cross-section for J/ψ in CDF Run I [18] compared to COM predictions [16].

$$I(\cos \theta) = \frac{3}{2(\alpha + 3)}(1 + \alpha \cos^2 \theta) \quad (2.15)$$

$$\alpha = \frac{\frac{1}{2}\sigma_T - \sigma_L}{\frac{1}{2}\sigma_T + \sigma_L} \quad (2.16)$$

A value of $\alpha = 0$ implies that the J/ψ is not polarised, $\alpha = +1$ a full transverse polarisation and $\alpha = -1$ a full longitudinal one. The value measured by CDF for prompt J/ψ production is shown in Fig. 2.7, together with an expected value from the COM. The observations lead to a polarised J/ψ while the COM tends towards a transverse polarisation. This disagreement indicates that the COM is not the final answer to explain charmonium production.

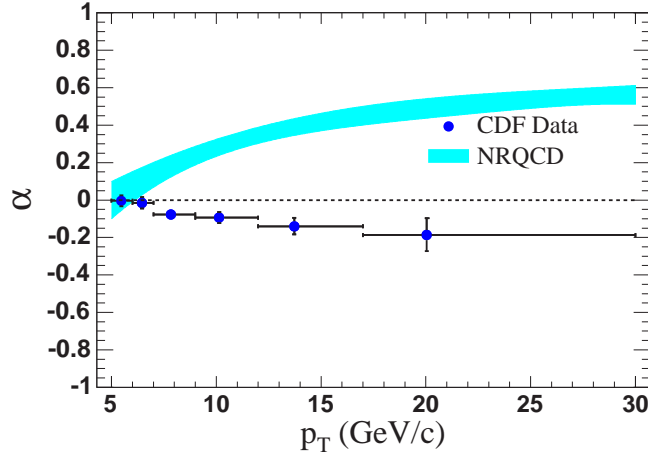


Figure 2.7: Polarisation α in CDF Run II compared to COM predictions [20].

Other models were developed to try to overcome these problems, but none of them succeeded to fully agree with the data. Measurements have been done at Tevatron [21] with a center of mass energy of 1.96 TeV while going lower in the J/ψ transverse momentum but they were not used for comparison with the models. A measurement of the cross-section at LHC energies is thus essential to shed light on quarkonium production. This thesis aims to study the feasibility of a cross-section measurement of the J/ψ production in the electron-positron final state with the ATLAS detector.

CHAPTER 3

The ATLAS Experiment at the LHC

*A dwarf standing on the shoulders
of a giant may see farther than a
giant himself.*

- Robert Burton

The ATLAS detector [22] is a multi-purpose detector located at one of the four interaction points on the LHC. It is designed to measure the properties of the proton collision products at 14 TeV of center of mass energy. In the following, the details of the construction of the detector and the accelerator complex are given.

3.1 The Large Hadron Collider

The LHC [23] is the largest particle accelerator ever built and is currently being operated. It is located in the already existing tunnel of the LEP [24] accelerator at the border between Switzerland and France and is 26.7 km long in circumference. Due to the geological conditions of the region, it lies between 45 and 170 m underground and has a 1.4 % tilt from planar, towards the Geneva lake. It hosts six experiments (with their location along the accelerator circumference): ATLAS (Point 1) and CMS [25] (Point 5), which are multi-purpose particle detectors, LHCb [26] (Point 8), dedicated to precise measurement of CP violation and rare decays, ALICE [27] (Point 2), to measure quark-gluon plasma properties in ion collisions, TOTEM [28] (near Point 5), which measures the total cross-section, elastic scattering and diffractive dissociation, and finally LHCf [29] (near Point 1), aiming to measure neutral particles emitted in the very forward region.

3.1.1 The CERN accelerator complex

The design of the LHC was greatly influenced by the decision to reuse the existing facilities of LEP and SPS, i.e. the tunnel and the pre-acceleration system [30], as shown in Fig. 3.1. Important upgrades were completed in 2000 on all these systems to make them suitable for the LHC operation scheme. The description of these systems following their upgrades is given below. At the origin of the beam, protons are

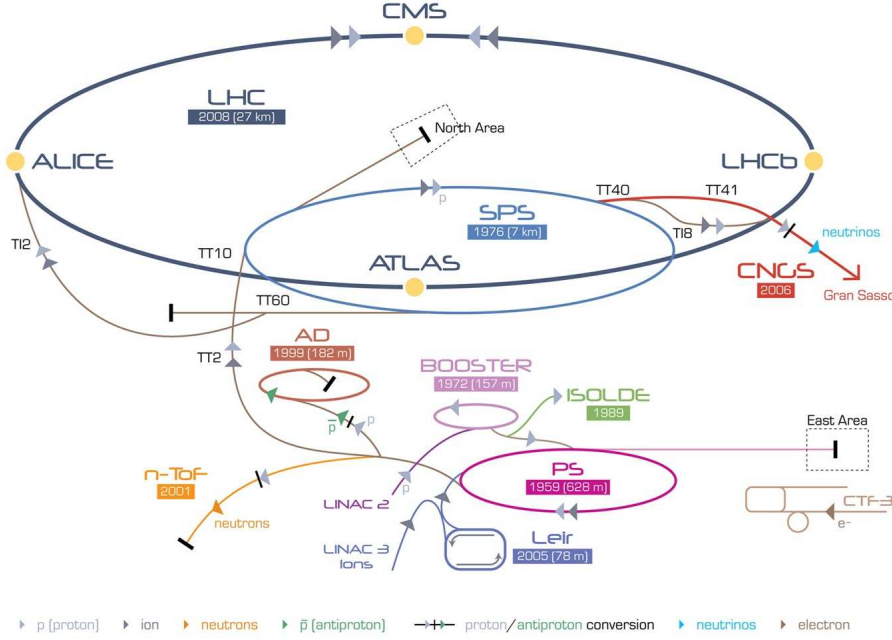


Figure 3.1: The LHC injection complex [31].

first extracted from hydrogen gas using an electric field, inside a Duoplasmatron [32] source with a beam current of 360 mA. The protons from the 90 kV platform are then injected in the pre-injector RFQ2 [33], which accelerates them to 750 keV. A linear accelerator, LINAC2 [34], brings them to an energy of 50 MeV with a current output of 170 mA and a pulse length of 30 μ s needed for LHC operation. A new linear accelerator, LINAC4 [35], is currently under construction and should replace LINAC2 in 2014. It will allow to double the beam brilliance through its increased extraction energy of 160 MeV.

The proton beam is then transferred to the Proton Synchrotron (PS) Booster [36], where the energy of the beam is raised to 1.4 GeV along the 157 m circumference before being injected in the PS itself [37], where the output energy is up to 26 GeV. The 628 m circumference PS also pulses the beam with the correct LHC frequency, 40 MHz. A new two-batch filling system from the Booster to the PS was put in

place in 2000 to meet the LHC requirements of bunch spacing. The bunches are sent through the TT2 and TT10 lines to reach the 7 km circumference SPS [38], where the proton energy reaches 450 GeV.

The beam is then ready to be injected in the two rings of the LHC using the transfer lines TI2 and TI8. 2808 bunches with a 25 ns spacing will be sent in each direction, each bunch containing 1.15×10^{11} protons for a beam current of 580 mA.

3.1.2 The LHC ring

The LHC is a superconducting magnet ring allowing a maximum center of mass p - p energy of 14 TeV¹. Fig. 3.2 shows the layout of the ring. Along its circumference, it is divided into eight sectors, each of them equipped with one arc and one straight section which can be used as an insertion (experimental cavern or accelerator utility). An arc is composed of 46 half arc cells (a pair of which forms an arc cell), which itself contains a Short Straight Section (SSS) and three dipole magnets. An SSS is made of one main quadrupole magnet (which can be focusing or defocusing, depending on the half-arc cell position in the arc) and many different types of higher order corrector magnets enclosed in a common cryostat, called the cold mass. Next to it, the dipole magnets are the main building blocks of the accelerator, in terms of cost and function, as they are used to bend the beam while higher order magnets are used to correct the trajectory. A total of 1232 dipoles, each weighing 27.5 t, 16.5 m long and containing coils made of NbTi superconductor, are installed along the ring, together with ~ 4800 orbit and multipole correctors. The straight section of each sector is built using quadrupole magnets and its exact layout depends on its location around the ring. Many other types of magnets come in to complete this picture, to correct the beam optics and to link the sections together.

All the magnets meet the requirement that both beam pipes have to be enclosed inside one vessel. This is needed due to the diameter of the existing LEP tunnel (3.7 m). In order to reach a magnetic field above 8 T on the dipoles, they need to be cooled using superfluid helium, reaching as low as 1.9 K. Each of the eight sectors is cooled independently by one refrigeration plant [40].

Each straight section is used for a specific purpose as shown in Fig. 3.2. Points 1, 2, 5 and 8 are occupied by experiments as described above. Points 3 and 7 contain two collimation systems used to clean the beam. Point 6 is equipped with kicker magnets to dump the beam. Finally, Point 4 is where the 400 MHz Radio Frequency superconducting cavities (RF) are installed. This is where the beam gets accelerated in an oscillating electric field from 450 GeV of the SPS to 7 TeV.

In order to maximise the instantaneous luminosity, the beams need to get squeezed. For that purpose, special magnets have to be used in the Interaction Regions (IR).

¹In 2009–2010, the maximum energy is 7 TeV.

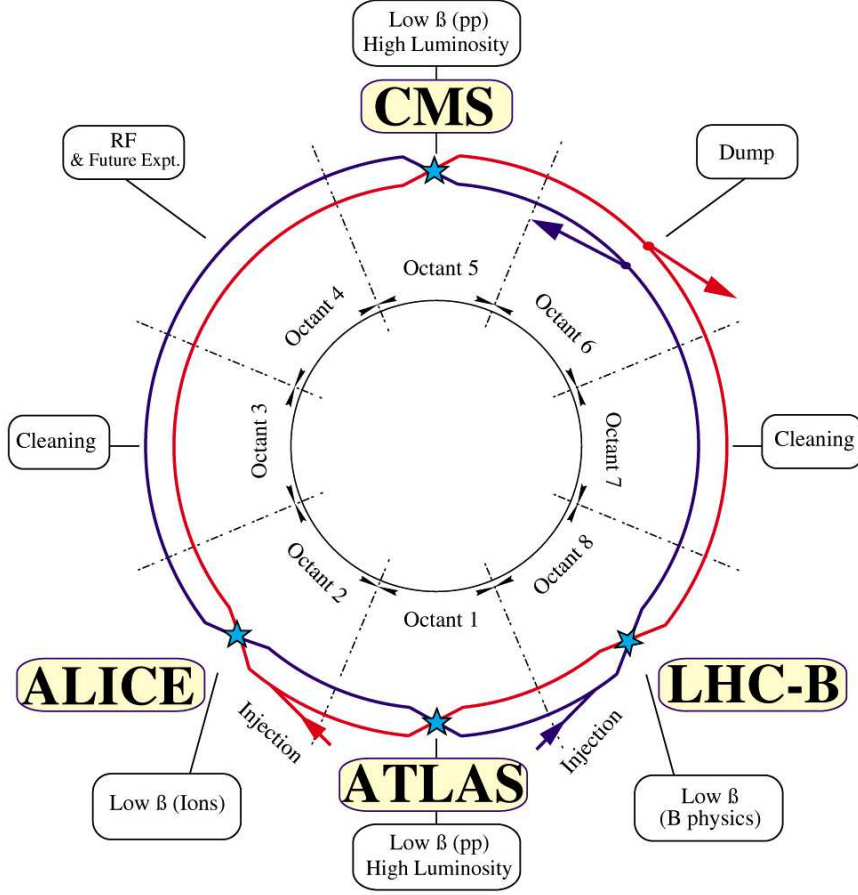


Figure 3.2: Layout of the LHC ring [39].

Inner triplets contain four quadrupoles together with orbit correcting magnets and are assembled in a single cryostat. The colliding beams should provide a design luminosity of $10^{34} \text{ cm}^{-2} \text{ s}^{-1}$. The luminosity delivered by the collider is defined in Eq. 3.1, where N_b is the number of particles per bunch, n_b is the number of bunches per beam, f_{rev} is the revolution frequency, γ_r is the relativistic gamma factor, ϵ_n is the normalised transverse beam emittance and β^* is the beta function at the collision point. F , the geometric luminosity reduction factor due to the crossing angle at the Interaction Point (IP), is defined in Eq. 3.2, where θ_c is the full crossing angle at the IP, σ_z is the RMS bunch length and σ^* is the transverse RMS beam size at the IP.

$$\mathcal{L} = \frac{N_b^2 n_b f_{rev} \gamma_r}{4\pi \epsilon_n \beta^*} F \quad (3.1)$$

$$F = \left(1 + \left(\frac{\theta_c \sigma_z}{2\sigma^*} \right)^2 \right)^{-\frac{1}{2}} \quad (3.2)$$

The expression for F assumes that the beams are round, with $\sigma_z \ll \beta$ and with same parameters for both beams. The main beam parameters with their value are listed in Table 3.1.

Beam parameter	Value
N_b	1.15×10^{11}
n_b	2808
f_{rev} (kHz)	11.245
γ_r	7461
ϵ_n ($\mu\text{m rad}$)	3.75
β^* at IP1 & IP5 (m)	0.55
Beam current (A)	0.582
Stored energy per beam (MJ)	362
F	0.836
θ_c (μrad)	285
σ_z (cm)	7.55
σ^* at IP1 & IP5 (μm)	16.7

Table 3.1: Beam parameters for the LHC at the collision point for nominal luminosity [41].

In 2010, the LHC began its operation successfully. Starting from two colliding bunches in March 2010, it has delivered an integrated luminosity of 45 pb^{-1} with an always increasing number of protons in the rings, and reaching the nominal bunch intensity. An instantaneous luminosity of $2 \times 10^{32} \text{ cm}^{-2} \text{ s}^{-1}$ was achieved, which was set as a goal for the 2010 run period.

3.2 The ATLAS Detector

The ATLAS experiment [22] is a multi-purpose detector which uses a cylindrical geometry with one end-cap on each side to ensure full coverage in solid angle, as can be seen in Fig. 3.3. It is divided into three main parts, each of them comprising several

subdetectors. The Inner Detector uses silicon pixels, silicon microstrips and gaseous straw tube technologies for tracking; the energy in the Calorimeter is measured with the Liquid Argon (LAr) and Tile subdetectors, and finally, the Muon spectrometer is made of several different types of gaseous drift chambers to record the muon tracks. The coordinate system of ATLAS is centered on the interaction point such that x points towards the centre of the LHC ring (horizontal), y point upwards and z is longitudinal to the beam. The polar angle θ is measured from the beam axis while the azimuthal angle ϕ wraps around the beam. The transverse quantities and the radius R are measured in the x - y plane.

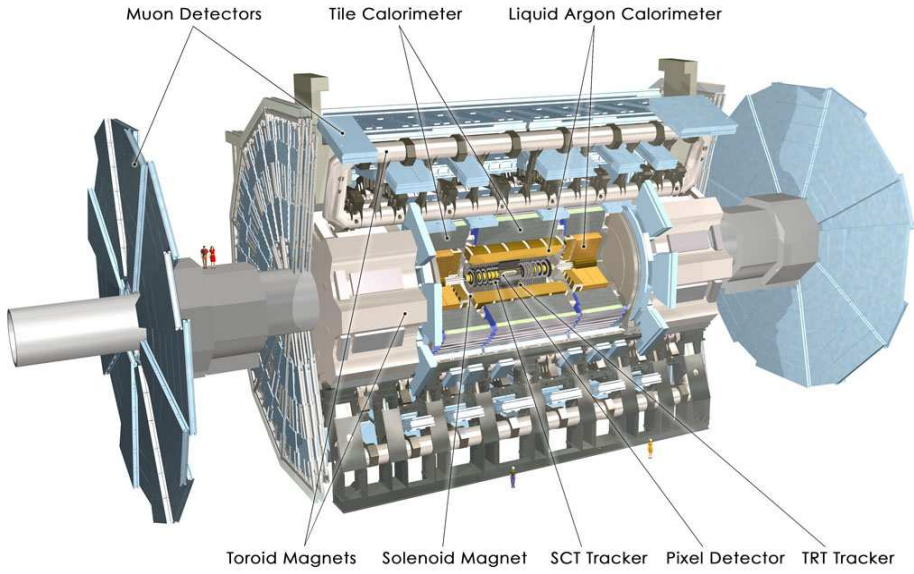


Figure 3.3: The ATLAS detector [22].

The design of the ATLAS detector was done in order to achieve specific physics goals and measurements. These include Standard Model parameters, discovery of the Higgs boson and observation of new physics at the TeV scale. Performance goals related to the latter were established and are listed in Table 3.2.

In order to distinguish the rare processes we expect to see through the QCD jets background unavoidably created by hadron collisions, good performance of the ATLAS detector is required. This means radiation-hard tracking with good momentum resolution and good vertexing capabilities for secondary decays. It also involves having the largest possible acceptance in pseudorapidity² and full coverage in the azimuthal plane to measure all the energy from every event. Electromagnetic particles are a key measurement in a QCD-filled environment and a good fake rejection is

²Pseudorapidity is defined as $\eta = -\ln(\tan(\theta/2))$ for massless objects.

Detector component	Required resolution	η coverage	
		Measurement	Trigger
Tracking	$\sigma_{p_T/p_T} = 0.05\% \ p_T \oplus 1\%$	± 2.5	
EM calorimetry	$\sigma_{E/E} = 10\%/\sqrt{E} \oplus 0.7\%$	± 3.2	± 2.5
Hadronic calorimetry (jets)			
barrel and end-cap	$\sigma_{E/E} = 50\%/\sqrt{E} \oplus 3\%$	± 3.2	± 3.2
forward	$\sigma_{E/E} = 100\%/\sqrt{E} \oplus 10\%$	$3.1 < \eta < 4.9$	$3.1 < \eta < 4.9$
Muon spectrometer	$\sigma_{p_T/p_T} = 0.05\%$ at $p_T = 1$ TeV	± 2.7	± 2.4

Table 3.2: Performance goals for the ATLAS detector [22].

achieved by having a good energy resolution and linearity in the calorimeter. Similarly, muons are golden signatures and, as for tracking, momentum resolution and charge identification are essential. Finally, all of this is only possible with an efficient trigger system, even at low transverse momentum, with a good background rejection.

3.2.1 The Inner Detector

The group of subdetectors closest to the beam pipe are used for precision tracking and momentum measurement of charged particles. They form the Inner Detector (ID) [42], together with the external services that are common to some or all of them. A layout of the ID is shown in Fig. 3.4.

The innermost layer of the ID is the Pixel detector [43]. It is used to measure the vertex position, both primary (the original proton collision point) and secondary (the position of further decay vertices, as in the case of B meson decays). The detector is composed of two end-caps and one barrel section. The latter is made of three layers of silicon. The innermost one, called the *b-layer*, is located near the beam pipe, at 5.05 cm from the IP and the outermost layer, at 12.25 cm. Each end-cap contains three wheels, hence adding three position measurements along the charged particle tracks in the forward direction.

About 80 million pixels of $50 \times 400 \mu\text{m}^2$ in size ($50 \times 600 \mu\text{m}^2$ on the module edge) are used to achieve this task. Pixels are grouped into 1744 identical rectangular modules [44], which are the building blocks of the detector. A module is composed of a sensitive area (facing the beam pipe) bump-bonded to the data acquisition chips of the backside. 13 barrel modules are assembled into a longitudinal ladder structure, called a *stave*. Two staves are assembled together to form a *bi-stave*, which corresponds to a cooling loop. 48 end-cap modules are put together to form a wheel. A precision of $10 \mu\text{m}$ in the in-plane transverse direction (R - ϕ) and $115 \mu\text{m}$ in the in-plane longitudinal direction (z for the barrel and R for the end-caps) can thus be achieved.

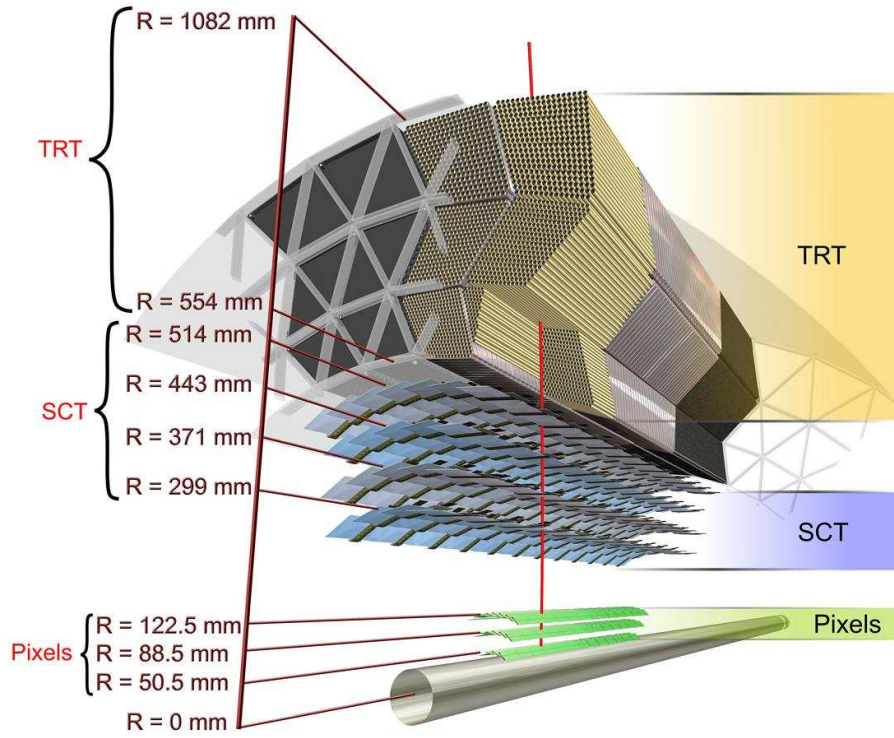


Figure 3.4: Layout of the Inner Detector barrel [22]. Support structures and services are not shown here.

A second silicon detector is used after the Pixel detector, the SemiConductor Tracker (SCT) [45]. In this case, a microstrip technology is used instead of pixels. This allows for a lower number of channels (about 6 million) while keeping a good position accuracy of $17 \mu\text{m}$ in local R - ϕ and $580 \mu\text{m}$ in local z (barrel) or R (end-cap). SCT modules are divided into four different geometries, depending on their location: one barrel and three end-cap modules. Out of two daisy-chained square wafers of $6 \times 6 \text{ cm}^2$ each, a barrel module [46] side is built. On the wafer, strips of $80 \mu\text{m}$ pitch are implanted. To form a barrel module, two sides are glued to a graphite baseboard, with a stereo angle of 40 mrad between them. 1536 strips (768 on each side) are located on each module. They are mounted in rows of 12 modules. The modules are arranged into four cylindrical barrels (made of a light-weight honeycomb carbon-fibre structure), containing respectively 32, 40, 48 and 56 rows.

In the two identical end-caps, modules [47] need to have a wedge-shaped geometry due to their radial arrangement on disks, as can be seen from Fig. 3.5. Each end-cap is made of nine disks (where disk numbers are ordered by their distance from the IP), which can have up to three rings of modules: the inner ring (disks 2 to 6), the middle ring (disks 1 to 8) and the outer ring (all). Each ring requires a particular module geometry. Inners are made of only one wafer on each side, while middles and outsers have two, with the exception of the short-middles on disk 8, which are made of one wafer on each-side. The pitch is varying from 70 to 90 μm . As for the barrel, modules have 1536 strips and are mounted on carbon-fibre structures. On these structures, the inner and outer rings of modules are placed on the side closer to the IP while the middle ring is on the opposite side, except for disk 9 which is inverted to increase acceptance to a pseudorapidity of $|\eta| = 2.5$. The SCT can thus add at least four position measurements to the track.

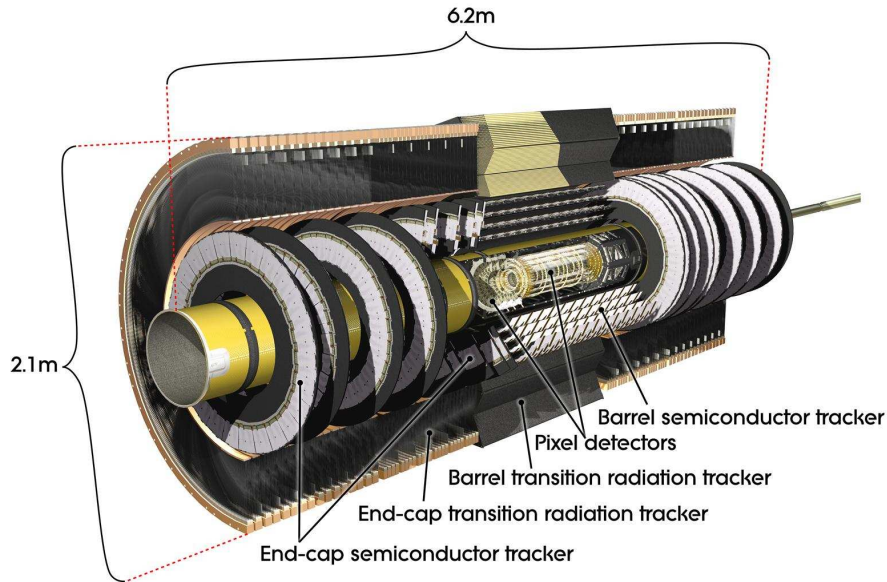


Figure 3.5: Layout of the Inner Detector with end-caps [22]. Services are not shown here.

As silicon detectors are located close to the beam pipe, they are subject to high radiation dose. The b -layer of the Pixel is already planned to be replaced after three years of LHC operation at full luminosity. The expected neutron equivalent fluence F_{neq} for the two other layers is about $8 \times 10^{14} \text{ cm}^{-2}$, so they will be used for the full lifetime of the initial LHC program. The radiation effects are not limited to the Pixel, and the innermost layer of the SCT is expected to receive a fluence $F_{neq} \simeq 2 \times 10^{14} \text{ cm}^{-2}$. As a result, the silicon sensors were developed for their radiation-hardness properties.

In the Pixel detector, oxygenated n-type silicon bulk with n^+ implants for pixel elements was used, while for the SCT, p-in-n bulk with AC coupled strips were used. In addition, the sensors have to be kept cold (-7°C for the SCT and -20°C for the Pixel, nominally) to reduce leakage current after irradiation and their bias voltage will increase with time (from 150 V to 500 V [600 V] for the SCT [Pixel]) to compensate for type inversion in the bulk.

The last layer of the ID consists of the Transition Radiation Tracker (TRT) [48]. It is a gaseous straw tube detector interleaved with thin foils which provide transition radiation photons to be detected by the straw tubes. In the barrel, the detector is divided into 32 modules composed of three rings and the straws are parallel to the beam axis. In each end-cap, 20 wheels are assembled together, in which the straws are perpendicular to the beam axis. The 4 mm straw tube forms the cathode and a $31\text{ }\mu\text{m}$ gold-plated tungsten wire forms the grounded anode. The cathode is kept at -1530 V . Inside the straws, a mixture of 70% Xe, 27% CO_2 and 3% O_2 is ionised by the transition radiation photon. A total of 351 000 channels are read-out for the entire detector. The TRT provides R - ϕ information and adds ~ 36 position measurements to the track (22 in the end-caps). The straw drift time accuracy is $130\text{ }\mu\text{m}$, since it does not record the z position.

The ID is equipped with a complex environment monitoring system, which controls the gas atmosphere inside the detector volumes, and an evaporative cooling system. To avoid condensation and risk of fire, the two silicon detectors are filled with N_2 while the TRT is filled with CO_2 to avoid contamination from the N_2 . A two-phase evaporative cooling system [49] is used in common for both Pixel and SCT (the TRT operates at room temperature) to remove about 85 kW of heat from the ID volume. It uses C_3F_8 as a coolant, which undergoes pressure drops along the pipe and is then brought to boil inside the detector. Counter-flow heat exchangers are installed at the input pipes to cool down the incoming coolant with the outgoing coolant (subcooling). Finally, a heater system is installed to boil the remaining liquid in the output pipes to avoid condensation along the calorimeter on their way back to the cooling plant.

The choice of silicon as active material for the ID is beneficial for the measurement accuracy, but disadvantageous for the material budget, which is higher than for a gaseous detector. The services between the barrel and the end-cap almost double the amount of material in front of the calorimeter, as can be seen in Fig. 3.6(a). Trajectories of particles crossing the tracking detectors are affected by the material mainly in two ways: charged particles undergo bremsstrahlung and photons convert into electron-positron pairs. Charged particles then lose part of their energy before reaching the calorimeter. Electrons are mostly affected by bremsstrahlung due to their low mass; muons are not significantly affected. Nonetheless, the ID achieves a good momentum resolution as a function of η , as was measured in cosmic ray data in 2008. Fig 3.6(b) shows that the momentum resolution is not dependent on pseudorapidity. An asymptotic resolution of $0.06\%p_{\text{T}}$ [GeV] was measured [50].

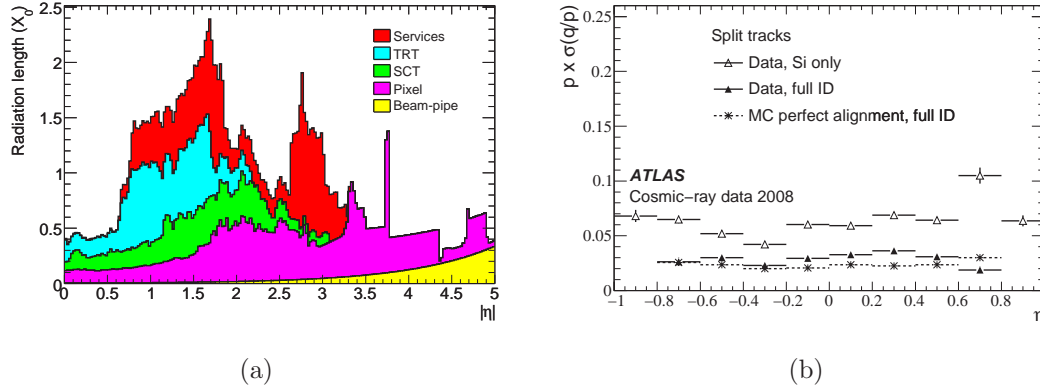


Figure 3.6: (a) Material distribution in the ID as a function of η [22]. The X_0 distribution is averaged over ϕ and the contribution from each subdetector is shown. (b) Momentum resolution in the ID as a function of η using 2008 cosmic ray data [50].

The ID is enclosed in a superconducting Solenoid [51] that provides the 2 T magnetic field needed for tracking. In order to reduce the material in front of the calorimeter, the solenoid is enclosed in the same cryostat as the Electromagnetic Calorimeter (see §3.2.2).

3.2.2 The Liquid Argon Calorimeter

Once they have crossed the tracking system, the neutral and charged particles reach the calorimeters, where they shower and hence their energy is deposited and measured in the detector. In this process, electromagnetic and hadronic matter behaves differently and needs to be treated by two separate calorimeter systems.

Fig. 3.8 shows how the calorimeter system is divided into an electromagnetic (EM) part and a hadronic part. In ATLAS, liquid argon technology is used for the full EM calorimeter and for the end-cap and forward part of the hadronic calorimeter [52]. The barrel part is described in §3.2.3.

The EM calorimeter design is based on the concept of the accordion geometry, as shown in Fig. 3.7(a). Lead plates are used as absorber material and copper/kapton electrodes for read-out. The two materials are interleaved and folded together. This geometry allows a good coverage in ϕ without cracks. The accordion is kept in a cold LAr vessel, which serves as the active material. Four individual vessels form the detector: two half-barrels and two end-caps, covering up to $|\eta| = 3.2$. There is a small gap at $|\eta| = 0$ and one at $1.37 < |\eta| < 1.52$. The calorimeter is segmented into three radial layers (two in certain regions of pseudorapidity) and has a decreasing

granularity as a function of the distance from the beam pipe, as can be seen in Fig. 3.7(b). The cell granularity varies also in $|\eta|$ from $\Delta\eta \times \Delta\phi = 0.0031 \times 0.1$ to 0.1×0.1 . The amount of material, in units of radiation length X_0 , varies in $|\eta|$ from 25 to 41, with peaks at $|\eta| = 0.8, 1.25, 2.5$ and 3.2 . The second layer contains most of the energy of the shower, the first layer is more finely segmented to precisely measure the direction of the particle and, when present, the back layer is coarsely segmented and designed to contain the electromagnetic shower. A presampler is installed to determine the energy lost in the material in front of the EM calorimeter in the range $|\eta| < 1.8$.

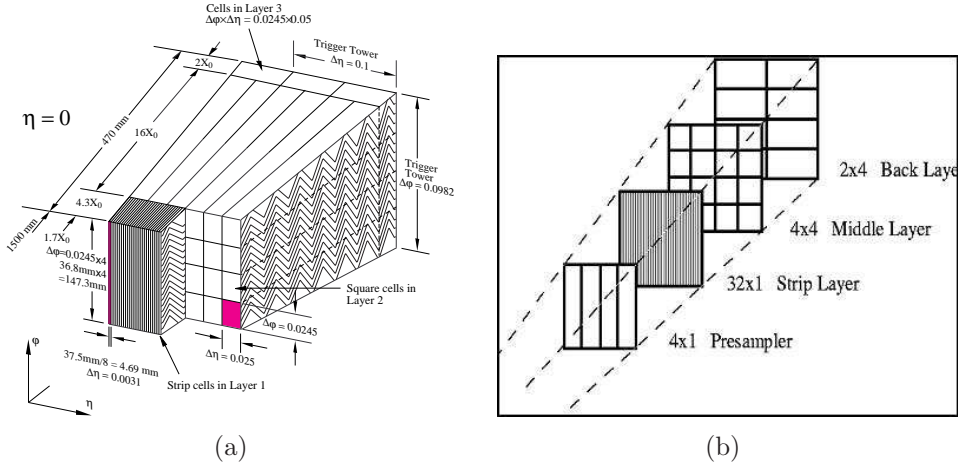


Figure 3.7: (a) EM Calorimeter accordion geometry. The three layers are visible, as well as their different granularities in (b) [53].

This design allows for a good measure of the electromagnetic shower shape to distinguish signal from fakes. A good resolution and linearity is achieved and was measured in the Combined Test Beam for the barrel (at $\eta = 0.687$), as shown in Eq. 3.3. The first term, called the *stochastic term*, indicates the accuracy due to statistical fluctuations in the shower development. The second term does not depend on energy and contains the accuracy due to non-linearities in the response.

$$\frac{\sigma(E)}{E} = \frac{(10.1 \pm 0.4)\%}{\sqrt{E(\text{GeV})}} \oplus (0.2 \pm 0.1)\% \quad (3.3)$$

The Hadronic Calorimeter (HCAL) uses two different technologies to absorb the hadrons from the collisions. At $1.5 < |\eta| < 3.2$, the Hadronic End-Caps (HEC) use LAr technology and are located inside the same cold vessels as the EM Calorimeter. The HEC is composed of two wheels, each equipped with 32 wedge-shaped modules, using copper plates as absorber material.

Finally, a Forward Calorimeter (FCal) system is needed to cover the pseudorapidity range up to 4.9. The FCal is made of three layers: one for EM particle detection using copper plates as absorber and two more for hadronic particle detection using tungsten plates as absorber. The detector is housed in the LAr vessel. It uses smaller LAr gaps between the plates to limit ion formation due to the high particle flux in this region.

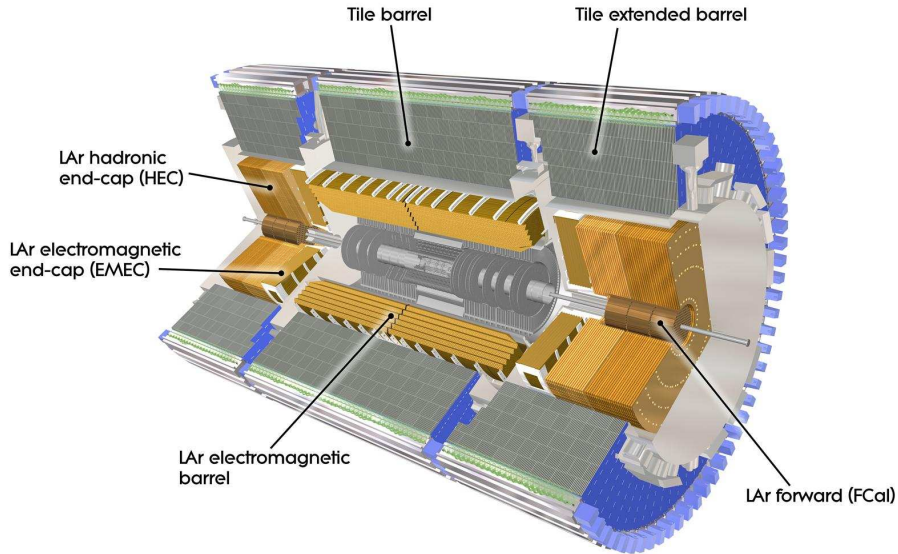


Figure 3.8: Calorimeter layout in ATLAS. The LAr and Tile detectors are indicated in different colours, with the FCal extending to $|\eta| = 4.9$ [22].

3.2.3 The Tile Calorimeter

Surrounding the EM and HEC calorimeters, the Tile Calorimeter (TileCal) [54] uses steel plates as absorber material interleaved with scintillator tiles as active material. The light from the scintillating tiles is read out by wavelength shifting fibres and 9852 photomultiplier tubes (PMT). It is divided into two parts: the Barrel covering the range $0 < |\eta| < 1.0$ and the Extended Barrel covering $0.8 < |\eta| < 1.7$. They are built of 64 wedge-shaped modules of size $\Delta\phi \sim 0.1$ rad. The gap between the Barrel and Extended Barrel is equipped with plug calorimeters to determine the amount of energy lost in this region.

3.2.4 The Muon Spectrometer

The toroidal magnet system [55] is the skeleton of ATLAS, hence determines the size of the detector, as shown in Fig. 3.9. It is composed of three toroids: one barrel and two end-caps. Each toroid consists of eight superconducting coils, equally separated in azimuth. The end-caps have a 22.5° angle in ϕ with the barrel toroid to provide radial overlap and optimise the bending power in the transition region between barrel and end-cap. The magnetic field strength is approximately 0.5 T in the barrel and 1 T in the end-cap. The barrel toroid provides a bending power of 2 to 6 T · m in the range $0 < |\eta| < 1.3$ while the end-cap toroids deliver 4 to 8 T · m in the range $1.6 < |\eta| < 2.6$.

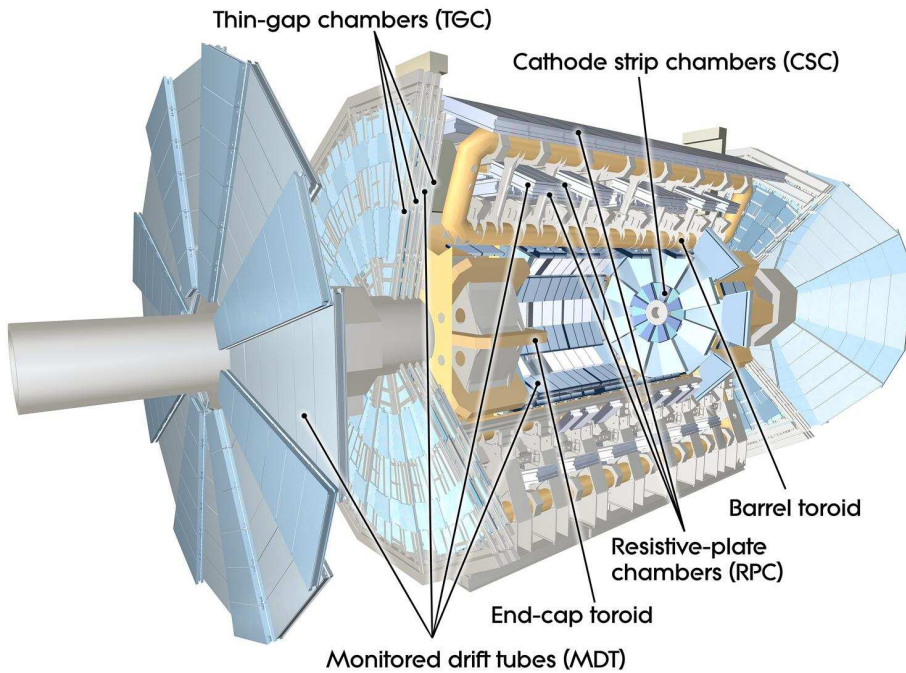


Figure 3.9: The Muon Spectrometer of ATLAS [22]. The toroidal magnet system is also visible in yellow.

Due to the high particle multiplicity in ATLAS, muons are a very important handle for the trigger system (see §3.4). The Muon Spectrometer [56] is then designed with two separate sets of detectors: trigger chambers (fast) and precision chambers (slow). The layout of the different detectors, covering up to $|\eta| = 2.7$, is shown in Fig. 3.9. They are enclosed in the toroidal magnet system of ATLAS which provides strong bending power in a large empty volume, allowing for a minimisation of multiple scattering effects and a good charge identification for high p_T muons. The precision

chambers allow one to have good momentum resolution (10% at 1 TeV) without loss of trigger efficiency.

The precision tracking muon system is composed of two subdetectors: the Monitored Drift Tubes (MDT) and the Cathode Strip Chambers (CSC). The MDT occupies most of the solid angle, with three concentric layers in the barrel and up to $|\eta| = 2.7$ in the end-cap small and big wheels (located on each side of the end-cap toroid). Each chamber consists of three to eight layers of drift tubes filled with gas. It has a maximum counting rate of 500 Hz/cm^2 . The CSC covers the range $2 < |\eta| < 2.7$ only for the innermost small wheel. This is needed due to the high particle flux in this region of high pseudorapidity. The CSC is a multiwire proportional chamber which uses two perpendicularly segmented cathode planes to locate particles. Its maximum counting rate is 1000 Hz/cm^2 . Both detectors use a mixture of Ar and CO_2 gas inside the chambers for particle detection.

The trigger chambers are also divided into two subdetectors: the Resistive Plate Chambers (RPC) in the barrel and the Thin Gap Chambers (TGC) in the end-cap. The RPC extends to $|\eta| = 1.05$ and uses the same detection principle as a spark chamber. The TGC covers the range $1.05 < |\eta| < 2.4$ and is a multiwire proportional chamber with a smaller wire-cathode gap than the wire-wire gap.

For the muon detectors, the time resolution is important for the trigger chambers, while the position accuracy is more relevant for precision chambers. The RPC has a 10 mm accuracy in z and ϕ with a 1.5 ns time resolution and the TGC, in the forward region, reaches 2–6 mm in z , 3–7 mm in ϕ and a 4 ns time resolution. The precision CSC chambers in comparison have a $40 \text{ }\mu\text{m}$ z accuracy, a 5 mm ϕ accuracy and a 7 ns time resolution, while the MDT reaches an average resolution of $35 \text{ }\mu\text{m}$ per chamber.

3.3 Luminosity measurement

The LHC delivers beam at a given luminosity (calculated using beam parameters), but each experiment needs to make an independent measurement of this quantity, to determine how much was actually recorded with good precision. In ATLAS, this measurement is performed by two detectors located in the high pseudorapidity region, along the beam pipe, as shown in Fig. 3.10.

The Luminosity measurement using Cerenkov Integrating Detector (LUCID) is designed to measure relative luminosity using inelastic p - p collisions [57]. It is located at 17 m from the IP. Further down the beam pipe, at 237 m, the Absolute Luminosity For ATLAS (ALFA) detector [58], as its name states, measures absolute luminosity by detecting elastic p - p collisions. ALFA detects charged particles using scintillating fibers located inside Roman Pots [59]. During injection and beam scraping, the Roman Pots are away from the beam. Later on when beams are stable, they are

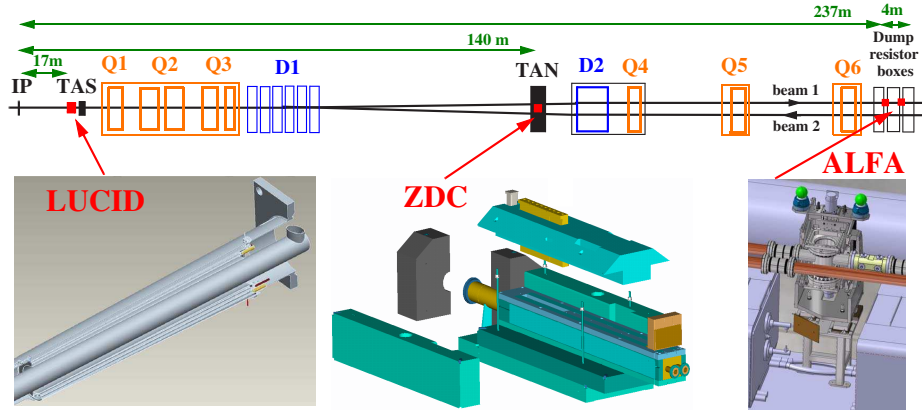


Figure 3.10: Forward detectors for ATLAS [22]. The distances from the IP are indicated.

put in the operating position (for ALFA, 1 mm from the beam) to detect beam halo particles.

In addition to the luminosity detectors, between LUCID and ALFA, at 140 m, the Zero Degree Calorimeter (ZDC) [60] detects very forward neutrons from heavy ion collisions and also from minimum bias events. The challenge for these detectors is the trigger system, as the time required for their signals to reach the Central Trigger Processor is much greater than that for the rest of ATLAS.

3.4 Data Acquisition and Trigger System

In order to collect data coming from the detector, three main systems are needed: the Trigger system, to filter the interesting data, the Data Acquisition (DAQ) system to record this data, and last but not least, the Detector Control System (DCS), to power and monitor the detector during operation. Fig. 3.11 describes the data-flow of the DAQ and the Trigger systems.

The amount of data provided by the LHC is enormous and not all of these collisions is worth recording. Only a small portion contains interesting physics, as shown in Fig. 3.12. Also, the hardware used for recording the data has intrinsic limitations in bandwidth. A 40 MHz of collision rate needs to be filtered down to a rate of ~ 200 Hz. To achieve this, a three-level trigger system is implemented in ATLAS. The Level 1 (L1) [61] is a hardware layer which needs to take a decision in less than $2.5 \mu\text{s}$. It introduces a new idea called Regions of Interest (RoI) where one triggered object (e.g. EM cluster, muon) can be found in a fixed-size region of the detector. The smallest detector element available at this level, called a *trigger tower*, has a size of $\Delta\eta \times \Delta\phi = 0.1 \times 0.1$; an RoI is typically built using several trigger towers.

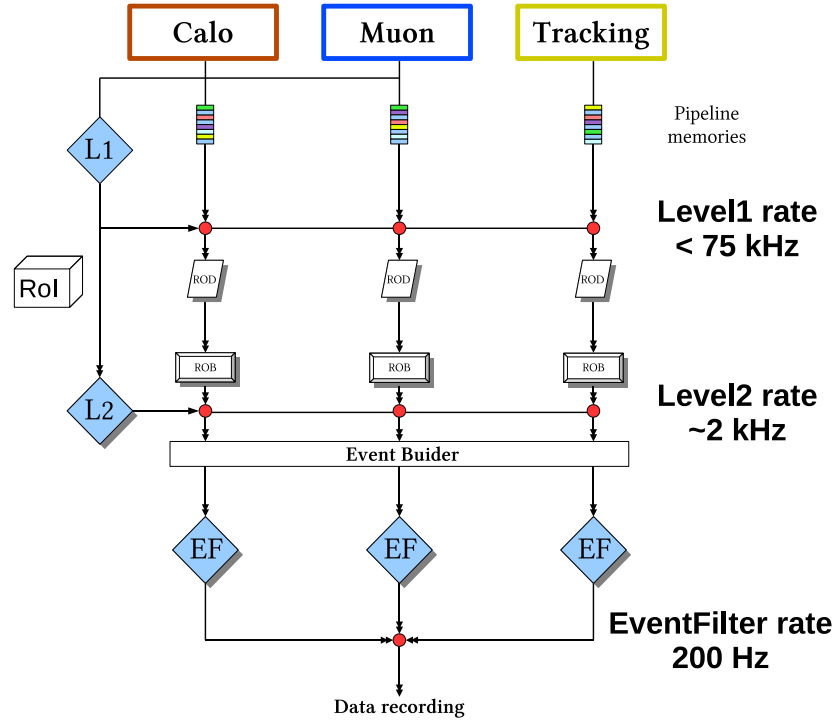


Figure 3.11: Trigger flow diagram showing the various rates to be reached by the different levels.

The RoIs are then given to the Level 2 (L2) which has access to the full detector granularity *within the RoI* to make a decision in 40 ms on average. If L2 accepts the event, it is passed to the Event Filter (EF) which uses the full event information to take a decision and classify the event in 4 s on average. L2 and EF form the High Level Trigger (HLT) [62] and are purely software based. The HLT algorithms work in steps and hence can reject an event as soon as possible.

A DAQ system is needed to collect data from the experiment and also to interact very closely with the trigger system. In ATLAS, the DAQ and trigger are designed with a common data flow system [62]. At L1, front-end electronics store the data in pipelines, waiting for the L1 decision. If L1 accepts the event, the data are transferred to a Read-Out Driver (ROD) in the standard ATLAS format. These data are then sent to the Read-Out System (ROS), which in turn sends it into Read-Out Buffers (ROB). The ROB can send data to the L2 processors on request. Finally, when the event is accepted by L2, the data are sent to the Event Builder (EB) and to the EF for one last trigger decision.

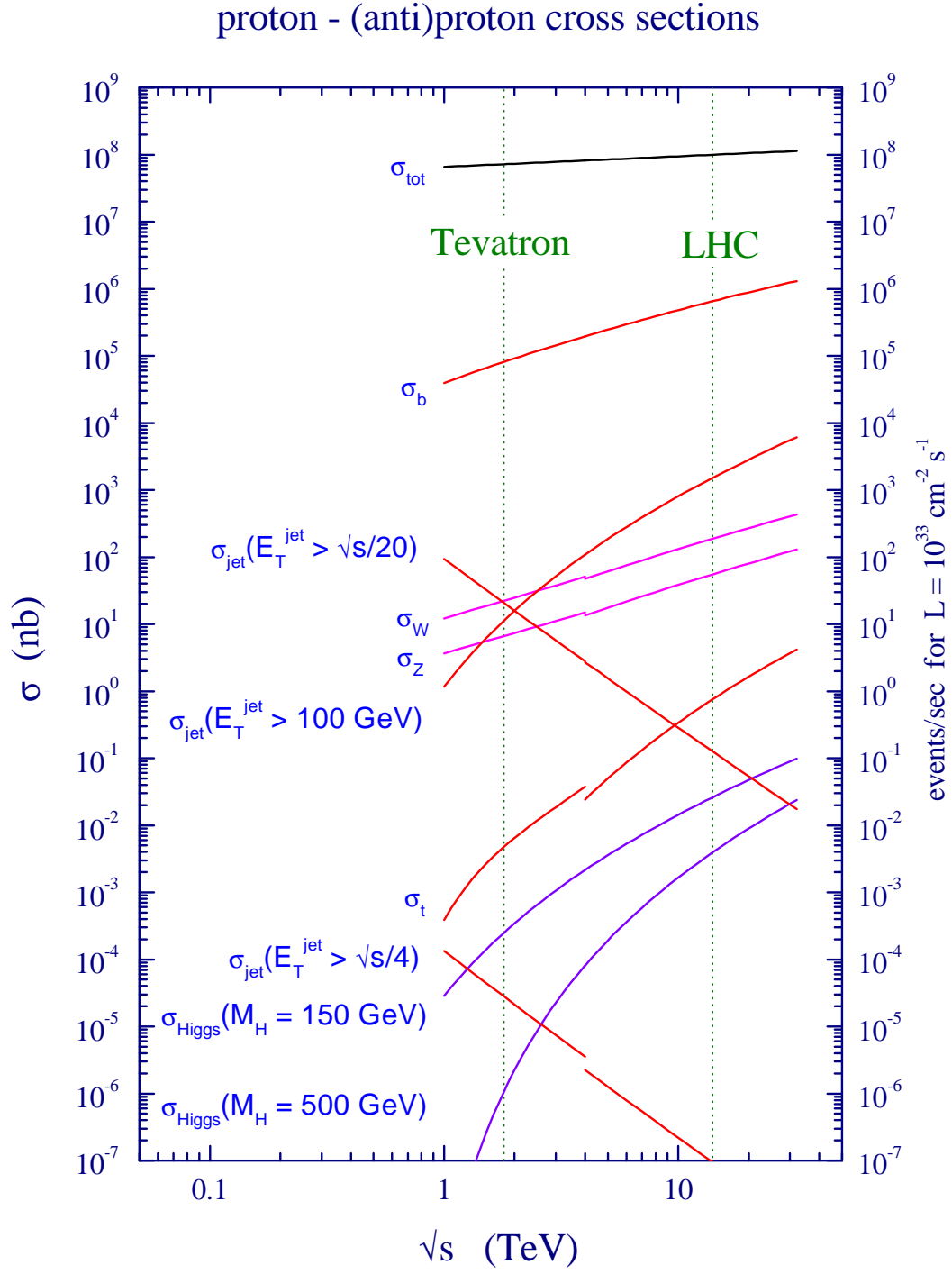


Figure 3.12: Expected cross-sections for various processes at the LHC, compared to Tevatron [63].

3.5 Detector Control System

In order for the two previous systems to be operational, the detector hardware needs to be fully functional and well monitored. This is where the Detector Control System [64] comes into play. The DCS task is to control and monitor all hardware systems in ATLAS and to ensure its safe operation; this means controlling and monitoring of power supply parameters, environmental parameters and gas supplies. The DCS can also enable manual and automatic safety actions in case of incidents. The DCS and DAQ system can exchange information using the DAQ-DCS Communication (DDC) protocol. The DCS data are stored online and a small portion is also sent to the offline database for reconstruction. A common hardware device, the Embedded Local Monitor Board (ELMB), is used throughout ATLAS for the DCS systems of individual subdetectors. A more detailed description of the DCS implementation for the SCT, including my contribution, is given in §4.

3.6 Event Data Model

The data collected at the LHC experiments require processing before being used for analysis. Due to the raw event size in ATLAS of 1.6 MB³, different formats [65] are needed to achieve an efficient treatment of the data, all based on the POOL ROOT technology. The starting point is the bytestream, which is the data format coming straight out of the detector DAQ. After being handled by the HLT, the data are organised in an object-oriented format, called RAW. This is the input format for reconstruction by the offline software. A similar chain exists for simulated data. The *evgen* format is the output of the physics generators. The HITS format is produced after *evgen* events are passed through a GEANT4 simulation of the ATLAS detector. Finally, the Raw Data Object (RDO) is obtained after digitisation of the HITS file. After reconstruction is completed, the Event Summary Data (ESD) is produced, together with the Analysis Object Data (AOD) data format, which contain the objects needed in a physics analysis. Various types of Derived Physics Data (DPD) are also available, which contain a combination of the objects available in the ESD and AOD, for specific usage. The TAG format is produced from the AOD and contains event-level metadata, to allow for a fast event selection without reading through the AOD. This chain is illustrated in Fig. 3.13.

The data being collected at the LHC experiments, even after the trigger filtering, is considerable and a single computer farm and storage space is not enough. For this reason, a world-wide grid was developed to, firstly, store this data in the various disk and tape storage facilities to make it available to a wide number of institutes

³With pile-up at full luminosity, this value almost doubles.

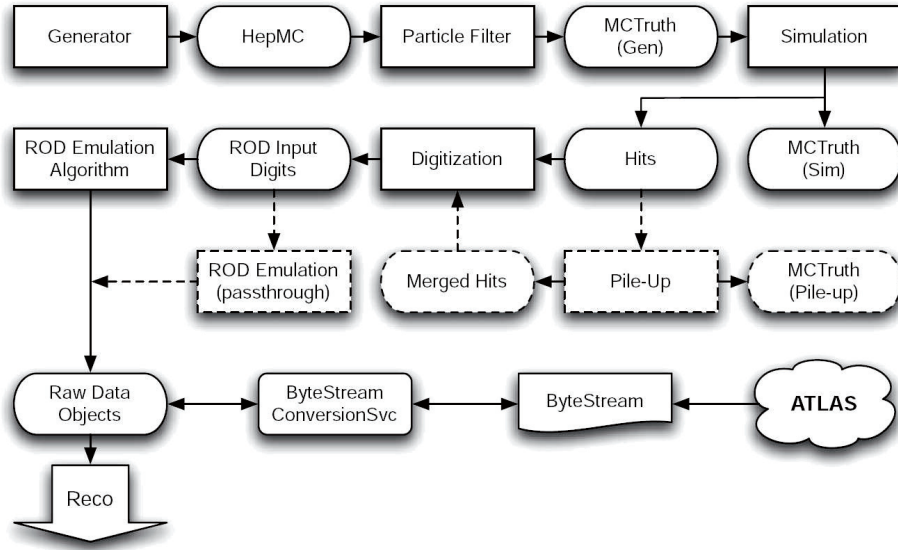


Figure 3.13: Data flow diagram before reconstruction for data and Monte Carlo simulation [65].

and, secondly, provide computing resources for data analysis and Monte Carlo production. ATLAS facilities follow a computing model [66] that groups the different sites in so-called *Tiers*. The central point of this system is the Tier-0, located at CERN. This is where the initial processing of the data takes place, together with calibration and monitoring. The raw data is then copied in parts to each of the ten Tier-1 national centres, scattered all over the world; the first-pass output of the reconstruction (ESD,AOD,DPD,TAG) are also sent to Tier-1 centres. They are also responsible for reprocessing of the data if new calibration and/or software improvements are available. Attached to each Tier-1 is a collection of Tier-2 centres, which then take care of hosting data formats more oriented towards physics analysis and code development. Finally, the Tier-3 centres are located in various institutions and are devoted to provide resources for physics analysis for their users. Fig. 3.14 illustrates this structure for a subset of the grid, centered around the Geneva University Tier-3 centre (UNIGE). The latter is linked to the Swiss Tier-2 in Manno (CSCS) and to the German Tier-1 in Karlsruhe (FZK), making it part of the German *cloud*. A cloud is defined as the arborescence of Tiers attached to a given Tier-1 site.

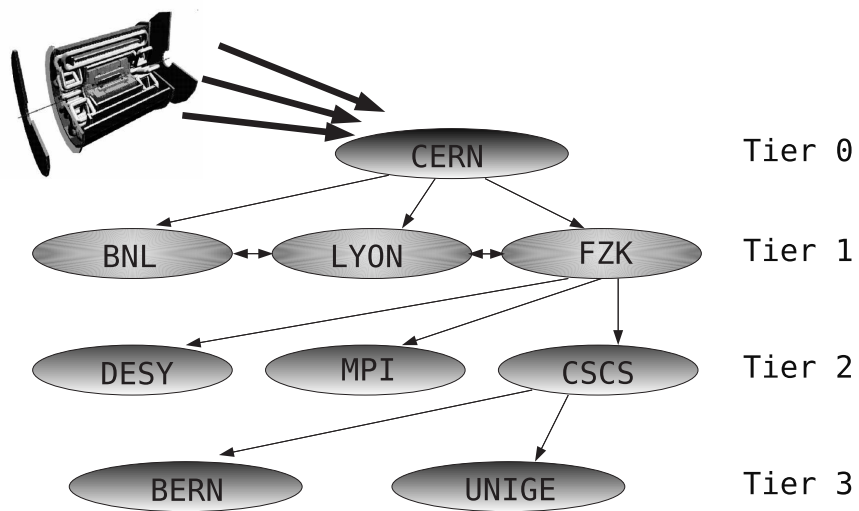


Figure 3.14: Tier structure of the ATLAS computing grid.

CHAPTER 4

The Detector Control System

A small leak can sink a great ship.

- Benjamin Franklin

In order to operate the ATLAS detector, two main systems are required: the Data Acquisition (DAQ) System (see §3.4) and the Detector Control System (DCS). The latter takes care of delivering power to the different detector modules and also monitors numerous parameters that are used to ensure the safety of the detector. It is an important part of the safety systems, together with the interlocks and the Detector Safety System (DSS) [67].

The DCS is a hierarchical system where the subdetectors are feeding information to a global operator node. This node is used as the main control point during ATLAS operations in the control room. A description of the overall structure followed by the specific DCS implementation in the case of the SemiConductor Tracker, where I was personally involved for two years, is given here.

4.1 The ATLAS DCS

The ATLAS DCS architecture is divided into layers of control stations, or PCs, arranged in a tree structure, as can be seen in Fig. 4.1. The top level is the Global Control Station (GCS) which controls the full ATLAS detector. The Subdetector Control Stations (SCS) are located on the next level. Each SCS is the top node for a given subdetector, again summarizing the DCS information coming from below. Finally, the lowest level is made of the Local Control Stations (LCS). They are directly

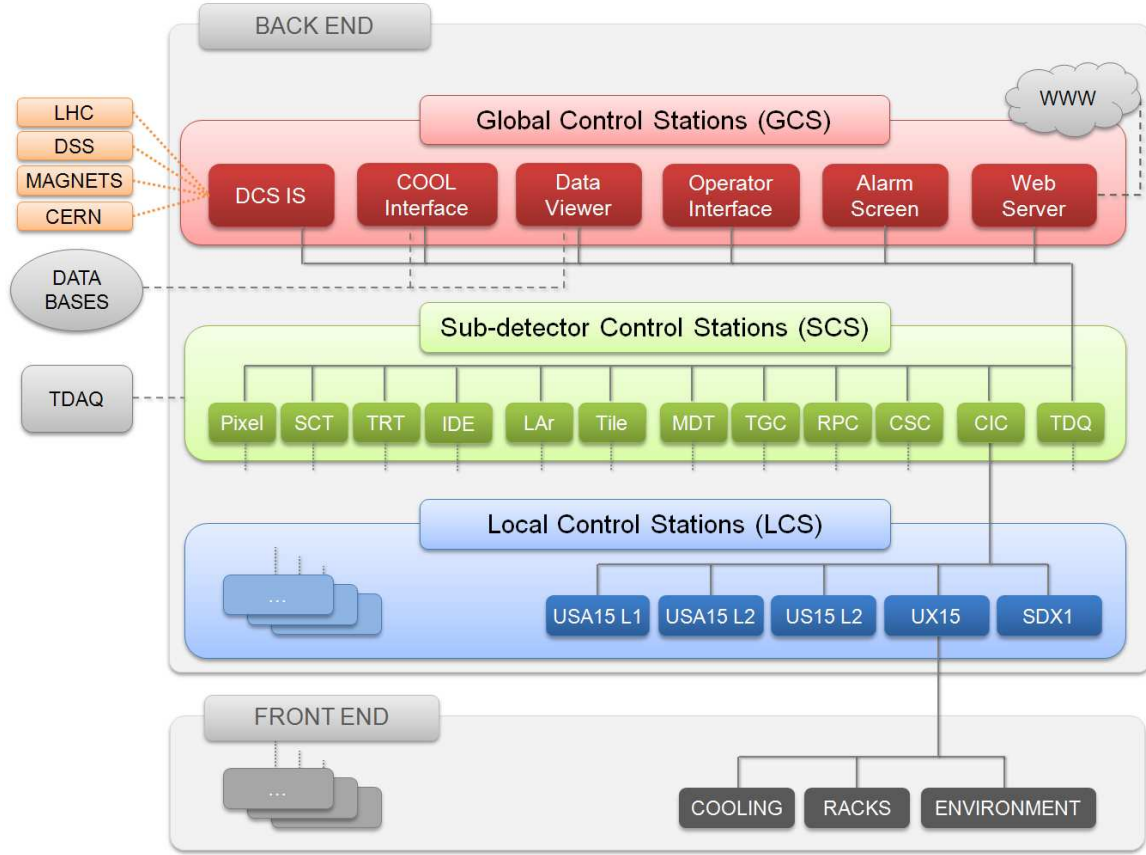


Figure 4.1: The global ATLAS DCS architecture [64].

connected to the hardware and they send their information to the higher levels of the hierarchy. All those stations are connected using the LAN and are also connected to the DAQ using DAQ to DCS Communication (DDC). DDC is used to share information on powering and monitored parameters which can be important for the run control. Finally, extra information is provided by external systems (i.e. not belonging to ATLAS DCS) using the Information Server (DCS-IS). External systems can be the LHC control or the DSS, their input being important to the running of ATLAS.

The ATLAS DCS is based on a custom solution developed for the LHC experiments and used by all subdetectors. A Supervisory Control And Data Acquisition (SCADA) system [68], PVSS II¹, allows for the aforementioned data communication, data display and error handling. The core of the software is developed by each sub-detector for its specific needs, written in the PVSS CTRL programming language, which

¹<http://www.pvss.com/>

is similar to the C programming language. The communication between the hardware and the SCADA software is provided by a Controller Area Network² (CAN) fieldbus. A custom developed Object linking and embedding for Process Control (OPC) server [69] is used to read out the data transferred through the CAN bus. The data from the front-end hardware is first sent to an Embedded Local Monitor Board (ELMB) [70] which provides an interface for the CAN bus and the read-out software.

At the GCS level, several tools are available to the operator. The main operator interface allows for control of the different subdetectors, through a Finite State Machine (FSM) structure, described in §4.1.2. The alarm screen is an efficient and rapid way to see if alarm conditions (see §4.4.2) are raised in the detector, without having to browse through the FSM tree. A web server also runs to allow a snapshot of the detector status (FSM and alarm screen) to be displayed on a monitoring web page and refreshed every 30 seconds³.

4.1.1 JCOP framework

To allow for a better uniformity between the different LHC experimental control systems, a set of common solutions was developed at CERN. These were bundled into the Joint CONTrols Project (JCOP framework [71]), to be used easily inside a PVSS-II-based DCS implementation. The JCOP functions are used heavily in the ATLAS DCS for various purposes, e.g. communication protocols, data archiving and control of common front-end devices (PLC, ELMB, CAEN and Wiener crates).

The framework provides the developer with several components which can be implemented through a common *Installation tool*. The *Core* component is required, but other components can be added or removed individually. A typical component contains code libraries, graphical interface panels, configuration files and sets of definitions for the desired device. Such components are produced by the CERN JCOP team and by the ATLAS DCS team, for specific needs of the experiment. The framework can then be used by the experiments to establish standards for their control systems, for example naming conventions or colour codes.

4.1.2 Finite State Machine

The ATLAS DCS system is a highly complex infrastructure: the number of parameters is large (several 100 000 parameters in total) and they vary greatly in usage (cooling, power, temperature, etc). In order to allow for an efficient control during ATLAS operations, an organisation scheme must be adopted. The Finite State Machine (FSM) [72] is the implementation used to achieve this task. It arranges the

²CAN in Automation (CiA), <http://www.can-cia.de>

³https://atlasop.cern.ch/atlas-point1/dcs/status_pages.html

different modular pieces of the DCS (*nodes*) in a tree structure. In an FSM, each node is described by a *unit* and has an assigned set of states and commands. There are three types of units available: the *device unit*, which is tailored for single hardware elements, the *logical unit* and the *control unit*, which group units into a logical structure for FSM state calculation. The state of a given node is propagated upwards from the hardware device units to the control units. On the contrary, the commands are propagated downwards, from control to device units. Each subdetector can define its own states/commands up to a certain level in the hierarchy, where the ATLAS standards start to apply.

In the ATLAS DCS, the operational behaviour of a node is defined by two independent quantities: the *state* and the *status*. The state tells the operator about the operational mode of the system while the status tells more about how the system is working for the given state. The status is in general linked to the presence of error conditions in the system. This implementation allows the user to keep track of the action the system is trying to perform, even if an error occurs. The compulsory states are READY and NOT_READY, and the standard status levels are OK, WARNING, ERROR and FATAL. Other intermediate states can be used between READY and NOT_READY, to fulfill the specific subdetector requirements, but the status levels cannot be changed. Colour codes for the standards are also fixed by the JCOP framework to ease the operation for the shifters [73].

4.2 The SemiConductor Tracker DCS

The main goal of the SCT DCS [74] is to control and monitor the supply of power and other necessary control signals to the modules as well as to protect the detector from any failure or error conditions. If any situation occurs where the detector is in danger, the DCS system should provide a rapid response, either by software actions (if possible) or by hardware interlocks. The SCT DCS also needs to provide a safe communication between the subsystems, with the ATLAS DCS as well as with the SCT data acquisition system (DAQ). Both transitions between operation states and errors need to be propagated to the ATLAS DCS and to the SCT DAQ in an unambiguous way.

The SCT DCS system is divided into two main subsystems: the Power Supply control, which monitors and controls the powering of individual SCT modules and the Environmental system, which monitors the temperature, humidity and dew point in various locations inside the detector volume. My personal contribution was to complete the development and the implementation of the Environmental DCS and the cooling interlock during the SCT macro-assembly and commissioning phases, hence delivering a working system for the years to come for the detector. The control and monitoring of the evaporative cooling system, which is used by the SCT, is provided by the Inner Detector DCS, described in §4.3.

4.2.1 Power Supply DCS

The Power Supply (PS) system is the main part of the SCT DCS. It provides power to many different components of the SCT modules: the bias voltage of the silicon, the low voltages needed to operate the read-out chips and the conversion of optical to electrical signals. It also provides slow commands for module configuration. These configurations are available for three possible states: ON, STANDBY and OFF.

Each SCT module is powered by two independent PS channels, High Voltage (HV) and Low Voltage (LV). The HV channel provides the 150–480 V needed to deplete the silicon sensors. The LV channel delivers the digital and analogue voltages for the read-out electronics on the module hybrid. In addition, the LV channel is also responsible for the powering and read-out of temperature sensors (two for a barrel module, one on each side, and one for an end-cap module) monitoring the hybrid temperature. This temperature is also used to set a firmware interlock threshold to avoid overheating the modules. The firmware switches off the power (both LV and HV) if the temperature goes above a programmable limit (can be set to a maximum of 38°C). In total, 14 parameters are monitored and controlled for each LV/HV channel.

The PS system is organised in 88 crates, each populated with 12 LV cards and six HV cards. An LV card services four channels while an HV card services eight channels. Each crate is controlled by a special board, the Crate Controller (CC), which serves as an interface between the HV/LV card firmware and the higher level DCS software. The CC is built around an ELMB128, housed on a motherboard, and it communicates with the DCS project through a CAN bus. It is responsible for holding the set of configurations for the module states mentioned above. The crate also contains a SCT Interlock Card (SIC) which is used to send the hardware interlock signals to switch off individual cards (see §4.2.3). The 88 crates are connected to 16 CAN bus branches. A pair of CAN buses is read out by one computer. This granularity ensures a satisfactory performance and a reasonable number of computers on the network.

The PS system is controlled by the *Monitor Power Supply* (MoPS) DCS project. The control can also be handled by the DAQ system using a DDC protocol. The navigation is done through a topological structure, dividing the detector into structures (quadrants, layers, etc) and linking it to the hardware structure (crate, card, etc) using an internal mapping.

4.2.2 Environmental DCS

The SCT is operated in specific environmental conditions (N_2 gas environment, C_3F_8 cooling), hence requiring careful monitoring to avoid thermal shocks and condensation on the modules. This is done through the Environmental (Envr) DCS. In order to monitor the temperature and the humidity inside the detector volume, slightly

over 1000 sensors are installed and monitored through the Envr DCS project. Negative Temperature Coefficient (NTC) thermistors⁴ are placed on various structures: at the exhaust of the cooling pipes, on some end-cap module cooling structures (for monitoring), on the carbon-fibre mechanical structure and floating in the detector air volume. Humidity sensors are also scattered across the volume. Two types of humidity probes are used: radiation-hard Xeritron⁵ and non-radiation-hard Honeywell⁶ sensors, the latter being more precise and easier to calibrate. The number of sensors in various locations on the detector is shown in Table 4.1.

Part	Cooling (Interlock)	Cooling (Monitoring)	Mechanical	Air	Humidity
Barrel 3	36	0	9	32	3
Barrel 4	44	0	9	32	4
Barrel 5	52	0	11	32	4
Barrel 6	60	0	14	32	4
External	0	0	0	8	0
Total Barrel	192	0	43	136	15
Disk 1	16	4	4	9	1
Disk 2	24	6	4	9	1
Disk 3	24	6	4(2)	9	1
Disk 4	24	6	4	9	1
Disk 5	24	0	4	9	1
Disk 6	24	6	4	3	1
Disk 7	16	0	4	3	1
Disk 8	16	0	4	3	1
Disk 9	8	2(0)	4	6(7)	0
Cylinder	0	29(27)	0	0	10
Total EC A	176	59	36	60	18
Total SCT	544	114	113	257	51

Table 4.1: The number of environmental sensors and their physical distribution. Numbers in parentheses are for End-Cap C. The total number for SCT takes into account that there are two end-caps.

Signals from the sensors are routed through several patch panels (PPB1 for barrel sensors, PPF0-PPF1 for end-cap sensors) and sent to Building Block Interlock Monitoring (BBIM) crates [75]. A BBIM crate is a hardware case containing one or more

⁴Type 4N103JT-025 from Semitec.

⁵Type XN1018 from Hygrometrix inc.

⁶Type HiH-3610 and HiH-4000.

BBIM *units*, as well as a power distribution board. A BBIM unit is made of a backplane with four input connectors, as shown in Fig. 4.2, each connected to either an Interlock Box (IBOX) or a Sensor Bias card, and one ELMB. The sensor signals are sent in parallel to the ELMB and to the signal processing card. The BBIM backplane also delivers power to the sensors. Sensor bias cards, as their name states, are used to provide the appropriate biasing to the temperature and humidity sensors, while the IBOX is used to process the temperature signals used as input to the Interlock system (see §4.2.3 for more details). The voltage read-out of the sensors is done by the ELMB, which sends the data via the CAN bus to the OPC server for conversion to relevant quantities ($^{\circ}\text{C}$ and $\%RH$) and calibration.

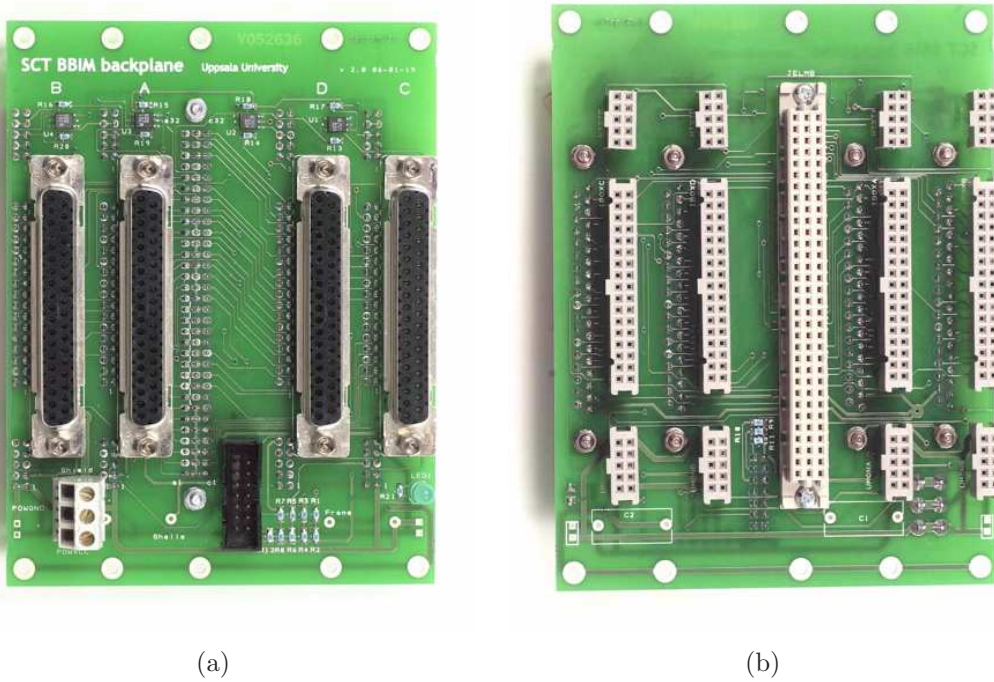


Figure 4.2: The BBIM backplanes: (a) Front view, with the four input connectors, and (b) Back view, with the four cards connectors and the ELMB connector in the middle [76].

The front-end hardware is divided in four racks (one for each quadrant), with four BBIM crates in each: two for the barrel and one for each end-cap. A barrel BBIM crate is composed of two BBIM units, while an end-cap crate contains three units. These crates are located inside the main ATLAS cavern (*UX15*) and must sustain high levels of radiation. The ELMB should tolerate radiation up to 5 Gy over ten years [77]. The PCs used for the DCS software are located in the service caverns, one

on each side of UX15, called *US15* and *USA15*. There is one Envr DCS PC in each side cavern, covering two quadrants of the detector each.

The Envr DCS software provides the interface for the monitoring of the sensor signals. A mapping between the hardware ELMB channels and their location on the detector is an input to the project. This information is then used to display the temperatures and humidities (computed by the OPC server) in an efficient way. Dew point temperatures are also calculated from temperature and humidity values located in the same physical region [78].

4.2.3 Interlock

The silicon modules of the SCT need to be protected against possible cooling incidents leading to module overheating and possible thermal runaway. An interlock system is implemented to achieve this task, based on the Envr temperature sensors located at the exhaust of the cooling pipes. A pair of temperature sensors controls 24 barrel modules and ten to 13 end-cap modules, depending on their radial location on the disk. The redundancy ensures that the interlock still works in case of a sensor failure. The signals from these sensors is read out in parallel by the ELMB board and by a comparator board, the IBOX. The IBOX is equipped with an interchangeable plugin which sets the threshold temperature for the comparison. If the temperature goes above this threshold, the IBOX sends a binary signal which makes the interlock fire in approximately one second.

The output of the IBOX is sent to an Interlock Matrix (IMatrix) which maps the temperature sensors to the PS channels. The interlock signal is then routed to the appropriate SIC, sitting in a PS crate, to turn off individual cards (LV and HV). The IMatrix⁷ uses a programmable firmware, written in VHDL, which can be easily changed in case of modification in the mapping and/or sensor failure. This makes a highly flexible safety system. Contrary to the Envr DCS, the interlock system is fully based on hardware.

The interlock system also offers protection against laser light coming from the optical read-out system of the SCT [79]. When the backdoor of a DAQ rack is opened, the interlock cuts the power to the on-detector opto-package. The interlock is also used to integrate safety actions provided by the DSS.

⁷The IMatrix uses a LC5768VG Complex Programmable Logic Device from Lattice Semiconductor Corporation.

4.3 The Inner Detector DCS

As described previously, the SCT DCS monitors and controls the detector structures and sensors located inside the thermal enclosure. However, some services are common to two or more detectors and this includes the evaporative cooling system, the different gas systems, the magnetic field measurements, the radiation monitors, the beam condition monitor and the thermal enclosure heaters system. Individual DCS projects are designed for each of these systems, grouped under the ID DCS top node [80]. Since these systems can affect the safety and control of the SCT, an interaction is needed between the ID DCS and the SCT DCS. Below is a description of the main systems for which the SCT DCS provides or requests information.

4.3.1 Cooling DCS

The main part of the ID DCS is the control and monitoring of the evaporative C_3F_8 cooling system [49]. In total 204 cooling loops, located in the SCT and Pixel detectors, are controlled by this system, out of which 116 are for the SCT alone. The cooling system is controlled using Programmable Logic Controllers (PLC) which are then connected to the LCS, where a DCS project and an FSM structure are implemented [80].

The cooling plant and each individual cooling loops are qualified by a STATE and STATUS word. This information is used by the MoPS project in the SCT DCS to allow the power to be applied to the modules on the corresponding cooling structure. The power will be cut in the case of a change of this information indicating a failure mode. The SCT Envr DCS also uses this information in order to set alert thresholds on the different temperature sensors in the detector volume (see §4.4.2).

4.3.2 Environmental DCS

As for the SCT detector volume, the ID volume needs constant monitoring of its environmental parameters. In particular, the temperature of the many cooling structures scattered across the volume and the humidity are very important in order to prevent and monitor cooling incidents. To achieve this, a set of sensors external to the individual detector volumes are installed: temperature sensors for the many cooling structures and ambient temperature, radiation-hard and non-radiation-hard humidity sensors. Dew point temperatures are calculated from the pairs of temperature and humidity sensors located in the same area.

The SCT and ID environmental monitoring are highly intricate. A fraction of the sensors used by the ID DCS are in fact provided by the SCT DCS (about 75 sensors, in addition to the sensors listed in Table 4.1). These sensors use the same

technology and read-out hardware as in the SCT DCS. For this reason, the calibration is maintained by the SCT DCS and only the calibrated outputs are sent to the ID DCS project, through a scattered PVSS project connection. The archiving of this data is done through the ID DCS and the databases need to account for this (see §4.4.3).

4.4 SCT DCS Operations

The operation of the SCT detector is highly linked with the SCT DCS. The modules need to be under cooling conditions and powered before the data acquisition can take place. Due to the complexity of the system, it is important to follow a specific sequence to avoid possible complications. One way to simplify this procedure is to use an FSM. In the following sections, the SCT DCS FSM is described as well as various aspects related to the operations of the system.

4.4.1 SCT DCS FSM

The FSM implementation for the SCT DCS should gather the information from both DCS projects and display it in a comprehensive way. In addition, it should allow for the control and monitoring of the infrastructure needed for the DCS hardware. The overall SCT DCS state and status are summarised by the top node. The latter is subdivided following the three TTC⁸ partitions: Barrel, End-Cap A and End-Cap C. In each of these partitions, three subsystems are represented: ENV, PS, ROD. The first two stand for each of the SCT DCS projects and the ROD subsystem controls and monitors the power infrastructure from the SCT RODs. In parallel to the three top nodes, an INF node monitors the infrastructure common to all partitions, like power packs for racks, CAN bus power, etc. The structure of the SCT DCS FSM relies on the cooling loop as the fundamental unit for operations, to allow for an easier interplay with the ID cooling DCS. In the following, the details of the structure of the two main components of the FSM, the PS and ENV nodes, are given.

For the PS system, the set of FSM states is based on the existing modules states defined in the project. The PS FSM [81] device unit is the SCT module. Depending on their location on the detector, the corresponding number of modules form a cooling loop control unit. The cooling loops are then grouped in quadrants under the PS subsystem node. In order to propagate the state and status upwards in the tree, a majority logic is used, i.e. the state shared by the majority of nodes below a given level

⁸TTC stands for Trigger, Timing and Controls. The TTC network serves as an interface between the L1 Trigger and the subdetectors DAQ [61]. Their usage in the DCS allows a better uniformity between the systems.

becomes the state assigned to this level. Partial states are used for the higher-level nodes, such that if a majority of modules, but not all, reach the requested state, this information gets propagated to the top node. Commands can be sent to the modules at any level of the FSM such that they propagate to the modules. The structure of the PS FSM is represented schematically in Fig. 4.3.

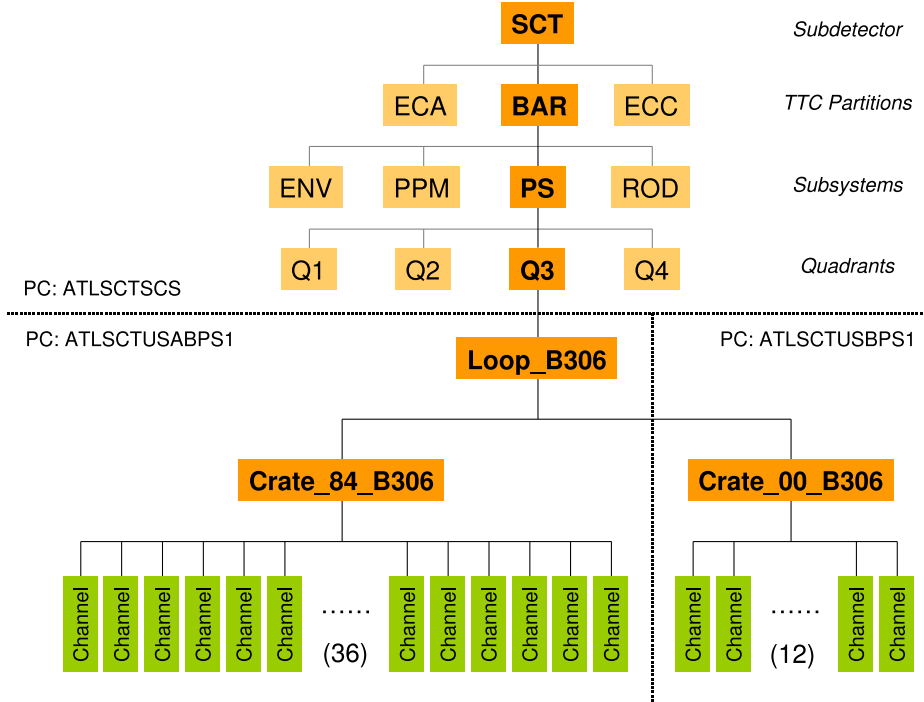


Figure 4.3: The PS FSM structure for the Barrel partition [81]. The TESTBOX partition is completely separate from the SCT FSM and should be ignored here.

The ENV FSM design follows the PS one closely. The device units in this case are individual sensors and they are first grouped according to their function (cooling loop temperature, air temperature, mechanical structure temperature and humidity) and then following their location on the detector. The cooling loop sensors have a different structure to allow for a better uniformity with the PS FSM: they are first grouped according to cooling loops. Fig. 4.4 shows the ENV FSM structure in detail. Note that some cooling loops have sensors in each of the side caverns and the barrel FSM needs to compensate for that. The ENV FSM design is simpler than the PS one since it provides only state propagation, but no commands.

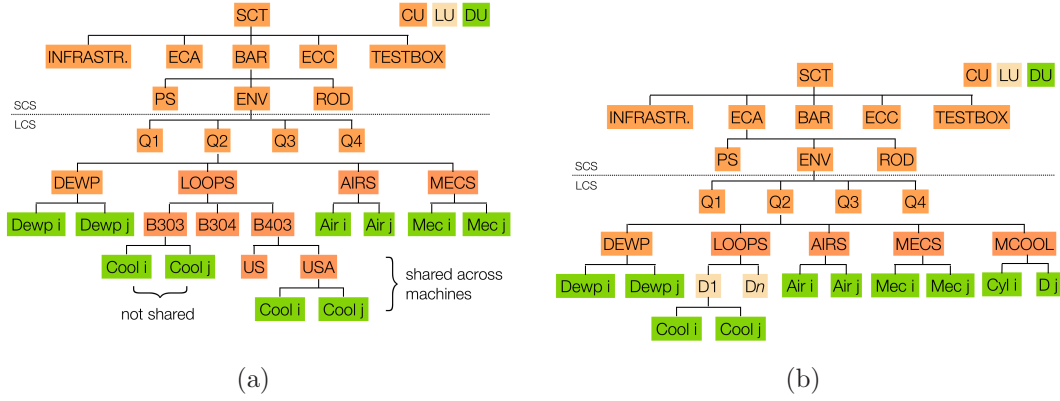


Figure 4.4: The ENV FSM structure (a) for the Barrel partition and (b) for the EC partitions [82]. The TESTBOX partition is completely separate from the SCT FSM and should be ignored here.

In order to operate the SCT, the modules must be in a state to allow DAQ operations. A detailed procedure is needed to bring them in such a state. First, the ID DCS cooling must bring the system up such that the temperature on the modules and from the Envr monitoring are acceptable (low enough to operate and above the dew point to avoid condensation). Using the SCT DCS FSM, the following sequence of commands should be applied.

1. **OFF**: HV/LV is OFF;
2. **INITIAL**: The temperature sensors on the modules can be monitored, but HV/LV is OFF;
3. **STARTING**: HV/LV is ramped up to STANDBY values;
4. **STANDBY**: LV is ramped up to ON, HV is still in STANDBY;
5. **ON**: HV/LV is ON.

After each step of the sequence, a thorough check of the success of the given command needs to be performed to avoid that the modules reach a non-defined state. Once the modules are in the ON state, data-taking can be performed.

4.4.2 Safety actions

The DCS can assign up to four alert settings to each parameter of the system: upper and lower thresholds for *warning* and *alarm* level. These alert levels are needed to

determine the actions to be taken to maintain the safety of the detector in case of failure. The value of the parameter is compared in real time with these thresholds and the corresponding alarm status is displayed in the software. For the MoPS project, the operational values are sent to the CC for fast state transitions, while the majority of alert thresholds are handled by the project. An extra level of safety has been implemented in the CC for some of the more critical “alarm high” alert levels (the hybrid temperature, the bias voltage and the HV current limits) so these levels are also stored in the CC for each module. For this reason, one never expects to observe any “alarm high” condition on module temperature or HV.

Communication is needed between the ID DCS and the SCT DCS to set the alert levels of the Envr DCS and implement some automatic safety actions. First the SCT DCS (both the PS and Envr) reads the state of each cooling loop from the ID Cooling DCS. For the Envr, this information is used to set the alert thresholds, since they cannot be the same for room temperature and for cold running at -7°C . In the case of the PS, a handshaking mechanism is in place between the two systems such that if the communication is broken, after five minutes, a warning message is issued. This is important since the PS uses the ID DCS information to determine if the modules can be turned on for a given cooling loop. It can also operate an emergency shutdown of modules on a given cooling loop when the loop state changes unexpectedly to a non-operational one.

4.4.3 Data archiving

The handling of DCS data follows different requirements than physics data. Part of the data is only needed online for operations and can be saved for bookkeeping and detector performance studies. Another part of the data is also needed offline to establish data-quality flags for the physics data. A custom solution based on a two-step archiving was developed to achieve this. The ATLAS DCS data is divided into two categories: conditions data, which comprises the values of the numerous parameters of a project, and configurations data, which includes the operational values of certain parameters, as well as mapping information and alert levels.

The conditions data are first saved in real time to an Oracle database using the PVSS Oracle Relational DataBase (RDB) manager. The parameters for archiving can be set globally or individually for a single channel within the projects. A reduction of the data volume is necessary, to avoid filling the disk space with values due to noise fluctuations. Consequently, “deadbands” are specified for all relevant values, which are written to the database only when new values are measured outside the deadband. In the SCT DCS, the deadbands are all specified in absolute values.

The data from all archived parameters are copied from Oracle to the COOL conditions database [65], to be made available to the ATLAS offline data analysis

(ATHENA) [65]. This is done using the PVSS2COOL program [83] running on a dedicated Linux machine. The DCS data for a specific module (currents, voltages, etc) are associated with its unique offline identifier in the database. Offline identifiers have also been developed for each Envr sensor, using the information about the sensor purpose and location. A reduction of data going from Oracle to COOL is not needed, but all the time stamps are rounded to the second. This is about the time resolution which is available from the DCS, although a better synchronisation of the distributed systems and a precise measurement of all the delays which are involved may allow for a better precision if required.

During the initial barrel tests (see §5) the DCS data were stored in the internal PVSS database and I was responsible for copying them to COOL manually. I also implemented an automatic back-up procedure for the DCS projects archives which was used extensively before the database solution was put in place.

The configurations data for the SCT DCS are stored in a different Oracle database, using a schema created with the JCOP framework functions [71]. The parameters are grouped per crate and per state and form a configuration unit or “recipe”, which are stored with an associated tag and a version number. This method allows different configurations to be stored for different conditions (e.g. for stable beam, for cosmic rays). Online changes to the configuration parameters can be made via the DCS interface and uploaded to the Oracle database.

4.5 SCT DCS Performance

The SCT DCS and the interlock were used throughout the various steps of the SCT commissioning, from individual module testing to running inside ATLAS. This section focuses on the period starting with the macro-assembly up to the underground installation and commissioning where I was directly involved (see §5 for more details on the commissioning steps).

Even though the implementation slightly differed from the final system, a DCS was implemented at the earliest stage of the SCT construction. The purpose of this DCS was the same as for the final system: monitoring, protection and control. It allowed for a study of the temperature uniformity across the SCT barrels [84]. This study showed a good uniformity for the module temperatures across the SCT barrels. Systematic effects were observed, such as cooling loop-to-loop variations, caused by the different back-pressure settings from the cooling system, and variation along the loop, which is expected due to the pressure gradient along the loop. The former is shown in Fig. 4.5(a), where the temperature trend along the loop is clearly visible, and the latter in Fig. 4.5(b), where some specific rows of 12 modules, or LMTs, are hotter than their neighbours. Once these effects are corrected for, we observe that 98.9% of modules are within 3σ of the average temperature.

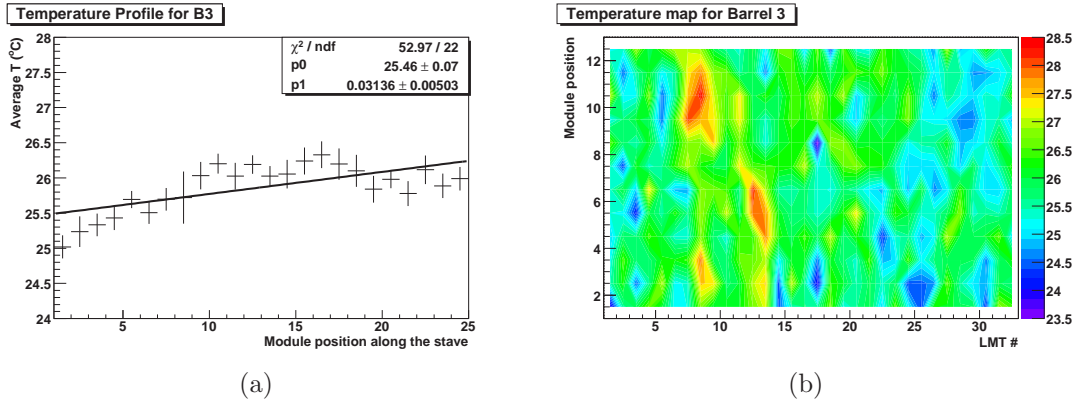


Figure 4.5: The SCT barrel temperature uniformity can be established, after correcting for systematic effects: (a) variation along a given cooling loop, where the x -axis shows the module position along the loop, and (b) loop-to-loop variations, which can be seen here for the first barrel layer, called *Barrel 3*. This map shows an unfolded barrel layer, where the rows of modules are called *LMT*.

More extensive tests of the DCS were made during cosmic ray data-taking, both on surface and underground (see §5.3.3), while scaling up the system at each iteration. These tests were used to validate the DCS before its final implementation in the cavern. The results obtained from these tests also help to understand the inner workings of the system and show its rapid response to problems in operations.

The thermal stability of the detector is essential for its stable operation. For this reason, supervision and evaluation of all temperature parameters are essential to the DCS. Fig. 4.6 shows the typical temperature development of a full cooling cycle (running warm with C_3F_8) as measured by the environmental cooling pipe temperatures during the reception tests at CERN (see §5.3.1).

At cooling start-up the temperatures drop from room temperature to $\sim 9^\circ\text{C}$ before stabilising at $\sim 12^\circ\text{C}$. The temperatures rise up to $\sim 14^\circ\text{C}$ when the module power is turned on and the hybrids start heating. At shutdown the inverse behaviour is seen. At around 17h00 a dip for all sensors is registered corresponding to a change in the back-pressure settings of the evaporative cooling system on all 16 pipes connected to this barrel. The individual sensors show an acceptable level of stability throughout the run. The spread of the temperatures remains low ($\sim 2.5^\circ\text{C}$).

A closer look at the temperature time-dependence reveals a regular pattern where the temperature oscillates with an amplitude of $\sim 0.25^\circ\text{C}$, with period of ~ 5 min. These oscillations are also found when monitoring the hybrid temperatures measured by the MoPS project as shown in Fig. 4.7. They originate from the changes in the

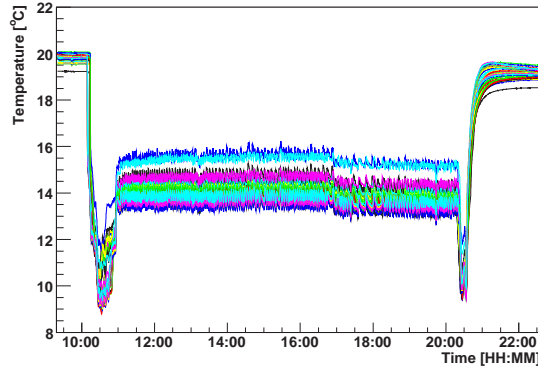


Figure 4.6: Evaporative cooling cycle as measured by the environmental cooling pipe temperature sensors on the innermost barrel during Reception Test. Each sensor (shown by a different colour) monitors the cooling temperature of 24 modules.

back-pressure due to its own regulation. The behaviour of the back-pressure regulator is shown in the same figure. The module only sees a back-pressure range of about half of the actual variation due to latency.

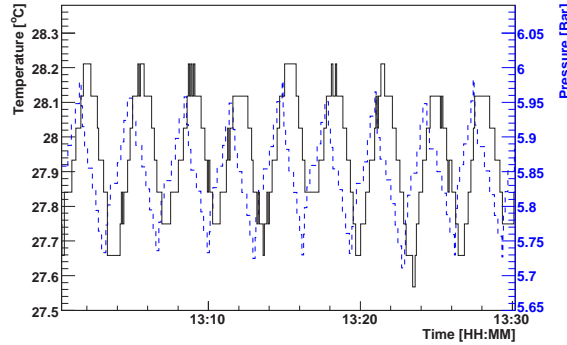


Figure 4.7: Hybrid temperature fluctuations (black line) and the corresponding back-pressure readings (blue dashed line) from the cooling plant during ID Barrel Combined Tests.

The temperature profile for the different types of temperature sensors in the SCT barrel can be seen in Fig. 4.8 for one cooling cycle. The coldest temperatures are measured on the cooling pipes whereas the mechanical temperatures slowly increase by $\sim 2^\circ\text{C}$. The air temperature and the module temperature follow the cooling pipe temperature with an offset of approximately 6°C and 13°C respectively. The effect

of the DAQ and PS operation, which shows as the dips in the central region, are naturally deeper for the module temperature than the cooling pipe temperature.

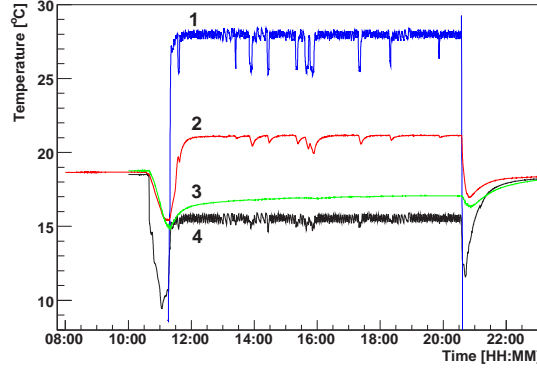


Figure 4.8: A view of all temperatures for a cooling cycle on the SCT: cooling pipe (black line – 4), air (red line – 2), mechanical (green line – 3) and module hybrid temperatures (blue line – 1) are shown for the data collected during Barrel Reception Tests.

The distributions of hybrid temperatures during cosmic ray data-taking are shown in Fig. 4.9. The uniformity is comparable with previous results [84]. The absolute temperature depends on the cooling temperature settings. The end-cap tests were made at a lower temperature than for the barrel test.

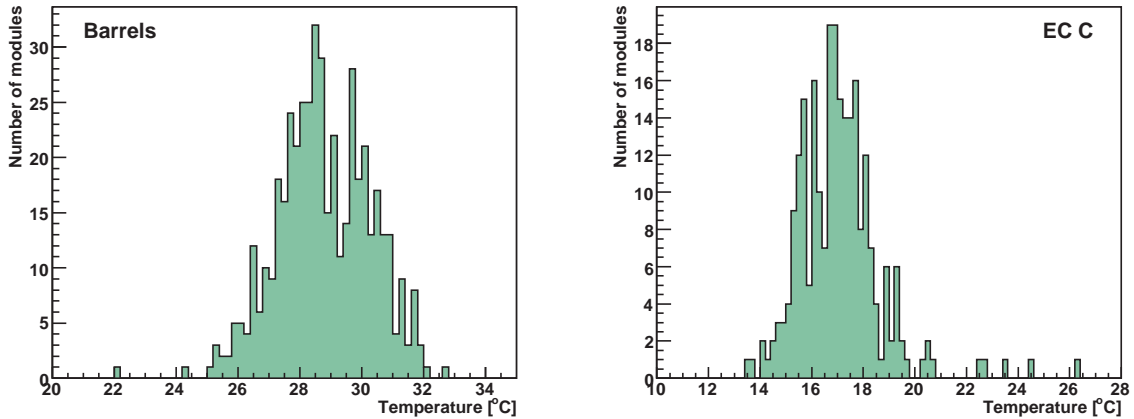


Figure 4.9: Module hybrid temperature distribution during ID Combined Tests (cosmic rays run). The left-hand plot shows the distribution for the four barrels and the right-hand plot, for the End-Cap C.

Fig. 4.10 shows the humidity trend recorded by the Xeritron humidity sensors when the *test enclosure*, which contained the individual barrels during reception test, was flushed with dry air. The slow response for these sensors at low humidity is known and described in [85], and is amplified if there is poor air circulation around the sensor. The response to increasing humidity, as can be seen from the same figure, is very rapid, as required.

The curves in Fig. 4.10 also show two dips, which correspond to the changes in temperatures of the SCT induced by turning the power on or off or by clocking the modules. This sensor temperature dependence can easily be corrected by a correction function based on the individual resistances and total resistance of the Xeritron sensor.

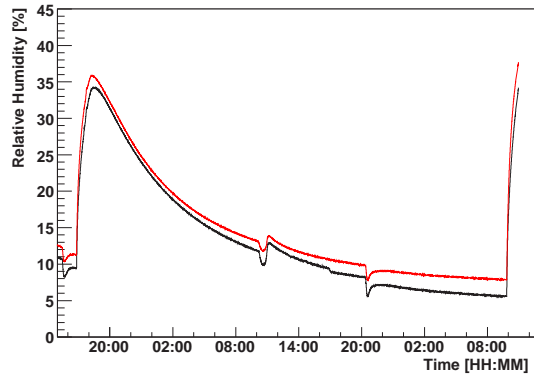


Figure 4.10: Relative humidity readings from the two Xeritron sensors (red and black lines) inside the detector volume during reception testing of the innermost barrel over 46 hours.

During the end-cap C testing the dew point calculation was made using non-radiation-hard Honeywell sensors mounted on the cylinder. Fig. 4.11 shows the dew point calculation for one of these sensors over a five day period. The value for the dew point is low (around -39°C) and stable, well below the monitored cooling temperature in the same region (around 12°C) indicating that there was no risk of condensation. The SCT specifications for humidity are also fulfilled since the difference is more than the required 5°C .

As described in §4.4.2, several hardware, firmware and software measures are taken in the case of over-temperature. In particular, the interlock system, as a fast hardware solution, acts independently whenever a failure is not identified by the other systems.

Fig. 4.12 shows a series of overheating incidents where the module temperatures rose quickly until the safety interlock acted to cut the power off. The failures happened when a capillary feeding a cooling half loop on the outermost barrel was blocked by debris present in the cooling system as a result of an earlier cooling pump failure.

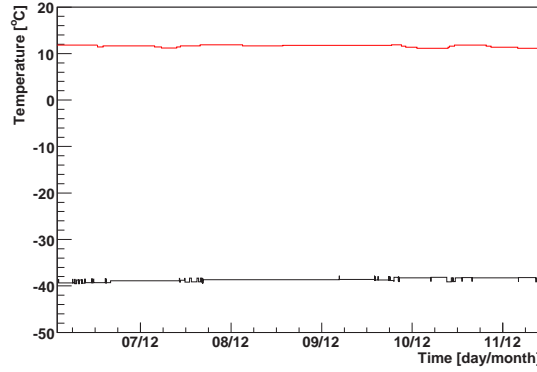


Figure 4.11: Dew point calculation (lower black line) and monitored cooling temperature (upper red line) during five days of data-taking for end-cap C cosmic rays tests.

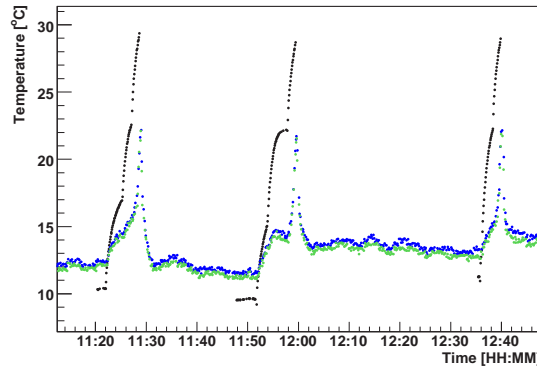


Figure 4.12: Module temperature (black dots) and cooling pipe temperature (blue and green dots) showing the typical behaviour at an interlock incident during ID Barrel Combined Tests.

In the absence of the heat load produced by the modules, the loop appeared to be behaving normally. When the modules were powered, there was insufficient fluid flow to cool them. Since the interlock signal brings the PS system to the OFF state, the module temperature cannot be monitored, as shown on the plot. This event and other related incidents shows that the interlock system acts reliably and fulfills the safety requirements.

CHAPTER 5

SCT Commissioning and Performance

Begin with the end in mind.

- Stephen Covey

The SemiConductor Tracker was previously described in §3.2.1. Together with the other ID detectors, it provides the tracking measurement for physics analysis with the ATLAS detector data. The SCT was installed in the underground ATLAS cavern in 2006 (barrel) and 2007 (end-caps). Before then, several years of module production, macro-assembly and testing were needed in order to commission its operation. Module production was a very complex process, divided between several production sites for barrel and end-cap modules respectively. After strict quality assurance, the modules were sent to the designated assembly sites to be mounted on the final structures (Oxford for barrels, NIKHEF for end-cap A and Liverpool for end-cap C). Finally, the individual barrel layers and the assembled end-caps were sent to CERN for final macro-assembly, testing and integration on the surface and underground. I was directly involved in this process, starting from the testing and integration phase up to the final commissioning in the underground ATLAS cavern. The different steps and results are summarised below, demonstrating the readiness of the SCT for LHC data-taking.

During module production and assembly into barrels and end-cap disks, extensive electrical and operation testing was performed on the individual modules and layers. In order to establish the data-taking performance, acquisition of cosmic ray data is a useful tool. For the ID, and the SCT in particular, cosmic ray data-taking took place both on the surface and underground.

5.1 The SCT module

The SCT contains 6.2 million read-out channels assembled into 4088 modules covering an area of 61 m^2 of silicon. The barrel is made of a total of 2112 modules, while each end-cap consists of 988 wedge-shaped modules. The barrel region covers up to $|\eta| = 1.1\text{--}1.4$ in pseudorapidity while the end-caps extend this value up to 2.5.

To achieve this, the modules have to meet specific design requirements. The barrel module [46] is made of four p-on-n silicon wafers from Hamamatsu each with 64 mm length and width, 285 μm thickness and 80 μm pitch. A schematic view of the barrel module is shown in Fig. 5.1(a). A pair of sensors are bonded together, resulting in a 128 mm strip-length sensor. Two of these sensors are then glued back-to-back with a 40 mrad stereo angle between them to form a double-sided module. Each side of the module has 768 strips which are read out by six 128-channel ABCD3TA [86] radiation hard ASICs using DMILL [87] technology. The 12 chips on a module are mounted on a Cu/Polyimide flexible circuit hybrid which wraps around the sensors at the module center. The sensors and the hybrid are connected to the central Thermal Pyrolytic Graphite (TPG) baseboard and its BeO facings for module cooling and mechanical support. The module is equipped with optical communication for command/clock and data signals. The end-cap modules [47] have four different radial geometries depending on their location with respect to the beam. A schematic for one of the geometries is shown in Fig. 5.1(b). In contrast to the barrel modules, they are wedge-shaped to match the circular shape of their support disks and consequently have a variable pitch along the strip length (between 57 and 90 μm). Their hybrid is placed at the end of the module, in contrast to the barrel where the hybrid is located at the center. All modules can be biased with a maximum voltage of 500 V and their

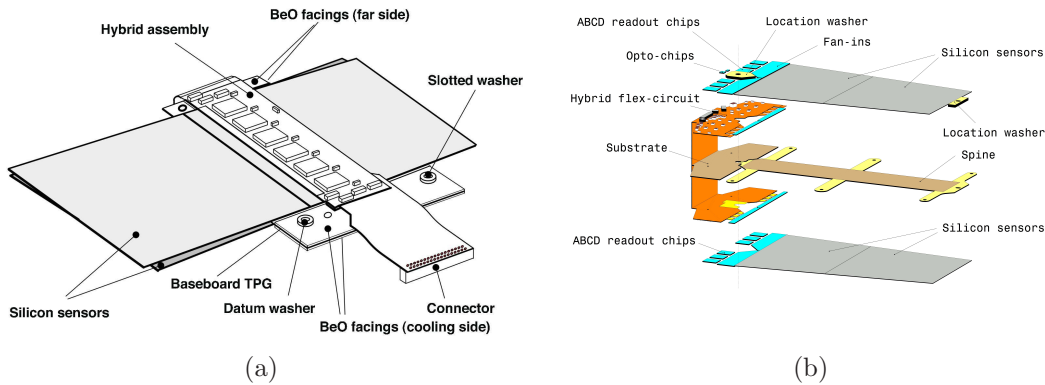


Figure 5.1: The SCT module (a) in the barrel [46], and (b) in the end-cap (middle) [47].

operation temperature inside ATLAS is designed to be -7°C to freeze out radiation damage to the sensors. The power consumption for a module is 5.6 W and is expected to increase to up to 10 W after ten years of LHC operation at the design luminosity.

5.2 SCT calibration

The SCT module uses an binary read-out; the analogue front-end shapes and discriminates the signal pulse against a pre-defined threshold for each channel and the digital pipeline stores the resulting binary information. The pipeline can provide this information upon receiving a clock signal from the ATLAS L1 trigger system. It is then essential to provide a good calibration for every channel since the analog information is discarded after the threshold comparison. Many calibration tests have been developed to adjust the various parameters of the DAQ system and are used between runs during data-taking.

Before any of the following calibrations can be applied, the optical communication between the modules and the DAQ hardware needs to be established. This is important since the quality of the calibration depends on all the information from the read-out chips reaching the DAQ software. A check of communication can be made using the clock signal that a module sends when powered. In addition, the modules can send the content of their registers when probed, hence allowing to check for an expected bit pattern. Further optical tuning can be made using the SCT DAQ.

The most important challenge of a binary read-out system is to set the discriminator threshold to an appropriate value for each channel, such that the efficiency is maximised while the noise is minimised. To achieve this, a good measure of the noise level is needed. A threshold determination is achieved by injecting charge in the chips and performing a threshold scan, where the occupancy is plotted as a function of the threshold for every channel. Many threshold scans are performed for different values of the injected charge and response curves are fitted to obtain the calibration parameters. Noise occupancy can be measured by threshold scans where no charge was injected [88].

5.3 Cosmic Rays on the surface

In 2006, the SCT acquired physics data from cosmic rays and the first reconstructed tracks were observed. A testing facility near the ATLAS cavern at CERN, SR1, was used for this purpose. It was equipped with a clean-room, a control room, a rack area (for services) and a cooling plant. To reach this important milestone, several steps of assembly were required, as described below.

5.3.1 Barrel Reception tests

The assembled barrel modules were sent to Oxford to be mounted on individual barrels. Four lightweight carbon-fiber barrels were used for mechanical support, module mounting points and services [89]. The modules were mounted by a robot onto the carbon-fiber structure in azimuthally parallel rows, allowing for a small overlap of modules from one row to the neighbouring one. Cooling pipes (Cu/Ni) run along the modules, in thermal contact with the TPG baseboards to dissipate the generated heat. The evaporative cooling system common to the SCT and Pixel detectors uses C_3F_8 as the coolant. Low-mass Kapton/Al tapes (LMT) are used to power the modules and also to read out the hybrid temperature provided by Negative Temperature Coefficient (NTC) sensors. For the barrel modules two NTCs are provided, one located on each side of the module; for the end-cap modules only one NTC is installed on the hybrid. This temperature reading also triggers a firmware interlock inside the power supply units to cut the power to the module if the temperature goes above a certain programmable threshold (see §4.2.1).

The assembled barrels were shipped to CERN during 2004 and 2005 and were visually inspected and tested upon their arrival. Reception tests included checks of cooling uniformity and stability, data acquisition (DAQ [90]) and detector control system (DCS [74]) operations, signal response and finally noise performance. The results showed that the module condition [91] was unchanged compared to module production and was well inside the required specifications.

The four individual barrels were then assembled into a single SCT assembly. The barrels were integrated from the largest down to the smallest and finally the inner and outer thermal enclosures, protecting the SCT environmental conditions, were installed. The operation was a success and was completed in September 2005 [22].

5.3.2 EC Reception tests

The two SCT end-caps are identical and were assembled in Liverpool and NIKHEF for end-cap C and A respectively. The end-cap modules were mounted on carbon-fiber disks using a mechanical mounting jig. They are laid out in up to three rings, inner, middle and outer, depending on the location of the disk inside the end-cap. Each ring has a specific module geometry associated with it and, as for the barrel, a small overlap between the rings allows for a hermetic coverage. Once the disks were populated with modules, they were positioned inside the end-cap cylinder. The full end-caps were shipped to CERN for final assembly during 2006. Both end-caps underwent visual inspection and reception testing similar to the barrels. The reception tests showed no change in noise occupancy from module production for both end-caps [92].

5.3.3 Combined Testing

Final assembly steps were performed on both end-caps at CERN, including DCS connections and installation of inner and outer thermal enclosures. Once completed, the three SCT parts were ready for integration with the TRT. To achieve this, the SCT was installed on a cantilever stand and the TRT was placed in a trolley, moving on rails. The TRT was then slid over the SCT. The barrel SCT was integrated first, followed by end-cap C and finally end-cap A.

After integration, the ID barrel and end-cap C were tested with cosmic rays [93]. For the ID barrel, two scintillators were placed above and below the barrel to trigger on cosmic rays crossing one upper and one lower sector of the detector. In total, $\frac{1}{8}$ of the TRT and $\frac{1}{4}$ of the SCT were operational for these tests. The SCT was tested with a C_3F_8 evaporation temperature of $\sim 10^\circ\text{C}$. This was the first attempt at synchronous operation of the four barrels. The aim was to retest the detector after integration to make sure nothing was damaged in the process and also to exercise the detector and the DAQ for cosmic ray data-taking.

During these tests, the noise performance of the SCT detector in operation was verified. The input noise was measured and the results were comparable to module production with an average ENC of 1600 e^- for a hybrid temperature of 30°C . Noise occupancy scans were also performed in standalone mode and in many different configurations: with TRT on/off, with different grounding schemes, with different trigger rates (varying between 5 Hz and 50 kHz), with thermal enclosure heater pads switching on and off. None of these configurations had any influence on the noise occupancy which stayed below the specifications with a mean value of 4.57×10^{-5} . The tests showed that 99.8% of the SCT barrel channels were functional after integration and only 0.03% were lost subsequent to the reception tests of the individual barrels at CERN.

About 450 000 cosmic ray events were collected during the ID barrel combined tests, between March and June 2006. Around 70% of these events contained good tracks as shown on Fig. 5.2. The SCT was operated at the nominal threshold of 1 fC. The barrel hit efficiency per layer for these cosmic ray events was greater than 98.8%, independent of the method used to calculate the efficiency. These first physics data for the ID also tested several components of the software, namely the online monitoring, the event display, the alignment and offline reconstruction software.

The ID end-cap C was subjected to similar testing in December 2006. To match the geometry of the end-cap, the two scintillators were placed at each end of the detector to trigger on horizontal cosmic ray tracks. Around 167 000 cosmic ray events were recorded and no influence on noise occupancy was observed from TRT activities, nor from variable trigger rate.

The ID combined tests were also a great testbench for the Detector Control System (DCS). The DCS went through a lot of development before the tests and operated

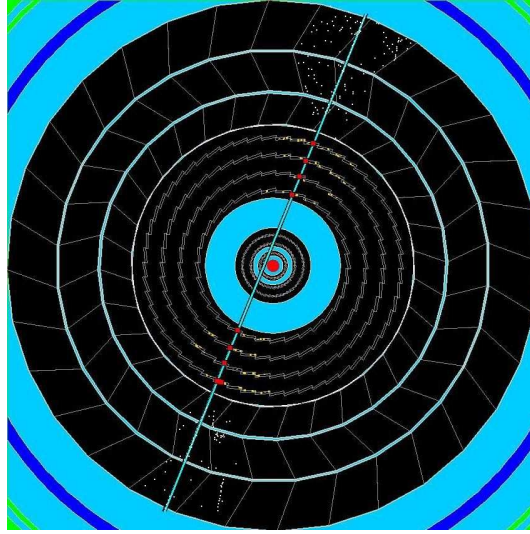


Figure 5.2: A cosmic ray track going through the ID barrel shown on the event display [94]. The pixel detector was not included in the run but was shown on the display.

reliably throughout this period. The communication with the DAQ system was established, to share monitoring information and also to control the power to the modules from the DAQ interface.

5.4 Cosmic rays in the ATLAS cavern

In summer 2006, the ID barrel was transported from the surface integration building and lowered in the ATLAS pit. It was then carefully slid into the solenoid magnet cryostat and placed at $z=0$ as shown on Fig. 5.3. The remainder of the year was used to connect cooling pipes, fibers, LMTs and DCS cables and to test all connections. The cabling was completed in February 2007. The ID end-caps A and C were lowered and installed respectively in May and June 2007 for end-cap A and C. Cabling and connection testing took place during the summer in order to be part of the ATLAS commissioning during Fall 2007.

As the detector was being installed, the online software was also developed towards its final stage. Both the DAQ and DCS software needed to finalise their core development and integrate within the central ATLAS control. For the DCS, a Finite State Machine was created to make operation from the central DCS possible. The SCT DCS software was then fully integrated with the ATLAS DCS. The SCT DAQ went through a similar successful integration process. The functionality of the software in both physics and calibration mode was exercised within the ATLAS main run control and it took part in many global runs with a few detector modules.

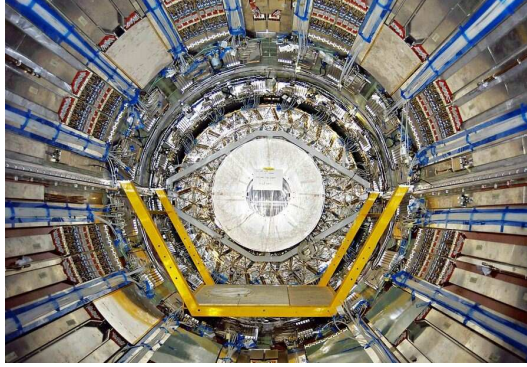


Figure 5.3: The ID barrel in its final position inside ATLAS [94].

In March 2007, the SCT barrel was tested more extensively with C_3F_8 evaporative cooling before the integration of the end-caps. All modules were tested. Noise occupancy runs were taken with the TRT on/off and with different grounding schemes. No evidence for pick-up noise from the TRT was found. Noise occupancy was measured after five days of continuous powering and was found to be 5.7×10^{-5} in physics mode as shown in Fig. 5.4. During the test, one faulty HV channel was discovered but the yield of functional channels was still high at $\sim 99.7\%$.

During these tests, the evaporative cooling system had a good overall performance from the detector viewpoint. It allowed all modules to be probed and calibration scans to be run. But the reliability of specific components of the system was discovered

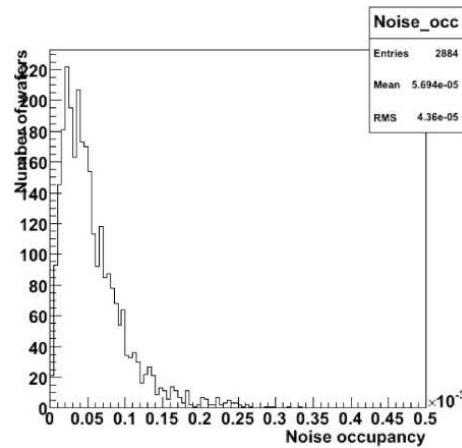


Figure 5.4: The noise occupancy measured for 75% of the SCT barrel modules in the ATLAS pit after five days of continuous powering [94]. There are two entries per module, one for each side.

to be an issue. The cooling system uses liquid C_3F_8 that is pumped into the SCT cooling pipes. The liquid partially evaporates inside the detector due to the heat being transferred to the coolant. At the exhaust of the SCT, the coolant is in a mixture of liquid and gas, but the cooling plant requires that only gas should be returned to the compressor. Furthermore, the coolant should be in a gaseous state before it leaves the ID volume to avoid condensation. For these reasons, heaters are installed at the exhaust of the detector to boil off the remaining liquid before it leaves the humidity-controlled ID volume. These heaters suffered from power connector faults during the SCT barrel tests in the pit and were shown to be unreliable for long term running. For this reason, the decision was taken to reposition them to be able to access them more easily if needed in the future. They were taken from inside the cryostat bore, which was inaccessible after the ID end-cap installation, to a location outside the cryostat. This allowed for continuous work on the Pixel and end-cap installation. Since then, the heater reliability problem was fixed to allow for a continuous operation.

5.5 Readiness for LHC data-taking

From module production to macro-assembly, the SCT successfully passed through different testing phases. The tests performed during assembly and especially the cosmic ray tests on the surface allowed for a better understanding of the three detector parts themselves (barrel, end-cap A and C) as well as of the online and offline software. The influence of various configurations on the noise occupancy, such as the presence of the TRT or the grounding scheme, was confirmed to be nonexistent. The input noise and noise occupancy of the SCT modules were measured to be well within specifications. Experience was gained on using the DAQ in physics mode which was an important preparation step towards first physics data acquisition in the ATLAS pit.

The SCT has been fully integrated inside the ATLAS detector, together with the other ID detectors, since August 2008. During Fall 2008, three different types of data were collected: single beam events from the LHC, ATLAS combined cosmic ray data and standalone ID cosmic ray data. These data samples allowed commissioning and performance benchmarks to be established for the SCT [50]. Some highlights from this effort are presented below.

The noise occupancy of the SCT was measured using calibration runs with bias voltage at 150 V in December 2008 and is shown in Fig. 5.5. Noisy strips with an occupancy higher than 10^{-3} were excluded ($\sim 0.02\%$ of all strips).

The hit efficiency in each silicon layer of the ID was measured in the 2008 cosmic ray data, as shown in Fig. 5.6. This measurement was performed with the Solenoid field on. The overall efficiency for the SCT is 99.78 ± 0.01 (stat.) %.

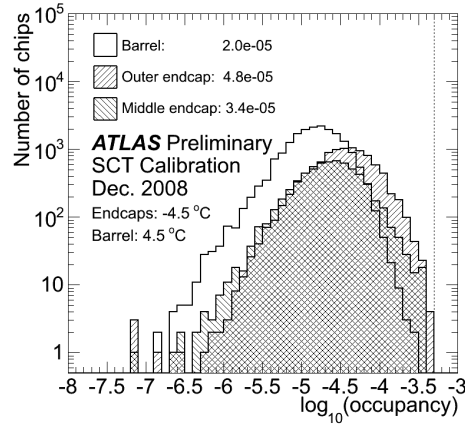


Figure 5.5: The SCT Noise Occupancy in 2008 cosmic ray data. The dashed vertical line shows the specifications [50].

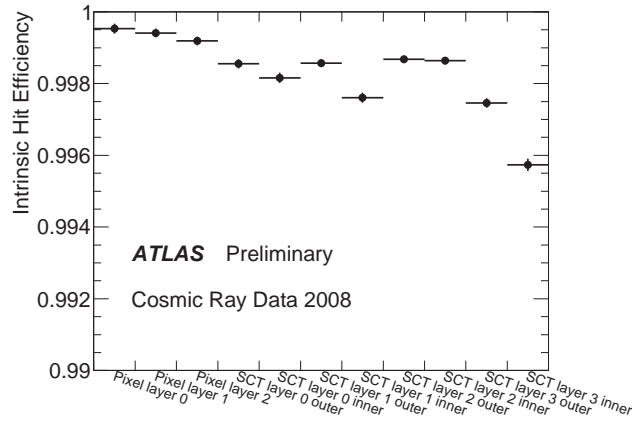


Figure 5.6: Silicon intrinsic hit efficiency per layer [50].

In summary, the SCT is showing a good performance well within its specifications, at all stages of commissioning. The SCT has now entered the era of data-taking and it is showing a high data-taking efficiency and good noise performance in the data acquired so far. As of late 2009, more than 98.5% of all SCT modules are functional and can be used in physics data-taking [95]. Based on these results, the SCT is ready to provide high-quality tracking for the ongoing LHC collisions.

CHAPTER 6

Electron reconstruction

L'essentiel est invisible pour les yeux.

- Antoine de Saint-Exupéry

In order to perform a physics measurement, it is essential to rely on specific event signatures in the ATLAS detector. These signatures are made by various particles moving from the interaction point and being recorded by the different subdetectors. The traces they leave behind as electronic signals in the DAQ systems need to be translated into physical quantities, such as energy, momentum and direction. This process is called *reconstruction* and is performed differently for every type of particle we expect to see in the detector. In this thesis, we look at the J/ψ meson decaying to electrons¹. The following section describes the technique used to reconstruct the electrons passing through ATLAS as physics objects usable by various analyses. The electron reconstruction is performed at two levels: online by the trigger and offline by the ATLAS software. We focus here on the offline implementation which is also used at the Event Filter trigger level. It requires two ingredients: a track in the Inner Detector and an energy deposit in the EM calorimeter.

¹In the following, the term *electron* is used to designate electron and positron.

6.1 Charged particle tracking

Since electrons are charged particles (contrary to the electromagnetic bosons, the photons), they leave an ionising track as they traverse the ID. It is thus important to reconstruct their path efficiently using a tracking algorithm.

In 2007, the ATLAS track reconstruction software [96] was completely revamped to incorporate the existing structure into a new software realm, called NEWT. As described previously in §3.2.1, the ID uses two different technologies to track charged particles, silicon and gaseous drift tubes, which need to be taken into account during reconstruction. Two sequences have been developed to achieve a good efficiency in track reconstruction, the *inside-out* and *outside-in*, as described below.

First, the inside-out sequence is applied to measurements from the detector. The pattern finding in this case starts from the detector elements of small granularity at small radii and develops further to larger radii. The initial step of this sequence is to build three-dimensional representations of the silicon measurements, called *spacepoints*. For the Pixel detector, this is trivial since the detector provides a three-dimensional measurement; it only needs to be converted from local (to the module) to global (to the detector) coordinates using the module positions. For the SCT, the spacepoints are built by combining two individual layer hits, one on each side of the module, which restricts the z -position of the hits. By combining two or more spacepoints, track seeds are then built. The seed direction defines a road window used for further track finding. Any new spacepoint found inside the road window goes through a simplified Kalman filtering [97] and smoothing approach, and hence is either added to the track or rejected, based on the result. Ambiguity solving is implemented using a scoring system attributed to each track. This score is based on the track characteristics and a weight is applied to favour more precise hits (e.g. Pixel with respect to SCT hits). At this stage, tracks are required to have a minimum transverse momentum of 500 MeV. These silicon-only tracks are then used to build track extensions, or *segments*, into the TRT. In this process, the input silicon track is not modified. After the extensions have been found, a combined track fit between the silicon-only track and the TRT extension is performed. The best fits are then kept to form the collection of tracks used for analysis.

The outside-in sequence is then applied. It is used to improve the track reconstruction efficiency, since some tracks are not picked-up by the inside-out procedure, i.e. tracks from secondary decays, photon conversions, electron bremsstrahlung with a large energy loss happening near the end of the silicon tracker. Standalone TRT segments are built from the hits that were not used in the TRT extension procedure of the inside-out sequence. Since the TRT does not provide longitudinal measurements, projective planes are used: R - ϕ for the barrel, R - z for the end-cap. The TRT segments are then propagated back into the silicon tracker (*backtracking*).

Since the amount of material in the ID is significant, electrons are prone to undergo bremsstrahlung in the ID (see §3.2.1). This is a challenge for the tracking since the track momentum is modified as the electron emits one or more photons along its trajectory. To correct for this effect, refitting algorithms [98] are run on the track used to build an electron object (see §6.3 for more details). Three refitters are used in ATLAS: the Gaussian Sum Filter (GSF) [99], the Dynamic Noise Adjustment (DNA), which need solely the tracking information as an input, and CaloBrem [100], which makes use of the calorimeter information. The results from these algorithms are saved in the data file alongside the original electron object.

6.2 Electromagnetic Clustering

After losing some of its energy in material interactions in the ID, the electron reaches the LAr EM calorimeter, where it is stopped by the calorimeter material. The energy of the electron is emitted in the EM showering process and recorded by the electrodes in multiple cells of the calorimeter. The digitised electronic pulses of each cell (the smallest subdivision of the calorimeter) are converted to energy by the Digital Signal Processors (DSP), located on the back-end boards. The raw energy in each cell is recorded by the DAQ in bytestream format, to be processed by the ATLAS ATHENA software. From the bytestream to the cell energies stored in the data files, a correction is applied to account for data-taking conditions and detector characteristics.

In order to find electromagnetic objects, clusters of energy above the noise level of the calorimeter are built by grouping individual cells. The default strategy chosen by ATLAS to perform electromagnetic clustering is based on a fixed size cluster and is called the *Sliding Window* algorithm. Another method called *topological clustering* is available and is used for the reconstruction of electrons in the forward region, as explained in §6.3.3.

6.2.1 Sliding Window

The Sliding Window algorithm [101] uses a fixed size cluster and looks for contiguous cells that fulfill certain requirements. The sizes of the windows used during the clustering process are chosen to optimise the cluster finding efficiency while reducing noise, as shown in Table 6.1. All EM calorimeter clusters inside the ID acceptance (for electrons and photons) are built using this algorithm. The clustering is performed in three steps: tower building, seed finding (pre-cluster) and cluster building.

As described earlier in §3.2.2, the calorimeter is divided in radial layers as well as in cells on the η - ϕ grid. A calorimeter tower is built using cells from all available layers for an element on the η - ϕ grid with area 0.025×0.025 . Since the size of cells varies between the different layers, only the fraction of energy corresponding to the

area intersected by the tower is used for cells larger than the tower size. To find seeds, a $N_\eta^{\text{seed}} \times N_\phi^{\text{seed}}$ window² is first slid throughout the calorimeter tower grid [102]. If the window transverse energy, E_T , which is the sum of the towers in the window, is above $E_T^{\text{threshold}}$, then a seed (pre-cluster) is formed. The position of the pre-cluster is the energy-weighted barycenter of the $N_\eta^{\text{position}} \times N_\phi^{\text{position}}$ window at the center of the original $N_\eta^{\text{seed}} \times N_\phi^{\text{seed}}$ sliding window. The resulting positions are labelled η_0 and ϕ_0 . A duplicate removal procedure is applied if two pre-clusters are within a $\Delta\eta^{\text{duplicate}} \times \Delta\phi^{\text{duplicate}}$ window of each other³. In such a case, the transverse energy of the two seeds in the window $N_\eta^{\text{duplicate}} \times N_\phi^{\text{duplicate}}$, $E_{T1}^{\text{duplicate}}$ and $E_{T2}^{\text{duplicate}}$, are compared. If the difference $\Delta E_T = |E_{T1}^{\text{duplicate}} - E_{T2}^{\text{duplicate}}| > 10\%$, only the seed with the highest E_T is kept; otherwise only the seed with the highest E_T in the central tower is kept.

For the cluster building step, towers are abandoned and the original cells in each layer are used. This final clustering step is iterative over all layers, starting with the middle one, since it usually contains the largest fraction of the energy of the shower. Using η_0 and ϕ_0 as the starting point, the energies of the cells in a $N_\eta^{\text{seed}} \times N_\phi^{\text{seed}}$ window are added together and a new barycenter, η_{middle} and ϕ_{middle} , is computed. The same procedure, using the last layer position to feed into the current one, is then applied to the front layer. The η_{front} position is refined around the most energetic cell and the presampler barycenter position is computed using η_{front} and ϕ_{middle} as an input. Finally, the back layer cells are added as previously, but using η_{middle} and ϕ_{middle} as an input due to its proximity. Further corrections are applied to the resulting cluster. The individual layer positions are corrected for known systematic biases due to the detector geometry and an overall cluster position is computed by combining the positions of the front and middle layers, since they have the best granularities. The energy of the cluster is a weighted sum of the energy of each layer, multiplied by an overall scale factor. This energy correction is meant to account for energy losses in the material in front of the calorimeter. The correction factors vary for the different η regions and energy ranges, and they differ for electrons and photons. Further corrections are applied for detector geometry effects [103].

After the $N_\eta^{\text{seed}} \times N_\phi^{\text{seed}}$ clusters are built, depending on the nature of EM particle they are associated with, either electron or photon, and their location (barrel or end-cap), a new cluster with a different size is built using the same cluster building procedure as described above and using η_0 and ϕ_0 as the starting point. This procedure is described in §6.3.1. The window sizes used in the Sliding Window algorithm are listed in Table 6.1. They were recently optimised to be robust against all cluster sizes used further in the reconstruction process.

²One unit in $\Delta\eta \times \Delta\phi$ corresponds to 0.025×0.025 .

³In the original setup, the tower geometrical center was used for the duplicate removal while in the optimised setup, the seed barycenter is used.

	$E_T^{\text{threshold}}$	$N_{\eta}^{\text{seed}} \times N_{\phi}^{\text{seed}}$	$N_{\eta}^{\text{position}} \times N_{\phi}^{\text{position}}$	$\Delta\eta^{\text{duplicate}} \times \Delta\phi^{\text{duplicate}}$	$N_{\eta}^{\text{duplicate}} \times N_{\phi}^{\text{duplicate}}$
Original	3 GeV	5×5	3×3	2×2	3×3
Optimised	2.5 GeV	3×5	1×1	2×4	3×5

Table 6.1: Sliding Window parameters, before and after optimisation. The *original* parameters were used for ATHENA releases < 15.3.0.2, after which the *optimised* parameters were used.

6.2.2 Duplicate Clusters

In the clustering algorithm described previously, the duplicate removal procedure was recently improved to be more efficient, as shown in Table 6.1 [104]. This change was initiated since, for electron objects from J/ψ decays, we observed a residual amount of clusters which could be linked to the same physical object. Also, some duplicate clusters were created by the Sliding Window algorithm with a highly off-centered energy in η . The observations made before the changes were implemented are outlined below.

We have performed a study using electrons from simulated J/ψ and Z decays reconstructed using ATHENA releases 14.5.0 and 14.5.1.2, respectively. A cluster was matched in angular distance ΔR , defined as $\sqrt{\Delta\eta^2 + \Delta\phi^2}$, to the closest generator-level electron, e^{\pm}_{true} , inside a cone of radius $R=0.2$. Duplicates were found if two or more clusters could be matched to the same e^{\pm}_{true} in the event. The duplicate cluster rate was computed using Eq. 6.1.

$$\text{Duplicate rate} = 1 - \frac{\# \text{ of unique true electrons matched to reconstructed electron object}}{\# \text{ of reconstructed electron objects matched to a true electron}} \quad (6.1)$$

Out of 86452 events, we observed that 2.4% of J/ψ reconstructed electron clusters were duplicates. This fraction decreased to 0.76% for electron objects with $E_T > 5$ GeV. For 10 000 $Z \rightarrow e^+e^-$ events, 0.8% of electron clusters were duplicates and this proportion dropped to zero when requiring $E_T > 20$ GeV.

Among the observed duplicate clusters in $J/\psi \rightarrow e^+e^-$ events, two interesting cases stood out. In the first, 5×5 EM clusters, after going through all steps of clustering, were found to have their barycenters separated by less than the window size required for duplicate cluster removal in Sliding Window, as shown in Fig. 6.1 for duplicate clusters only. The two bands in the $\Delta\eta_0$ direction show a significant fraction of duplicate clusters separated by approximately one or two units. This was due to the fact that the duplicate removal of pre-clusters was performed using the towers geometrical centers rather than their barycenters. This was modified such

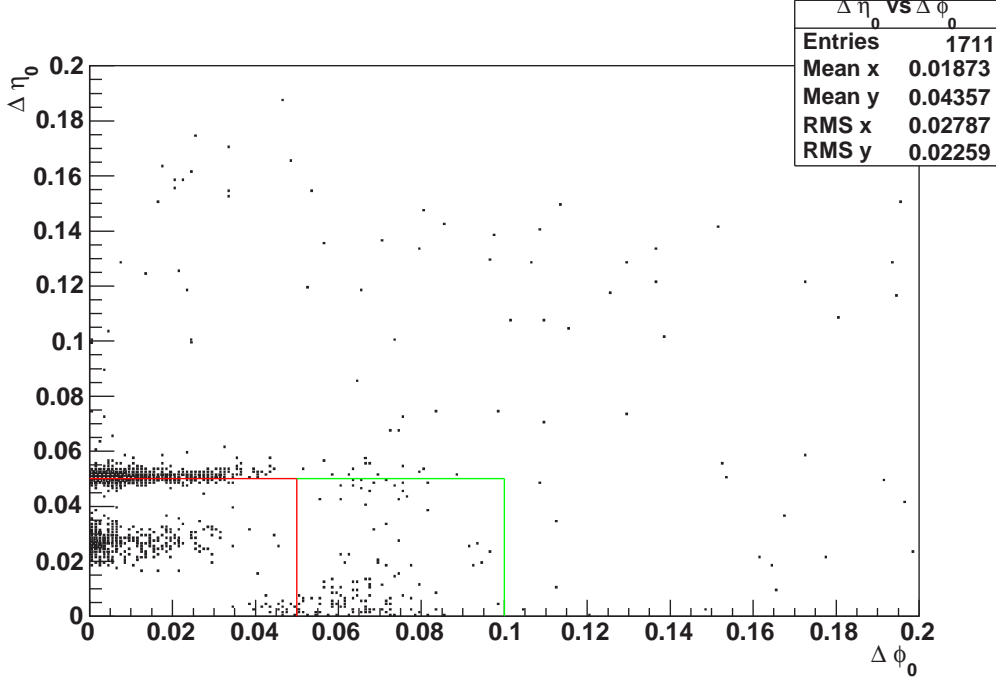


Figure 6.1: Distance between cluster seed positions η_0 and ϕ_0 for duplicate clusters in J/ψ decays. The red square indicates the original duplicate removal window (2×2) and the green square shows the size of the current duplicate removal window (2×4).

that the positions used for duplicate removal are η_0 and ϕ_0 . Also, by increasing the duplicate removal window size $\Delta\phi^{\text{duplicate}}$, the occurrence of such clusters was significantly reduced.

Secondly, some duplicate clusters were found to poorly measure the energy of the e^{\pm}_{true} matched to them. Their energy was very much off-centered in the η direction, i.e. the most energetic cell was located at the cluster edge. As these were duplicates, another cluster measured the same energy much better, since the most energetic cell was then located in the cluster center. This energy loss can be shown to come from the reclustering of electrons during the calibration process, going from the EM cluster size (5×5) to the electron cluster size (3×7). The energy loss is shown in Fig. 6.2, where a significant fraction of duplicates have a value of the ratio between the energies of the pre-cluster and the final electron cluster considerably larger than one. In the case of Fig. 6.2(a), where all electrons are considered, 3% of electron clusters have $E_{5 \times 5}/E_{3 \times 7} > 1.2$, while in the case of Fig. 6.2(b), in which only duplicate clusters are present, the above condition is fulfilled by 27.1% of electron clusters. This indicates that duplicate clusters tend to be more off-centered than other clusters. This problem

was solved by reducing the seed window size, $N_{\eta,\phi}^{\text{seed}}$, to 3×5 , hence making it smaller than any of the electron cluster sizes used after track-matching, namely 3×7 in the barrel and 5×5 in the end-cap.

A measure of the improvement in the duplicate cluster rate was performed in [104] and is shown in Fig. 6.3. The duplicate rate is reduced considerably using the modified parameters, while the Sliding Window algorithm overall performance in terms of cluster finding efficiency, energy resolution and tail fraction is similar or even improved in certain cases. The small fraction of remaining duplicate clusters is removed in the final analysis by a cut on the ΔR between the electron objects.

6.3 Reconstruction algorithms

From the two ingredients described previously, electron objects are built following certain criteria. Depending on their characteristics, several algorithms are used to reconstruct electrons. A standard one, seeded by the EM cluster, is used by most analyses, and by the electron trigger, since it has the highest efficiency for the whole tracking η range and a wide range in E_T . A track-based algorithm was developed for electrons with lower E_T and finally, a specific algorithm exists for electrons in the η range where tracking is not available.

The electron objects created with all algorithms are stored in a common container inside the data file. An *author* bit-word saves the information concerning the algorithm used for a given object. Overlaps can exist between these algorithms; the ones between the cluster-based and track-based algorithm are dealt with by the software, as explained in §6.5 while the forward electron algorithm cannot overlap with the other two since it is applied in a complementary pseudorapidity range.

6.3.1 Cluster-seeded electrons

The most commonly used algorithm for electron reconstruction is the cluster-based algorithm. The inputs of the algorithm are the tracks and clusters described previously. For each reconstructed cluster in a given event, a match is searched for among all reconstructed tracks. After extrapolation to the middle layer of the calorimeter, the track must be matched to this cluster layer within a $\Delta\eta \times \Delta\phi = 0.05 \times 0.1$ window. The extrapolation uses η and ϕ from the last measurement on the track as an input. Priority is given to tracks with silicon hits over TRT-only tracks, where TRT-only tracks are required to have less than 4 silicon hits (Pixel+SCT). An exception is made for the latter case since η is not measured by the TRT barrel; the track-matching is only performed in ϕ for these tracks. The closest track in ΔR ($\Delta\phi$) is kept as the electron track. All tracks fulfilling the $\Delta\eta$ - $\Delta\phi$ matching criteria are kept in the AOD and can be accessed from the electron object, if needed.

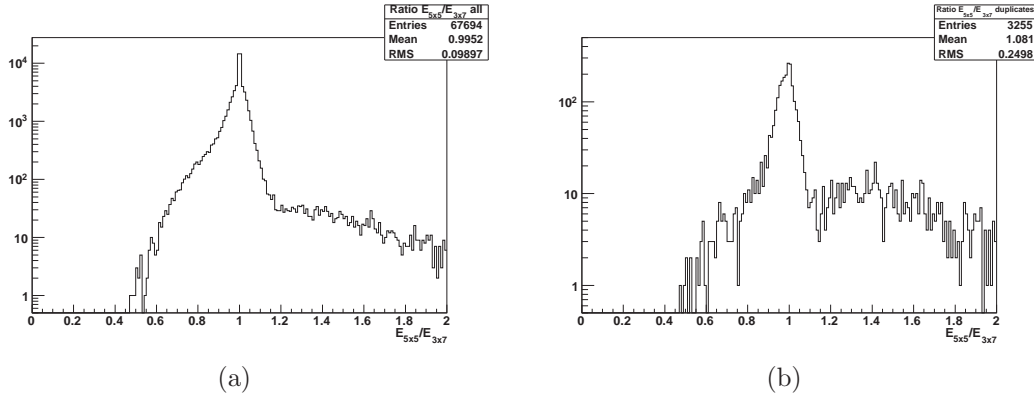


Figure 6.2: Energy ratio distribution between 5×5 and 3×7 clusters (a) for all electrons matching a true J/ψ electron and (b) for electrons having duplicate clusters.

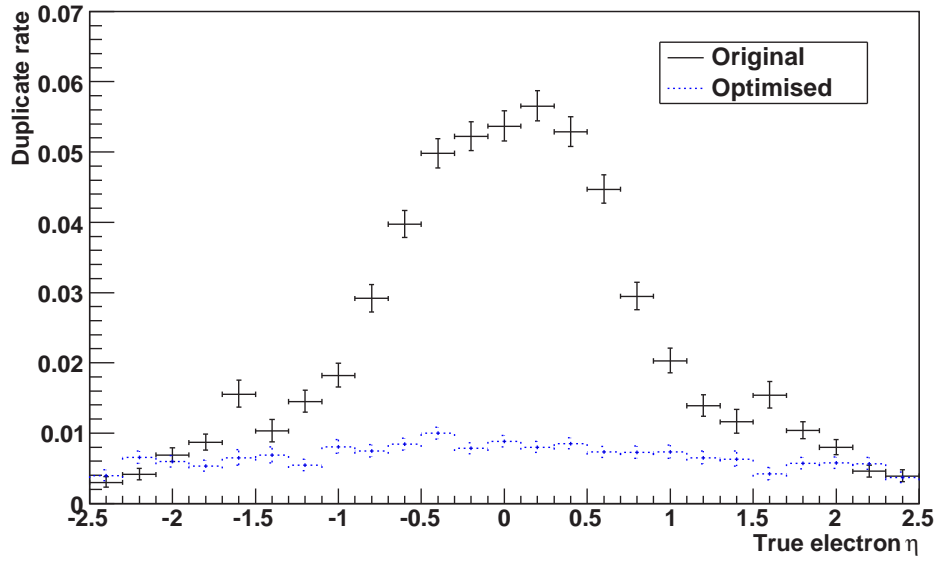


Figure 6.3: Duplicate rate for J/ψ clusters as a function of the electron pseudorapidity [104]. The black solid crosses are for the original Sliding Window parameters while the blue dotted crosses are for the optimised parameters.

All clusters with a matching track are classified as electron objects. Since calibration differs between electrons and photons, a new clustering step is needed after determination of the EM particle nature. For electrons in the barrel, a 3×7 cluster is built from the Sliding Window seed positions η_0 and ϕ_0 , following the same procedure as explained in §6.2.1. The size in the ϕ direction is larger to accommodate electrons which undergo bremsstrahlung in the ID. In the end-caps, the electron cluster size is 5×5 .

6.3.2 Track-seeded electrons

For low energy electrons, it was found that the efficiency can be improved using an alternative algorithm. In this case, the reconstruction is seeded by the tracking. This allows to go lower in the seed E_T , compared to an EM cluster, which needs a higher threshold to reduce noise. However, the track multiplicity being much higher than the cluster multiplicity in ATLAS, strict preselection requirements on the track are necessary. A sample of good quality tracks is formed from all reconstructed tracks for which:

- $p_T > 2 \text{ GeV}$,
- number of *b-layer* hits ≥ 1 ,
- number of Pixel hits ≥ 2 ,
- number of silicon (Pixel+SCT) hits ≥ 7 ,
- number of TRT hits ≥ 20 ,
- number of high-threshold TRT hits ≥ 1 .

Since the TRT extends only up to $|\eta| < 2$, there is an implicit pseudorapidity cut for these electrons. Each of these preselected tracks is extrapolated to the calorimeter. An EM cluster is then built with the usual cluster size (i.e. 3×7 in the barrel, 5×5 in the end-caps), using the track impact position to the middle layer of the calorimeter as the cluster center. The cluster building and corrections used here are the same as used for the last step of the Sliding Window algorithm. The newly built cluster must have:

- $E/p > 0.7$,
- $E/p < 4$,
- $E_1^{cl}(3 \times 1)/E^{cl}(\text{core}) > 0.03$,
- $E_3^{cl}(3 \times 3)/E^{cl}(\text{core}) < 0.5$.

In the above, $E_1^{cl}(3 \times 1)$ is the energy in the 3×1 physical cells at the center of the front layer and $E_3^{cl}(3 \times 3)$ is the energy in the 3×3 cells at the center of the back layer. $E^{cl}(\text{core})$ is the sum of layer energies at the core of the EM shower, computed as follows: 3×3 cells in the presampler, 15×3 cells in the front layer, 5×5 cells in the middle layer and 3×5 cells in the back layer⁴.

6.3.3 Forward electrons

In the two previously described algorithms, the presence of a track matched to an EM cluster is what distinguishes an electron from a photon. Of course, this requirement can only be applied in the acceptance of the tracking system, which is $|\eta| < 2.5$. But electrons from physics processes reach further and can be reconstructed using a specific algorithm for the region $2.5 < |\eta| < 4.9$. These objects are referred to as *forward electrons*.

The reconstruction of forward electrons is based on a different clustering algorithm, called *topological clustering* [101]. In this case, instead of a fixed-size cluster building, a seed cell with an energy significance, i.e signal-to-noise ratio, above a certain threshold is found and neighbouring cells are added to it, given that their significance is above a threshold lower than the seed one. A splitting procedure is implemented to find local maxima and create new topological clusters if needed. With this procedure, the clusters can have a different number of cells and size. Noise suppression is performed during cluster building.

The energy of the cluster is computed as the sum of the cluster cells and the direction by their barycenter. A candidate forward electron is reconstructed if a cluster with $E_T > 5$ GeV is found. In order to identify the electron over hadronic background, strict cuts on the shower shape and cluster moments are applied. These identification cuts differ from the ones used for cluster-seeded and track-seeded electrons, as defined in §6.4 [102].

6.4 Electron Identification

After the electron object is built, in order to reject background more efficiently, identification cuts are defined. For this purpose, the ATLAS electron reconstruction defines a set of standard cuts grouped in three sequential levels, referred to as *loose*, *medium* and *tight*. They are described in detail in the following.

Electron identification is made using rectangular cuts over tracking and shower shape variables that allow a good separation between the isolated electron signal and

⁴Note that the sizes here are given in number of cells in $\eta \times \phi$, not in $\eta \times \phi$ units, as used previously for cluster sizes. The cell size in η and ϕ can vary, depending on the position of the cell inside the detector.

η	E_T (GeV)
< 0.1	< 5
$0.1-0.6$	$5-10$
$0.6-0.8$	$10-15$
$0.8-1.15$	$15-20$
$1.15-1.37$	$20-30$
$1.37-1.52$	$30-40$
$1.52-1.81$	$40-50$
$1.81-2.01$	$50-60$
$2.01-2.37$	$60-70$
$2.37-2.47$	$70-80$
—	> 80

Table 6.2: Bin definitions in η and E_T for identification cuts.

the hadronic background. The cuts have values optimised in different ranges of E_T and η , where η is from the middle layer of the EM cluster and E_T is computed from the cluster energy and η of the middle layer. The ranges used for the identification cuts are shown in Table 6.2; a cut value is defined for each of the 110 range combinations. The list of cuts was recently optimised to make them more robust for early data-taking [102]. Each cut is applied independently of the others and its result is saved as a single bit in a bit-word, unique for each electron. The three predefined sets of cuts are bit masks which are then compared to the bit-word.

The loose selection is based solely on shower shape cuts in the middle layer of the EM calorimeter. The variables are:

- η_{cl} : the calorimeter pseudorapidity range ($0 < |\eta_{cl}| \leq 2.47$),
- R_{had} : the ratio of E_T between the hadronic and the EM calorimeter (for $|\eta| < 0.8$ and $|\eta| > 1.37$) (typically $R_{had} \leq 0.018$),
- R_{had1} : R_{had} using only the first layer of the hadronic calorimeter (for $0.8 < |\eta| < 1.37$) (typically $R_{had1} \leq 0.018$),
- $w_{\eta2}$: the lateral cluster width in η in the middle layer defined as $\sqrt{\frac{\sum E_i \times \eta_i^2}{\sum E_i} - \left(\frac{\sum E_i \times \eta_i}{\sum E_i}\right)^2}$ (typically $w_{\eta2} \leq 0.013$),
- R_η : the ratio in η of energies in the 3×7 cluster with respect to the 7×7 region in the middle layer (typically $R_\eta > 0.852$).

Values in parentheses are given when the cut is constant for all bins, otherwise a typical value is given for the bins $(|\eta|, E_T) = (<0.6, 5-10)$. The medium selection includes the loose one, and adds cuts to it. It is based on extra shower shape cuts in the front layer and tightens the reconstruction track-matching requirements. The added variables are:

- w_{stot} : the total cluster width in the front layer defined as $\sqrt{\frac{\sum E_i \times (i - i_{max})^2}{\sum E_i}}$, where i_{max} is the index of the most energetic strip (typically $w_{stot} < 3.18$),
- E_{ratio} : the ratio of the difference between the largest and second largest energy deposit over the sum these energies in the front layer (typically $E_{ratio} > 0.61$),
- n_{pixel} : the number of hits in the Pixel detector ($n_{pixel} \geq 1$),
- $n_{silicon}$: the number of hits in the Pixel and the SCT detectors ($n_{silicon} \geq 7$),
- d_0 : the transverse impact parameter with respect to the beam position ($d_0 \leq 5$ mm),
- $\Delta\eta$: the track-matching $\Delta\eta$ between the cluster front layer and the track ($\Delta\eta \leq 0.01$).

The tight selection includes the medium one and tightens the track matching even more. It makes use of the TRT electron/hadron separation power and uses the Pixel b -layer against conversions. The added variables are:

- $n_{b-layer}$: the number of hits in the b -layer of the Pixel detector ($n_{b-layer} \geq 1$),
- $\Delta\phi$: the track-matching $\Delta\phi$ between the cluster middle layer and the track ($\Delta\phi \leq 0.02$),
- E/p : the ratio of cluster energy to the track momentum (typically $0.8 \leq E/p \leq 2.5$),
- n_{TRT} : the number of hits in the TRT (typically $n_{TRT} \geq 16$),
- f_{hTR} : the number of high-threshold hits to the total number of hits in the TRT (typically $f_{hTR} \geq 0.085$).

The bins in η used for the last two cuts in the tight selection are modified to account for the geometry of the TRT and are defined as $|\eta| = [<0.1, 0.1-0.625, 0.625-1.07, 1.07-1.304, 1.304-1.752, 1.752-2.0]$. Typical values are given for the second bin only ($0.1 < |\eta| < 0.625$).

For medium and tight selections, isolation criteria can be applied in addition to the cuts mentioned above [105]. New sets of cuts called *medium_iso* and *tight_iso* are hence

introduced. The isolation determination is performed separately from the standard identification cuts to ensure robustness in early data and also to allow flexibility for analysis needs. Calorimetric and tracking information are used in the isolation discriminator. First, the reconstructed transverse energy inside a cone of radius $R_0=0.3$ around the electron object, $E_T^{cone}(0.3)$, is computed, excluding the energy of the electron itself. Then, the sum of the scalar p_T of a selection of tracks found inside the cone, $p_T^{cone}(0.3)$, is computed. The tracks must not come from secondary vertices, must have $p_T > 1$ GeV and must satisfy track quality criteria, such as number of b -layer hits, silicon hits and impact parameter cuts. The tracks must not be matched to a conversion vertex if they are within $\Delta R < 0.1$ of the electron. Calorimetric and track isolation are measured in a cut-based fashion, by comparing both $E_T^{cone}(0.3)/E_T$ and $p_T^{cone}(0.3)/E_T$ to a specific set of thresholds, defined in bins of E_T and η (E_T and η are the four-momentum combined quantities, see §6.6.1). The binning in η is the same as previously mentioned in Table 6.2, but a different E_T binning is used for isolation. Cut values have been optimised in such a way that an efficiency of 99% for isolated electrons is reached in all bins. The results of the cuts are stored in three bits which are part of the electron identification bit-word: one for calorimetric isolation, one for track isolation and one for their combination.

6.5 Overlap between cluster- and track-seeded algorithms

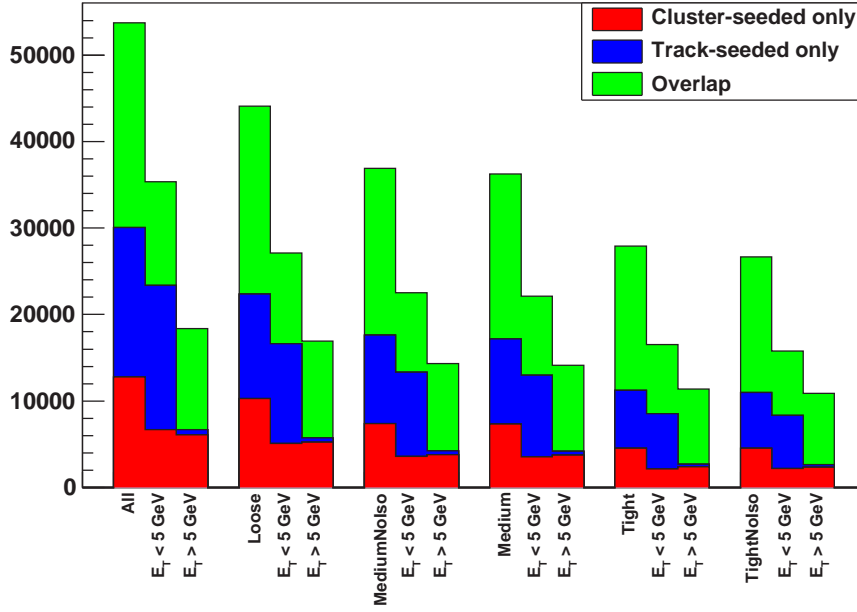
In the electron reconstruction described above, two different algorithms are used in the same pseudorapidity range: cluster-seeded and track-seeded. These algorithms are each optimised for electrons in a certain E_T range, however they can also happen to reconstruct the same physical electrons. For this reason, an overlap removal procedure is used during the reconstruction step to avoid double-counting the objects in the data files. As the cluster-seeded algorithm is the baseline used for trigger and offline reconstruction, the overlap removal is applied during the track-seeded building step. For each object built by the track-seeded algorithm, a check is made on the preselected track. If this track is already used by a cluster-seeded object, the object information is changed to identify the object as an overlap. In addition, the reconstructed quantities from the cluster-seeded algorithm are kept for the final object.

Given the high track multiplicity in ATLAS and the different requirements on track selection between the two algorithms, some electrons fail the standard reconstruction. We have performed a study to understand this overlap, using ATHENA releases 14.2.0 and 14.2.20.1, respectively, for J/ψ and Z , for reconstruction and identification. The main differences between the current setup and the one used for the plots below are:

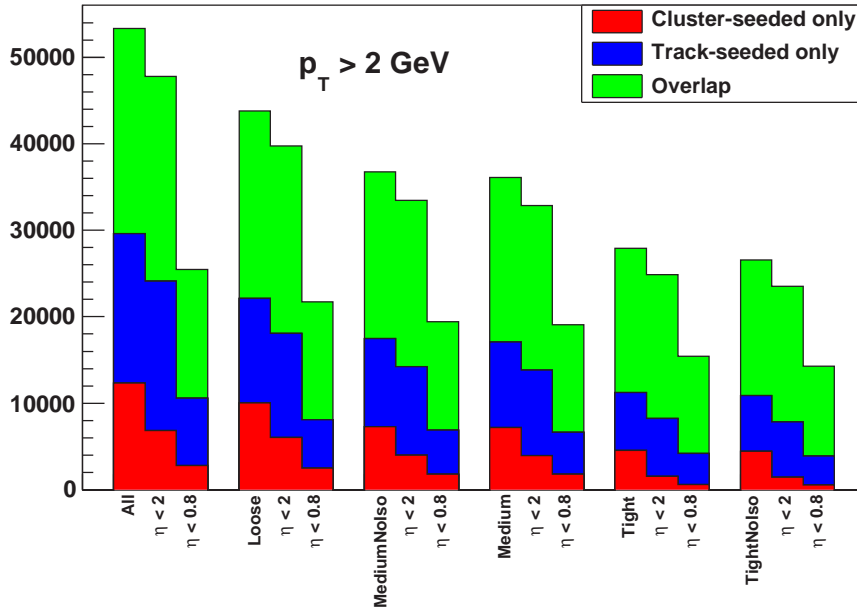
- In the cluster-seeded reconstruction algorithm:
 - $E/p < 10$ was required during the track matching step,
 - the choice of a track matching the cluster was based on the smallest value of E/p .
- In the track-seeded reconstruction algorithm:
 - the cluster size in the barrel was 3×5 .
- In the electron identification procedure:
 - isolation cuts using the $E_T^{cone}(0.45)$ variable were used for the reference sets of cuts (medium and tight),
 - reference cuts without the isolation requirement were available for the medium and tight sets (*medium_noiso* and *tight_noiso*),
 - the selection of variables used for the reference sets of cuts was different, as well as the cut values themselves.

From the J/ψ and Z simulated samples, reconstructed electron objects that could be matched to a generator-level electron within $\Delta R \leq 0.2$ were selected. Electron objects reconstructed from duplicate clusters were removed, keeping the electron object with the value for E/p closest to one. The author of the reconstructed electron objects was used to classify them in three categories: cluster-seeded only, track-seeded only and overlap between cluster- and track-seeded. The results are shown in Fig. 6.4. The electron object numbers are shown for each set of identification cuts and also according to their E_T in Fig 6.4(a). The track-seeded algorithm can be seen to reconstruct a larger number of electrons at $E_T < 5$ GeV. Another classification was made in Fig 6.4(b) in various pseudorapidity ranges, after a cut of $p_T > 2$ GeV was applied. This p_T cut, together with the $|\eta| < 2$ requirement, allows the comparison between track- and cluster-seeded algorithms within the same acceptance. Restricting the $|\eta|$ range to two shows the contribution of cluster-seeded only reconstruction up to $|\eta| = 2.5$. Fig 6.4(b) also shows that the cluster-seeded algorithm finds electrons which were not found by the track-seeded algorithm even inside its acceptance; this is explained by the tighter track preselection in the track-seeded case. The range $|\eta| < 0.8$ was chosen since the amount of material is considerably smaller in this region.

Similar results were obtained for $Z \rightarrow e^+e^-$ events and it was shown that, even after an $E_T > 20$ GeV requirement, the track-seeded algorithm could still reconstruct electrons that were not reconstructed by the cluster-seeded algorithm. This can be seen in Fig. 6.5, where 1.6% of reconstructed electrons and 1.2% of tight electrons



(a)



(b)

Figure 6.4: Author distributions of electron objects in J/ψ events for all identification cuts (a) for all electrons and (b) after a p_T cut of 2 GeV on the electron track. Duplicate cluster removal was performed in both plots.

were coming from the track-seeded algorithm only. The same selection cuts were applied as for J/ψ events.

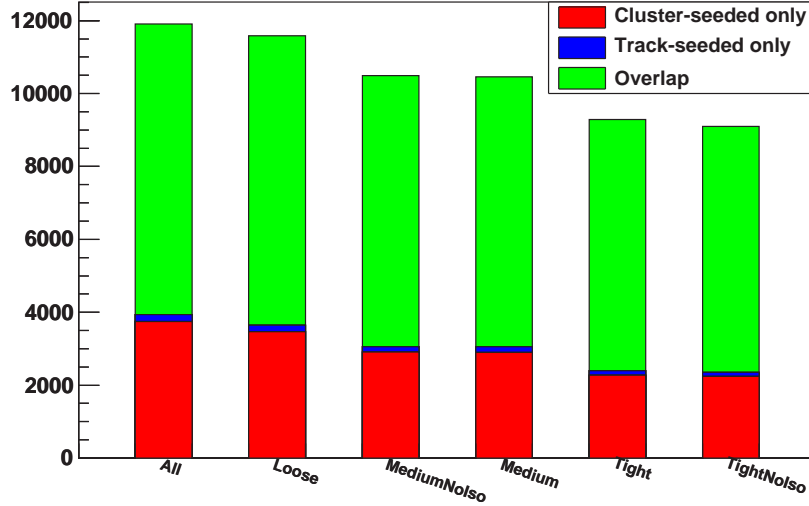


Figure 6.5: Author distributions of electron objects in $Z \rightarrow e^+e^-$ events for all identification cuts. Duplicate cluster removal was performed.

In an attempt to improve the electron reconstruction, the preselection cuts for the track-seeded algorithm were temporarily modified as shown in Table 6.3. The modified cuts increased the proportion of electron objects reconstructed by both algorithms (overlap), as expected. The resulting distributions for J/ψ events are shown in Fig. 6.6. Unfortunately, these modified cuts were shown to have a smaller rejection power against jets by a factor of three [106]. Due to that, the preselection cuts for the track-seeded algorithm were reverted to the original ones shortly after.

This study showed that, for $E_T > 5$ GeV, the cluster-seeded reconstruction, which is also used in the electron trigger, has a better performance on electrons from J/ψ decays. In the final analysis, they are used exclusively to select electron candidates.

6.6 Performance for low p_T electrons

In order to reconstruct $J/\psi \rightarrow e^+e^-$ events, it is important to understand the performance of the calorimeter and of the reconstruction algorithms for low p_T electrons. This assessment was performed using the most recent software development [102]. For low p_T electrons, simulated J/ψ events were used. To account for the acceptance

Original cuts	Modified cuts
$p_T > 2 \text{ GeV}$	$p_T > 2 \text{ GeV}$
$n_{b\text{-layer}} \geq 1$	$n_{b\text{-layer}} \geq 1$
$n_{\text{pixel}} \geq 2$	$n_{\text{pixel}} \geq 2$
$n_{\text{silicon}} \geq 7$	$n_{\text{silicon}} \geq 7$
$n_{TRT} \geq 20$	$f_{hTR} > 0.05$
$n_{hTR} \geq 1$	$E/p > 0.4$
$E/p > 0.7$	
$E_1^{cl}(3 \times 1)/E^{cl}(\text{core}) > 0.03$	Cuts removed
$E_3^{cl}(3 \times 3)/E^{cl}(\text{core}) < 0.5$	

Table 6.3: Track-seeded preselection cuts before and after modification.

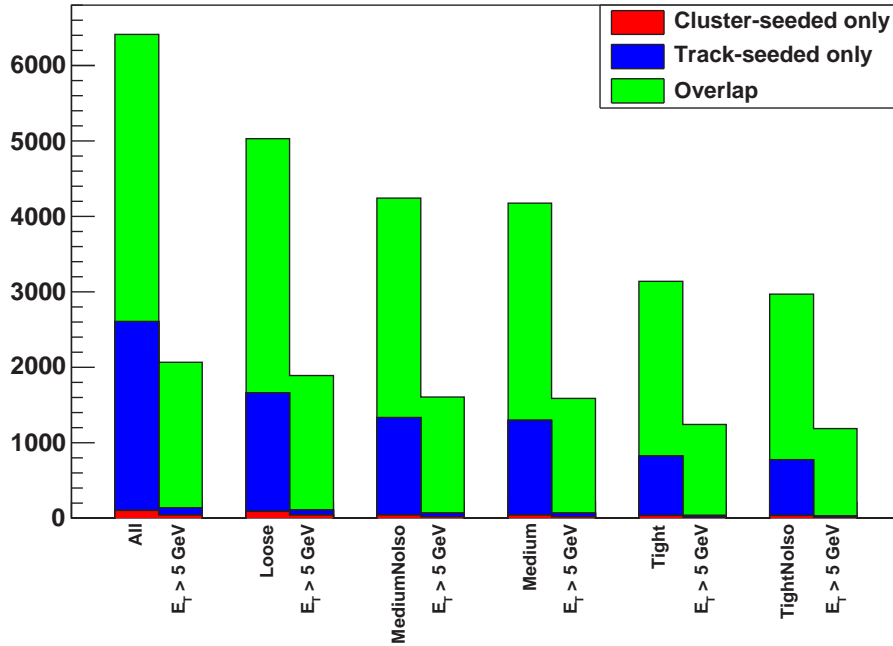


Figure 6.6: Author distributions of electron objects in J/ψ events with modified preselection cuts. Duplicate cluster removal was performed.

of the trigger and the calorimeter, only electrons with $E_T > 5$ GeV and $|\eta| < 2.47$ were selected for both the truth and reconstruction levels. The overall reconstruction and identification efficiencies are given in Table 6.4, where the transition region between the barrel and the end-cap EM calorimeter, which covers $1.37 < |\eta| < 1.52$, is excluded from the pseudorapidity range. In this acceptance, 71% of the true electrons from J/ψ decays are reconstructed by any of the algorithms presented in §6.3 and 85.9%, 82.1% and 69.7%, respectively, of these reconstructed electron objects satisfy the requirements for loose, medium and tight electron identification. The efficiency distributions as a function of the transverse energy and pseudorapidity are shown in Fig. 6.7, for each set of identification cuts, with respect to the reconstruction. In this case, the transition region mentioned previously is not removed; a dip in the efficiency in this range of pseudorapidity can thus be observed.

Efficiencies (%)			
$\epsilon_e^{\text{Reconstruction}}$	$\epsilon_e^{\text{Loose}}$	$\epsilon_e^{\text{Medium}}$	$\epsilon_e^{\text{Tight}}$
71.0	61.0 (85.9)	58.3 (82.1)	44.6 (69.7)

Table 6.4: Reconstruction and identification performance for J/ψ electrons. Numbers in parentheses are efficiencies computed with respect to the reconstruction efficiency. The statistical error on the efficiency is typically 0.1 [102].

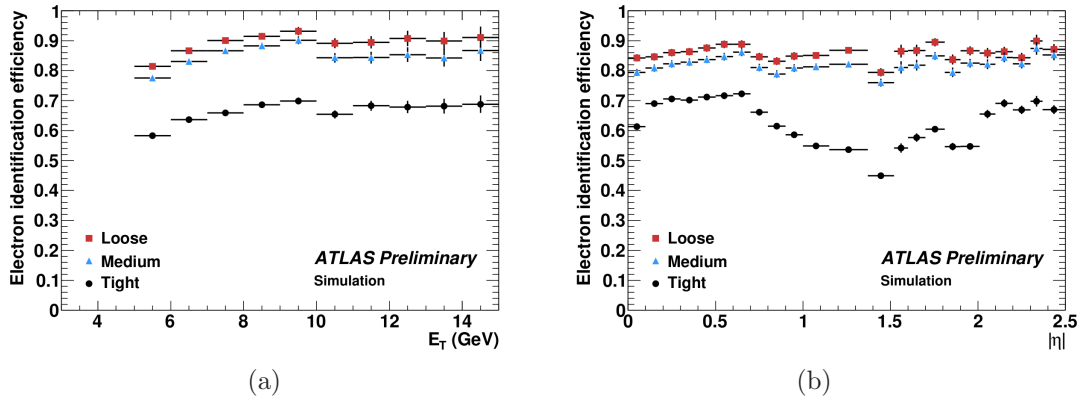


Figure 6.7: Efficiency for electrons from J/ψ (a) as a function of the transverse energy and (b) as a function of the pseudorapidity [102].

6.6.1 Four-momentum reconstruction

As described above, the reconstructed electron is a composite object built from calorimetric and tracking information. Nominally, the electron energy is obtained from the EM calorimeter and the direction comes from the ID, based on the best intrinsic accuracy of each subdetector, to build the four-momentum for the electron object. Within the reconstruction software, it is also possible to combine the measurements from the two detectors to build a four-momentum object and its associated error matrix, as shown in Fig 6.8. The combination is applied based on the value of a parameter, σ , measuring the deviation between the EM cluster energy and the track momentum. If this parameter is greater than an adjustable value (initially set to 3), the cluster energy is used for the four-momentum energy; otherwise, a combined value from the cluster energy and the track momentum is used. For the electron object direction, the combination is applied based on the number of silicon hits. If more than three silicon hits are found on the electron track, the track parameters η and ϕ are used; otherwise, only the pseudorapidity η is combined from the track and cluster values and ϕ is determined from the track.

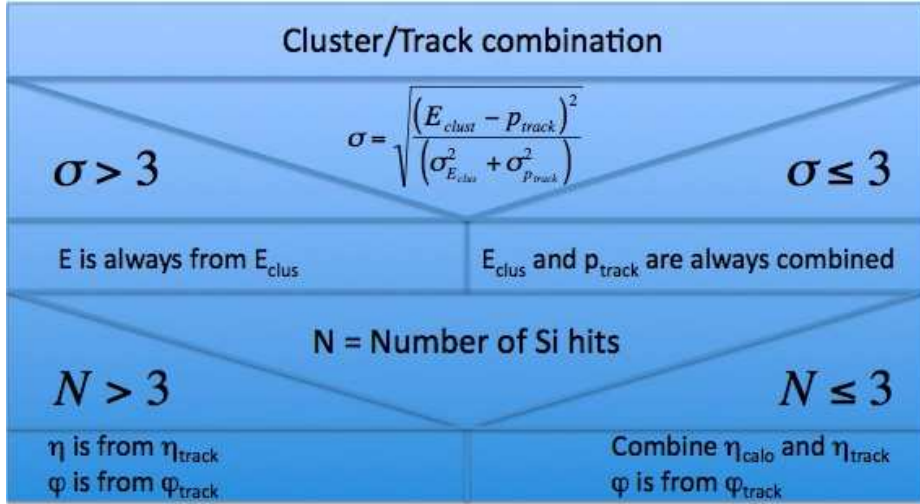


Figure 6.8: Calorimetric and track information combination for electron objects [107].

Using electrons from simulated J/ψ decays reconstructed using ATHENA release 15.3.0.1 passing the *tight_noiso* identification cuts, we checked the effect of this combination on the dielectron mass and energy resolution. The energy resolution was computed using the ratio of the reconstructed energy to the true electron energy and is shown in Fig 6.9(a). The energy scale is visibly reduced to be lower than one while the RMS of the distribution is improved. The same can be seen for the dielectron invariant mass distribution in Fig 6.9(b). An asymmetric Gaussian function was fitted

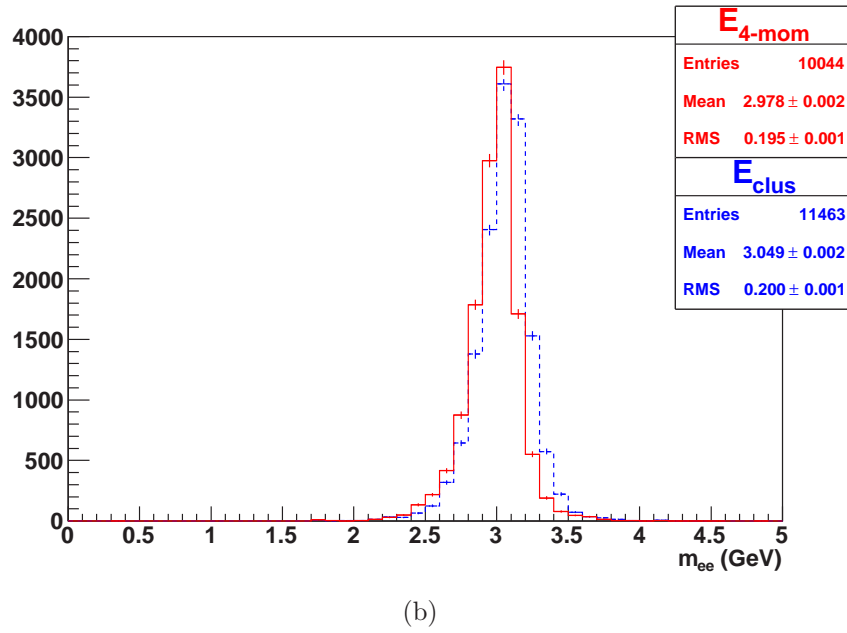
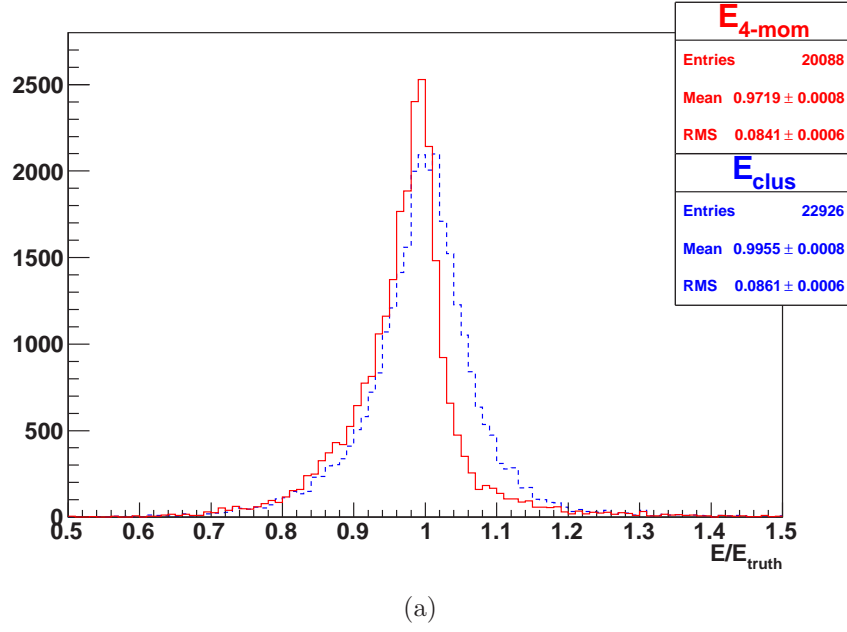


Figure 6.9: Four-momentum reconstruction checks for electrons from J/ψ (a) on the energy resolution and (b) on the dielectron invariant mass. The dotted blue line shows the distribution when using the cluster energy and the track direction and the solid red line show the distribution when using the four-momentum combination.

to the invariant mass distribution to allow the comparison. The combination improves the mass resolution (from 0.15 GeV to 0.14 GeV) but shifts the mass towards lower values, and away from the true mass of 3.096 GeV, by 2.7%, from 3.11 GeV to 3.03 GeV. Despite the improved resolution, this mass shift indicates that the method is not fully understood. Therefore, the final analysis does not use the combined values for the electron four-momentum, but rather uses the nominal quantities from the cluster and the track.

6.7 Trigger selection for electrons

During data-taking, the first filtering of interesting events is done by the trigger system, described previously in §3.4. The specific trigger implementation used for electrons is described here.

At L1, the trigger selection is performed using only the information from the calorimeters. Due to time constraints, the L1 trigger uses towers of size $\Delta\eta \times \Delta\phi = 0.1 \times 0.1$, which are larger than for offline clustering. A window of 4×4 towers is considered to find a L1 EM cluster. Only the central 2×2 towers are used for energy calculation; the surrounding 12 towers are used for isolation, if explicitly required by the L1 trigger signature. A L1 EM cluster is formed if at least one of the four two-tower transverse EM energy sums, as shown in Fig. 6.10(a), is strictly greater than a predefined E_T threshold. The comparison with the threshold is done using ADC bits, where one bit is converted in energy to 1 GeV. This implies that the minimum E_T value for a given L1 EM cluster is 1 GeV greater than the predefined threshold. The values of the thresholds used for this analysis are listed in Table 6.5. Since all windows separated by 0.1 in either η or ϕ are considered by the L1 trigger, multiple counting of clusters could happen. To avoid this, a procedure illustrated in Fig. 6.10(b) ensures that the chosen cluster core is a local maximum by comparing its energy (computed from the 4 EM towers and the 4 hadronic towers) to its eight nearest neighbouring 2×2 windows. The local maximum position determines the coordinates of the EM cluster RoI which is passed to L2 for further selection [108].

Chain	L1	L2					
	E_T	$\Delta\eta$	$\Delta\phi$	E_T	R_η	E_{ratio}	R_{had}
e5_medium	3 GeV	0.05	0.1	4 GeV	0.65	0.1	0.058

Table 6.5: L1 & L2 thresholds used for the trigger chain e5_medium. The direction of the cuts is indicated in the text. For R_η , E_{ratio} and R_{had} , the direction of the cuts is the same as for the electron identification cuts listed in §6.4. The quantities $\Delta\eta$ and $\Delta\phi$ are computed between the track and the cluster.

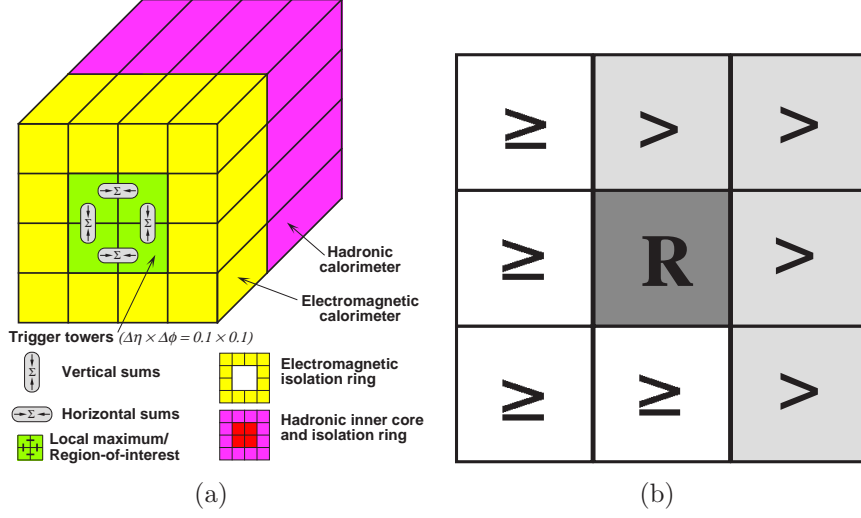


Figure 6.10: L1 EM algorithm diagrams [108]. (a) Schematic of the algorithm used for electron/photon- and τ -specific trigger chains. (b) Schematic of the E_T local energy maximum test for a cluster/RoI candidate. η runs from left to right and ϕ , from bottom to top. The 2×2 window being tested is identified with the R symbol.

At L2, the trigger algorithms are seeded by the L1 RoIs. Within the RoI, fast clustering and tracking algorithms are run using the full granularity of the detector. The clustering uses the most energetic cell in the EM calorimeter middle layer within a cone of size $\Delta R=0.15$ as a seed and then proceeds using similar cluster building and calibration steps as previously described in §6.2.1 for the offline implementation⁵. This seeding allows the reconstruction of many L2 electrons out of a single L1 EM cluster, which increases the efficiency of finding collimated electron pairs by the trigger. Three tracking algorithms, designed specifically to address the trigger requirements for timing and complexity, are available at L2: IdScan, SiTrack and TRTSegFinder. As their names suggest, IdScan and SiTrack use Pixel and SCT spacepoints exclusively while TRTSegFinder uses only the TRT information to build tracks. Tracks reconstructed using IdScan or SiTrack are used for the trigger signature used for electrons from J/ψ . A track-matching criterion is applied between the tracks and the cluster using $\Delta\eta$ and $\Delta\phi$ as well as various cuts on shower shape variables, as shown in Table 6.5. The transverse energy of the cluster must be greater than or equal to 4 GeV. Finally, if the event is accepted at L2, the EF processes the detector information using its full granularity. The algorithms used at the EF are the same as for the offline

⁵The L2 trigger uses the same cluster size (3×7) for the complete pseudorapidity range of the calorimeter and different calibration constants.

implementation. For the e5_medium chain, a cut of $E_T^{cluster} \geq 5$ GeV and medium identification cuts, based on the offline implementation, are applied [102, 109].

CHAPTER 7

J/ψ Cross-Section Analysis

*If you can not measure it, you can
not improve it.*

- Lord Kelvin

The J/ψ mesons can decay to kinematically allowed leptons (electrons and muons), each with a 5.94% branching ratio. Using the electrons reconstructed as previously described, we design a selection using simulated ATLAS data to measure the J/ψ production cross-section. The selection needs to reject a high level of electron-faking background, as well as real electrons from semileptonic decays of heavy flavours. Drell-Yan electron pair production is also present in our selection.

In the following, the simulation used to produce events is described in detail, as well as the event selection and the analysis procedure.

7.1 Monte-Carlo simulation

Monte-Carlo simulation is used to generate p - p collision events and simulate the passage of the produced particles through the ATLAS detector, before being reconstructed as for real data. Simulated data are produced in samples, each one corresponding to one process¹ of interest. All samples used in this analysis are generated using the 2→2 PYTHIA [110] generator (version 6.4²), interfaced with PHOTOS [111]

¹Sometimes, more than one, if they are logically associated, like B-hadrons decays.

²Version 6.418 is used for heavy flavour background samples, non-prompt signal and unfiltered minimum bias while version 6.415 is used for filtered minimum bias, prompt signal and Drell-Yan.

for QED bremsstrahlung simulation for the signal (prompt and non-prompt) and Drell-Yan samples. For this analysis, all samples were generated during the ATLAS *mc08* exercise, which defines common software releases and settings for simulation and reconstruction. The center of mass energy is set to 10 TeV.

7.1.1 Signal sample

To simulate prompt production of $J/\psi \rightarrow e^+e^-$, we used a single sample which includes four different production channels: direct J/ψ (through colour-singlet [CSM] or colour-octet [COM]) production, χ_{c0} , χ_{c1} and χ_{c2} decays. The production of J/ψ through ψ' feed-down is not included since the COM matrix elements for this process are not present in the PYTHIA generator. This accounts for 7.5% of the production of J/ψ^3 . In this event generation, the decays for the relevant particles are forced: J/ψ only decays to e^+e^- and χ_c 's to $J/\psi\gamma$. The relevant parameters used for the generation are outlined in Table 7.1. The MSEL switch ensures that the sub-process codes 421–439 are used exclusively. The definition of the sub-process codes is given in Table 7.2. The CKIN(3) parameter sets the minimum scale for the hard-interaction, \hat{p}_\perp . It takes the value of 1 GeV by default but it is modified for this sample to 3 GeV. After the event generation, a MultiLepton filter is applied which selects the event if at least two leptons (electrons or muons) with $p_T > 3$ GeV and $|\eta| < 2.7$ are found. This filter, with an efficiency of 2.7%, allows for a more efficient production of events inside the detector acceptance, without spending CPU power or disk space for events that would not pass the selection cuts.

Kinematics		NRQCD		
Parameter	Value	Parameter	Value	Matrix Element
MSEL	61	PARP(141)	1.16	$\langle \mathcal{O}^{J/\psi} [{}^3S_1^{(1)}] \rangle$
ISUB	421–439	PARP(142)	0.0119	$\langle \mathcal{O}^{J/\psi} [{}^3S_1^{(8)}] \rangle$
CKIN(3)	3 GeV	PARP(143)	0.01	$\langle \mathcal{O}^{J/\psi} [{}^1S_0^{(8)}] \rangle$
—	—	PARP(144)	0.01	$\langle \mathcal{O}^{J/\psi} [{}^3P_0^{(8)}] \rangle / m_c^2$
—	—	PARP(145)	0.05	$\langle \mathcal{O}^{\chi_{c0}} [{}^3P_0^{(1)}] \rangle / m_c^2$

Table 7.1: Parameters of the PYTHIA generator used for the production of the prompt J/ψ sample. The matrix element values are obtained from fits to the CDF data [112].

³This effect is not corrected for in the analysis.

ISUB	Sub-process	Model
421	$g+g \rightarrow c\bar{c}[{}^3S_1^{(1)}]+g$	J/ψ colour singlet
422	$g+g \rightarrow c\bar{c}[{}^3S_1^{(8)}]+g$	J/ψ colour octet
423	$g+g \rightarrow c\bar{c}[{}^3S_0^{(8)}]+g$	
424	$g+g \rightarrow c\bar{c}[{}^3P_J^{(8)}]+g$	
425	$g+q \rightarrow q+c\bar{c}[{}^3S_1^{(8)}]$	
426	$g+q \rightarrow q+c\bar{c}[{}^1S_0^{(8)}]$	
427	$g+q \rightarrow q+c\bar{c}[{}^3P_J^{(8)}]$	
428	$q+\bar{q} \rightarrow g+c\bar{c}[{}^3S_1^{(8)}]$	
429	$q+\bar{q} \rightarrow g+c\bar{c}[{}^1S_0^{(8)}]$	
430	$q+\bar{q} \rightarrow g+c\bar{c}[{}^3P_J^{(8)}]$	
431	$g+g \rightarrow c\bar{c}[{}^3P_0^{(1)}]+g$	χ_{c0} colour singlet
432	$g+g \rightarrow c\bar{c}[{}^3P_1^{(1)}]+g$	χ_{c1} colour singlet
433	$g+g \rightarrow c\bar{c}[{}^3P_2^{(1)}]+g$	χ_{c2} colour singlet
434	$g+q \rightarrow q+c\bar{c}[{}^3P_0^{(1)}]$	χ_{c0} colour singlet
435	$g+q \rightarrow q+c\bar{c}[{}^3P_1^{(1)}]$	χ_{c1} colour singlet
436	$g+q \rightarrow q+c\bar{c}[{}^3P_2^{(1)}]$	χ_{c2} colour singlet
437	$q+\bar{q} \rightarrow g+c\bar{c}[{}^3P_0^{(1)}]$	χ_{c0} colour singlet
438	$q+\bar{q} \rightarrow g+c\bar{c}[{}^3P_1^{(1)}]$	χ_{c1} colour singlet
439	$q+\bar{q} \rightarrow g+c\bar{c}[{}^3P_2^{(1)}]$	χ_{c2} colour singlet

Table 7.2: Definition of the PYTHIA generator sub-process codes used for prompt J/ψ production.

In PYTHIA, when a decay channel is forced, the branching ratio for this channel is set to one. In samples where only one production channel is used, the cross-section reported by the event generator should be multiplied by the branching ratio. However when several channels with different branching ratios are forced, the proportions of events of each channel in the sample are wrong and need to be corrected. We calculate⁴ event weights w_i as follows:

⁴The derivation is given in Appendix A.

$$w_i = \frac{BR_i}{\sum_j BR_j \times f_j^{bef}}, \quad (7.1)$$

where $i, j \in \{J/\psi, \chi_{c0}, \chi_{c1}, \chi_{c2}\}$ represents the production channel of interest, BR_i is the branching ratio for i to decay to J/ψ and f_i^{bef} is the fraction of events before the MultiLepton filter is applied. It is important that the fractions are considered before the filter since the efficiency for the MultiLepton filter is not the same for all processes, as can be seen in Fig. 7.1. Since the cross-sections for the $q + \bar{q}$ processes are low at a $p-p$ collider, no event passes the filter for these points (e.g. sub-process codes 428–430 and 438–440). Therefore, these are not considered in the plot. The values entering Eq. 7.1 are shown in Table 7.3, together with f^{corr} , the fraction of events after correction, calculated as $w \times f^{bef}$. After correcting for the forced decays⁵, the sample cross-section is estimated to be 105.5 nb.

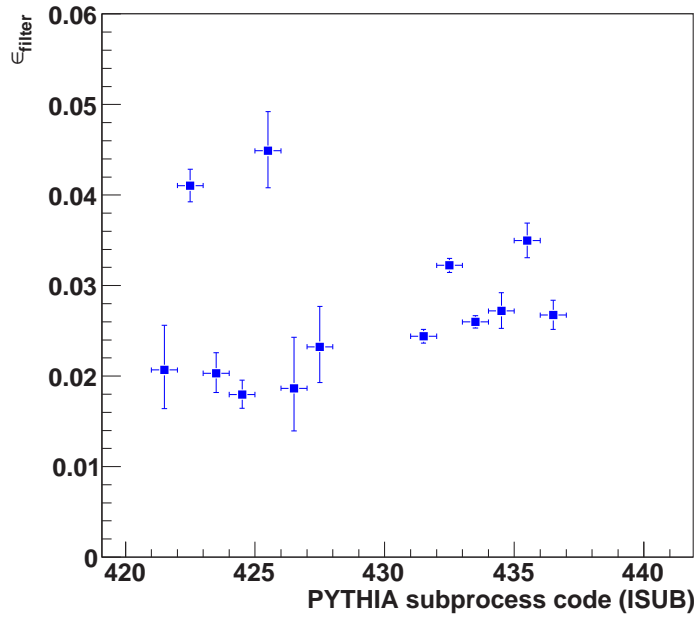


Figure 7.1: MultiLepton filter efficiency as a function of the PYTHIA sub-process code (see Table 7.2). Binomial errors are shown here. The sub-processes for $q + \bar{q}$ production are not included in the plot.

The generation of the non-prompt J/ψ signal sample is discussed later, together with the heavy flavour samples.

⁵See Appendix B for details on the corrected cross-section calculation.

Process	BR($\rightarrow J/\psi$)	f^{bef}	w	f^{corr}
Direct J/ψ	1	15.3%	3.066	46.9%
χ_{c0}	1.28%	23.1%	0.039	0.9%
χ_{c1}	36%	29.4%	1.104	32.5%
χ_{c2}	20%	32.2%	0.613	19.7%

Table 7.3: Event weights and fractions for the prompt J/ψ sample. Values of branching ratios are obtained from the PDG group [13].

7.1.2 Background samples

In real p - p collisions, several processes exhibit a similar signature to the signal we try to measure, which is a pair of low energy electrons with opposite charge. These background processes need to be added to our simulated signal individually. Processes generating real electron pairs are considered, such as low mass Drell-Yan and heavy flavours ($b\bar{b}$ and $c\bar{c}$), but also hadrons which can fake electrons. These low energy hadron fakes are coming dominantly from non-diffractive soft QCD interactions, where non-diffractive means that the non-perturbative collisions are equally distributed in rapidity⁶ y . This process is called *minimum bias* in the ATLAS simulation, since it is not biased by any trigger requirement.

The Drell-Yan sample contains events where a pair of quarks annihilates through an excited photon or a Z boson and creates an electron pair. This sample is focused on the mass region below the Z resonance. To generate it, the PYTHIA settings of Table 7.4 are used, where the bosons are forced to decay to e^+e^- . The mass range for the hard interaction is defined by the CKIN parameters such that $1 < \sqrt{\hat{s}} < 60$ GeV. As for the signal sample, a MultiLepton filter is applied where at least two leptons (electrons or muons) are required to have $p_T > 3$ GeV and $|\eta| < 2.7$.

Parameter	Value	Process
MSEL	0	—
ISUB	1	$f_i + \bar{f}_i \rightarrow \gamma^*/Z$
CKIN(1)	1 GeV	—
CKIN(2)	60 GeV	—

Table 7.4: Parameters of the PYTHIA generator used for the production of the low-mass Drell-Yan sample.

⁶Rapidity y is defined as $\frac{1}{2} \ln \frac{E+p_z}{E-p_z}$. In the massless approximation, it becomes the pseudorapidity η .

The minimum bias sample is generated with PYTHIA using the parameters of Table 7.5. For this analysis, a filter is applied to this sample which selects events in which a truth jet object with $E_T > 6$ GeV is found. A truth jet is defined as the sum of transverse energies of all generator level particles inside a box in $\Delta\eta \times \Delta\phi = 0.12 \times 0.12$. This filter has an efficiency of 4.31%. An unfiltered sample is also generated and is used for a filter bias study in §7.3.1.

Parameter	Value	Process
MSEL	1	—
ISUB	11	$q_i + q_j \rightarrow q_i + q_j$
	12	$q_i + \bar{q}_i \rightarrow q_k + \bar{q}_k$
	13	$q_i + \bar{q}_i \rightarrow g + g$
	28	$q_i + g \rightarrow q_i + g$
	53	$g + g \rightarrow q_k + \bar{q}_k$
	68	$g + g \rightarrow g + g$

Table 7.5: Parameters of the PYTHIA generator used for the production of the minimum bias sample.

Heavy flavour production is generated in three different samples. While the samples are produced using the PYTHIA event generator, a dedicated interface is used to increase the efficiency of heavy flavour generation, PythiaB [113]. Separate samples are created for $b\bar{b} \rightarrow e^\pm X$ and $c\bar{c} \rightarrow e^\pm X$, as well as for non-prompt J/ψ ($b\bar{b} \rightarrow J/\psi \rightarrow e^+e^-$) production. A list of the parameters for each of these samples is given in Table 7.6. All samples are generated using the same sub-process list as for the minimum bias sample, shown in Table 7.5. Various PythiaB filters are used during the event generation process. A heavy quark of the desired flavour is required, inside a phase space determined by the *cutbq* parameter. In the case of the non-prompt J/ψ sample, one of the b quarks is forced to decay to J/ψ , the latter being subsequently forced to decay to e^+e^- . Also, an electron must be found in the event, with its own phase space requirements, determined by the *lvl2cut* parameter. PythiaB allows the parton content of the event to undergo several hadronisation steps to ensure that, on average, one of them would be accepted by the phase space cuts. In the case of the non-prompt J/ψ sample, a MultiLepton filter is also applied where at least two leptons (electrons or muons) are required to have $p_T > 3$ GeV and $|\eta| < 2.7$.

As discussed above, several samples use the same set of generated processes (MSEL=1), which creates overlap of events between the samples. These overlaps have to be removed before performing the analysis to avoid an overestimation of the

Parameter	Value for $b\bar{b}$, $c\bar{c}$	Value for $b\bar{b} \rightarrow J/\psi$
CKIN(3)	7	1
PythiaB.cutbq	$p_T > 6 \text{ GeV}$ $ \eta < 4.5$	$p_T > 0 \text{ GeV}$ $ \eta < 102.5$
PythiaB.lvl2cut	$p_T > 5 \text{ GeV}$ $ \eta < 2.5$	$p_T > 3 \text{ GeV}$ $ \eta < 2.7$

Table 7.6: Parameters of the PYTHIA generator (and PythiaB interface) used for the production of the heavy flavour samples.

event rates. Due to the presence of $pp \rightarrow b\bar{b}c\bar{c}X$ events, an overlap of events is found between the $b\bar{b}$ and the $c\bar{c}$ samples. In order to remove this double-counting, events from the $c\bar{c}$ sample for which a b quark and an electron that satisfies the phase space cuts of Table 7.6 are found, are vetoed. A similar procedure needs to be applied to the filtered minimum bias sample, where events with heavy flavour production are also included. In the case of the minimum bias sample, both b and c production within the phase space are removed. In addition to this, an extra step is applied to the minimum bias, $b\bar{b}$ and $c\bar{c}$ samples to remove all $J/\psi \rightarrow e^+e^-$ events.

In summary, the cross-section, filter efficiency and scale factor for each sample used in this analysis are given in Table 7.7. The scale factors are given for an integrated luminosity of 5 pb^{-1} and are applied on all subsequent plots, unless stated otherwise. The overall fractions of events removed from the QCD samples to avoid overlaps described previously are listed in Table 7.7.

7.1.3 Detector simulation

The sequence of file formats used for analysis in ATLAS is described previously in §3.6. All these formats correspond to a processing step, either in the data stream or in the Monte-Carlo simulation. The event generation step is described above; it is followed by detector simulation, where the particle four-vectors are converted into physics objects of the same type as for the data. To achieve this, a model [114] of the ATLAS detector is built using the GEANT4 [115] software, which simulates the energy loss due to the passage of particles through matter. The full geometry of the detector is hence simulated, both the active components (detector elements) and the dead material (electronics, cables and support structures). The result of this simulation, composed of energy deposits in detector elements, is stored in the HITS file. For these quantities to be usable by the reconstruction software, they need to be translated into actual detector responses, i.e. electronic signals, voltage levels and noise, for every read-out channel of ATLAS. This is done during the digitisation step

Sample	Cross-section [μb]	ϵ_{filter} [%]	# events	Overlap [%]	Scale factor for $\int \mathcal{L} dt = 5 \text{ pb}^{-1}$
$pp \rightarrow J/\psi \rightarrow e^+e^-$	0.1055	2.71	500k	—	1
$b\bar{b} \rightarrow J/\psi \rightarrow e^+e^-$	0.0283	3.3	200k	—	0.708
Drell-Yan $\rightarrow e^+e^-$	0.00268	0.86	500k	—	0.027
Filtered minimum bias	2801.5	4.31	10M	0.4	1400.75
Minimum bias	65000	—	4M	—	81250
$b\bar{b} \rightarrow e^\pm X$	6.22	—	1M	2.5	31.1
$c\bar{c} \rightarrow e^\pm X$	3.31	—	500k	18.3	33.1

Table 7.7: Cross-section information about all samples used in this analysis. ϵ_{filter} is shown for the MultiLepton filter, except for the filtered minimum bias sample, where it corresponds to a generator level jet filter, as described in the text. The QCD overlap is indicated here, but all other values are obtained before the removal. The unfiltered minimum bias sample is not used for the final results in the analysis, therefore its QCD overlap is not studied here.

and the output is stored in the RDO file. From then on, the simulated and the real data are treated equally, through reconstruction.

For the specific samples used in this analysis, the software versions for the simulation and digitisation steps are the same for all *mc08* samples. The reconstruction is performed using ATHENA release 15.3.1.6.

7.2 Event selection

To extract a signal from the stream of acquired events, it is necessary to make a selection which maximises the signal while minimising the background. In this analysis, this is done using cuts over sensitive quantities aimed at selecting dielectrons. These cuts are applied after the reconstruction of electron objects, as described in §6. In the case of simulated data, the quantities used by the trigger selection are simulated at digitisation and the trigger selection is applied at the reconstruction step. The output of the trigger selection is stored regardless of its success, unlike in real data where the events which do not pass the trigger requirement are discarded.

7.2.1 Trigger cuts

The ATLAS trigger is divided in three levels and for each of them, a set of signatures is defined to form a *trigger menu*. A *trigger chain* is composed of one signature per level and is normally driven by physics requirements. For low transverse energy dielectron selection, the *2e5* chain is used. As its name states, it requires at least 2 trigger electron objects to be present in the event, each with $E_T > 5$ GeV. More precisely, the chain is composed of the three following signatures:

L1_2EM3

L1 signature which requires at least two RoIs containing an EM cluster, each with $E_T \geq 4$ GeV, to be found in the event.

L2_2e5_medium

L2 signature which requires at least two trigger electron objects to be found in input L1 RoIs, each with $E_T \geq 4$ GeV and passing shower shape and track-cluster matching cuts.

EF_2e5_medium

EF signature which requires at least two trigger electron objects to be found, each with $E_T \geq 5$ GeV and passing the medium electron identification cuts.

The selected events are requested to have successfully passed all three signatures to satisfy the trigger chain. A more complete description of the trigger selection for electrons is given in §6.7. In this analysis on simulated data, the trigger selection is applied at the end of the event selection (see §7.2.2).

7.2.2 Offline cuts

Once the events are fully reconstructed, additional offline cuts are applied to make a more efficient dielectron selection based on the electron identification methods described in §6.4. Starting from all the reconstructed electrons, the following preselection cuts are applied:

- i) at least two cluster-seeded electrons are found in the event (electrons reconstructed only by the track-seeded algorithm and electrons found in the forward calorimeters, are not included),
- ii) the electromagnetic cluster of each of the electrons satisfies $0 \leq |\eta_{cluster}| \leq 1.37$ and $1.52 \leq |\eta_{cluster}| \leq 2.47$, and
- iii) has a transverse energy $E_T \geq 5$ GeV.

The η cut is applied to exclude the transition region, where the electron reconstruction efficiency is lower and the energy reconstruction accuracy is degraded. The E_T cut is chosen to be consistent with the trigger cuts.

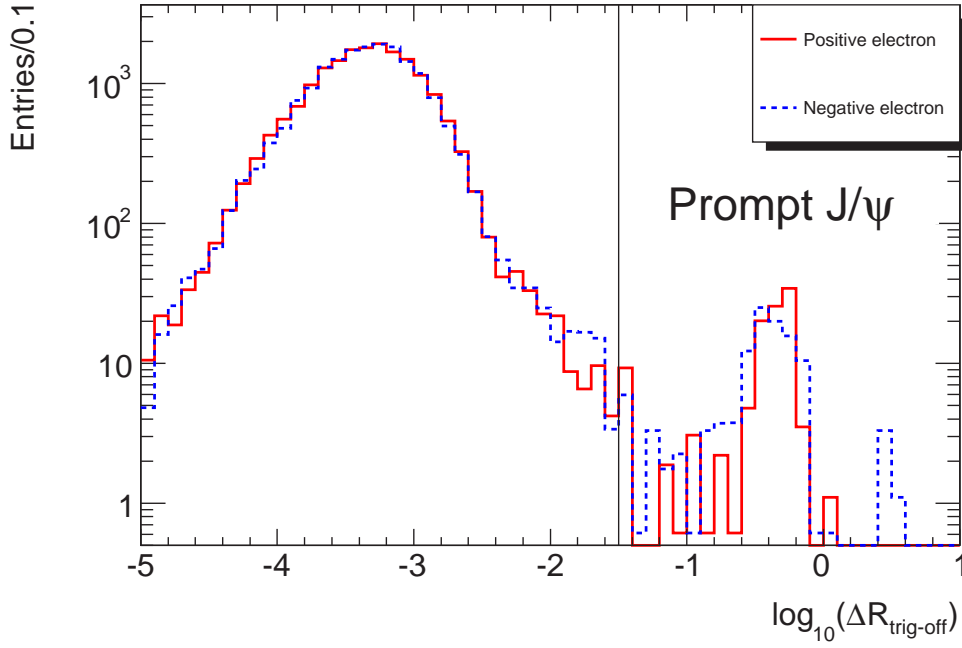
After the preselection cuts described above, the electron objects are passed to a vertex refitting procedure [116] which forms all possible pairs of oppositely charged tracks from this sample and fits them to a common vertex. In the case where three or more electron objects satisfy the preselection criteria, the same electron can be found in several pairs (respecting the opposite charge combination). The following cuts are then applied:

- iv) opposite-charge selection and common vertex refitting,
- v) $\chi^2 < 6$ on the vertex refit of the pair of tracks,
- vi) the electromagnetic clusters belonging to the two electrons are separated by $\Delta R_{cluster} = \sqrt{(\Delta\eta_{cluster})^2 + (\Delta\phi_{cluster})^2} > 0.1$ (to remove possible duplicates between nearby electromagnetic clusters - see §6.2.2),
- vii) the dielectron invariant mass is $2 \text{ GeV} \leq m_{ee} \leq 4 \text{ GeV}$,
- viii) both electrons pass the tight identification cuts,
- ix) the event passes the 2e5 trigger chain and the angular distance between the EF trigger object and the offline electron is $\Delta R \leq 0.03$ for both electrons in the pair,
- x) if more than one refitted electron pair is found, the one with the highest refitted p_T is kept.

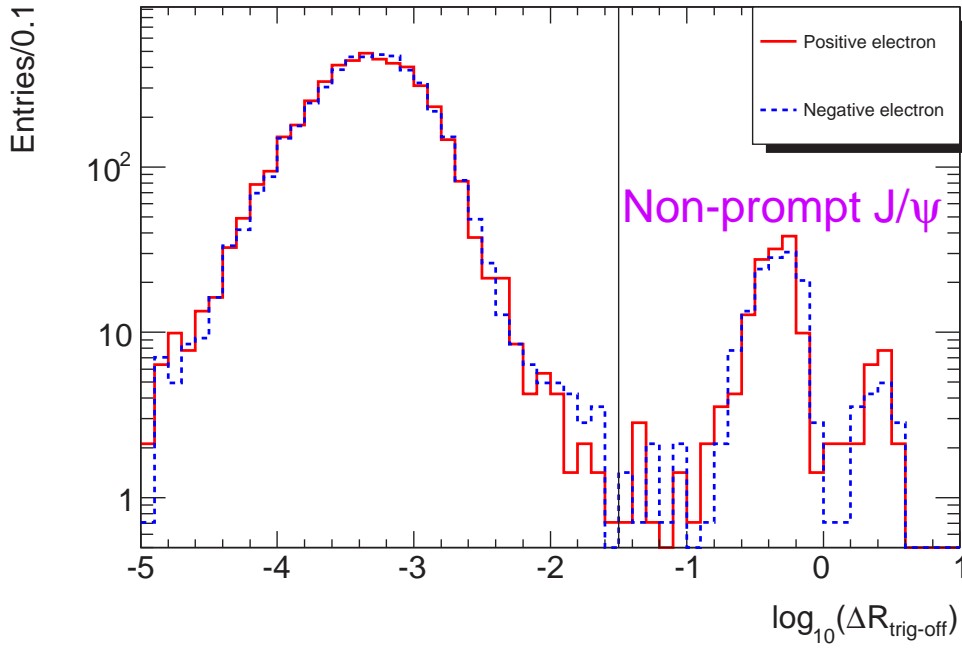
The dielectron invariant mass, m_{ee} , is defined in Eq. 7.2, where $i = 1, 2$ are the individual electrons in the selected pair, E_i is the energy measured by the calorimeter and \vec{p}_i is the momentum vector built from the calorimeter energy and the track direction.

$$m_{ee} = \sqrt{\left(\sum_{i=1}^2 E_i\right)^2 - \left\|\sum_{i=1}^2 \vec{p}_i\right\|^2} \quad (7.2)$$

To determine the trigger-offline objects matching cut, the distribution of the smallest ΔR between trigger and offline positions for reconstructed electron objects is studied, as shown in Fig. 7.2. The track angles are used to compute ΔR for both objects. The minimum ΔR for reconstructed electrons matched to a generator level electron from a J/ψ decay and passing the 2e5 trigger chain is shown respectively in dashed blue and solid red for positive and negative charge. The chosen cut value, illustrated



(a)



(b)

Figure 7.2: ΔR between EF trigger and offline electron objects for the signal samples. The distributions for (a) the prompt and (b) the non-prompt samples, normalised to $\int \mathcal{L} dt = 5 \text{ pb}^{-1}$, are shown. The dashed blue and solid red lines show the electrons matched to generator level electrons from a J/ψ decay (passing the 2e5 trigger chain) for each charge. The vertical line indicates the cut value.

by a vertical line, ensures that the J/ψ electron pair is kept while rejecting the wrong matches with the trigger.

The efficiencies for each of the above cuts are then obtained. In order to have a meaningful comparison between the different samples, the efficiencies are also computed with respect to the generator level events for which at least two electrons satisfy the following acceptance cuts⁷:

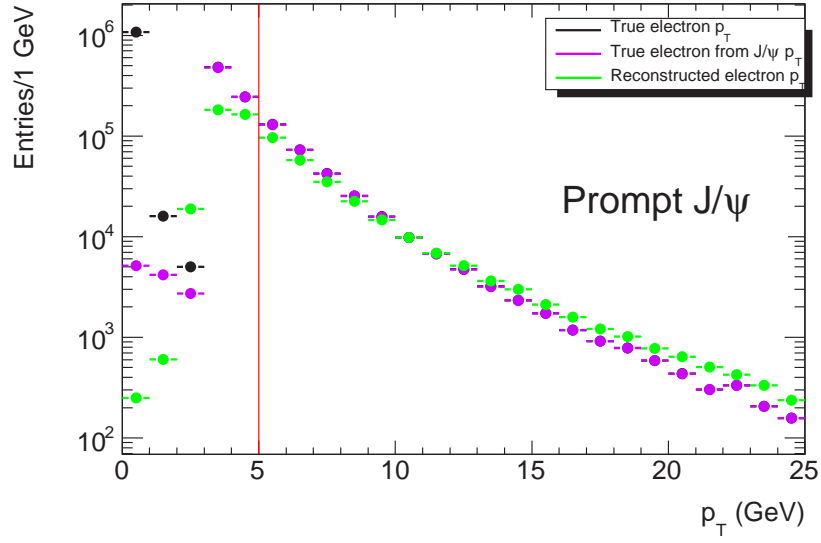
- a) the generator level electron satisfies $E_T \geq 5$ GeV,
- b) it is produced within $|\eta| \leq 2.47$,
- c) it must be a generator stable particle (status=1), and
- d) it must not be a GEANT particle (barcode<100000), i.e. not coming from material interactions in the detector.

The fraction of events surviving after each of the above cuts is shown in Table 7.8. As can be seen from these numbers, the QCD (minimum bias) background includes a large contribution of reconstructed hadronic fakes that are rejected by the selection cuts before the electron identification is applied. The small acceptance of the heavy flavour samples is mainly due to the fact that only a single electron filter is applied at generator level. Also, the acceptance for the non-prompt sample is higher than in the prompt case due to the presence of other electrons in the event. The loss of signal efficiency results mainly from the E_T cut and the electron trigger and identification cuts. As shown in Fig 7.3, a good fraction of the electrons from J/ψ decays for all reconstructed events have a transverse momentum smaller than 5 GeV, explaining the efficiency loss. For electrons within the acceptance cuts, the energy resolution at low p_T is the cause of the drop in efficiency for the E_T cut. Electrons from non-prompt J/ψ decays have a lower efficiency due to the trigger and identification cuts. This comes from the fact that these electrons are less isolated than those coming from prompt J/ψ production, due to the presence of hadrons around them (see §7.4.1 for more details). The efficiencies in Table 7.8 are calculated after the QCD overlap, described in §7.1.2, is removed. After tight identification cuts and trigger-offline matching, the QCD overlap is 96.7% for $c\bar{c}$ and 41.7% for $b\bar{b}$, which is a significant increase compared to the fraction of QCD overlap present at truth level, shown in Table 7.7. The effect of the dielectron pair refitting can be seen in Fig. 7.4, where the shift in p_T between the reconstructed and generator level p_T is shown, with and without refitting. The track refit shifts the dielectron p_T closer to the generator level J/ψ p_T value.

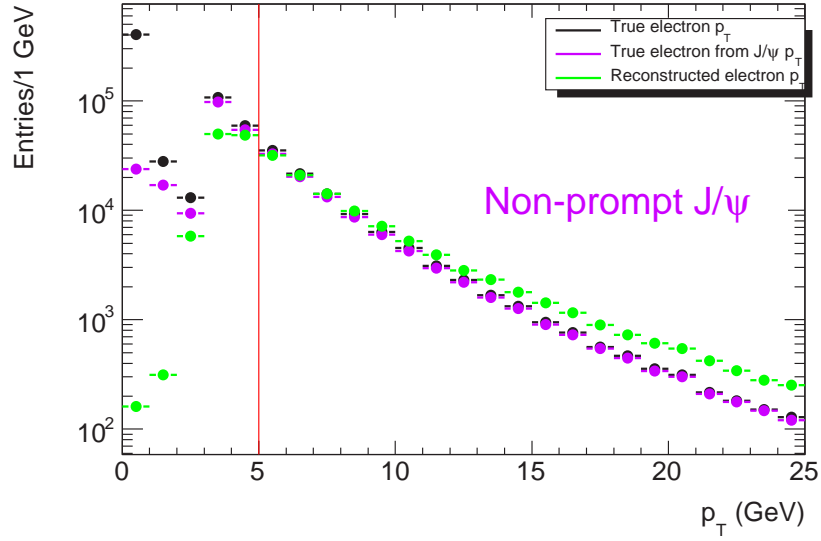
⁷All selection cuts are listed in Appendix C for easy reference.

Cuts	$pp \rightarrow J/\psi \rightarrow e^+e^-$		$b\bar{b} \rightarrow J/\psi \rightarrow e^+e^-$		$DY \rightarrow e^+e^-$		fMinBias		$c\bar{c} \rightarrow e^\pm X$		$b\bar{b} \rightarrow e^\pm X$	
	ϵ^{acc}	ϵ^{all}	ϵ^{acc}	ϵ^{all}	ϵ^{acc}	ϵ^{all}	ϵ^{acc}	ϵ^{all}	ϵ^{acc}	ϵ^{all}	ϵ^{acc}	ϵ^{all}
All events		499727		199678	498664		9908638		407384		983429	
Acceptance		10.9%		14.9%	29.6%		0.0008%		0.3%		0.8%	
2 cluster-seeded electrons	80.2	36.7	87.3	45.0	82.8	46.5	68.0	7.6	85.2	29.9	87.9	23.8
$\eta_{cluster}$ cut	74.7	34.6	82.9	42.7	75.6	42.7	65.3	7.1	81.5	28.0	83.7	22.2
$E_T \geq 5$ GeV	52.9	7.6	64.1	15.1	61.4	19.9	53.3	1.9	68.8	13.8	65.1	10.0
Opp. Ch. & Refit	49.0	6.6	54.5	11.6	57.6	18.4	30.7	1.1	52.0	8.5	52.1	6.1
$\chi^2_{refit} < 6$	41.5	5.6	44.8	9.1	46.2	14.7	26.7	0.8	41.3	6.3	34.8	4.0
$\Delta R_{cluster} \geq 0.1$	41.4	5.5	44.7	9.1	46.2	14.7	26.7	0.8	41.1	6.1	34.5	4.0
$2 \text{ GeV} \leq m_{ee} \leq 4 \text{ GeV}$	38.8	4.8	37.2	6.4	1.4	0.4	0	0.06	3.3	0.4	7.5	0.5
Loose	30.0	3.6	17.6	3.0	1.1	0.3	0	0.002	0.2	0.02	2.1	0.06
Medium	27.5	3.3	15.7	2.6	1.0	0.3	0	0.00001	0.2	0.002	1.8	0.02
Tight	17.9	2.1	10.0	1.7	0.7	0.2	0	0	0.07	0.0002	1.3	0.01
$2e5 \Delta R_{trig-off} < 0.03$	15.4	1.8	8.4	1.4	0.6	0.2	0	0	0.07	0.0002	1.1	0.01

Table 7.8: Selection efficiencies (in %) for individual cuts on all samples. The number of reconstructed events, before selection and without QCD overlap is shown in the first rows for each sample, together with the effect of the acceptance cuts a)-d) based on MC truth, described in the text. For each selection step, the efficiency is given both for all reconstructed events and for events within the acceptance cuts a)-d).

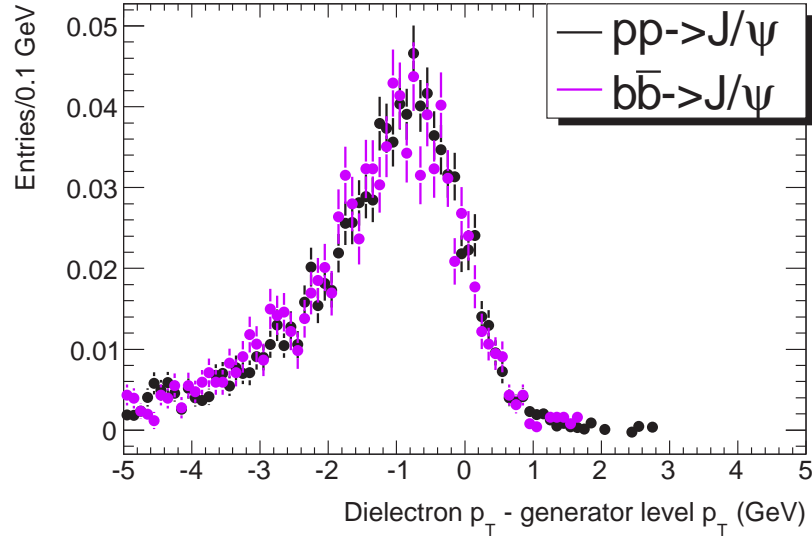


(a)

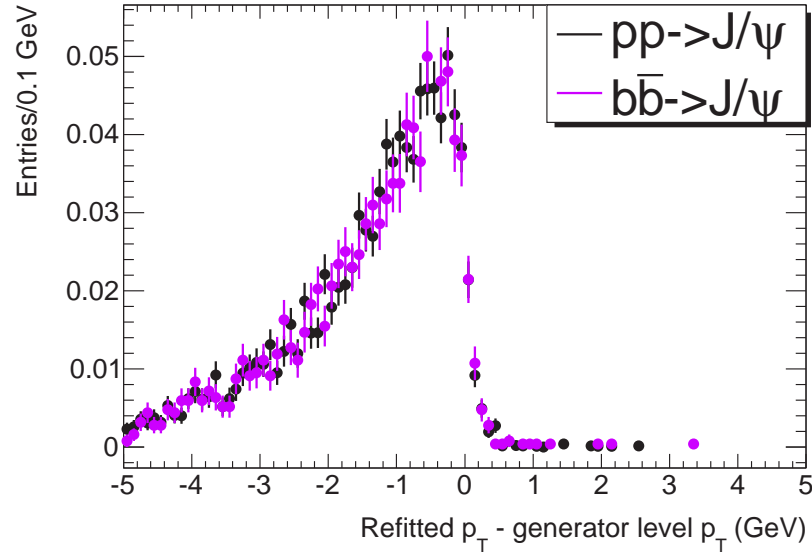


(b)

Figure 7.3: Transverse energy distributions before and after reconstruction for electrons from (a) prompt and (b) non-prompt J/ψ decays, normalised to $\int \mathcal{L} dt = 5 \text{ pb}^{-1}$. The red line indicates the value for cut iii). The true electrons are selected using cuts c)-d) and the reconstructed electron distribution includes all cluster-seeded electron objects. The shape around 3 GeV before reconstruction is caused by the MultiLepton filter.



(a)



(b)

Figure 7.4: Difference between the J/ψ p_T and the generator level p_T for the prompt and the non-prompt contributions overlaid and normalised to unit area. (a) The dielectron p_T , computed from cluster quantities and (b) the refitted J/ψ p_T are compared to the generator level p_T .

7.3 Simulation studies

To maximise the accuracy of our prediction, a careful study is made of issues arising from the particular event generation and simulation that we use with respect to the selection used in this analysis. In particular, four studies are described below:

- the effect of the jet filter used on our minimum bias sample,
- the effect of the event reweighting procedure needed for the prompt J/ψ sample,
- a study of the cut on \hat{p}_\perp used for the prompt J/ψ sample and
- a detailed description of the background sample composition.

The samples used for the three first studies are reconstructed with a different ATHENA release, 14.2.20.3, based on the event generation and simulation described in §7.1.2; the background composition study is performed using the same reconstruction as used for the final analysis.

For these studies, unless stated otherwise, a simplified electron pair selection is used for which the electron pairs are not refitted to a common vertex and no trigger requirement is applied. The cuts used for this selection, applied after preselection cuts i)-iii), are shown below⁸.

- xi) $\Delta R_{cluster} > 0.1$,
- xii) at least one electron of each charge,
- xiii) both electrons passing the identification cuts (loose, medium, medium_noiso, tight or tight_noiso),
- xiv) if more than one opposite-sign electron-pair combination is found, the combination with the highest p_T is kept.

7.3.1 Effect of the minimum bias filter

As described in §7.1.2, the minimum bias sample used in this analysis is filtered at the generator level for jet-like objects with $E_T > 6$ GeV. This generator filter inevitably biases the sample since events containing lower energy objects, which could reveal themselves after reconstruction, are excluded. This could affect the shape of the background in the various distributions we are interested in. Furthermore, the event selection used for this analysis contains an E_T cut at 5 GeV at both trigger and offline

⁸All selection cuts are listed in Appendix C for easy reference.

levels. The effect of the induced bias is studied by comparing an unfiltered minimum bias sample with the filtered sample used in this analysis.

All cluster-seeded electrons are considered. The transverse energy distribution of the leading electron in the event is shown in Fig. 7.5. The effect of the generator filter is visible since less electrons are found at $E_T < 6$ GeV for the filtered sample. The bias in the $5 < E_T < 6$ GeV bin is estimated by the ratio of filtered to unfiltered events, which is 0.77. This bias is slightly higher for the electron identification selections: 0.67 for loose, 0.75 for medium_noiso and 0.62 for tight_noiso, as defined in §6.5.

To determine if this bias affects the electron selection used in this analysis, it is necessary to study the same effect after applying the cuts. The transverse energy distribution for the loose selection is shown in Fig. 7.6. The bias estimation in the $5 < E_T < 6$ GeV bin in this case is 1.02, meaning that, within statistical errors, the filtered and unfiltered sample give the same result. We can then conclude that this analysis is not affected by the generator filter bias. It is not possible to compare the two samples for tighter identification cuts (such as medium_noiso and tight_noiso) due to the low statistics remaining after selection.

The filter bias is significantly reduced by the cut on the $\Delta R_{cluster}$ quantity. To illustrate this, a reduced selection, shown in Table 7.9 is used (due to the low available statistics for the minimum bias samples), where the cut on E_T , which is the most efficient cut, is removed (an implicit cut of $E_T > 2.5$ GeV is still applied from the Sliding Window cluster seeding). Two sets of selection cuts are created: a *NoETCut* selection and a *NoETCut+dR* selection, where only the cut on $\Delta R_{cluster}$ is added going from the former to the latter. The electron transverse energy distribution of the NoETCut loose selection shows a filter bias of 84% while the NoETCut+dR loose selection reduces it to 92%. The same comparison for the medium_noiso identification selection shows that the filter bias is completely removed, within large statistical errors. The four aforementioned distributions are shown in Fig. 7.7.

Selections	NoETCut	NoETCut+dR
Cuts	i) ≥ 2 cluster-seeded electrons	i) ≥ 2 cluster-seeded electrons
	ii) $\eta_{cluster}$ cut	ii) $\eta_{cluster}$ cut
	xiii) loose identification cuts	xiii) loose identification cuts
	—	xi) $\Delta R_{cluster} > 0.1$

Table 7.9: NoETCut and NoETCut+dR selections used for the minimum bias filter bias study.

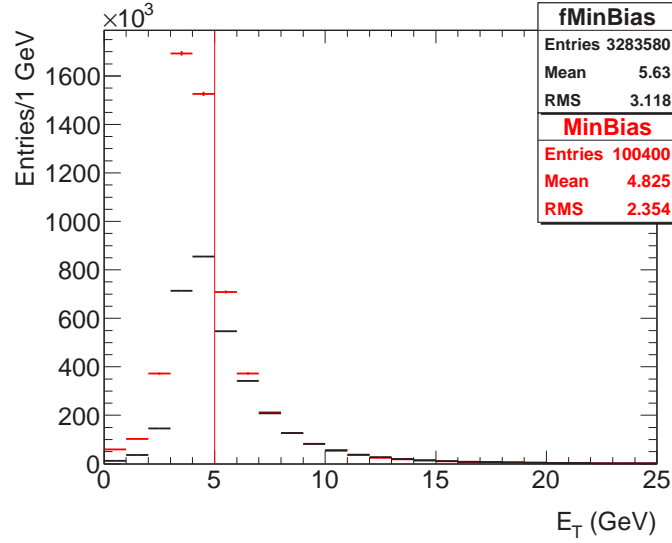


Figure 7.5: Leading electron reconstructed transverse energy comparison between filtered (black) and unfiltered (red) minimum bias event. The unfiltered minimum bias distribution is normalised to the luminosity of the filtered sample. The red vertical line indicates the E_T cut value used in the analysis.

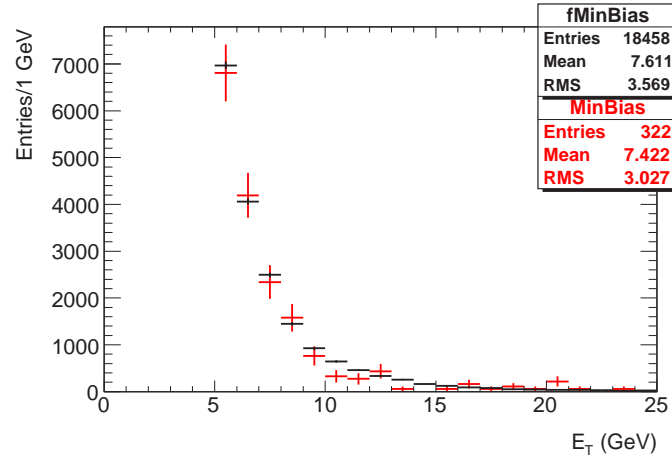


Figure 7.6: Electron reconstructed transverse energy comparison between filtered (black) and unfiltered (red) minimum bias events after event selection. The event selection is performed using the loose identification cuts. The unfiltered minimum bias distribution is normalised to the luminosity of the filtered sample.

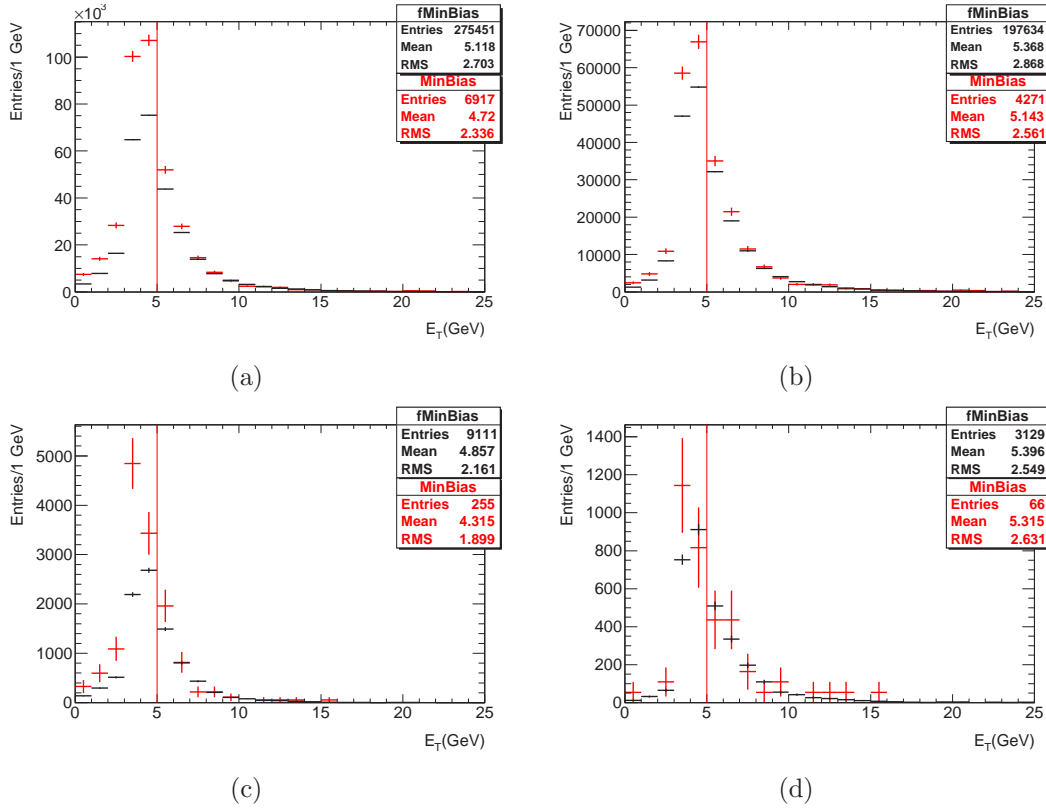


Figure 7.7: Electron reconstructed transverse energy distribution for the reduced event selection, for the filtered sample in black and for the unfiltered sample in red. (a) NoETCut selection for loose identification, (b) NoETCut+dR selection for loose identification, (c) NoETCut selection for medium_noiso identification, (d) NoETCut+dR selection for medium_noiso identification. The red vertical line shows the E_T cut value in the standard event selection. The unfiltered minimum bias distribution is normalised to the luminosity of the filtered sample.

7.3.2 Effect of event weights for prompt signal

As explained in §7.1.1, to correct for the mixing of the various production channels of the J/ψ mesons in the prompt signal sample, event weights have to be applied. The effect of the weights on the signal yield is quantified by comparing the invariant mass distribution with and without weighting. The result can be seen in Fig. 7.8. The weights from Table 7.3 are used here. An increase in the yield of 14% and 17% can be observed respectively for the loose and medium_noiso identification cuts. This is explained by the different efficiencies of the production processes, shown in Table 7.12

and discussed in §7.3.3. These efficiencies are computed the same way as the values for ϵ_{all} in Table 7.8, with the exception that the simplified electron pair selection is used. Direct production, for which the event weights increase the contribution by a factor ~ 3 , has a higher efficiency than the χ_c decays.

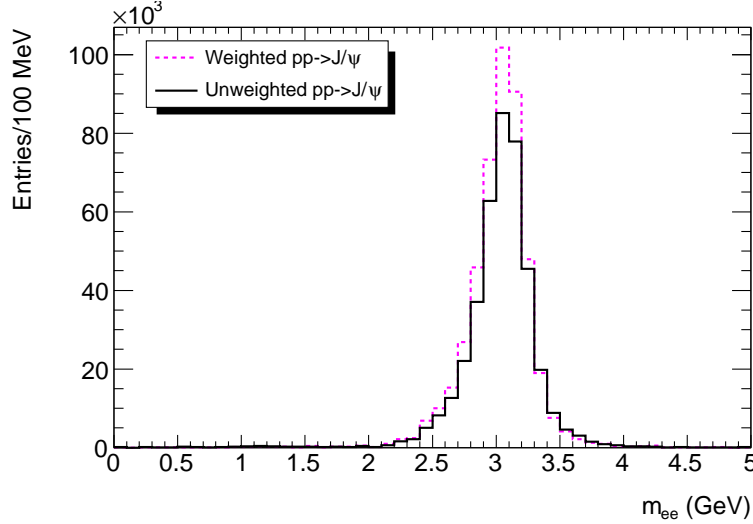


Figure 7.8: Invariant mass comparison for prompt J/ψ events before (solid black line) and after (dashed purple line) event reweighting. The invariant mass is shown here for the simplified electron pair selection using the loose identification cuts and normalised to $\int \mathcal{L} dt = 5 \text{ pb}^{-1}$.

7.3.3 Study of the kinematic cuts in PYTHIA

As can be seen in Table 7.1, the prompt J/ψ signal sample is generated with the value of the CKIN(3) parameter, set to 3 GeV in PYTHIA, which corresponds to the minimum \hat{p}_\perp of the hard interaction. This regulates the cross-section in the non-perturbative regime. The default value is set to 1 GeV in PYTHIA. To quantify the effect of this parameter, we produced a new prompt J/ψ sample of 200k events using the same software version as the $\hat{p}_\perp > 3 \text{ GeV}$ sample, modifying only the value of the CKIN(3) parameter to 1 GeV. The complete simulation and reconstruction chain is then applied to 100k events, using the same software versions as used for the $\hat{p}_\perp > 3 \text{ GeV}$ sample. For this study, the $\hat{p}_\perp > 3 \text{ GeV}$ sample was limited to 200k events.

Already at generator level, we observe an increase in the normalised cross-section⁹ for $E_T^{electron} > 3 \text{ GeV}$, $|\eta^{electron}| < 2.7$, defined in Eq. B.2, for prompt J/ψ production, from 105.5 nb to 194.3 nb. The event weights are also modified since the fractions

⁹See Appendix B for more details on the normalised cross-section calculation.

of the different production channels are modified, as can be seen in Table 7.10. An increase of about 40% is observed in the event weights compared to the $\hat{p}_\perp > 3$ GeV sample, listed in Table 7.3. It should be noted that the fractions of events for each production type, before and after reweighting, are modified such that the direct and χ_{c1} contributions are lower and χ_{c0} and χ_{c2} are higher compared to the values in Table 7.3.

Process	BR($\rightarrow J/\psi$)	f^{bef}	w	f^{corr}
Direct J/ψ	1	10.5%	4.287	45%
χ_{c0}	1.28%	36.6%	0.055	2%
χ_{c1}	36%	11.0%	1.543	17%
χ_{c2}	20%	42.0%	0.857	36%

Table 7.10: Event weights and fractions for the prompt signal sample with $\hat{p}_\perp > 1$ GeV. Values of branching ratios are obtained from the PDG [13].

The increase in yield for the $\hat{p}_\perp > 1$ GeV sample can be quantified already at the generator level, before the MultiLepton filter is applied, using the luminosity scale factors for each production channel, s_i , defined in Appendix A. These scale factors are calculated for each sample using Eq. 7.3 (same as Eq. A.20 and reproduced below for clarity). After applying the event weights w_i , the value for the generated luminosity of the combined sample, \mathcal{L}^{gen} , is obtained using Eq. 7.4 (using Eq. 7.1 to substitute for w_i in Eq. 7.3).

$$\begin{aligned}
s_i &= \frac{\mathcal{L}}{\mathcal{L}_i^{gen}} = w_i \times \frac{\mathcal{L}}{\mathcal{L}^{gen}} \\
&= \frac{\mathcal{L}}{N_{tot}^{bef}} \times \sigma^{gen} \times BR_i \times BR_{J/\psi \rightarrow e^+e^-}
\end{aligned} \tag{7.3}$$

$$\mathcal{L}^{gen} = \frac{N_{tot}^{bef}}{\sigma^{gen} \times BR_{J/\psi \rightarrow e^+e^-} \times \sum_j BR_j \times f_j^{bef}} \tag{7.4}$$

For the $\hat{p}_\perp > 3$ GeV sample, $\mathcal{L}^{gen} = 2.0 \text{ pb}^{-1}$, while it becomes 1.1 pb^{-1} for the $\hat{p}_\perp > 1$ GeV sample (0.55 pb^{-1} when used for simulation and reconstruction). These values are computed for the same number of generated events, 200k, in each sample. The values of the individual s_i for the $\hat{p}_\perp > 1$ GeV sample increase by 155% compared to the $\hat{p}_\perp > 3$ GeV sample values, when choosing a common luminosity \mathcal{L} . After the MultiLepton filter is applied and the events are simulated and reconstructed, an

increase of 82% is still observed for the $\hat{p}_\perp > 1$ GeV sample, by comparing the sum of s_i for each sample in Table 7.11.

Identification cuts	$\sum_{evts} s_i$		Ratio
	$\hat{p}_\perp > 1$ GeV	$\hat{p}_\perp > 3$ GeV	
Loose	15534	9499	1.635
Medium_noiso	10657	6763	1.576
Medium	10227	6404	1.597
Tight_noiso	6400	4283	1.494
Tight	6693	4316	1.551
All events	363371	199626	1.82

Table 7.11: Expected signal rates for prompt J/ψ signal after applying the simplified electron pair selection for each set of identification cuts.

The simplified electron pair selection cuts are applied to the reconstructed events for all the electron identification set of cuts, described in §6.5. The absolute selection efficiencies per production channel are shown in Table 7.12 for $\hat{p}_\perp > 1$ GeV and $\hat{p}_\perp > 3$ GeV samples.

Identification cuts	$\hat{p}_\perp > 1$ GeV				$\hat{p}_\perp > 3$ GeV			
	J/ψ	χ_{c0}	χ_{c1}	χ_{c2}	J/ψ	χ_{c0}	χ_{c1}	χ_{c2}
Loose	4.4%	3.7%	3.7%	3.7%	5.5%	3.0%	3.8%	3.3%
Medium_noiso	3.2%	2.5%	2.5%	2.4%	4.1%	2.0%	2.6%	2.2%
Medium	3.1%	2.4%	2.4%	2.3%	3.8%	2.0%	2.5%	2.1%
Tight_noiso	2.0%	1.6%	1.4%	1.4%	2.6%	1.3%	1.6%	1.4%
Tight	2.0%	1.7%	1.6%	1.5%	2.6%	1.4%	1.7%	1.4%
Loose	4.3%				4.8%			
Medium_noiso	2.9%				3.4%			
Medium	2.8%				3.2%			
Tight_noiso	1.8%				2.1%			
Tight	1.8%				2.2%			

Table 7.12: Absolute selection efficiencies per production channel for the simplified electron pair selection, and varying the electron identification cuts. No acceptance cuts are applied to MC truth quantities. The statistical error on the efficiencies is $\leq 0.2\%$.

The overall efficiencies for each identification cut are smaller for the lower value of \hat{p}_\perp . Furthermore, the efficiencies for the χ_{c0} and χ_{c2} feed-downs are higher for the $\hat{p}_\perp > 1$ GeV sample while the efficiencies for direct J/ψ production and χ_{c1} feed-down are smaller. This observation is in agreement with the observed fractions of events at the generator level for the $\hat{p}_\perp > 1$ GeV sample of Table 7.10. The variation in the selection efficiencies can be traced back to the acceptance; when calculated within acceptance, the efficiencies between the production channels are comparable. This effect can be explained by the intrinsic polarisation of the different states.

The compared distributions of kinematical quantities between the $\hat{p}_\perp > 3$ GeV and the $\hat{p}_\perp > 1$ GeV samples for the loose identification cuts are shown in Fig. 7.9. The normalised distribution for the electron transverse energy is shown in Fig. 7.9(a) and the dielectron quantities, invariant mass, transverse momentum and pseudorapidity, are shown in Fig. 7.9(b), 7.9(c) and 7.9(d), respectively. As expected, the $\hat{p}_\perp > 3$ GeV sample has a harder p_T spectrum than the $\hat{p}_\perp > 1$ GeV sample.

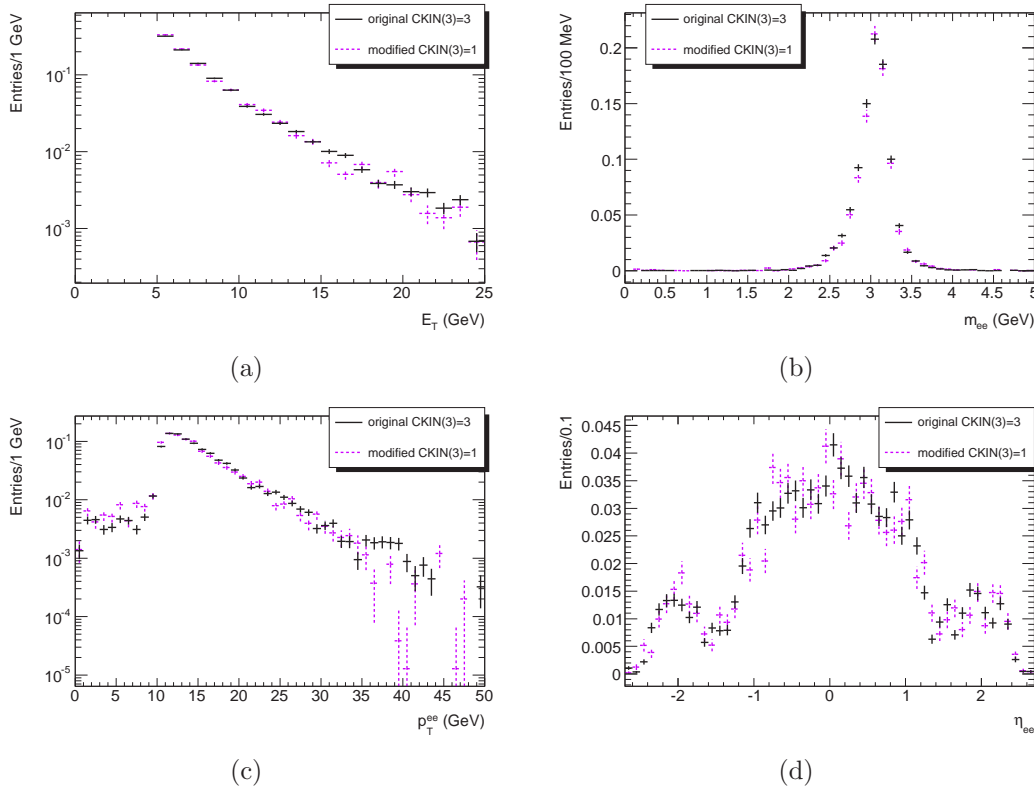


Figure 7.9: Shape comparison plots using the simplified electron pair selection with loose identification cuts for different \hat{p}_\perp values: (a) electron reconstructed transverse energy, (b) dielectron invariant mass (c) dielectron reconstructed transverse momentum and (d) dielectron reconstructed pseudorapidity. The solid black line shows the $\hat{p}_\perp > 3$ GeV sample and the dashed purple line shows the $\hat{p}_\perp > 1$ GeV sample. The distributions are normalised to unit area.

The expected signal rates are shown in Table 7.11, obtained by summing the event weights for a given selection. The ratio between the $\hat{p}_\perp > 1$ GeV and $\hat{p}_\perp > 3$ GeV sum of weights is shown to quantify the increase in yield. The difference between the $\hat{p}_\perp > 1$ GeV and the $\hat{p}_\perp > 3$ GeV sample is larger when isolation is required in the electron identification cut.

Based on these results, it was recommended that the official sample production divides the production channels into four separate samples to simplify the combination. The value used for the CKIN(3) parameter was also changed from 3 GeV to 1 GeV. These changes have been implemented for the *mc09* simulation exercise. A theoretical uncertainty is assigned to this effect in §8.5.

7.3.4 Background composition and shape

To understand the shape of the background distributions, it is important to have a good knowledge of the composition of the background samples used in the analysis. Using simulated samples reconstructed with ATHENA release 15.3.1.6, it is possible to match the reconstructed object with the generator level particle which created it. In the following, the matching is performed using a tool called EgammaMCTruthClassifier [117]. This tool uses the reconstructed electron track and the true electron track to compute the probability of a match based on the number of hits the two objects share in the tracking system. Based on the matching generator level object, the reconstructed object is classified using predefined particle *types* and *origins*, described in Table 7.13. Many origins can be associated with a single type but the origin cannot be used by more than one type. Some of the categories presented below were modified in later versions of the tool, due to inaccuracies, e.g. J/ψ as a source of non-isolated electrons or Υ as a source of background electrons.

The results for each background sample are presented before event selection for all cluster-seeded electrons in Table 7.14 and after the simplified electron pair selection for tight identification cuts in Table 7.15. The QCD overlap described in §7.1.2 is removed from the samples before the classification is performed. The values represent the fractions of the total number of cluster-seeded electrons found in all events, before and after selection, classified into each particle type and origin. The values for each sample do not add up to 100%, since a small fraction is either not successfully matched or matched to a generator level muon. As expected, these numbers show that, after reconstruction, the filtered minimum bias sample is an important source of hadronic fakes and electrons from background processes, such as photon conversions and Dalitz decays. As expected, the electrons of the Drell-Yan sample come mainly from Z decays. Also, the majority of electrons in the heavy flavour samples originate from hadrons of the specific flavour of the sample.

The shape of the dielectron invariant mass distribution for the background contributions after the loose event selection is shown in Fig. 7.10, scaled to a luminosity of

Particle type	Description	Particle origin	Description
ElectronNIso	Non-isolated electron	CharmedMeson	Meson containing at least a c and no b quark
		CharmedBaryon	Baryon containing at least a c and no b quark
		TauLep	τ lepton decay
		BottomMeson	Meson containing at least a b and no c quark
		BottomBaryon	Baryon containing at least a b and no c quark
ElectronBkg	Background electron	PhotonConv	Conversion: $\gamma \rightarrow e^+e^-$
		DalitzDec	Dalitz decay: $\pi^0 \rightarrow \gamma e^+e^-$
		LightMeson	Meson containing u and d quarks
		BBbarMeson	Υ meson
ElectronIso	Isolated electron	ZBoson	Z boson decay
Hadron	Hadron	—	—

Table 7.13: Predefined particles types and origins used by the EgammaMCTruthClassifier tool and their description. The origin of hadrons is not classified.

Classification		$DY \rightarrow e^+e^-$	fMinBias	$c\bar{c} \rightarrow e^\pm X$	$b\bar{b} \rightarrow e^\pm X$
ElectronNIso	CharmedMeson	0.09	0.2	51.5	5.3
	CharmedBaryon	<0.01	<0.01	1.6	0.2
	TauLep	<0.01	<0.01	0.2	0.8
	BottomMeson	0.07	0.1	0.02	52.0
	BottomBaryon	<0.01	0.01	<0.01	5.1
ElectronBkg	PhotonConv	5.8	23.0	11.0	10.1
	DalitzDec	0.03	0.2	1.7	0.4
	LightMeson	<0.01	0.03	0.4	0.09
	BBbarMeson	<0.01	<0.01	<0.01	0.02
ElectronIso	ZBoson	87.7	—	—	—
Hadron	—	4.4	66.4	28.5	21.1

Table 7.14: Truth classification for background samples before event selection. The fraction of cluster-seeded electrons in each category is given in % after QCD overlap removal. No selection cuts are applied here.

Classification		$DY \rightarrow e^+e^-$	fMinBias	$c\bar{c} \rightarrow e^\pm X$	$b\bar{b} \rightarrow e^\pm X$
ElectronNIso	CharmedMeson	<0.01	—	62.7	12.3
	CharmedBaryon	—	—	0.8	0.5
	TauLep	<0.01	—	—	1.6
	BottomMeson	0.01	—	—	72.0
	BottomBaryon	—	—	—	6.1
ElectronBkg	PhotonConv	0.3	16.7	7.6	1.1
	DalitzDec	<0.01	41.7	10.2	0.6
	LightMeson	<0.01	16.7	4.2	0.1
	BBbarMeson	—	—	—	1.8
ElectronIso	ZBoson	99.6	—	—	—
Hadron	—	0.02	25	14.4	3.7

Table 7.15: Truth classification for background samples after the simplified electron pair selection with tight identification cuts is applied. The fraction of cluster-seeded electrons in each category is given in % after QCD overlap removal.

5 pb^{-1} . A double peak structure can be seen in the distribution, with a trough in the mass region of interest for the J/ψ meson, around 5 GeV. To study the origin of this shape, the invariant mass distribution for the least biased case, using the unfiltered minimum bias sample, is used. The result is shown in Fig. 7.11. All possible pairs are formed from cluster-seeded electron objects. The angular distance ΔR and the azimuthal angle difference $\Delta\phi$ between the two electrons forming the pair are calculated and their correlation with the invariant mass is shown in Fig. 7.12. A clear correlation can be seen between high mass events ($m_{ee} > 5 \text{ GeV}$) and back-to-back electrons forming a pair (where $\Delta\phi \sim 3$), showing that the shape results from a kinematical effect.

Other correlations are observed among the background samples. They are shown here for the filtered minimum bias after the simplified electron pair selection with loose identification cuts in Fig. 7.13. The shapes are similar for all background sources. We can see that, since the decaying J/ψ is boosted, the angular distance between the decay products is anti-correlated to transverse momentum of the J/ψ . Furthermore, the angular distance is correlated with the reconstructed mass of the decaying particle. From these correlations, we can conclude that it is possible to remove the high mass component of the selected sample by applying a cut on the dielectron p_T or ΔR . As we focus on the invariant mass below 5 GeV for this analysis, such a cut is not applied.

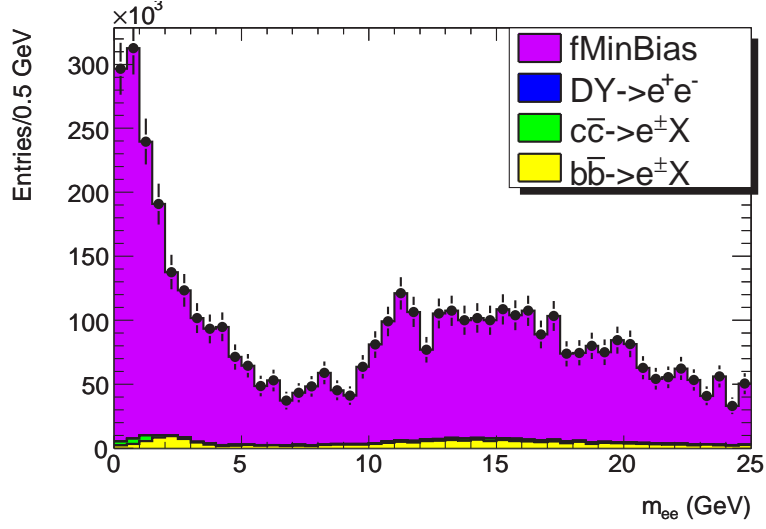


Figure 7.10: Invariant mass distribution after the simplified electron pair selection with loose identification cuts for background samples only and normalised to $\int \mathcal{L} dt = 5 \text{ pb}^{-1}$.

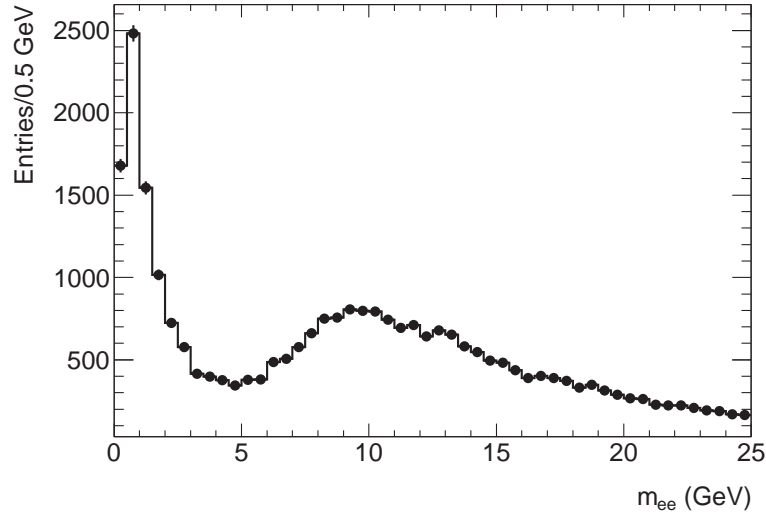


Figure 7.11: Invariant mass distribution after reconstruction for the unfiltered minimum bias sample and normalised to $\int \mathcal{L} dt = 5 \text{ pb}^{-1}$. All cluster-seeded electrons pairs are considered here. The background shape observed previously is also seen here.

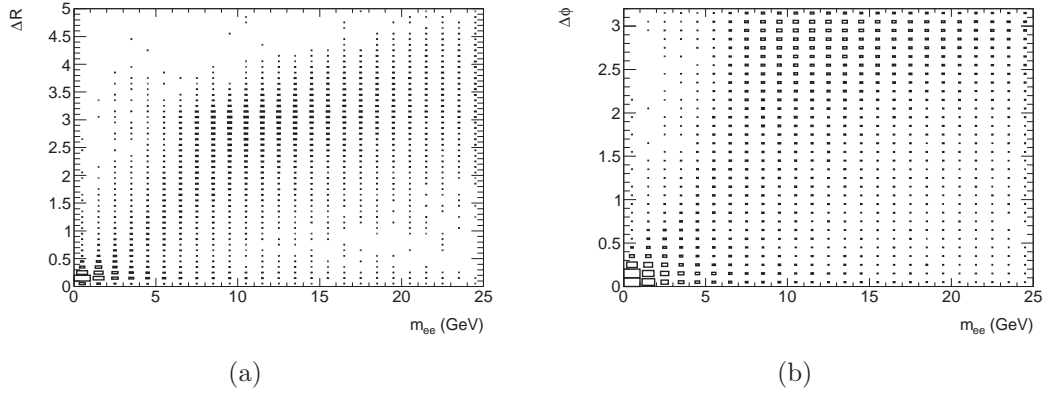


Figure 7.12: Correlations between the reconstructed angular distance and the mass of electron pairs for unfiltered minimum bias events. Both the correlation between the invariant mass and (a) ΔR and (b) $\Delta\phi$ are shown.

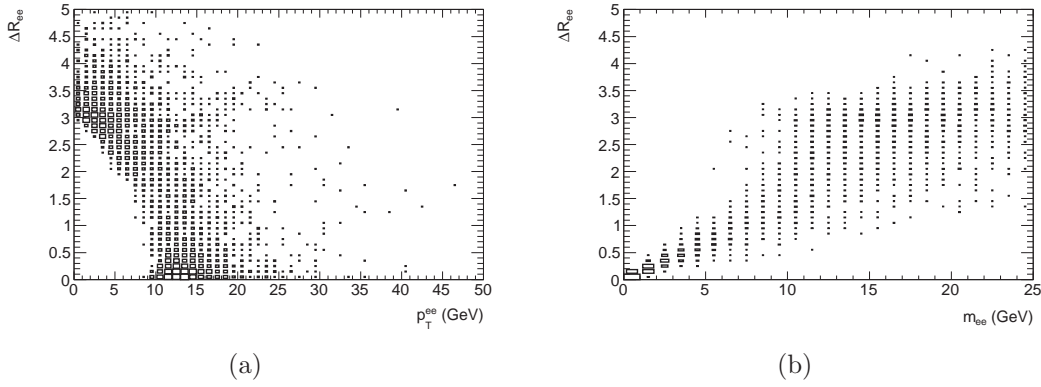


Figure 7.13: Correlations between reconstructed kinematical variables for filtered minimum bias. The correlation between (a) ΔR and p_T , as well as between (a) ΔR and m_{ee} are shown for the simplified electron pair selection after loose identification cuts.

In order to study the combinatorial background, the invariant mass distribution using same-charge electron pairs is produced. As in the opposite-charge case, one pair of same-charge electrons is chosen per event. The selection uses the p_T of the pair to select the highest value. In the case where one pair of each charge satisfies all selection cuts, the pair with the charge assignment of the highest p_T electron in the event is chosen. After applying the simplified electron pair selection, the invariant mass for each charge selection case is obtained and overlaid, as shown in Fig. 7.14. More opposite-charge pairs are found than same-charge pairs for all components of the

background. This is explained by the different physics processes involved depending on the background source which cannot be faked by combinatorial background. In the case of $c\bar{c} \rightarrow e^\pm X$ decays, semileptonic D meson decays, for which the hadronic leg fakes an electron, create more pairs in the opposite-charge selection in the range $m_{ee} < 2$ GeV. For $b\bar{b} \rightarrow e^\pm X$ decays, sequential semileptonic $B \rightarrow D$ meson decays, for which the two electrons, one created in each decay, have opposite charge, are found in greater numbers in the range $2 < m_{ee} < 3$ GeV than same-charge pairs. Finally, photon conversions, which are made of a true pair of opposite-charge electrons, add more pairs than for the same-charge case in the range $m_{ee} < 1$ GeV for the filtered minimum bias sample.

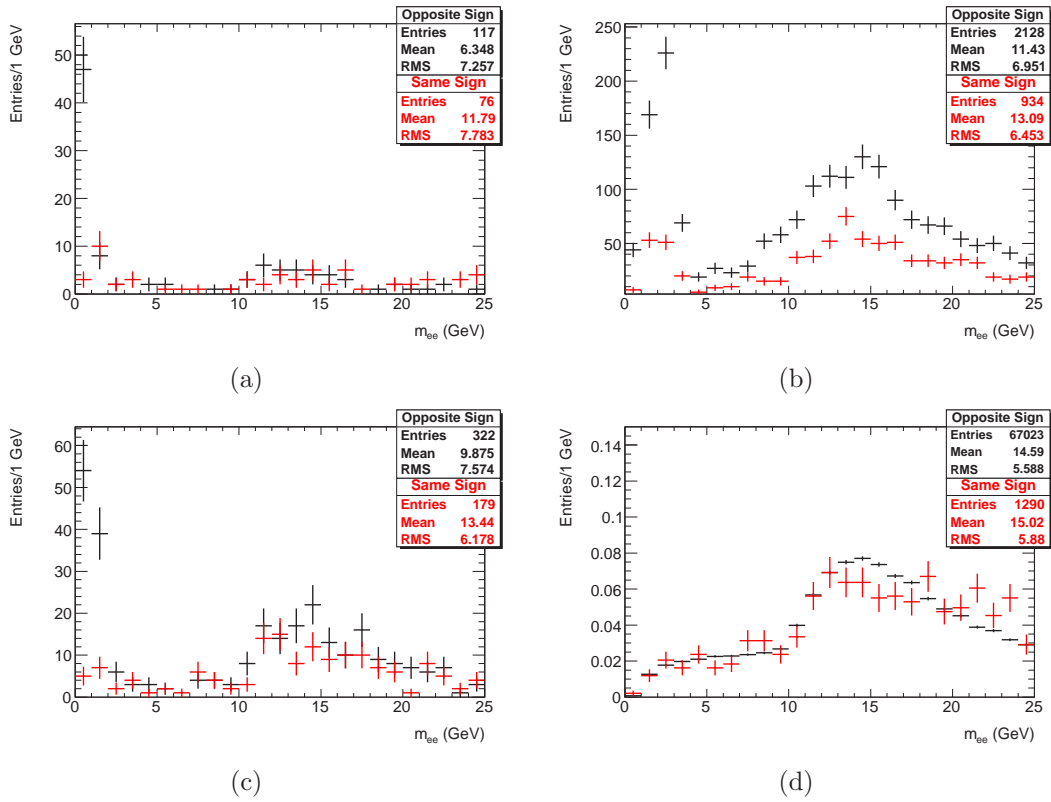


Figure 7.14: Invariant mass comparison between the opposite-sign and the same-sign selection for backgrounds. The distribution for the same-sign selection is shown in red and the opposite-sign selection is represented by black points. The invariant mass distributions for (a) filtered minimum bias, (b) $b\bar{b} \rightarrow e^\pm X$ and (c) $c\bar{c} \rightarrow e^\pm X$ are normalised to the same luminosity while for (d) Drell-Yan $\rightarrow e^+e^-$, the two distributions are normalised to unit area to compare the shape.

The possibility of using the same-charge pair selection and subtracting it from the opposite-charge selection to remove background was studied. However, due to the observations mentioned above, this technique did not provide enough rejection power to be useful for the cross-section calculation and is therefore not used in the final analysis.

7.4 Cross-Section Calculation

Using the events reconstructed and selected from the signal and background samples, we estimate the J/ψ production cross-section. The event selection described in §7.2 is used in the following, unless stated otherwise. The formula used to compute the $J/\psi \rightarrow e^+e^-$ production cross-section σ is shown in Eq. 7.5, where N_{signal} is the number of measured signal events, ϵ is the combined reconstruction, trigger, selection and identification efficiency, ϵ_{filter} is the fraction of events passing the MultiLepton requirements which represents the kinematical acceptance of the detector, and \mathcal{L} is the integrated luminosity.

$$\sigma = \frac{N_{signal}}{\epsilon_{filter}\epsilon\mathcal{L}} \quad (7.5)$$

For this analysis, several quantities are studied: the total and differential prompt and non-prompt $J/\psi \rightarrow e^+e^-$ production cross-sections. Given that this study is performed on simulated events only, the kinematical acceptance, considered after the generator level MultiLepton filter requirement and related to the trigger chain used, and the efficiency components are computed together in a single efficiency, ϵ . For reference, the expected values of the acceptance are given for each sample in Table 7.8.

In the following sections, the evaluation of the various quantities needed for the cross-section calculation is presented. The details of the calculation for their associated systematic uncertainties are given in §8.

7.4.1 Efficiency estimation

To compute the cross-section, it is necessary to estimate the efficiency of our event selection. Given that this study was performed solely on simulated events, we calculate the efficiencies using Eq. 7.6, for the total sample and in bins of the generator level J/ψ p_T .

$$\epsilon = \frac{\# \text{ of selected events}}{\# \text{ of generated events}} \quad (7.6)$$

We obtain a value of $\epsilon_p = 0.0169 \pm 0.0002$ for the prompt signal efficiency and $\epsilon_{np} = 0.0135 \pm 0.0003$ in the non-prompt case. These values are also listed in Table 7.18. This section describes some aspects that are important to consider when measuring efficiencies in data, such as the response of prompt and non-prompt contributions, as well as a first look into trigger efficiencies.

As shown previously in Table 7.8, the non-prompt J/ψ electrons have a lower selection efficiency than electrons from prompt J/ψ decays. The efficiency as a function of the generator level J/ψ p_T is shown at the bottom of Fig. 7.15 for the prompt case on the left hand side, and on the right-hand side for the non-prompt J/ψ . On the top of Fig. 7.15, the generator level p_T is shown for electron pairs with only acceptance cuts c) and d) applied together with the offline selected pairs. For the latter, a matching is performed using the smallest angular distance ΔR , within a cone of size $\Delta R=0.2$, between the generator level and the reconstructed electrons. We can see that the two signal contributions have a different dependence on p_T for the efficiency, as well as a different overall scale. The efficiency drops at higher p_T for both samples, but more significantly in the non-prompt case. The ratio of non-prompt-to-prompt efficiency is shown in variable p_T ranges with equal statistics in Fig. 7.16, where the dependence can be clearly seen.

This shape can be explained by hadron contamination in the electron cluster in the case of non-prompt J/ψ decays, causing them to be less isolated than electrons from prompt J/ψ mesons. With the presence of a B -meson in the event, there is more hadronic activity than in the case of prompt J/ψ production from the hard interaction. The measurement of the energy of these hadrons would shift the energy of the cluster to higher values, compared to the energy of the generator electron it is matched to. To illustrate this, the energy shift was compared for both samples, as shown in Fig. 7.17. The shift is calculated for selected reconstructed electrons and their generator level matching electron. A shift towards higher positive values is seen for the non-prompt case, with a mean of -0.01 compared to -0.06 for the prompt J/ψ events.

Some cuts used for the identification of electrons are more sensitive to hadron contamination in the cluster and can affect the efficiency at higher p_T . Given that the cuts are applied sequentially, we can compare the effect of each cut on the signal samples by calculating the rejection of each cut with respect to the previous cut. This rejection is defined in Eq. 7.7.

$$R_{cut} = \frac{\# \text{ of events passing cut (n-1) - } \# \text{ of events passing cut n}}{\# \text{ of events passing cut (n-1)}} \quad (7.7)$$

The result is shown in Fig. 7.18(a), where the rejection is computed sequentially, starting from electrons passing the preselection cuts i)-iii). From this plot, we see that all identification cuts reject more electrons from non-prompt J/ψ decays than

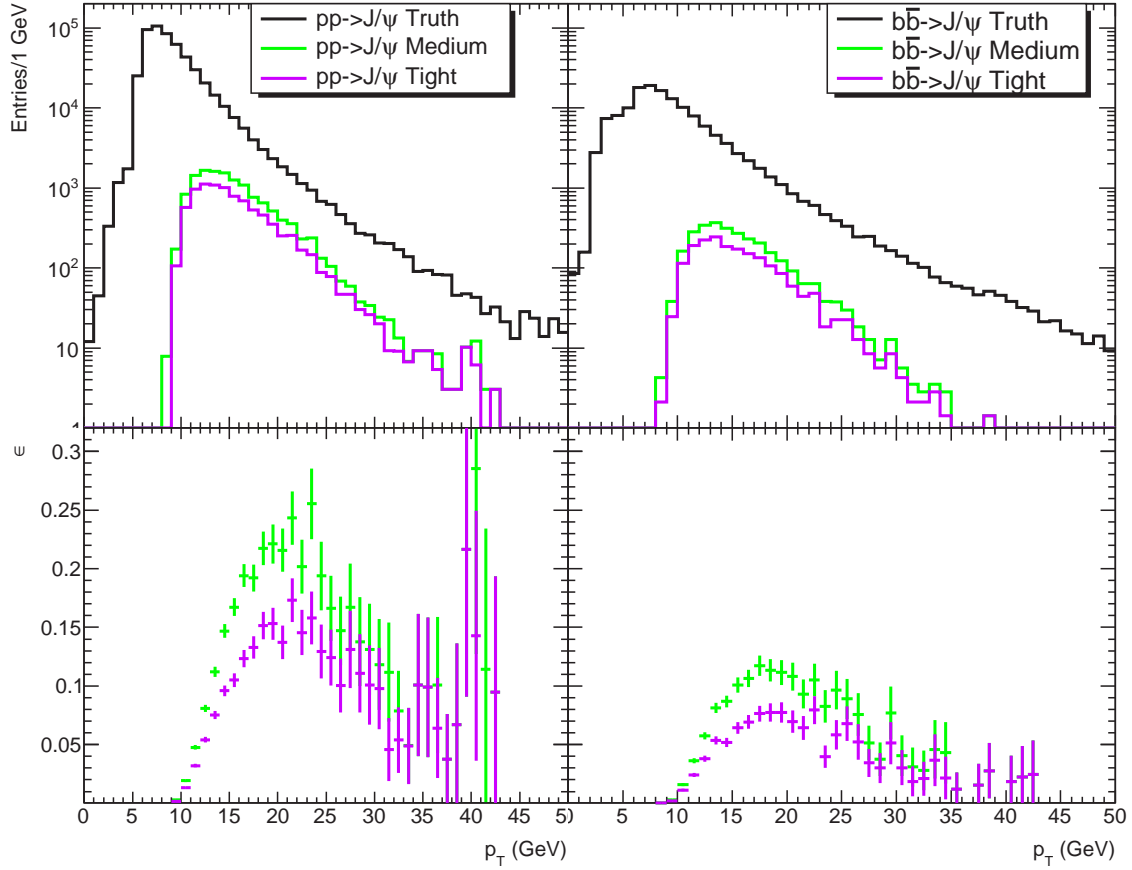


Figure 7.15: Selection efficiency as a function of the generator level p_T for the prompt (left) and non-prompt (right) signal sample. The upper plots show the dielectron p_T distribution, normalised to $\int \mathcal{L} dt = 5 \text{ pb}^{-1}$, while the lower plots show the efficiency for the medium and tight electron identification cuts. A restricted mass window of $2.5 < m_{ee} < 3.5 \text{ GeV}$ was applied.

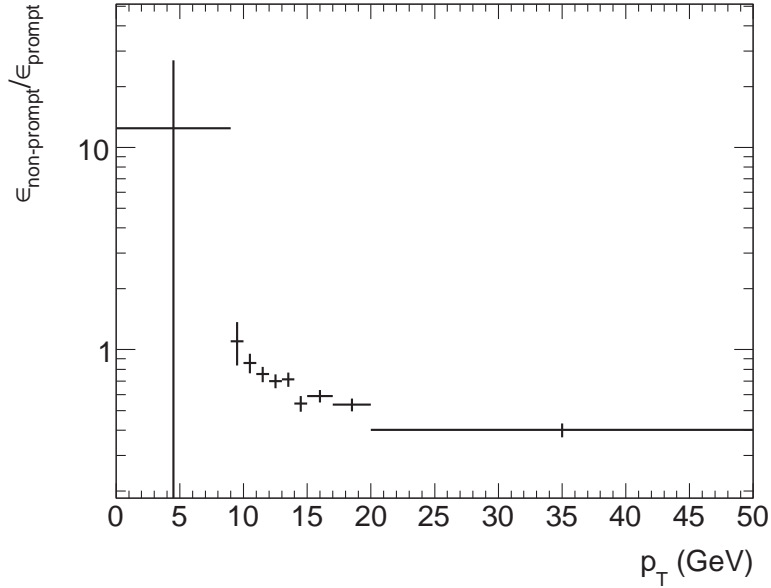


Figure 7.16: Ratio of non-prompt-to-prompt selection efficiency as a function of the generator level p_T . A restricted mass window of $2.5 < m_{ee} < 3.5$ GeV was applied.

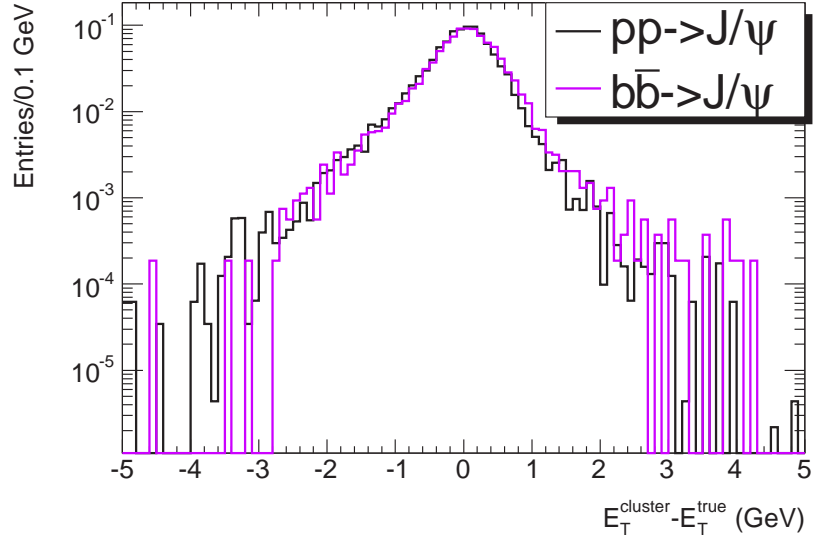
from prompt J/ψ . Moreover, the difference in the rejection between the two samples is larger for the hadronic leakage cut (R_{had}) as well as for the ratio of energy in the cluster core (R_η).

Similar results are obtained when looking at the effects of each cut individually. In this case, the rejection is computed as shown in Eq. 7.8. The values obtained are shown in Fig. 7.18(b).

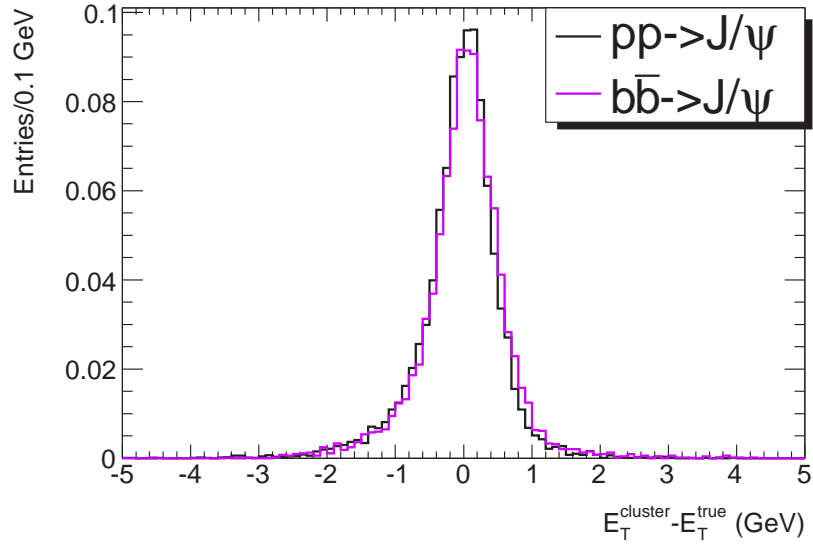
$$R_{cut}^{n-1} = \frac{\# \text{ of events passing tight while cut } n \text{ is relaxed} - \# \text{ of events passing tight}}{\# \text{ of events passing tight while cut } n \text{ is relaxed}} \quad (7.8)$$

The selection efficiencies were also calculated with respect to the pseudorapidity η and the azimuthal angle ϕ . The results are shown in Fig. 7.19 and Fig. 7.20. The same difference in overall efficiency is seen in both distributions, but the shape is similar between the two types of signal.

Trigger efficiencies are obtained after the event selection is applied, to study the effect of the trigger on selected electron pairs. Ideally, the trigger cuts should be looser than the offline cuts and should not bias the selection. The trigger efficiencies are computed using Eq. 7.9.

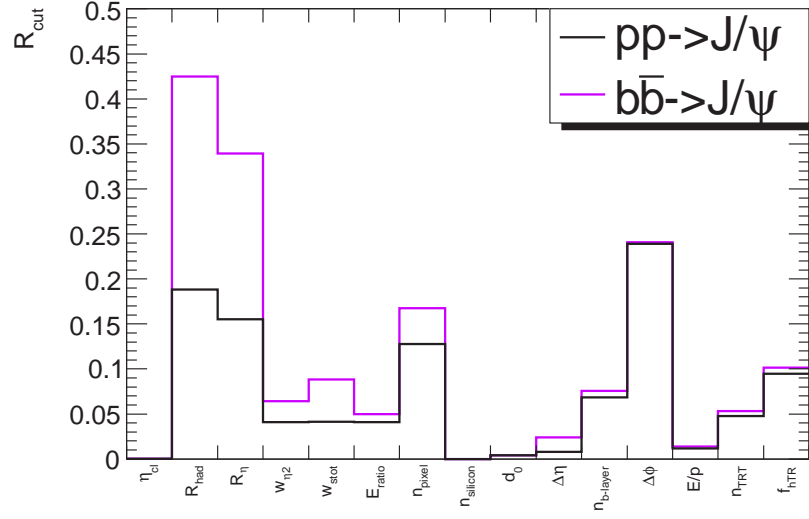


(a)

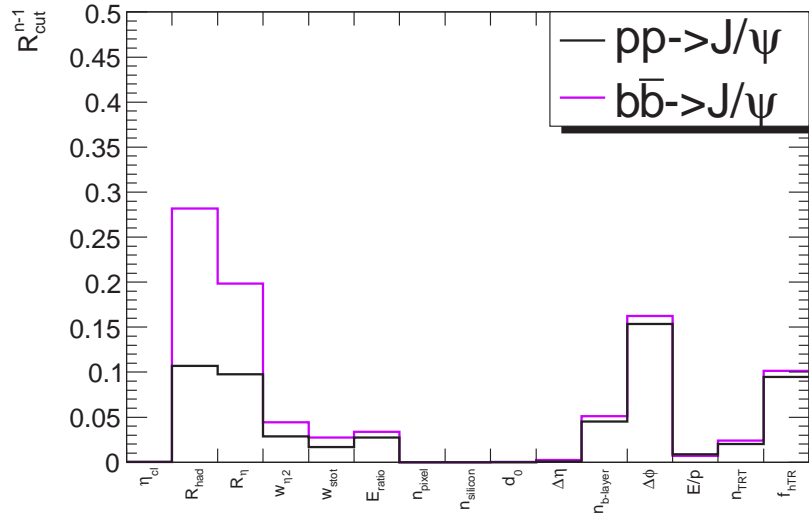


(b)

Figure 7.17: Energy shift for electrons from prompt (black line) and non-prompt (purple line) J/ψ production on (a) logarithmic and (b) linear scale. The plots are normalised to unit area.



(a)



(b)

Figure 7.18: Rejection of individual electron identification cuts for electrons from prompt (in black) and non-prompt (in purple) J/ψ . Rejection (a) for cuts applied sequentially and (b) for cuts applied individually.

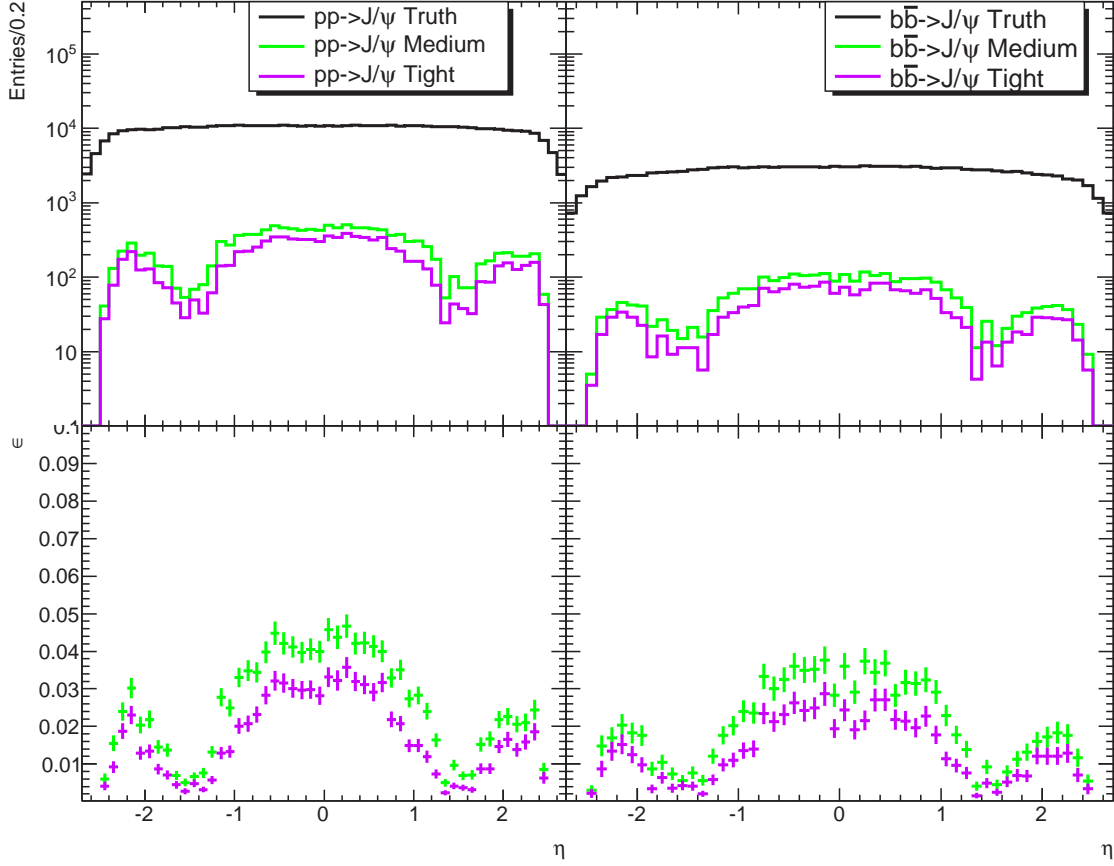


Figure 7.19: Selection efficiency as a function of the generator level η for the prompt (left) and non-prompt (right) signal sample. The upper plots show the dielectron η distribution, normalised to $\int \mathcal{L} dt = 5 \text{ pb}^{-1}$, while the lower plots show the efficiency for the medium and tight electron identification cuts. A restricted mass cut of $2.5 < m_{ee} < 3.5 \text{ GeV}$ was applied.

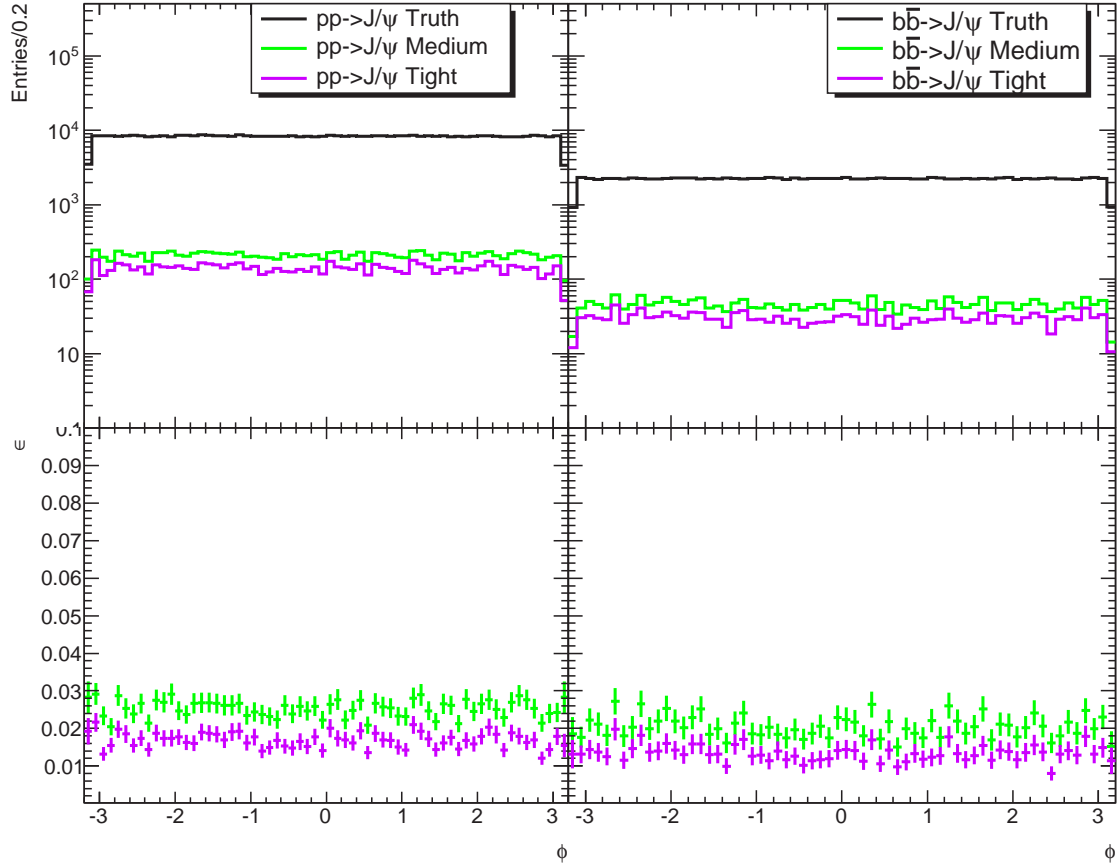


Figure 7.20: Selection efficiency as a function of the generator level ϕ for the prompt (left) and non-prompt (right) signal sample. The upper plots show the dielectron ϕ distribution, normalised to $\int \mathcal{L} dt = 5 \text{ pb}^{-1}$, while the lower plots show the efficiency for the medium and tight electron identification cuts. A restricted mass cut of $2.5 < m_{ee} < 3.5 \text{ GeV}$ was applied.

$$\epsilon_{trig} = \frac{\# \text{ of selected events passing } 2e5 \text{ trigger chain and trigger-offline matching}}{\# \text{ of selected events without trigger requirement}} \quad (7.9)$$

Two types of selection are used: the *tight* selection, where cuts i)-viii) and x) are required and the *reco* selection, where only the preselection cuts, i.e. i)-iii), are required. The L1 efficiency is computed with a different trigger-offline object matching requirement than the one used for the EF selection, described in §7.2.2: the ΔR is calculated from the cluster quantities, a cut of $\Delta R \leq 0.16$ between the offline and trigger object is applied and the event is only required to pass the 2EM3 trigger signature. The results are shown in Fig. 7.21 for the reco selection and in Fig. 7.22 for tight selection, with respect to the refitted dielectron p_T .

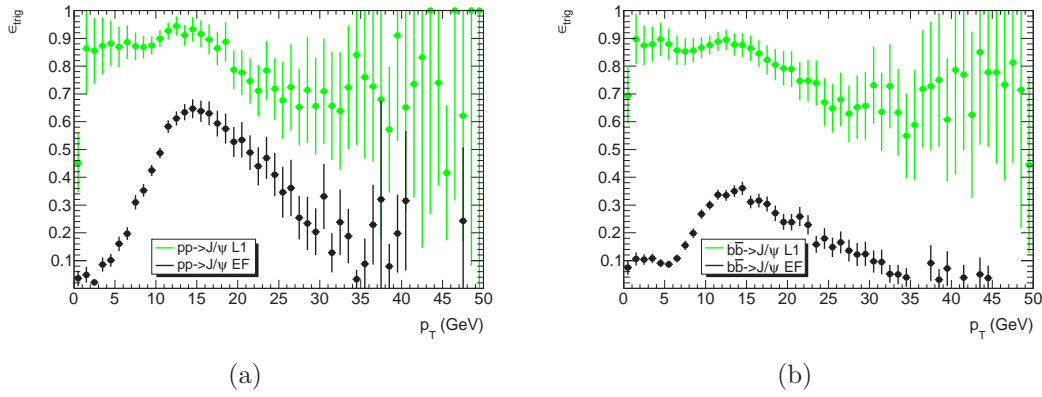


Figure 7.21: Trigger efficiencies after reconstruction for electrons pairs from (a) prompt J/ψ and (b) non-prompt J/ψ . The L1 efficiency is shown in green while the EF efficiency is shown in black.

At the reconstruction level, the L1 efficiency exhibits a much flatter distribution than the EF efficiency. Moreover, the ratio between the non-prompt and prompt efficiency at L1 is much closer to one, suggesting that the selection can be improved to have a more similar response from the two contributions. The shape observed at higher p_T values in the L1 efficiency is explained by the decreased angular distance between the electrons in the pair; the size of the L1 RoI exceeds this distance and this creates inefficiencies. The turn-on effect of the 2e5 trigger chain is spread between 5 and 12 GeV due to the dielectron pairing. A plateau is reached around 12 GeV, followed by a drop in efficiency for higher p_T . This is the same effect as seen in the selection efficiency, traced back to some electron identification variables which are more sensitive to hadron contamination. The same variables, R_{had} and R_η , are actually used by the L2 trigger, as described in §6.7. In a few cases, and only for

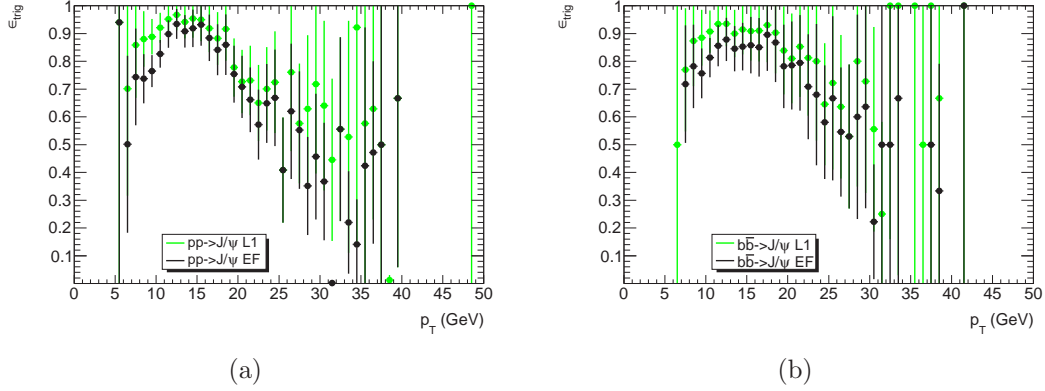


Figure 7.22: Trigger efficiencies after event selection for electrons pairs from (a) prompt J/ψ and (b) non-prompt J/ψ . The L1 efficiency is shown in green while the EF efficiency is shown in black.

the non-prompt contribution, the L1 efficiency is lower than the EF efficiency. This is caused by the splitting of trigger RoIs at L2, as explained in §6.7. For the non-prompt J/ψ contribution, other physical objects in the event can create a L1 trigger cluster, hence making the event pass the L1_2EM3 signature, even though only one RoI originates from the collimated electrons from J/ψ . The offline electrons are therefore matched in ΔR to the same L1 RoI, as this is allowed by the trigger-offline matching procedure used in this analysis. In these rare cases, the trigger-offline object matching requirement might not be fulfilled at L1, but will be for EF, hence creating this behaviour.

7.4.2 Invariant mass fit

To determine the width of the J/ψ peak, a Crystal Ball function [118], defined in Eq. 7.10, is used to describe the signal shape. It represents a Gaussian peak along with a radiative tail at low mass due to electron bremsstrahlung.

$$f(x; \alpha, n, \mu, \sigma) = N \cdot \begin{cases} e^{-\frac{(x-\mu)^2}{2\sigma^2}} & \text{if } \frac{x-\mu}{\sigma} \geq -\alpha, \\ \left[\left(\frac{n}{|\alpha|} \right)^n e^{-\frac{|\alpha|^2}{2}} \right] \cdot \left[\frac{n}{|\alpha|} - |\alpha| - \frac{x-\mu}{\sigma} \right]^{-n} & \text{if } \frac{x-\mu}{\sigma} < -\alpha. \end{cases} \quad (7.10)$$

The results of the fit of the sum of a linear background and the signal shape are shown in Fig. 7.23. We obtain a width of 136 ± 8 MeV and a mass of 3.082 ± 0.008 GeV.

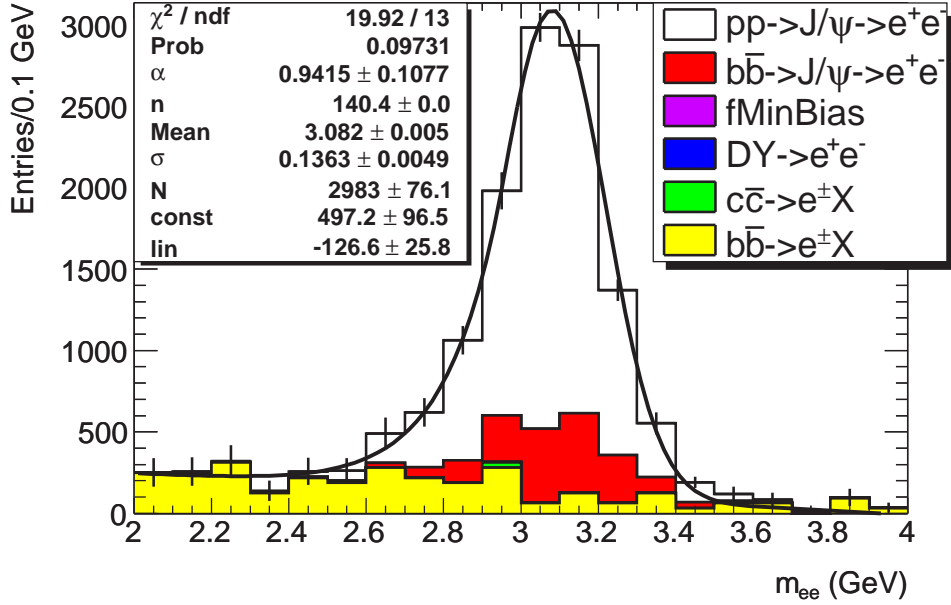


Figure 7.23: Fitted invariant mass distribution, normalised to $\int \mathcal{L} dt = 5 \text{ pb}^{-1}$, with a Crystal Ball function used for the signal shape for inclusive J/ψ production. The fit results are shown on the plots.

7.4.3 Background subtraction

Before estimating the fraction of prompt and non-prompt J/ψ decays, it is necessary to perform background subtraction on the selected electron pair events. A simple sideband subtraction is applied to the events in the selected mass region $2 < m_{ee} < 4 \text{ GeV}$. Assuming that the background is linear in the mass region of interest, we choose two symmetric intervals, $2 < m_{ee} < 2.5 \text{ GeV}$ and $3.5 < m_{ee} < 4 \text{ GeV}$, around the core of this mass region, as shown in Fig. 7.24(a). The linearity of the background events is shown in Fig. 7.24(b), where a linear function is fitted to the background events in the mass region of interest.

In forming kinematic distributions, the events in the shaded sideband regions, which are mostly background, are weighted with a negative value, hence compensating for the background events located in the core mass region, which are weighted with a positive value. The absolute value of the weight depends on the sample: for the prompt J/ψ sample, the event weights defined in Table 7.3 are used, while the value of their specific luminosity normalisation factor is used for all other samples. A cross-check is performed to verify the linearity of the subtraction: the number of events with negative weight should be equal, within statistical uncertainty, to the number of events with positive weight. This is verified for all background samples combined

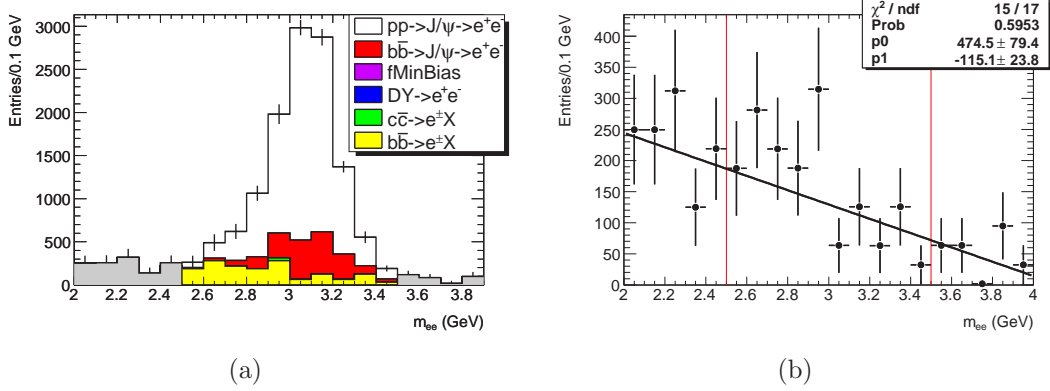


Figure 7.24: (a) Dielectron invariant mass distribution showing the mass regions used for the sideband background subtraction. (b) Linear fit to the sum of all backgrounds in the mass region of interest. Both plots are normalised to $\int \mathcal{L} dt = 5 \text{ pb}^{-1}$.

with 1411 ± 209 events with negative weight and 1600 ± 222 events with positive weight.

The distributions of dielectron kinematical quantities before and after background subtraction are shown in Fig. 7.25, for all the background samples combined and scaled to $\int \mathcal{L} dt = 5 \text{ pb}^{-1}$. The distributions for the pseudo-proper time (defined in §7.4.4), in Fig. 7.25(a), the dielectron p_T , in Fig. 7.25(b), the dielectron η , in Fig. 7.25(c) and the dielectron ϕ , in Fig. 7.25(d) are shown here for the loose identification cuts and without trigger requirements, due to low statistics for tighter cuts. The means are consistent with 0 for all quantities, indicating that the procedure works as expected.

In order to estimate the number of signal events for $\int \mathcal{L} dt = 5 \text{ pb}^{-1}$, we use the result of the background subtraction method described above. It allows us to obtain a measurement for the inclusive number of signal events, i.e. the sum of the prompt and the non-prompt J/ψ contributions, in the signal region, which is $2.5 < m_{ee} < 3.5 \text{ GeV}$. The inclusive number of events is used in §7.4.5 to obtain the prompt and the non-prompt cross-sections separately.

The expected yields of events in the different mass ranges are listed in Table 7.16. The number of signal events in the sidebands accounts for 1.5% of the total inclusive number of signal events. After background subtraction, we obtain 10811 ± 339 events for the inclusive J/ψ selection, which is in agreement with the expected value.

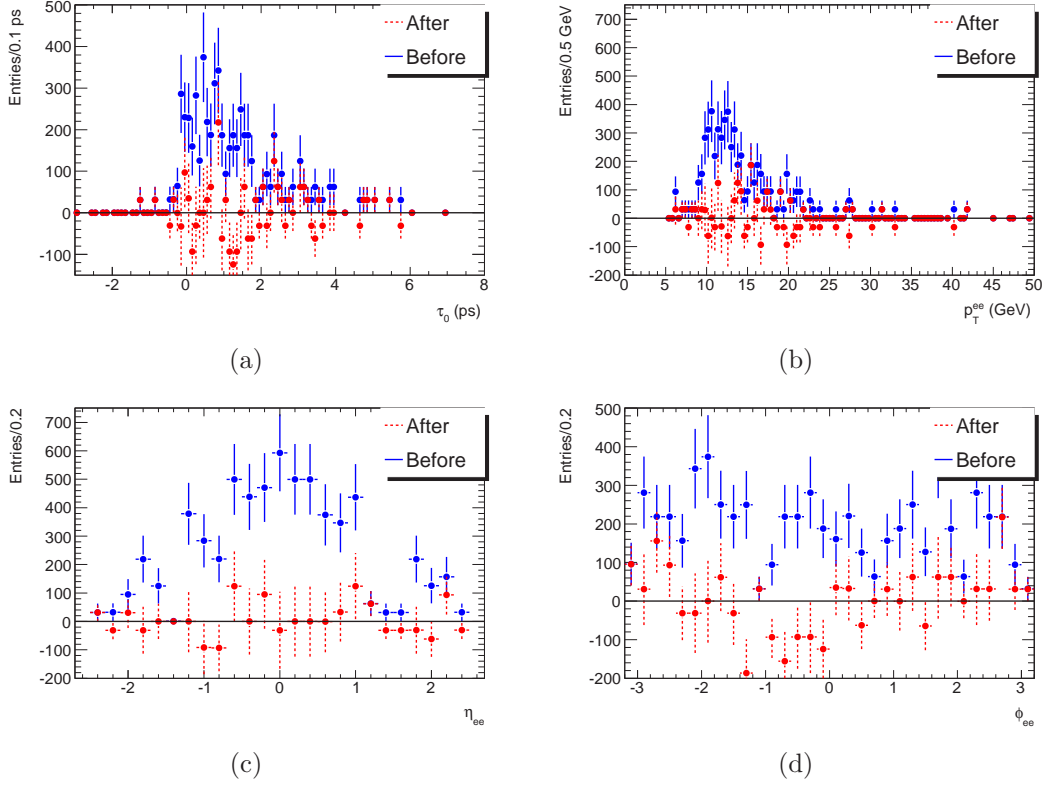


Figure 7.25: Dielectron reconstructed distributions, normalised to $\int \mathcal{L} dt = 5 \text{ pb}^{-1}$, for the background contributions after sideband subtraction. (a) Pseudo-proper time, (b) transverse momentum, (c) pseudorapidity and (d) azimuthal angle distributions are shown before subtraction in solid blue and after subtraction in dashed red. The loose identification cuts are used here, without trigger requirement to increase the available statistics.

	$2 < m_{ee} < 4 \text{ GeV}$	$2.5 < m_{ee} < 3.5 \text{ GeV}$
Prompt signal	9016	8886
Non-prompt signal	1937	1902
Total	10953	10788

Table 7.16: Expected yields of signal events for $\int \mathcal{L} dt = 5 \text{ pb}^{-1}$.

7.4.4 Prompt and non-prompt fraction estimation

B hadrons decay via weak interactions, which gives them a longer lifetime in the detector than light hadrons. The proper decay time is normally calculated from the kinematics of the decaying B hadron. In the present case, we use the kinematics of the decay product, the J/ψ meson, to estimate the B hadron properties. Therefore, a variable, called the *pseudo-proper time* [21], is used for this analysis and is defined in Eq. 7.11, where L_{xy} is the decay length in the transverse plane¹⁰ of the J/ψ , p_T is its transverse momentum, $M=3.096$ GeV is the PDG value for J/ψ mass [13] and c is the speed of light in vacuum.

$$\tau_0 = \frac{L_{xy} \cdot M}{p_T \cdot c} \quad (7.11)$$

The resulting distribution for all samples is shown in Fig. 7.26. In an attempt to separate the prompt contribution, a new cut is investigated on the pseudo-proper time. Based on the shape of the τ_0 distribution, we place the cut at $\tau_0 < 0.5$ ps. This cut has an efficiency of $97.6 \pm 0.2\%$ on the prompt J/ψ sample and $31.1 \pm 0.9\%$ on the non-prompt J/ψ sample. As the numbers in Table 7.16 show, this cut leads to a $6.4 \pm 0.3\%$ contamination of non-prompt signal events in the sample, which is clearly visible in the invariant mass distribution, shown in Fig. 7.27. Therefore, such a cut is not used to estimate the prompt cross-section.

	$2 < m_{ee} < 4$ GeV	$2.5 < m_{ee} < 3.5$ GeV
Prompt signal for $\tau_0 < 0.5$ ps	8797	8671
Non-prompt signal for $\tau_0 < 0.5$ ps	601	590
Total	9398	9261

Table 7.17: Expected yields of signal events for $\int \mathcal{L} dt = 5 \text{ pb}^{-1}$. Numbers are given before and after the pseudo-proper time cut.

When a cut on τ_0 is applied, 9002 ± 217 events are measured, which is smaller but still compatible with the expected value of 9261. This comes from the fact that the τ_0 cut removes more background events in the signal region than in the sidebands.

The measured number of events after the τ_0 cut is not used in further calculations. Instead, the distribution for the pseudo-proper time is fitted to the function shown in Eq. 7.12 [119]. This function represents the sum of a δ -function and an exponential part, smeared with a normalised Gaussian function. The first term describes the prompt J/ψ events while the non-prompt J/ψ contribution is described by the second term. Four parameters are fitted from the function: the resolution σ of the Gaussian

¹⁰The definition for L_{xy} is given in Appendix D.

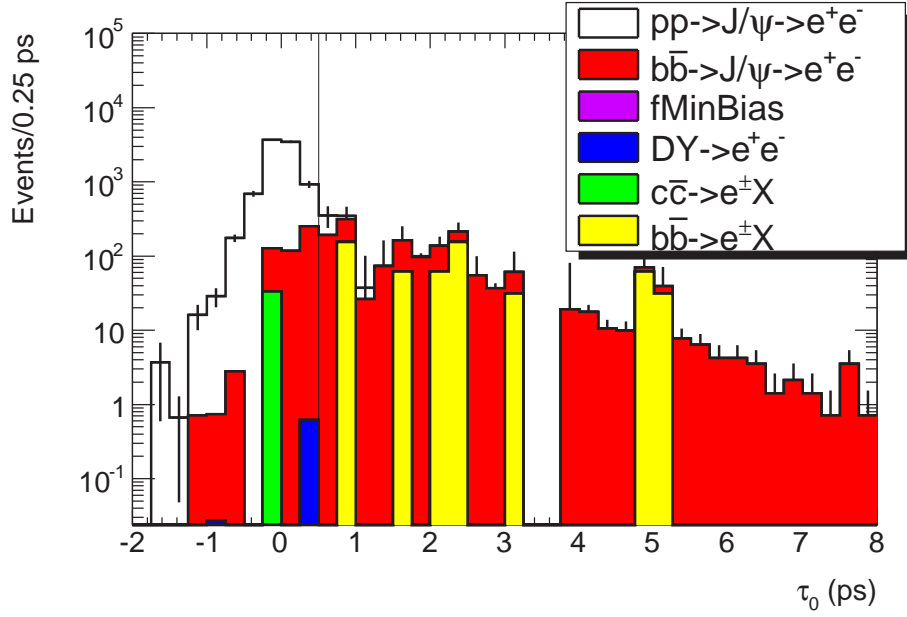


Figure 7.26: Pseudo-proper time distribution for all the samples, normalised to $\int \mathcal{L} dt = 5 \text{ pb}^{-1}$. The black vertical line indicates the cut value used to select the prompt contribution.

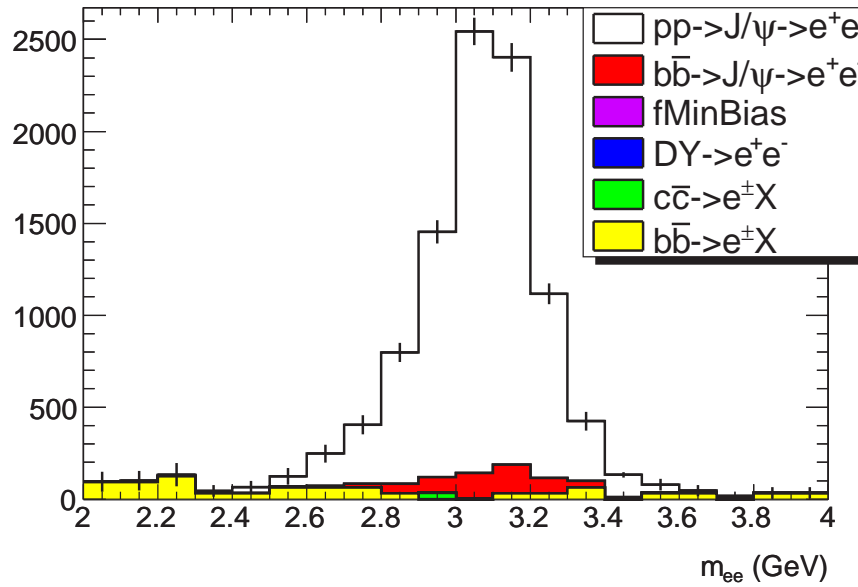


Figure 7.27: Invariant mass distribution with signal shape after τ_0 cut, normalised to $\int \mathcal{L} dt = 5 \text{ pb}^{-1}$. No background subtraction is used here.

function, the slope Γ of the exponential part, a normalisation constant C and \mathcal{R} , the ratio of the non-prompt-to-prompt J/ψ cross-sections.

$$f(\tau_0) = \frac{C}{\sqrt{2\pi}\sigma} \exp\left(-\frac{\tau_0^2}{2\sigma^2}\right) + \mathcal{R} \cdot C \cdot \Gamma \cdot \exp\left(\frac{\Gamma^2\sigma^2}{2} - \Gamma\tau_0\right) \cdot \frac{1}{2} \left[1 + \operatorname{erf}\left(\frac{\tau_0 - \Gamma\sigma^2}{\sqrt{2}\sigma}\right)\right] \quad (7.12)$$

Since the ratio of efficiencies between the non-prompt and the prompt contributions is different from one, the fitted value for \mathcal{R} actually reflects the ratio between the observed number of events for the two contributions. The fitted pseudo-proper time distribution using only the selected events from the prompt and the non-prompt signal samples is shown in Fig. 7.28. The function is fitted in the range $\tau_0 = -0.5$ to 8 ps. A value of 0.25 ± 0.01 for \mathcal{R} is obtained from the fit. The p_T dependence for \mathcal{R} is shown in §7.4.6.

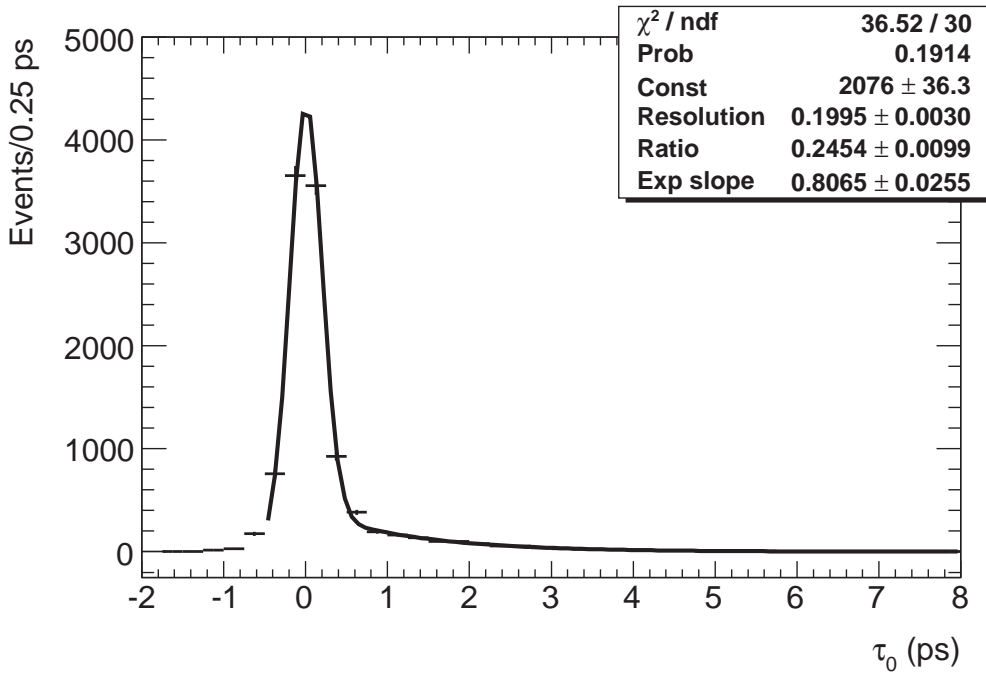


Figure 7.28: Fitted pseudo-proper time distribution for the signal samples, normalised to $\int \mathcal{L} dt = 5 \text{ pb}^{-1}$.

In order to cross-check the value obtained for the ratio \mathcal{R} using signal samples, we calculate the expected value after the full selection from Table 7.16. We obtain

that $\mathcal{R}_{expected}=0.214 \pm 0.004$. It is clear that the value obtained from the signal-only fit overestimates the ratio of non-prompt-to-prompt event numbers. A correction, based on simulation, then needs to be applied to compensate for this effect. A linear correction is obtained by modifying the ratio, using predetermined values, between the prompt and the non-prompt contributions in the simulation and fitting the resulting distributions to obtain \mathcal{R} . To extract \mathcal{R}_{corr} , the corrected ratio, from \mathcal{R}_{fit} , the fitted value, we use the correction function shown in Eq. 7.13. Given its shortcomings, the whole correction is considered as a systematic uncertainty in §8.4.

$$\mathcal{R}_{corr} = \frac{\mathcal{R}_{fit} - (0.02)}{1.05} \quad (7.13)$$

We can correct the signal-only value using the result above and we obtain 0.22 ± 0.02 , which now agrees with $\mathcal{R}_{expected}$. The same correction is then applied to the global pseudo-proper time fit, including background contributions.

The fitted pseudo-proper time distribution after applying sideband subtraction is shown in Fig. 7.29. A value of 0.24 ± 0.03 for \mathcal{R} is obtained from the fit. Using the correction of Eq. 7.13, we obtain that $\mathcal{R}_{corr} = 0.21 \pm 0.03$.

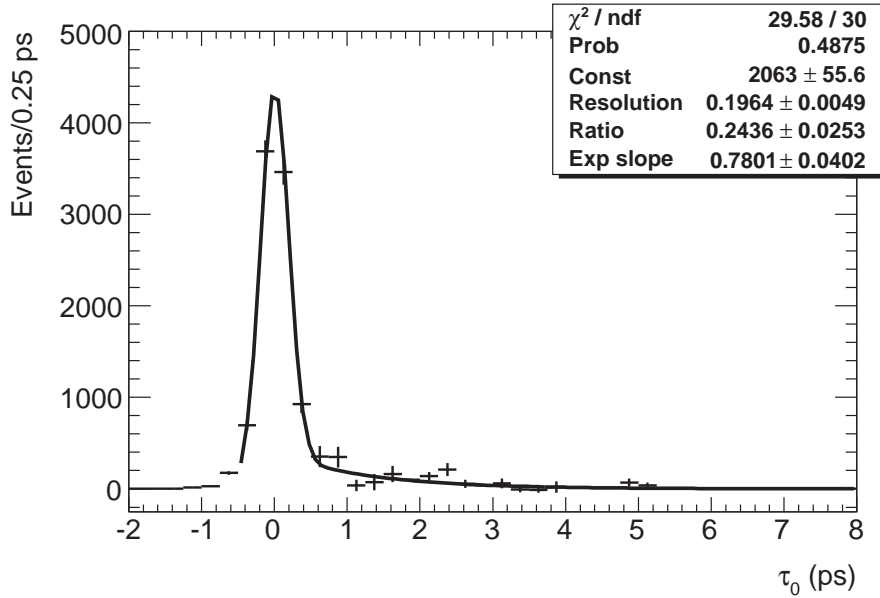


Figure 7.29: Fitted pseudo-proper time distribution for all samples, normalised to $\int \mathcal{L} dt = 5 \text{ pb}^{-1}$. The fit results are shown on the plot.

7.4.5 Total fiducial prompt and non-prompt J/ψ cross-sections

With the knowledge of all the quantities mentioned above, listed in Table 7.18, we obtain a final result for both the prompt (σ_p) and non-prompt (σ_{np}) J/ψ cross-sections, within the fiducial acceptance of the MultiLepton filter ($E_T^{electron} > 3$ GeV, $|\eta^{electron}| < 2.7$). We derive the expression to use for each of the cross-sections as follows.

Quantity	Value
Inclusive number of signal events (N)	10811 ± 339
Selection efficiency for prompt J/ψ (ϵ_p)	0.0169 ± 0.0002
Selection efficiency for non-prompt J/ψ (ϵ_{np})	0.0135 ± 0.0003
Non-prompt-to-prompt ratio \mathcal{R}	0.21 ± 0.03
Signal-to-background ratio	6.7 ± 0.9

Table 7.18: Results summary for the cross-section calculation. The quantities, given here for $\int \mathcal{L} dt = 5 \text{ pb}^{-1}$, are defined in the text.

$$\begin{aligned} \sigma_p &= \frac{N_p}{\epsilon_p \mathcal{L}} \\ &= \frac{N}{(1 + \mathcal{R})\epsilon_p \mathcal{L}} \end{aligned} \tag{7.14}$$

$$\begin{aligned} \sigma_{np} &= \frac{N_{np}}{\epsilon_{np} \mathcal{L}} \\ &= \frac{N\mathcal{R}}{(1 + \mathcal{R})\epsilon_{np} \mathcal{L}} \end{aligned} \tag{7.15}$$

In the above expressions, ϵ_p is the efficiency and N_p is the number of events measured for the prompt J/ψ signal, ϵ_{np} is the efficiency and N_{np} is the number of events measured for the non-prompt J/ψ signal, N is the measured inclusive number of events and \mathcal{L} is the luminosity, which is set to 5 pb^{-1} in this analysis. Eq. 7.14 and Eq. 7.15 assume that $\mathcal{R} = N_{np}/N_p$ to obtain expressions for the two cross-sections separately from a single measurement of the inclusive number of events. A value of 106 ± 4 (stat.) nb is obtained for the prompt cross-section and 28 ± 1 (stat.) nb for the non-prompt cross-section. These results are in good agreement with the predicted PYTHIA values of 105.5 ± 0.4 (stat.) nb and 28.3 ± 0.3 (stat.) nb for the prompt and non-prompt cross-sections, respectively, which serves to validate the method used in this analysis to compute the J/ψ cross-section. The p_T dependence of the cross-section is described in §7.4.6.

7.4.6 Differential prompt and non-prompt J/ψ cross-sections

We calculate the value for the cross-sections in 8 bins of J/ψ p_T , starting from 10 GeV. The ranges are chosen such that the statistics of signal events, both prompt and non-prompt, is similar in all bins. The threshold in p_T is chosen to account for the efficiency shape described in §7.4.1. The cross-section is evaluated using the same method as described in §7.4.5. The different parameters involved in the calculation are evaluated for each bin, such as the number of signal events and the fitted value of \mathcal{R} in all bins. The correction function for \mathcal{R} defined in Eq. 7.13 is used in all bins. The results, together with the expected values, are shown in Fig. 7.30.

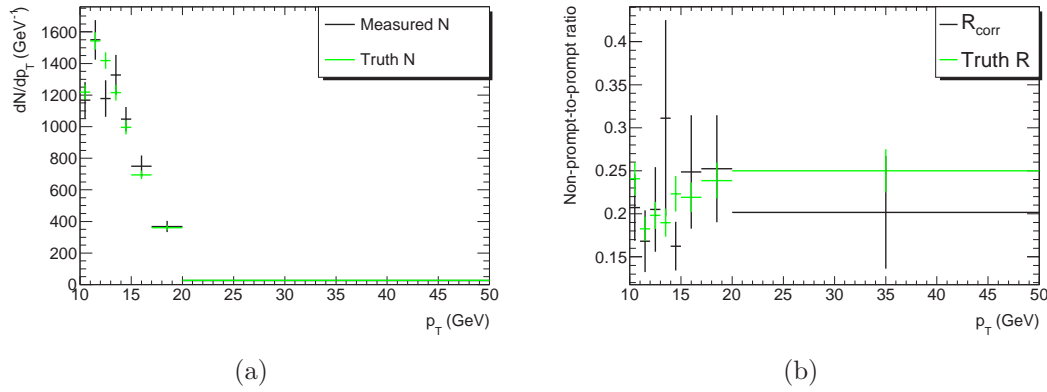


Figure 7.30: (a) Inclusive number of events, normalised to $\int \mathcal{L} dt = 5 \text{ pb}^{-1}$, and (b) corrected \mathcal{R} values in reconstructed p_T bins. The truth values are overlaid in green.

In order to correct for the detector resolution and efficiencies with respect to the generator in all bins, an unfolding procedure is applied, using the RooUnfold [120] package. The bin-by-bin method is used here in order to account correctly for the p_T bin migration which is important when the difference between the reconstructed and the generator level p_T is larger than the chosen bin size. This difference computed for the present analysis is discussed in §7.2 and shown in Fig. 7.4. The unfolding is done separately for the prompt and non-prompt samples. Using the expressions of Eq. 7.14 and Eq. 7.15 to calculate the prompt and non-prompt J/ψ cross-sections, respectively, we first obtain the measured distributions of the number of events for each signal contributions in Fig. 7.31(a) and Fig. 7.31(c), compared with the corresponding PYTHIA prediction. These distributions are given as input to the unfolding procedure to obtain the measured distributions of Fig. 7.31(b) and Fig. 7.31(d), also compared to the generator level p_T spectrum. The distributions of Fig. 7.31 are all divided by the bin width. We can see that, both before and after the unfolding, the bins showing the largest discrepancy between the measured value and the PYTHIA

prediction are centered around the 12–13 GeV bin, which comes from the discrepancy observed for \mathcal{R} in Fig. 7.30(b). The unfolded number of events, hence corrected for the efficiency in each bin, is divided by the chosen luminosity ($\int \mathcal{L} dt = 5 \text{ pb}^{-1}$) to obtain the cross-section. The production cross-section is then obtained after dividing by the MultiLepton efficiency in p_T bins. The filter efficiency curve is shown in Fig. 7.32 for the prompt and non-prompt cases.

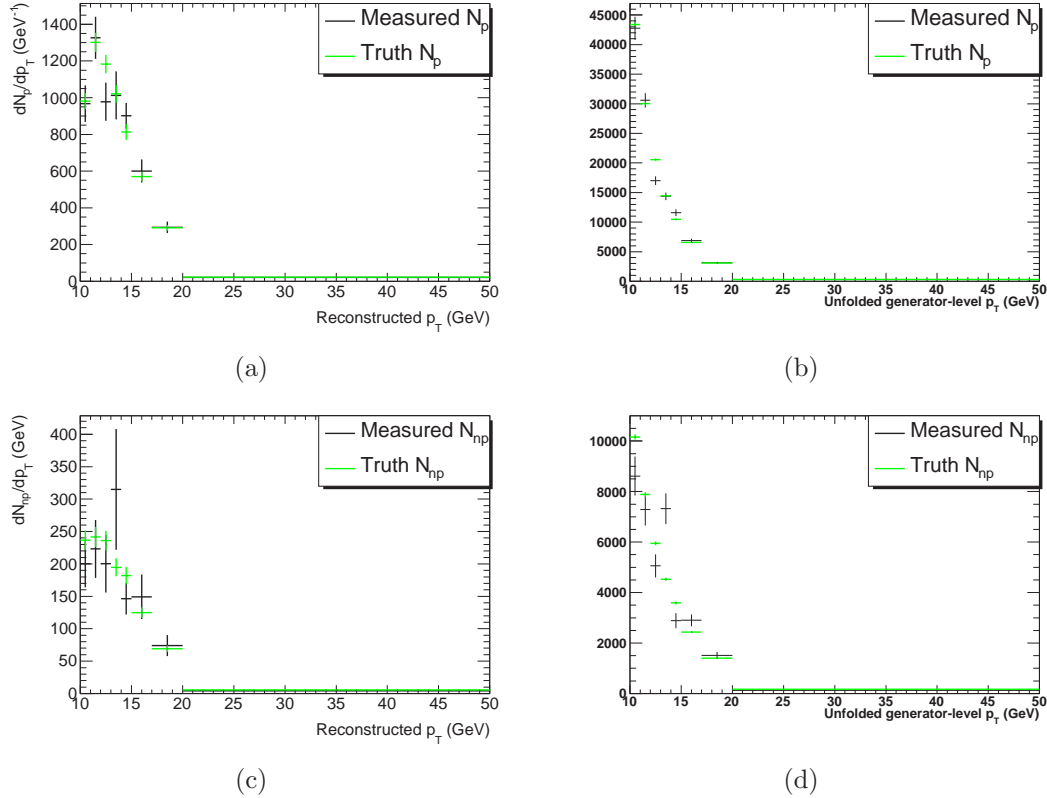
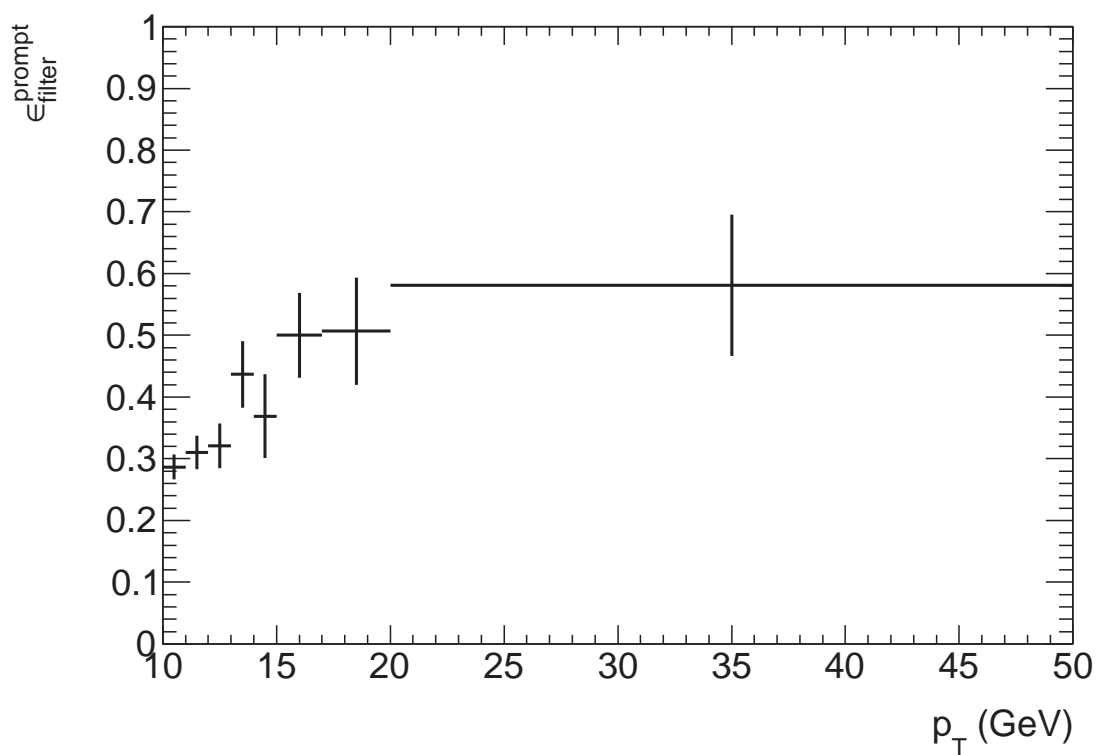
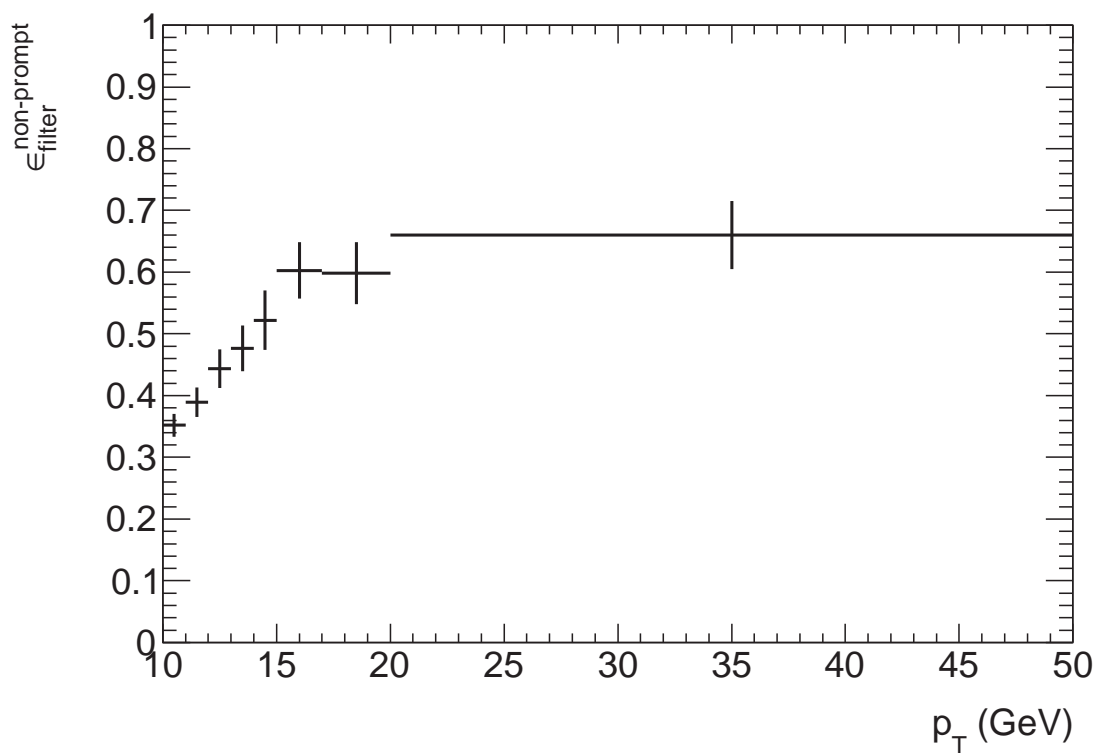


Figure 7.31: p_T distributions before and after unfolding, normalised to $\int \mathcal{L} dt = 5 \text{ pb}^{-1}$. The top plots show the prompt sample distributions for: (a) refitted dielectron p_T and (b) unfolded p_T . The bottom plots show the non-prompt sample distributions for: (c) refitted dielectron p_T and (d) unfolded p_T .

The obtained J/ψ production cross-sections are listed in Table 7.19, along with the expected values. The values for the quantities used in bins are listed in Table 7.20. The prompt and non-prompt J/ψ production cross-sections obtained from the inclusive number of events measured are shown in Fig. 7.33, together with the computed PYTHIA prediction. Since we use variable bin width in p_T , the cross-section value is divided by the bin width. The shape agrees well in both prompt and non-prompt



(a)



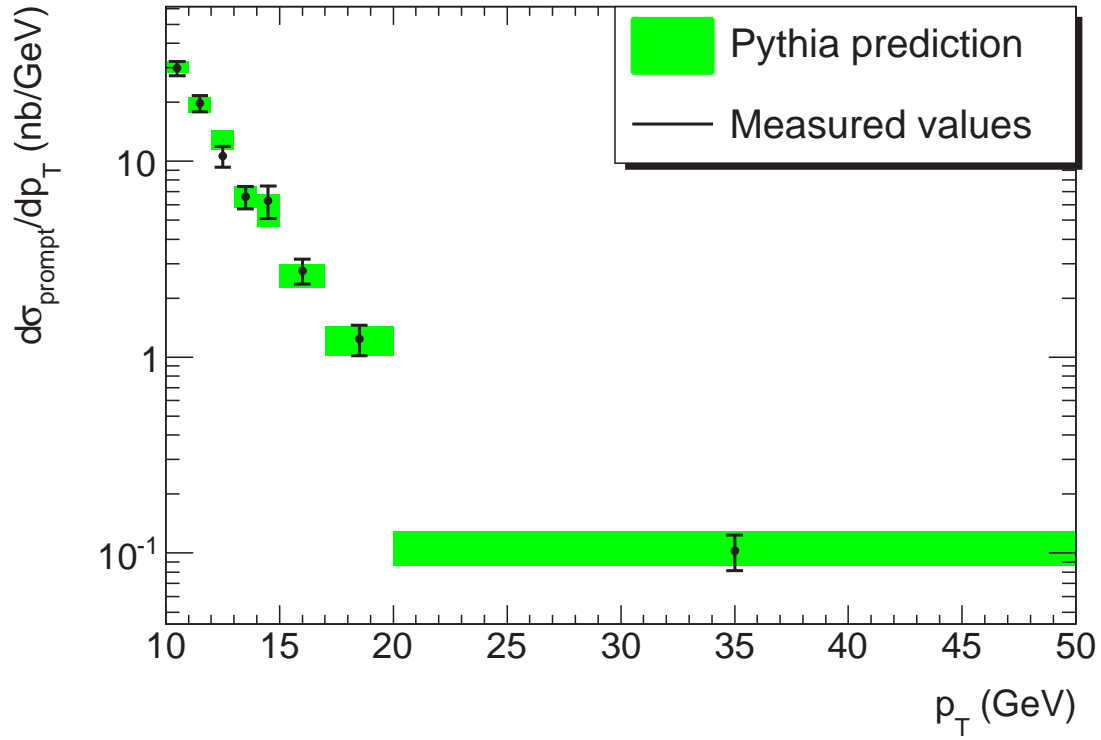
(b)

Figure 7.32: MultiLepton filter efficiency as a function of the generator level J/ψ p_T for (a) the prompt and (b) the non-prompt case.

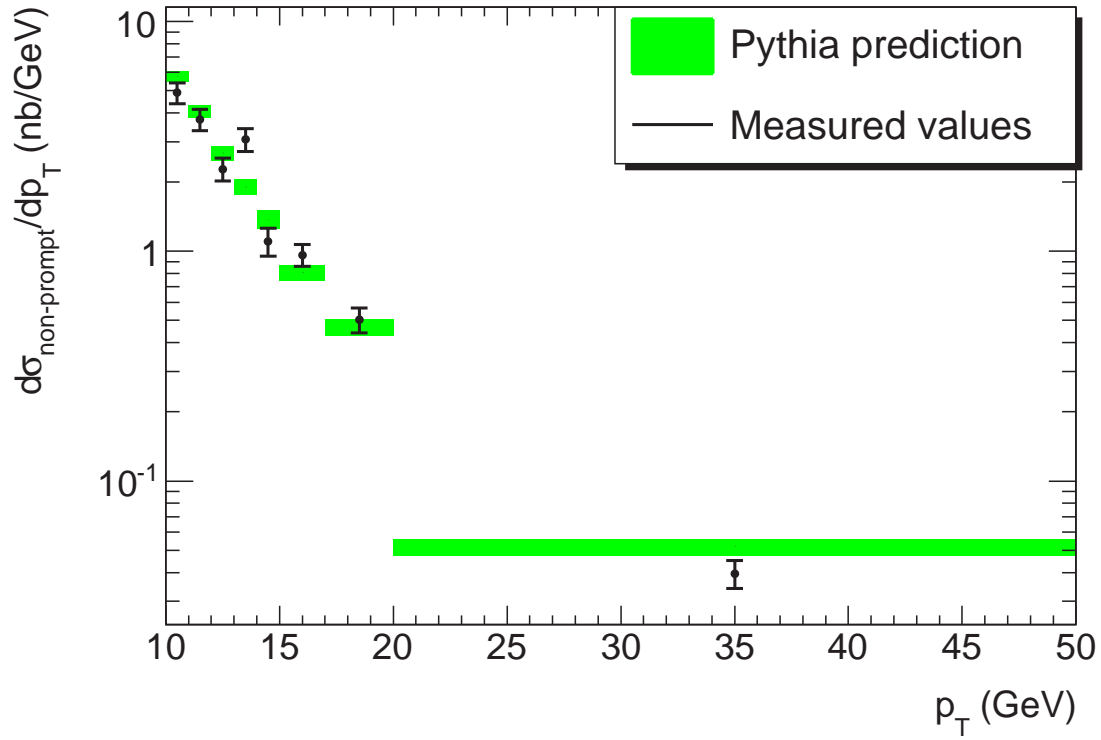
cases with the theory prediction. A good agreement is seen within statistical errors between the PYTHIA prediction and the production cross-section for the prompt and the non-prompt contributions. Since the efficiencies are drastically reduced at low p_T , especially in the two first bins, we compute the total cross-sections for $p_T > 10$ GeV by integrating the corresponding bins from the differential calculation. We obtain 85 ± 4 (stat.) nb for the prompt and 19.7 ± 0.8 (stat.) nb for the non-prompt production cross-sections in this p_T range. Both cross-sections are in agreement with the expected values of 87 ± 3 (stat.) nb and 20.4 ± 0.5 (stat.) nb for the prompt and non-prompt contributions, respectively. These production cross-section cannot be compared to the previous results for the fiducial cross-sections in §7.4.5 since the effect of the generator level filter is removed here.

p_T range (GeV)	$d\sigma_{\psi}/dp_T$ (nb/GeV)		$d\sigma_{n\psi}/dp_T$ (nb/ GeV)	
	Estimated	Expected	Estimated	Expected
10–11	30 ± 2	30 ± 2	4.9 ± 0.5	5.8 ± 0.3
11–12	20 ± 2	19 ± 2	3.7 ± 0.4	4.1 ± 0.3
12–13	11 ± 1	13 ± 1	2.3 ± 0.3	2.7 ± 0.2
13–14	6.6 ± 0.9	6.6 ± 0.8	3.1 ± 0.4	1.9 ± 0.2
14–15	6 ± 1	6 ± 1	1.1 ± 0.2	1.4 ± 0.1
15–17	2.8 ± 0.4	2.6 ± 0.4	1.0 ± 0.1	0.81 ± 0.06
17–20	1.2 ± 0.2	1.2 ± 0.2	0.50 ± 0.06	0.47 ± 0.04
20–50	0.10 ± 0.02	0.11 ± 0.02	0.040 ± 0.005	0.052 ± 0.004

Table 7.19: Differential prompt and non-prompt J/ψ production cross-sections results.



(a)



(b)

Figure 7.33: Differential (a) prompt and (b) non-prompt production cross-sections as a function of the generator level J/ψ p_T . The PYTHIA predictions are overlaid in green.

p_T range (GeV)	N	\mathcal{R}	ϵ_p (%)	ϵ_{np} (%)	ϵ_{filter}^p	ϵ_{filter}^{np}	s_B ratio
10–11	1168 ± 114	0.21 ± 0.04	1.31 ± 0.05	1.1 ± 0.1	0.29 ± 0.02	0.35 ± 0.02	8 ± 3
11–12	1550 ± 125	0.17 ± 0.04	3.2 ± 0.1	2.4 ± 0.2	0.31 ± 0.03	0.39 ± 0.02	7 ± 3
12–13	1178 ± 116	0.20 ± 0.05	5.4 ± 0.2	3.8 ± 0.2	0.32 ± 0.04	0.44 ± 0.03	22 ± 15
13–14	1328 ± 127	0.3 ± 0.1	7.5 ± 0.2	5.3 ± 0.3	0.44 ± 0.05	0.48 ± 0.04	4 ± 1
14–15	1047 ± 77	0.16 ± 0.03	9.6 ± 0.3	5.2 ± 0.4	0.37 ± 0.07	0.52 ± 0.05	11 ± 6
15–17	1499 ± 136	0.25 ± 0.07	11.3 ± 0.3	6.7 ± 0.4	0.50 ± 0.07	0.60 ± 0.05	4 ± 1
17–20	1104 ± 105	0.25 ± 0.06	14.4 ± 0.4	7.6 ± 0.4	0.51 ± 0.09	0.60 ± 0.05	7 ± 3
20–50	766 ± 88	0.20 ± 0.07	13.0 ± 0.3	5.2 ± 0.3	0.6 ± 0.1	0.66 ± 0.06	13 ± 9

Table 7.20: Results summary in p_T bins for the cross-section calculation. The signal-to-background (s_B) ratio is indicated here for reference.

CHAPTER 8

Evaluation of systematic uncertainties

*Every detection of what is false
directs us towards what is true:
every trial exhausts some
tempting form of error.*

- William Whewell

Measurements always come with uncertainties, which are of two kinds: *statistical*, which comes from the random fluctuations occurring when repeating an experiment several times (in our case, a p - p collision) and *systematic*, which means to account for possible biases in the measurement procedure. Statistical uncertainties are listed together with the measured values in §7. Systematic uncertainties, on the other hand, can come from various sources that need to be estimated individually and then added in quadrature, assuming they are uncorrelated.

In the following, the possible sources of systematic uncertainties for the cross-section calculation are listed and a selection of them are estimated: the luminosity, the variation of offline selection cuts, the electron identification, the background subtraction method, the evaluation of the non-prompt-to-prompt ratio \mathcal{R} and the choice of scale for the hard interaction in the simulation. Some sources of uncertainties are listed but are not evaluated: theoretical uncertainties on the models used for event generation, the J/ψ polarisation, the electron reconstruction method and the trigger efficiency. The results are presented for the total production cross-section value obtained after a cut of $p_T > 10$ GeV at the generator level is applied on the J/ψ p_T . This result, which serves as a measure of the order of magnitude of the error we can

expect from a real data measurement, is then applied to the differential cross-section results. This method is used since the statistics are limited for the individual bins such that the systematic uncertainty is dominated by statistical fluctuations. The total combined error from the different sources listed below is given at the end.

8.1 Luminosity

During LHC data-taking in 2010, the luminosity was measured using the LUCID detector [121], as described briefly in §3.3. A systematic uncertainty estimation on the measurement was performed, and a value of 11% was obtained. This uncertainty is largely dominated by the uncertainty on the beam intensities, as provided by the LHC, which accounts for 10%. As the LHC operation gets better understood, this uncertainty is likely to be reduced to 5%.

We then need to consider this uncertainty to estimate its effect on a possible measurement using real LHC data. We calculate the J/ψ cross-section considering a luminosity value of $5.00 \pm 0.55 \text{ pb}^{-1}$ and we obtain an asymmetric error of $^{+12\%}_{-10\%}$. However, for the purpose of our estimation, we consider a symmetric error of 11%. Once this uncertainty is propagated to our cross-section result, we obtain a systematic uncertainty of $\pm 9 \text{ nb}$ for the prompt and $\pm 2 \text{ nb}$ for the non-prompt total production cross-sections. When considering an uncertainty of 5%, we obtain a systematic uncertainty of $\pm 4 \text{ nb}$ for the prompt and $\pm 1 \text{ nb}$ for the non-prompt total production cross-sections.

8.2 Efficiency

In this analysis, the biases in efficiencies are the largest source of systematic uncertainties. A bias in efficiency is observed due to the electron identification cuts. The selection cut values are also individually varied around the central value to evaluate their impact.

8.2.1 Identification efficiency

As described in §6.4, the electron identification is performed by several cuts combined and applied in bins of η and E_T . In order to evaluate the systematic uncertainty induced by these cuts, we modify the value of the cut for each variable separately, while keeping the other cuts untouched, and determine the difference in efficiency obtained from this change. Only cuts which are demonstrated to have an effect on the identification are considered, as can be seen in Fig. 7.18(b). The value chosen for the cut variation, as well as the direction of the variation, is determined by data-simulation

comparison performed on real 2010 data from p - p collisions [122]. The individual shifts in cut value and the resulting variations in efficiency are listed in Table 8.1. The sign of the computed error is given, but a symmetric error is considered for the final result. The total is computed by adding the individual errors in quadrature.

Identification cut	Δvalue	$\Delta\epsilon_p/\epsilon_p$	$\Delta\epsilon_{np}/\epsilon_{np}$
R_{had}/R_{had1}	0.00134	0.3%	0.5%
R_η	-0.0271	0.9%	2.8%
$w_{\eta2}$	0.0004	0.08%	0
w_{stot}	0.2294	0.3%	0.2%
E_{ratio}	-0.0472	0.09%	0.2%
$\Delta\eta$	-0.0006	0	-0.08
$n_{b-layer}$	-0.0166	1.7%	1.7%
$\Delta\phi$	0.0009	1.3%	1.1%
E/p	0.0174	0.05%	0.1%
n_{TRT}	-0.6653	0.3%	0.3%
f_{hTR}	-0.0313	5.8%	5.5%
Total	—	6.3%	6.5%

Table 8.1: Efficiency variations for the electron identification cuts. The sign of the computed error is indicated here, but a symmetric error is considered in the final result. The integer quantities, such as n_{TRT} and $n_{b-layer}$, are allowed to have non-integer shifts. In particular, n_{TRT} is averaged over η bins.

We clearly see that the dominant source of systematic uncertainty is the f_{hTR} cut as well as R_η in the non-prompt case. The distributions for selected identification variables were also measured in 2010 data and are shown, for R_η , in Fig. 8.1, E_{ratio} , in Fig. 8.2, for $w_{\eta2}$, in Fig. 8.3, for w_{stot} , in Fig. 8.4 and for f_{hTR} in Fig. 8.5, where the shifts are visible. For a more accurate error estimation on the electron identification, the correlations between variables, such as for shower shapes, should be taken into account. For the purpose of our estimation, we assumed that these correlations are negligible.

8.2.2 Cut variation

We verify the effect of the choice of the offline selection cuts used in this analysis¹ on the cross-section value obtained. To achieve this, in absence of real data comparison, we use the following cut variations and repeat the analysis with the modified values:

¹A description of the original selection cuts can be found in Appendix C.

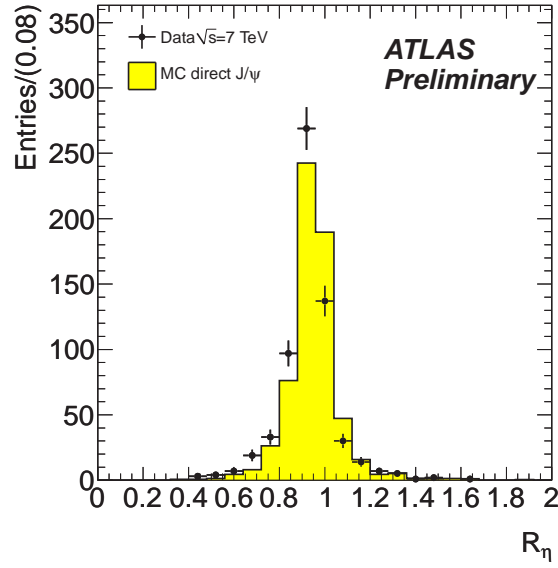


Figure 8.1: Distribution for R_η on real 2010 collision data compared to simulation [123].

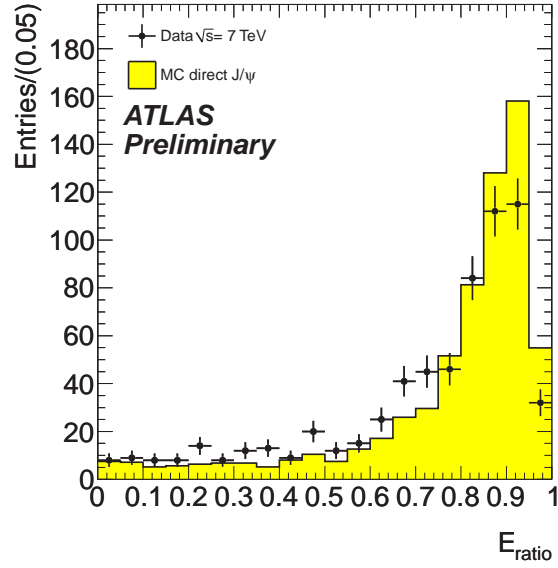


Figure 8.2: Distribution for E_{ratio} on real 2010 collision data compared to simulation [123].

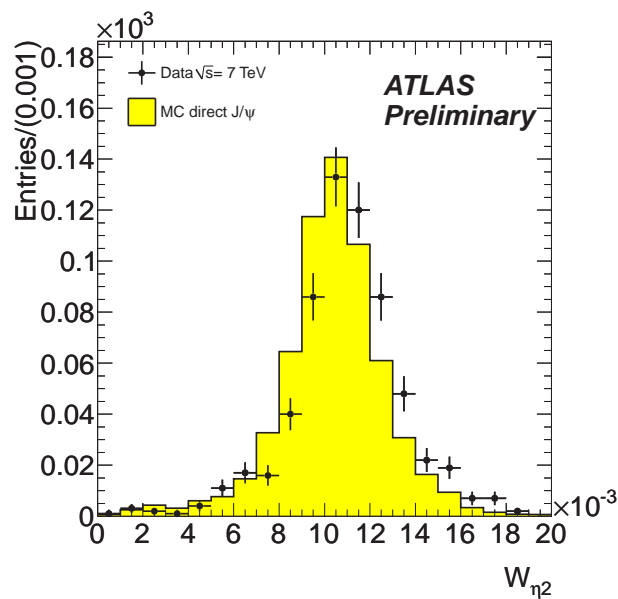


Figure 8.3: Distribution for $w_{\eta 2}$ on real 2010 collision data compared to simulation [123].

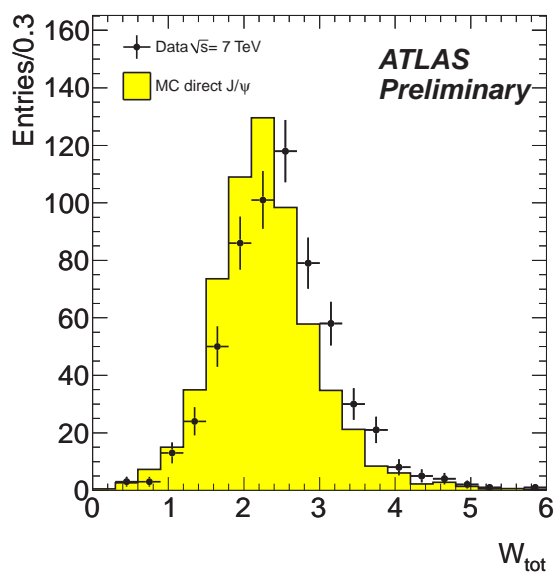


Figure 8.4: Distribution for w_{stot} on real 2010 collision data compared to simulation [123].

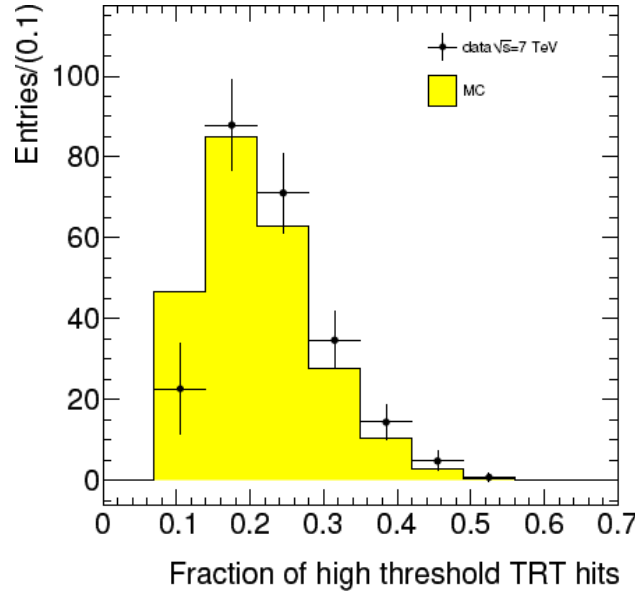


Figure 8.5: Distribution for f_{hTR} on real 2010 collision data compared to simulation [124].

- 1) $E_T \geq 6$ GeV,
- 2) $\chi^2 < 4$ and $\chi^2 < 8$,
- 3) $\Delta R_{cluster} > 0.05$ and $\Delta R_{cluster} > 0.15$,
- 4) ΔR between the EF trigger object and the offline electron < 0.01 and < 0.1 ,
- 5) $1.8 \text{ GeV} \leq m_{ee} \leq 4.2 \text{ GeV}$ and $2.2 \text{ GeV} \leq m_{ee} \leq 3.8 \text{ GeV}$.

In the case of the modified invariant mass cut 5), the sideband background subtraction method is modified to use corresponding sidebands, $1.8 \text{ GeV} \leq m_{ee} \leq 2.4 \text{ GeV}$ and $3.6 \text{ GeV} \leq m_{ee} \leq 4.2 \text{ GeV}$; $2.2 \text{ GeV} \leq m_{ee} \leq 2.6 \text{ GeV}$ and $3.4 \text{ GeV} \leq m_{ee} \leq 3.8 \text{ GeV}$, respectively. The results are listed in Table 8.2. As expected, the E_T and invariant mass cuts have the largest impact. In the case of the invariant mass, the effect is larger when widening the mass window, since the background becomes underestimated in the sidebands. This effect is not found when reducing the mass window.

8.3 Number of events estimation

In order to determine the number of signal events needed for the cross-section calculation, a sideband background subtraction is performed, under the assumption that

Offline cut	$\Delta\sigma_p/\sigma_p$	$\Delta\sigma_{np}/\sigma_{np}$
E_T	-4%	-5%
$\chi^2 < 4$	3%	3%
$\chi^2 < 8$	-1%	-0.6%
$\Delta R_{cluster} > 0.05$	0	0
$\Delta R_{cluster} > 0.15$	0.1%	0.2%
$\Delta R_{trigger-offline} > 0.01$	-0.02%	0.007%
$\Delta R_{trigger-offline} > 0.1$	-0.006%	0.03%
$1.8 \text{ GeV} \leq m_{ee} \leq 4.2 \text{ GeV}$	8%	7%
$2.2 \text{ GeV} \leq m_{ee} \leq 3.8 \text{ GeV}$	0.8%	-0.1%
Total	9.5%	9.1%

Table 8.2: Offline selection cut systematic uncertainties.

the background has a linear shape. A systematic uncertainty is determined on the background shape by changing the linear shape assumption to use an exponential or a second-degree polynomial fitting function. The fit is performed on the mass range $2 \text{ GeV} \leq m_{ee} \leq 4 \text{ GeV}$ and the results are shown in Fig. 8.6. We then compare the number of events computed as the integral of the fitted function in the signal mass region, i.e. $2.5 \text{ GeV} \leq m_{ee} \leq 3.5 \text{ GeV}$, for each fitting function. We obtain a value of 1293 for the linear function integral, 1161 for the integral of the exponential fit and 1206 for the second-degree polynomial. By comparing these values to 1411, the estimated amount of background in the sidebands obtained in §7.4.3, and choosing the largest difference, a systematic error of 2% is assigned for the background shape, which translates into $\pm 2 \text{ nb}$ for the prompt and $\pm 0.5 \text{ nb}$ for the non-prompt total production cross-sections.

As mentioned in §7.4.3, we observe a 1.5% signal contamination in the sidebands used for background subtraction and we take this fraction as a systematic uncertainty on the inclusive number of events. This corresponds to an uncertainty of $\pm 1 \text{ nb}$ for the prompt and $\pm 0.3 \text{ nb}$ for the non-prompt total production cross-sections.

8.4 Non-prompt-to-prompt ratio

As explained in §7.4.4, an ad hoc correction is applied to the non-prompt-to-prompt event ratio \mathcal{R} such that its fitted central value is closer to the expected value. We consider here the scale of this correction to be a systematic uncertainty in our result and calculate the corresponding error by comparing the obtained cross-section without this correction to the original value. We arrive at a value of 2%, or $\pm 2 \text{ nb}$, for the prompt total production cross-section and 12%, or $\pm 2 \text{ nb}$, in the non-prompt case.

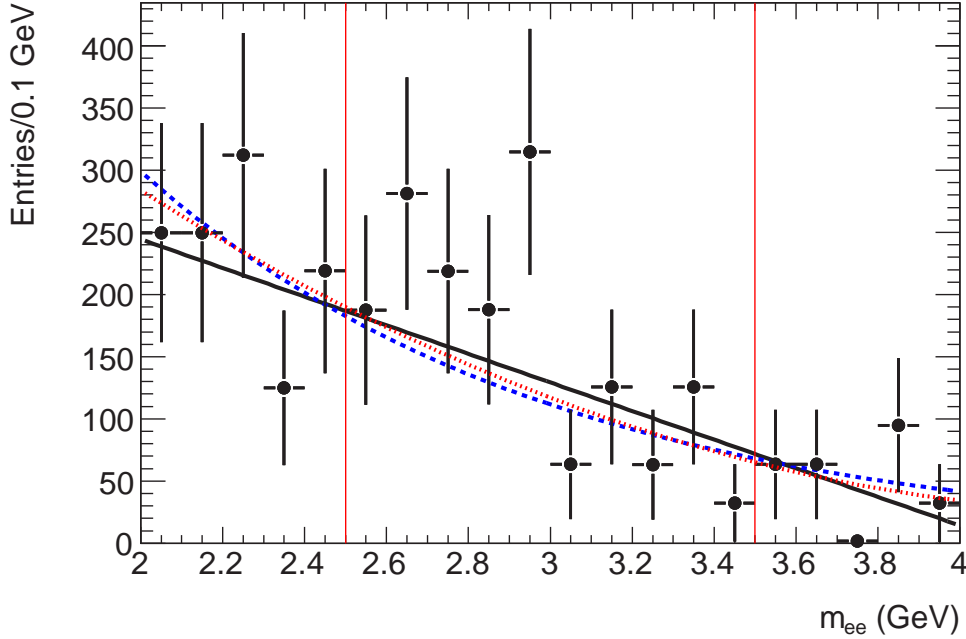


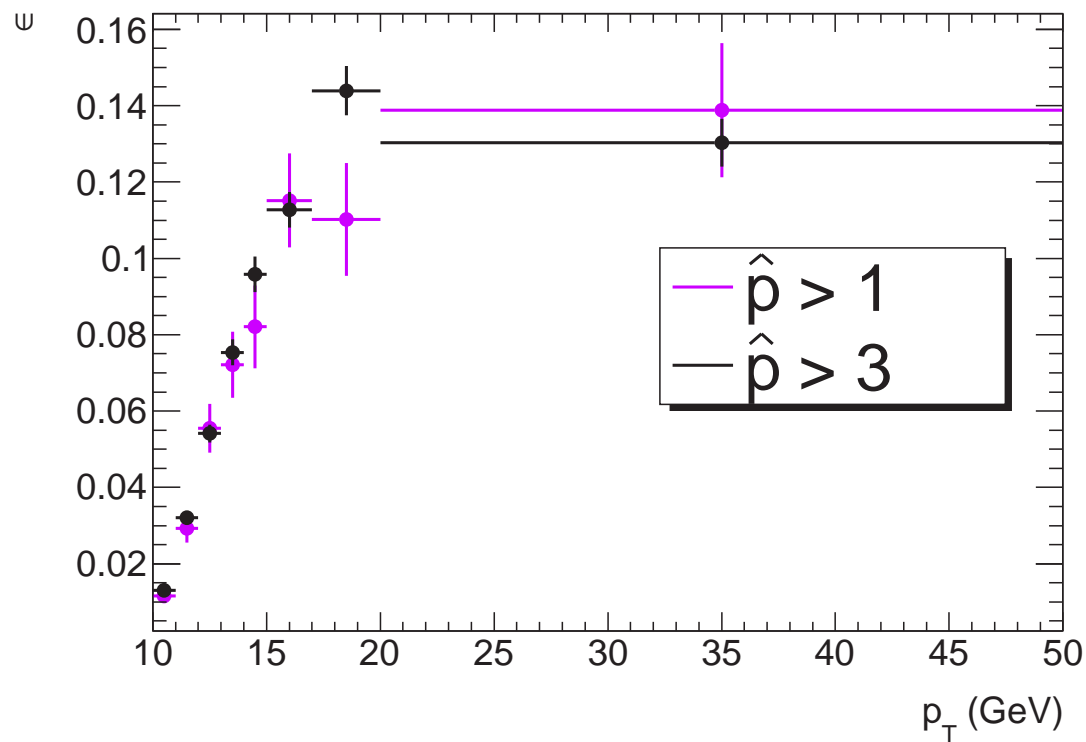
Figure 8.6: Fit to the background shape in the invariant mass window. The linear fit is shown in solid black, together with the exponential fit in dashed blue and the second-degree polynomial in dotted red.

8.5 Acceptance

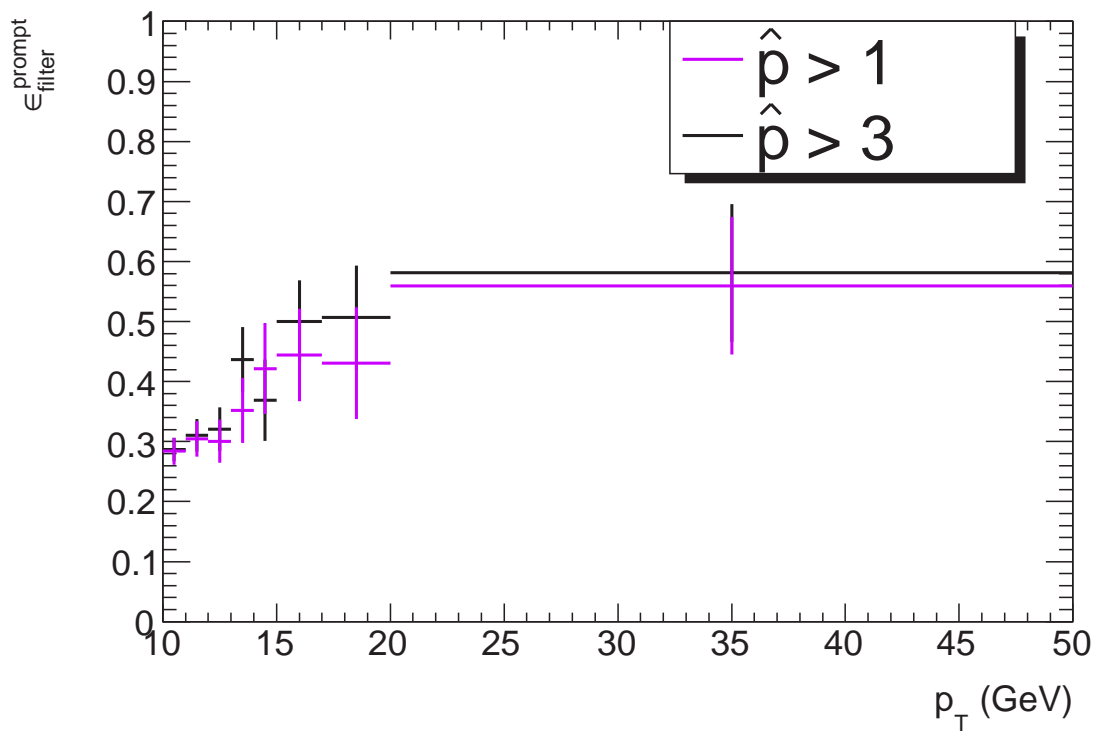
We identify sources of systematic error which relate to the theoretical model used for the J/ψ production and affect the acceptance for these events.

As noted in §7.3.3, the value of the hard interaction scale \hat{p}_\perp impacts on the selection efficiency, through the acceptance, and on the MultiLepton filter efficiency for the prompt J/ψ signal sample. We consider this effect as a systematic uncertainty. The difference in selection and MultiLepton filter efficiency for generator level p_T bins is shown in Fig. 8.7 for the prompt case. In order to compute the systematic error, the cross-sections obtained through unfolding using the $\hat{p}_\perp > 1$ GeV sample information are compared to the original results. An uncertainty of 11%, or ± 9 nb for the prompt total production cross-section, is obtained. This error is also used on the non-prompt sample as an estimate since this sample was only generated with $\hat{p}_\perp > 1$ GeV.

In the PYTHIA generator, the polarisation of the J/ψ decay product is not implemented. The angular distribution of events should be proportional to $1 + \cos^2 \theta$, where θ is the angle between the e^+ direction in the J/ψ rest frame and the J/ψ direction in the lab frame, as previously defined in §2.3.3. In our simulation, an isotropic



(a)



(b)

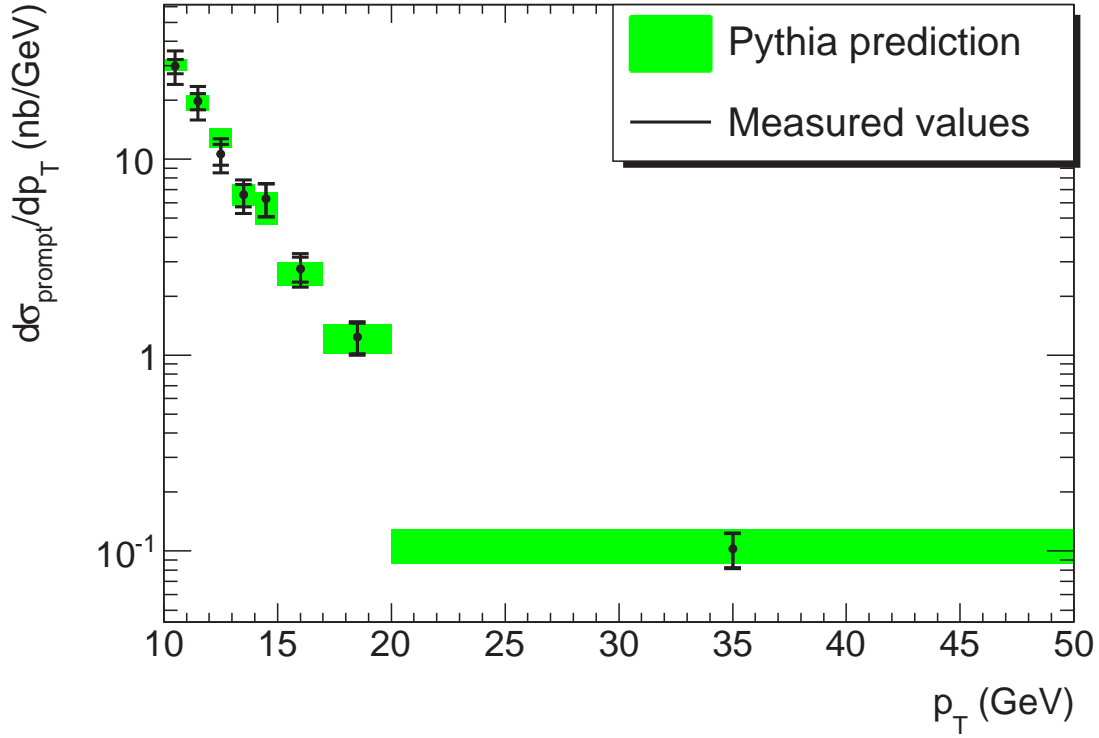
Figure 8.7: Comparison between $\hat{p}_\perp > 1$ GeV and $\hat{p}_\perp > 3$ GeV samples as a function of the generator level p_T for (a) the offline selection efficiency and (b) the filter efficiency.

distribution is obtained for $\cos\theta$. In order to estimate the effect of the polarisation on our calculation, we can obtain the p_T distribution for different models of polarisation. An estimation of the systematic uncertainty can be obtained by considering the extremums of the variations for all models. This uncertainty is not evaluated in this thesis, but it appears to be the dominant source of theoretical error on the acceptance [125].

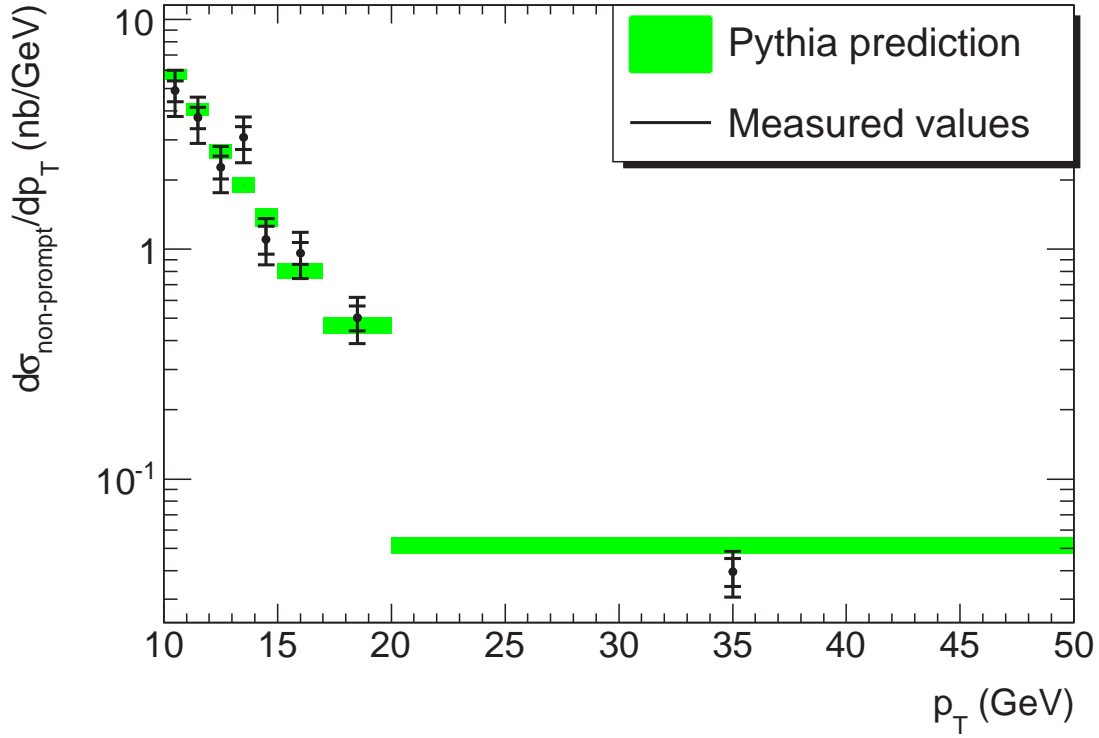
8.6 Combined systematic error and final result

Although the estimation of a selection of the most important sources of systematic uncertainties is performed here, other contributions should be considered for an accurate measurement using real LHC data. As mentioned in §8.5, the J/ψ polarisation is one of the missing contribution to the acceptance systematic uncertainty, but also the impact of the parton distribution function should be considered. This analysis was performed using the PYTHIA generator, but a systematic uncertainty should be assigned on the parton shower, the hadronisation and underlying event model by comparing with other generators. The possible biases induced by electron reconstruction aspects, such as material effects, p_T resolution and scale, and vertexing (both for particle tracks and refitting to a common vertex for electron pairs), are likely to be significant and therefore would need to be studied more carefully. Also, the systematic uncertainty from the efficiency of the chosen trigger chain needs to be considered in a real data measurement.

The uncertainties discussed in the previous sections need to be combined in a single systematic uncertainty for the cross-section values we obtained. Assuming that these errors are uncorrelated, we add them in quadrature to arrive at a total uncertainty of 16.2% for the prompt and 19.9% for the non-prompt case. The acceptance systematic error is considered separately as a theoretical uncertainty. Table 8.3 shows the values for the differential cross-section results, where the theoretical uncertainty on the prompt production is then added in quadrature to the systematic uncertainty. The differential cross-sections for prompt and non-prompt J/ψ production are shown in Fig. 8.8. In the case of the non-prompt J/ψ cross-section in Fig. 8.8(b), the calculated value in the p_T range 13–14 GeV shows a disagreement with the prediction. This originates from the estimation of the non-prompt-to-prompt ratio \mathcal{R} in the same range, as shown in Fig. 7.30(b), which emphasises the need to improve the fit method used to obtain \mathcal{R} . For the total cross-section for $p_T > 10$ GeV, the final results become $\sigma_p = 85 \pm 4$ (stat.) ± 14 (syst.) ± 9 (theo.) nb and $\sigma_{np} = 20 \pm 1$ (stat.) ± 4 (syst.) ± 2 (theo.) nb. It is important to note the possibly dominant missing contribution due to the unknown J/ψ polarisation and the effect of inactive material on the electron reconstruction.



(a)



(b)

Figure 8.8: Differential (a) prompt and (b) non-prompt production cross-sections as a function of the generator level J/ψ p_T . The PYTHIA predictions are overlaid in green. The full error bars show the combined error for each bin, with the statistical uncertainty overlaid.

p_T range (GeV)	$d\sigma_{\eta}/dp_T$ (nb/GeV)		$d\sigma_{\eta\psi}/dp_T$ (nb/GeV)	
	Estimated	Expected	Estimated	Expected
10–11	30 ± 2 (stat.) ± 6 (syst.)	30 ± 2	5 ± 1 (stat.) ± 1 (syst.)	5.8 ± 0.3
11–12	20 ± 2 (stat.) ± 4 (syst.)	19 ± 2	4 ± 1 (stat.) ± 1 (syst.)	4.1 ± 0.3
12–13	11 ± 1 (stat.) ± 2 (syst.)	13 ± 1	2.3 ± 0.3 (stat.) ± 0.5 (syst.)	2.7 ± 0.2
13–14	7 ± 1 (stat.) ± 1 (syst.)	6.6 ± 0.8	3.1 ± 0.4 (stat.) ± 0.7 (syst.)	1.9 ± 0.2
14–15	6 ± 1 (stat.) ± 1 (syst.)	6 ± 1	1.1 ± 0.2 (stat.) ± 0.3 (syst.)	1.4 ± 0.1
15–17	2.8 ± 0.4 (stat.) ± 0.5 (syst.)	2.6 ± 0.4	1.0 ± 0.1 (stat.) ± 0.2 (syst.)	0.81 ± 0.06
17–20	1.2 ± 0.2 (stat.) ± 0.2 (syst.)	1.2 ± 0.2	0.5 ± 0.1 (stat.) ± 0.1 (syst.)	0.47 ± 0.04
20–50	0.10 ± 0.02 (stat.) ± 0.02 (syst.)	0.11 ± 0.02	0.04 ± 0.01 (stat.) ± 0.01 (syst.)	0.052 ± 0.004

Table 8.3: Differential prompt and non-prompt J/ψ production cross-section results, with systematic uncertainties.

CHAPTER 9

Conclusion and Outlook

In the analysis presented in this thesis, we propose a method for a cross-section measurement of the $J/\psi \rightarrow e^+e^-$ decay in p - p collisions using the ATLAS detector. For this purpose, we presented the current state of the theory of J/ψ meson production in hadron collisions. There are currently several models available to describe the J/ψ production, among which the Colour Singlet Model and the Colour Octet Model were discussed, but none have fully described the currently available hadron collision data. With the help of the freshly acquired LHC data, a J/ψ cross-section measurement at a center of mass energy of 7 TeV should contribute to the ongoing effort. In order to perform this measurement using electron pairs, the ATLAS detector is used and its description was given, with emphasis on the SCT and the development of its Environmental Detector Control System. The SCT provides high-quality tracking information through silicon technology, which is a key element to electron reconstruction in ATLAS. The methods developed to reconstruct and identify electrons within the ATLAS software were described, together with studies aimed at understanding low p_T electrons, performed in the scope of this thesis.

Using simulated data, two main goals were achieved: the validation of the analysis method was obtained for the fiducial cross-section measurement and an estimation of the error we can expect on the production cross-section measurement. The accuracy of a production cross-section measurement was estimated to be, for prompt and non-prompt contributions respectively, $\sigma_p = 85 \pm 4$ (stat.) ± 14 (syst.) ± 9 (theo.) nb and $\sigma_{np} = 20 \pm 1$ (stat.) ± 4 (syst.) ± 2 (theo.) nb for an integrated luminosity of 5 pb^{-1} . The results are discussed in §8.6 and show a good agreement with the PYTHIA prediction. The main sources of experimental uncertainty were found to

be on the efficiency, more specifically by varying the cut on the fraction of high-threshold transition radiation hits in the TRT, used for electron identification, and by varying the invariant mass window, hence being sensitive to the background shape. Moreover, the technique used to extract the non-prompt-to-prompt ratio \mathcal{R} could be improved, given the fluctuations observed between p_T bins and the need for a linear correction. The uncertainty on the J/ψ polarisation description was estimated for the $J/\psi \rightarrow \mu^+\mu^-$ cross-section measured at 7 TeV and is the most important source of theoretical uncertainty [125]. Nevertheless, the results shown in this work demonstrate the feasibility of a $J/\psi \rightarrow e^+e^-$ measurement with the ATLAS detector. We also argue that measuring the J/ψ mesons in both of their leptonic decay channels, muon and electron pairs, not only for performance benchmarking but also for physics measurements, is important for cross-checks, and we have the possibility to perform both.

Since we used simulated data to perform this analysis, it was possible to estimate the selection efficiency with respect to the generator level information. When performing the measurement in real p - p collisions, the individual efficiencies, for trigger, offline selection and identification should be evaluated separately from data. The double-object trigger efficiency for the 2e5 chain can be obtained using a technique known as Tag and Probe. Using the equivalent single-object trigger chain, e5, one can obtain a sample of good electrons (the “tag”), search for a second object (the “probe”) and compute the efficiency on this probe to satisfy the trigger cuts. The square of this single-object efficiency gives an estimate of the 2e5 trigger chain efficiency. The same technique can be used to obtain the offline selection and identification efficiencies, using electron pairs. In the beginning, simulated data will most probably be used to obtain the reconstruction efficiency, which quantifies our detector’s ability to reconstruct dielectron pairs. To take into account the possible differences in shape between the reconstructed and the generator level distributions, unfolding is necessary and can be obtained by training on a simulated sample.

As of Spring 2010, the LHC is providing 7 TeV proton collisions to the ATLAS detector and the J/ψ meson was observed. Using a modified electromagnetic clustering, which uses a different seeding, a mass spectrum was obtained using 77.8 nb^{-1} of data. The obtained invariant mass spectrum is shown in Fig. 9.1.

In their quest to understand the hadroproduction of charmonium, physicists can use different tools at their disposal. As shown here, the cross-section is one of those, together with polarisation. Recent theoretical developments suggest to look at new quantities, such as the hadronic activity surrounding charmonium production, by searching for the associated production of a heavy quark pair [126]. Such channels are known from measurements performed at B -factories to be an abundant source of J/ψ and likely to bring new information to test the various production models available to determine their validity.

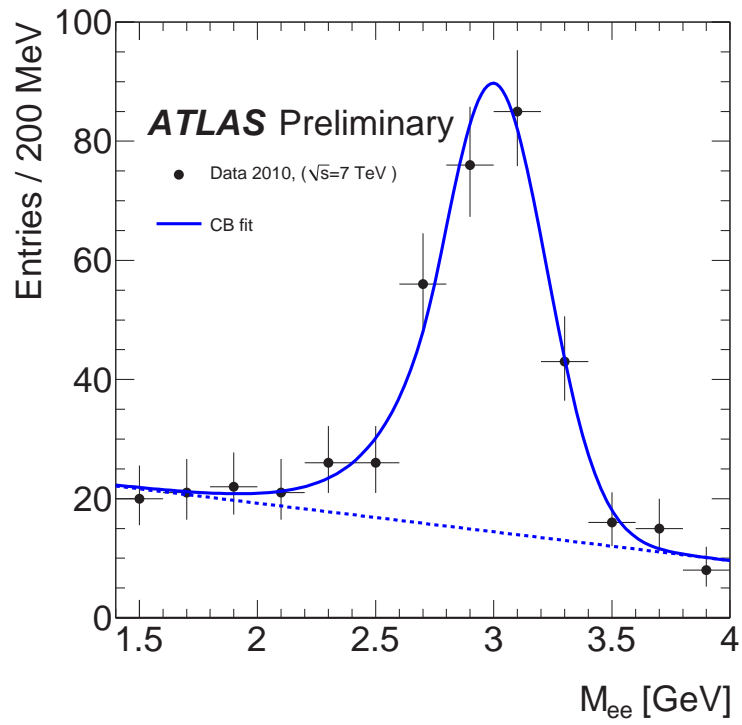


Figure 9.1: Dielectron invariant mass in the J/ψ mass range using 77.8 nb^{-1} of 2010 LHC data [123]. The data points are fitted using a Crystal Ball function.

Glossary

ALFA	Absolute Luminosity For ATLAS
ALICE	A Large Ion Collider Experiment
AOD	Analysis Object Data
ASIC	Application-Specific Integrated Circuit
ATLAS	A Toroidal Lhc ApparatuS
BBIM	Building Block Interlock Monitoring
CAN	Controller Area Network
CC	Crate Controller
CMS	Compact Muon Solenoid
COM	Colour Octet Model
CSC	Cathode Strip Chambers
CSM	Colour Singlet Model
DAQ	Data AcQuisition
DCS	Detector Control System
DDC	DAQ-DCS Communication
DMILL	Durcie Mixte sur Isolant Logico-Linéaire (Rad-Hard Mixed Analog-Digital on SOI)
DPD	Derived Physics Data
DSP	Digital Signal Processor
EB	Event Builder
EF	Event Filter
ELMB	Embedded Local Monitor Board
EM	ElectroMagnetic
ENC	Equivalent Noise Charge
ESD	Event Summary Data

EVGEN	Event GENeration format
FCal	Forward Calorimeter
HCAL	Hadronic Calorimeter
HEC	Hadronic End-Caps
HLT	High Level Trigger
IBOX	Interlock Box
ID	Inner Detector
IP	Interaction Point
IR	Interaction Region
JCOP	Joint COntrols Project
L1	Level 1 Trigger
L2	Level 2 Trigger
LAr	Liquid Argon
LEP	Large Electron Positron collider
LHC	Large Hadron Collider
LHCb	The Large Hadron Collider beauty experiment
LO	Leading Order
LUCID	LUMinosity measurement using Cerenkov Integrating Detec- tor
MDT	Monitored Drift Tubes
NRQCD	Non-Relativistic Quantum ChromoDynamics
NTC	Negative Temperature Coefficient
OPC	Object linking and embedding for Process Control
PLC	Programmable Logic Controller
PMT	PhotoMultiplier Tubes
PS	Proton Synchrotron
QED	Quantum Electrodynamics
RDO	Raw Data Object
RF	Radio Frequency systems
RFQ	Radio Frequency Quadrupole
ROB	Read-Out Buffer
ROD	Read-Out Driver
ROS	Read-Out System
RPC	Resistive Plate Chambers
SCADA	Supervisory Control And Data Acquisition
SCT	SemiConductor Tracker
SIC	SCT Interlock Card
SPS	Super Proton Synchrotron
SSS	Short Straight Section
TGC	Thin Gap Chambers

TileCal	Tile Calorimeter
TOTEM	TOTAL Elastic and diffractive cross-section Measurement
TRT	Transition Radiation Tracker
ZDC	Zero Degree Calorimeter

Bibliography

- [1] S. Weinberg, *The Quantum Theory of Fields*, vol. 2: Modern Applications. Cambridge University Press, 1996. 489 p.
- [2] D. H. Perkins, *Introduction to High Energy Physics*. Cambridge University Press, 4th ed., 2000.
- [3] V. D. Barger and R. J. N. Phillips, *Collider Physics*. Frontiers in Physics. Addison-Wesley, 1987.
- [4] C. S. Wu, E. Ambler, R. W. Hayward, D. D. Hoppes, and R. P. Hudson, *Experimental Test of Parity Conservation in Beta Decay*, Phys. Rev. **105** (1957) no. 4, 1413–1414.
- [5] R. K. Ellis, W. J. Stirling, and B. R. Webber, *QCD and Collider Physics*. Cambridge Monographs on Particle Physics, Nuclear Physics and Cosmology. Cambridge University Press, 1996.
- [6] D. J. Gross and F. Wilczek, *Ultraviolet Behavior of Non-Abelian Gauge Theories*, Phys. Rev. Lett. **30** (1973) no. 26, 1343–1346.
H. D. Politzer, *Reliable Perturbative Results for Strong Interactions?*, Phys. Rev. Lett. **30** (1973) no. 26, 1346–1349.
H. D. Politzer, *Asymptotic Freedom: An Approach to Strong Interactions*, Phys. Rept. **14** (1974) no. 4, 129–180.
D. J. Gross and F. Wilczek, *Asymptotically Free Gauge Theories. I*, Phys. Rev. **D8** (1973) no. 10, 3633–3652.

- [7] N. Cabibbo, *Unitary Symmetry and Leptonic Decays*, Phys. Rev. Lett. **10** (1963) no. 12, 531–533.
- [8] S. L. Glashow, J. Iliopoulos, and L. Maiani, *Weak Interactions with Lepton-Hadron Symmetry*, Phys. Rev. **D2** (1970) no. 7, 1285–1292.
- [9] J. J. Aubert, U. Becker, P. J. Biggs, J. Burger, M. Chen, G. Everhart, P. Goldhagen, J. Leong, T. McCorriston, T. G. Rhoades, M. Rohde, S. C. C. Ting, S. L. Wu, and Y. Y. Lee, *Experimental Observation of a Heavy Particle J* , Phys. Rev. Lett. **33** (1974) no. 23, 1404–1406.
- [10] J.-E. Augustin, A. M. Boyarski, M. Breidenbach, F. Bulos, J. T. Dakin, G. J. Feldman, G. E. Fischer, D. Fryberger, G. Hanson, B. Jean-Marie, R. R. Larsen, V. Lüth, H. L. Lynch, D. Lyon, C. C. Morehouse, J. M. Paterson, M. L. Perl, B. Richter, P. Rapidis, R. F. Schwitters, W. M. Tanenbaum, F. Vannucci, G. S. Abrams, D. Briggs, W. Chinowsky, C. E. Friedberg, and G. Goldhaber, *Discovery of a Narrow Resonance in e^+e^- Annihilation*, Phys. Rev. Lett. **33** (1974) no. 23, 1406–1408.
- [11] C. Bacci et al., *Preliminary Result of Frascati (ADONE) on the Nature of a New 3.1-GeV Particle Produced in e^+e^- Annihilation*, Phys. Rev. Lett. **33** (1974) no. 23, 1408–1410.
- [12] G. S. Abrams et al., *The Discovery of a Second Narrow Resonance in e^+e^- Annihilation*, Phys. Rev. Lett. **33** (1974) no. 24, 1453–1455.
- [13] Particle Data Group Collaboration, C. Amsler et al., *Review of Particle Physics*, Phys. Lett. **B667** (2008) no. 1–5, 1–1340.
- [14] J.-P. Lansberg, *J/ψ , ψ' and Υ production at Hadron Colliders: a review*, Int. J. Mod. Phys. **A21** (2006) no. 19–20, 3857–3916, [arXiv:hep-ph/0602091](#).
- [15] J. C. Collins, D. E. Soper, and G. Sterman, *Factorization of Hard Processes in QCD*, Adv. Ser. Direct. High Energy Phys. **5** (1988) 1–91, [arXiv:hep-ph/0409313](#).
- [16] M. Krämer, *Quarkonium Production at High-Energy Colliders*, Prog. Part. Nucl. Phys. **47** (2001) no. 1, 141–201, [arXiv:hep-ph/0106120](#).
- [17] CDF Collaboration, *J/ψ , $\psi' \rightarrow \mu^+\mu^-$ and $B \rightarrow J/\psi$, ψ' Cross Sections*, [arXiv:hep-ex/9412013](#). Fermilab-Conf-94/136-E.
- [18] CDF Collaboration, F. Abe et al., *Production of J/ψ Mesons from χ_c Meson Decays in $p\bar{p}$ Collisions at $\sqrt{s} = 1.8$ TeV*, Phys. Rev. Lett. **79** (1997) no. 4, 578–583.

- [19] V. Fock, *Konfigurationsraum und zweite Quantelung*, Z. Phys. **75** (1932) no. 9, 622–647.
- [20] CDF Collaboration, A. Abulencia et al., *Polarizations of J/ψ and $\psi(2S)$ Mesons Produced in $p\bar{p}$ Collisions at $\sqrt{s} = 1.96$ TeV*, Phys. Rev. Lett. **99** (2007) no. 13, 132001, [arXiv:0704.0638 \[hep-ex\]](#).
- [21] CDF Collaboration, D. E. Acosta et al., *Measurement of the J/ψ meson and b -hadron production cross sections in $p\bar{p}$ collisions at $\sqrt{s} = 1960$ GeV*, Phys. Rev. **D71** (2005) 032001, [arXiv:hep-ex/0412071](#).
- [22] ATLAS Collaboration, G. Aad et al., *The ATLAS Experiment at the CERN Large Hadron Collider*, JINST **3** (2008) S08003.
- [23] L. Evans et al., *LHC Machine*, JINST **3** (2008) S08001.
- [24] R. Aßmann, M. Lamont, and S. Myers, *A Brief History of the LEP Collider*, Nucl. Phys. Proc. Suppl. **109B** (2002) no. 2–3, 17–31.
- [25] CMS Collaboration, R. Adolphi et al., *The CMS experiment at the CERN LHC*, JINST **3** (2008) S08004.
- [26] LHCb Collaboration, A. A. Alves et al., *The LHCb Detector at the LHC*, JINST **3** (2008) S08005.
- [27] ALICE Collaboration, K. Aamodt et al., *The ALICE experiment at the CERN LHC*, JINST **3** (2008) S08002.
- [28] TOTEM Collaboration, G. Anelli et al., *The TOTEM Experiment at the CERN Large Hadron Collider*, JINST **3** (2008) S08007.
- [29] LHCf Collaboration, O. Adriani et al., *The LHCf detector at the CERN Large Hadron Collider*, JINST **3** (2008) S08006.
- [30] M. Benedikt, P. Collier, V. Mertens, J. Poole, and K. Schindl, *LHC Design Report v.3: the LHC Injector Chain*, Tech. Rep. CERN-2004-003-V-3, CERN, Geneva, 2004.
- [31] CERN, *The CERN accelerator complex*, <http://cds.cern.ch>, 2008. CERN-DI-0812015.
- [32] B. Vošicki, M. Buzić, and A. Cheretakis, *The Duoplasmatron Source for the CERN-PS Linac*, in *Proc. Linear Accelerator Conference*. 1966. Los Alamos.
M. Hone, *The Duoplasmatron Ion Source for the New CERN Linac Preinjector*, Tech. Rep. CERN/PS/LR 79-37, CERN, Geneva, 1979.

- [33] M. Weiss, *The RFQ2 complex: The future injector to CERN Linac 2*, in *EPAC 92: Proceedings of the Third European Particle Accelerator Conference, Berlin, Germany*, vol. 1. Editions Frontières, 24-28 March, 1992.
- [34] C. E. Hill, A. M. Lombardi, E. Tanke, and M. Vretenar, *Present performance of the CERN proton linac*, in *19th International Linear Accelerator Conference (Linac 98), Chicago, IL, USA*, p. 427. 23-28 August, 1998.
- [35] R. Garoby et al., *Linac4, A New Injector for the CERN PS Booster*, in *European Particle Accelerator Conference (EPAC 06), Edinburgh, Scotland*. 26-30 June, 2006.
F. Gerigk, C. Carli, R. Garoby, K. Hanke, A. M. Lombardi, R. MacCaferri, S. Maury, C. Rossi, and M. Vretenar, *Construction Status of Linac4*, Tech. Rep. CERN-sLHC-PROJECT-Report-0027, CERN, Geneva, May, 2009.
- [36] K. H. Reich, *The CERN Proton Synchrotron Booster*, IEEE Trans. Nucl. Sci. **16** (1969) no. 3, 959–961.
- [37] E. Regenstreif, *The CERN Proton Synchrotron 1*, Tech. Rep. CERN-59-29, CERN, Geneva, 1959.
E. Regenstreif, *The CERN Proton Synchrotron 2. injection*, Tech. Rep. CERN-60-26, CERN, Geneva, 1960.
E. Regenstreif, *The CERN Proton Synchrotron 3*, Tech. Rep. CERN-62-03, CERN, Geneva, 1962.
- [38] R. Levy-Mandel, *The CERN proton super synchrotron*, Revue Française de l'Electricité **48** (1975) 12–17.
- [39] CERN, *LHC Layout*, <http://cds.cern.ch>, 1997. LHC-PHO-1997-060.
- [40] O. S. Brüning, P. Collier, P. Lebrun, S. Myers, R. Ostojčić, J. Poole, and P. Proudlock, *LHC Design Report v.1: the LHC Main Ring*, Tech. Rep. CERN-2004-003-V-1, CERN, Geneva, 2004. 309–338.
- [41] O. S. Brüning, P. Collier, P. Lebrun, S. Myers, R. Ostojčić, J. Poole, and P. Proudlock, *LHC Design Report v.1: the LHC Main Ring*, Tech. Rep. CERN-2004-003-V-1, CERN, Geneva, 2004. 3–20.
- [42] ATLAS Collaboration, *ATLAS inner detector: Technical Design Report, 1*, Tech. Rep. CERN-LHCC-97-016, CERN, Geneva, 1997.
ATLAS Collaboration, *ATLAS inner detector: Technical Design Report, 2*, Tech. Rep. CERN-LHCC-97-017, CERN, Geneva, 1997.

- [43] ATLAS Collaboration, *ATLAS pixel detector: Technical Design Report*, Tech. Rep. CERN-LHCC-98-013, CERN, Geneva, 1998.
- [44] G. Aad et al., *ATLAS pixel detector electronics and sensors*, JINST **3** (2008) P07007.
- [45] Y. Unno, *ATLAS silicon microstrip Semiconductor Tracker (SCT)*, Nucl. Inst. Meth. **A453** (2000) no. 1–2, 109–120.
- [46] A. Abdesselam et al., *The barrel modules of the ATLAS semiconductor tracker*, Nucl. Inst. Meth. **A568** (2006) no. 2, 642–671.
- [47] A. Abdesselam et al., *The ATLAS semiconductor tracker end-cap module*, Nucl. Inst. Meth. **A575** (2007) no. 3, 353–389.
- [48] ATLAS TRT Collaboration, E. Abat et al., *The ATLAS TRT Barrel Detector*, JINST **3** (2008) P02014.
ATLAS TRT Collaboration, E. Abat et al., *The ATLAS TRT end-cap detectors*, JINST **3** (2008) P10003.
- [49] D. Attree et al., *The evaporative cooling system for the ATLAS inner detector*, JINST **3** (2008) P07003.
- [50] ATLAS Collaboration, G. Aad et al., *The ATLAS Inner Detector commissioning and calibration*, Eur. Phys. J. C **70** (2010) no. 3, 787–821, [arXiv:1004.5293 \[physics.ins-det\]](#).
- [51] A. Yamamoto et al., *The ATLAS central solenoid*, Nucl. Inst. Meth. **A584** (2008) no. 1, 53–74.
- [52] ATLAS Collaboration, *ATLAS liquid-argon calorimeter: Technical Design Report*, Tech. Rep. CERN-LHCC-96-041, CERN, Geneva, 1996.
- [53] ATLAS Collaboration, F. Hubaut and P. Pralavorio, *Probing the material in front of the ATLAS electromagnetic calorimeter with energy flow from $\sqrt{s}=7$ TeV minimum bias events*, Tech. Rep. ATL-COM-PHYS-2010-270, CERN, Geneva, May, 2010.
- [54] ATLAS TILECAL Collaboration, J. Abdallah et al., *Design, Construction and Installation of the ATLAS Hadronic Barrel Scintillator-Tile Calorimeter*, Tech. Rep. ATL-TILECAL-PUB-2008-001, CERN, Geneva, 2007.
- [55] ATLAS Collaboration, *ATLAS magnet system: Technical Design Report, 1*, Tech. Rep. CERN-LHCC-97-018, CERN, Geneva, 1997.

- [56] S. Palestini, *The muon spectrometer of the ATLAS experiment*, Nucl. Phys. Proc. Suppl. **125** (2003) 337–345.
- [57] ATLAS Collaboration, P. Jenni and M. Nessi, *ATLAS Forward Detectors for Luminosity Measurement and Monitoring*, Tech. Rep. CERN-LHCC-2004-010, CERN, Geneva, March, 2004.
- [58] ATLAS Collaboration, P. Jenni, M. Nordberg, M. Nessi, and K. Jon-And, *ATLAS Forward Detectors for Measurement of Elastic Scattering and Luminosity*, Tech. Rep. CERN-LHCC-2008-004, CERN, Geneva, 2008.
- [59] U. Amaldi et al., *Measurements of the proton-proton total cross section by means of Coulomb scattering at the CERN intersecting storage rings*, Phys. Lett. **B43** (1973) no. 3, 231–236.
- [60] ATLAS Collaboration, P. Jenni, M. Nessi, and M. Nordberg, *Zero Degree Calorimeters for ATLAS*, Tech. Rep. CERN-LHCC-2007-001, CERN, Geneva, January, 2007.
- [61] S. Ask et al., *The ATLAS central level-1 trigger logic and TTC system*, JINST **3** (2008) P08002.
- [62] ATLAS Collaboration, P. Jenni, M. Nessi, M. Nordberg, and K. Smith, *ATLAS high-level trigger, data-acquisition and controls: Technical Design Report*, Tech. Rep. CERN-LHCC-2003-022, CERN, Geneva, 2003.
- [63] J. Campbell, J. Huston, and W. Stirling, *Hard interactions of quarks and gluons: A primer for LHC physics*, Rept. Prog. Phys. **70** (2007) no. 1, 89–193, [arXiv:hep-ph/0611148](https://arxiv.org/abs/hep-ph/0611148).
- [64] A. Barriuso Poy et al., *The detector control system of the ATLAS experiment*, JINST **3** (2008) P05006.
- [65] G. Duckeck et al., *ATLAS computing: Technical Design Report*, Tech. Rep. CERN-LHCC-2005-022, CERN, Geneva, 2005.
- [66] R. W. L. Jones and D. Barberis, *The ATLAS Computing Model*, J. Phys.: Conf. Ser. **119** (2008) 072020.
- [67] O. Beltramello et al., *The Detector Safety System of the ATLAS experiment*, JINST **4** (2009) P09012.

- [68] A. Daneels and W. Salter, *Selection and evaluation of commercial SCADA systems for the controls of the CERN LHC experiments*, in *Accelerator and Large Experimental Physics Control Systems: Proceedings*. Trieste, Italy, 4-8 Oct, 1999. Prepared for 7th International Conference on Accelerator and Large Experimental Physics Control Systems (ICALEPCS 99).
- [69] V. Filimonov, *OPC CANopen Server User Guide*, Tech. Rep. ATL-DQ-ON-0007, CERN, Geneva, 2005.
- [70] B. Hallgren, H. Boterenbrood, H. J. Burckhart, and H. Kvedalen, *The Embedded Local Monitor Board (ELMB) in the LHC Front-End I/O Control System*, in *7th Workshop on Electronics for LHC Experiments - LEB 2001: Proceedings*, p. 325, LECC - LHC Electronics Coordinating Committee. Stockholm, Sweden, 10-14 Sep, 2001. CERN-2001-005.
- [71] O. Holme, M. Gonzalez Berges, P. Golonka, and S. Schmeling, *The JCOP Framework*, in *Europhysics Conference Abstracts*, vol. 29J, pp. WE2.1–6O. 2005. CERN-OPEN-2005-027.
- [72] A. Barriuso Poy et al., *Hierarchical Control for the ATLAS Experiment*, in *Europhysics Conference Abstracts*, vol. 29J, pp. TU2.4–20. 2005.
- [73] S. Schlenker and A. Barriuso Poy, *FSM Integration Guidelines*, Tech. Rep. ATL-DQ-ON-0010, CERN, Geneva, 2007.
- [74] A. Abdesselam et al., *The detector control system of the ATLAS SemiConductor Tracker during macro-assembly and integration*, JINST **3** (2008) P02007.
- [75] R. Brenner, *The SemiConductor Tracker Detector Control System Services*, Tech. Rep. ATL-IS-EN-0017, CERN, Geneva, 2008.
- [76] N. Bingefors, *DCS interlock components*, <http://www4.tsl.uu.se/~Atlas/DCS/DCSIL/DCSIL.html>.
- [77] H. Burckhart, B. Hallgren, and H. Kvedalen, *Irradiation Measurements of the ATLAS ELMB*, Tech. Rep. DCS-IWN9, CERN, Geneva, 2001. <http://collection.europarchive.org/cern/20080528215627/atlas.web.cern.ch/atlas/groups/daqtrig/dcs/iwn.html>.
- [78] A. Sfyrlla et al., *The Detector Control System for the ATLAS Semiconductor Tracker Assembly Phase*, IEEE Trans. Nucl. Sci. **52** (2005) no. 4, 938–943.

- [79] A. Abdesselam et al., *The optical links of the ATLAS SemiConductor Tracker*, JINST **2** (2007) P09003.
- [80] L. Luisa, *Detector Control System (DCS) for the Evaporative Cooling Plant for the ATLAS Inner Detector and Tools for the DCS Offline Monitoring*. PhD thesis, Università degli studi di Udine, Italy, 2009.
- [81] P. Phillips, *ATLAS SCT Power Supply system*, in *Proceedings of the Topical Workshop on Electronics for Particle Physics, formerly LECC Workshop TWEPP-07*, pp. 365–368. Prague, Czech Republic, 3-7 Sep, 2007. CERN-2007-007.
- [82] A. Robichaud-Véronneau and J. Mitrevski, *SCT Environmental DCS software*, <https://twiki.cern.ch/twiki/bin/view/Atlas/SctEnvSoftware>.
- [83] J. Cook, *Conditions Database for PVSS*, Tech. Rep. ATLAS-DQ-ON-0009, CERN, Geneva, 2007.
- [84] G. Viehhauser, B. Mikulec, A. Sfyrta, and A. Robichaud-Véronneau, *Temperature behaviour and uniformity of SCT barrels during assembly and reception testing*, Internal note ATL-INDET-PUB-2006-009, CERN, Geneva, 2006.
- [85] R. Brenner, N. Bingefors, and B. Mohn, *Evaluation of a Humidity Sensor for Use in an Environment Exposed to Radiation*, J. Test. Eval. **35** (2007) no. 5, 469–476.
- [86] F. Campabadal et al., *Design and performance of the ABCD3TA ASIC for readout of silicon strip detectors in the ATLAS semiconductor tracker*, Nucl. Inst. Meth. **A552** (2005) no. 3, 292–328.
- [87] M. Dentan et al., *DMILL, A Mixed Analog-Digital Radiation-Hard BICMOS Technology for High Energy Physics Electronics*, IEEE Trans. Nucl. Sci. **43** (1996) no. 3, 1763–1767.
- [88] A. Abdesselam et al., *The data acquisition and calibration system for the ATLAS Semiconductor Tracker*, JINST **3** (2008) P01003.
Bilge Demirköz, *Construction and Performance of the ATLAS SCT Barrels and Cosmic Tests*. PhD thesis, Oxford University, England, 2007.
- [89] A. Abdesselam et al., *The integration and engineering of the ATLAS SemiConductor Tracker Barrel*, JINST **3** (2008) P10006.
R. B. Nickerson et al., *Robotic mounting of ATLAS barrel SCT modules*, Nucl. Inst. Meth. **A568** (2006) no. 2, 686–691.

- [90] H. Sandaker, *The read-out and control system For the ATLAS SemiConductor Tracker*, Nucl. Inst. Meth. **A541** (2005) no. 1–2, 96–103.
- [91] B. Mikulec, *Tests and Final Integration of the ATLAS SemiConductor Tracker*, in *2005 IEEE NSS Conference Record*, vol. 3, pp. 1480–1484. El Conquistador Resort, Puerto Rico, 23–29 Oct. 2005. CERN-OPEN-2006-055.
- [92] P. J. Bell and C. Lacasta, *The ATLAS SCT: From End-Cap Module Assembly to Detector Operation*, in *2005 IEEE NSS Conference Record*, vol. 2, pp. 1093–1097. El Conquistador Resort, Puerto Rico, 23–29 Oct. 2005.
- [93] E. Abat et al., *Combined performance tests before installation of the ATLAS Semiconductor and Transition Radiation Tracking Detectors*, JINST **3** (2008) P08003.
- [94] A. Robichaud-Véronneau, *Semiconductor tracker final integration and commissioning in the ATLAS detector*, Nucl. Inst. Meth. **A596** (2008) no. 1, 1–4.
- [95] ATLAS Collaboration, *Approved SCT Plots*, <https://twiki.cern.ch/twiki/bin/view/AtlasPublic/ApprovedPlotsSCT>.
- [96] T. Cornelissen, M. Elsing, I. Gavrilenko, W. Liebig, E. Moyse, and A. Salzburger, *The new ATLAS Track Reconstruction (NEWT)*, J. Phys.: Conf. Ser. **119** (2008) 032014.

T. Cornelissen, M. Elsing, S. Fleischmann, W. Liebig, E. Moyse, and A. Salzburger, *Concepts, Design and Implementation of the ATLAS New Tracking (NEWT)*, Tech. Rep. ATL-SOFT-PUB-2007-007, CERN, Geneva, March, 2007.
- [97] R. E. Kalman, *A New Approach to Linear Filtering and Prediction Problems*, Trans. ASME J. Basic Eng. **82** (1960) 35–45. Series D.
- [98] V. Kartvelishvili, *Electron bremsstrahlung recovery in ATLAS*, Nucl. Phys. Proc. Suppl. **172** (2007) 208–211. Proceedings of the 10th Topical Seminar on Innovative Particle and Radiation Detectors.

M. Elsing et al., *ATLAS Detector Paper Back-Up Note: Electrons and Photons*, Tech. Rep. ATL-INDET-PUB-2008-013, CERN, Geneva, July, 2008.
- [99] T. M. Atkinson, *Electron Reconstruction with the ATLAS Inner Detector*. PhD thesis, The University of Melbourne, Australia, 2006.

- [100] A. K. Morley, *Electron Bremsstrahlung Studies and Track Based Alignment of the ATLAS Detector*. PhD thesis, The University of Melbourne, Australia, 2010.
- [101] W. Lampl, S. Laplace, D. Lelas, P. Loch, H. Ma, S. Menke, S. Rajagopalan, D. Rousseau, S. Snyder, and G. Unal, *Calorimeter Clustering Algorithms: Description and Performance*, Tech. Rep. ATL-LARG-PUB-2008-002, CERN, Geneva, April, 2008.
- [102] N. Kerschen et al., *Electron performance in the ATLAS experiment*, Tech. Rep. ATL-COM-PHYS-2010-208, CERN, Geneva, April, 2010.
- [103] ATLAS Collaboration, G. Aad et al., *Expected performance of the ATLAS experiment: Detector, Trigger and Physics*, Tech. Rep. CERN-OPEN-2008-020, CERN, Geneva, 2009. [arXiv:0901.0512 \[hep-ex\]](#).
- [104] G. Pásztor and G. Unal, *Duplicate cluster study and improvements to LAr cluster finding*, Retrieved from <http://indico.cern.ch/contributionDisplay.py?contribId=2&confId=48804>, July, 2009.
- [105] J. Hartert and I. Ludwig, *Electron isolation in the ATLAS experiment*, Tech. Rep. ATL-COM-PHYS-2010-070, CERN, Geneva, February, 2010.
- [106] F. Derue, *Comparison of egamma and soft π in 15.0.0*, Retrieved from <http://indico.cern.ch/contributionDisplay.py?contribId=7&confId=48786>, April, 2009.
- [107] J. Mitrevski, *Electron variables definitions in AOD*, <https://twiki.cern.ch/twiki/bin/view/AtlasProtected/EgammaAOD>.
- [108] R. Achenbach et al., *The ATLAS Level-1 Calorimeter Trigger*, JINST **3** (2008) P03001.
- [109] P. Urquijo, *Functional commissioning of the electron triggers with first collisions*, Tech. Rep. ATL-COM-DAQ-2009-142, CERN, Geneva, November, 2009.
- [110] T. Sjöstrand, S. Mrenna, and P. Skands, *PYTHIA 6.4 Physics and Manual*, JHEP **2006** no. 05, 026, [arXiv:hep-ph/0603175](#).
- [111] E. Barberio and Z. Wąs, *PHOTOS - a universal monte carlo for QED radiative corrections: version 2.0*, Comp. Phys. Comm. **79** (1994) no. 2, 291–308.

- E. Barberio, B. van Eijk, and Z. Waś, *Photos - a universal monte carlo for QED radiative corrections in decays*, Comp. Phys. Comm. **66** (1991) no. 1, 115–128.
- [112] E. Etzion, J. Ginzburg, V. G. Kartvelishvili, and D. Price, *Heavy Quarkonium Production Simulations at ATLAS*, Tech. Rep. ATL-PHYS-INT-2007-001, CERN, Geneva, September, 2006.
- [113] Smižanská, Mária, *PythiaB, an interface to Pythia6 dedicated to simulation of beauty events*, Tech. Rep. ATL-COM-PHYS-2003-038, CERN, Geneva, 2003.
- [114] ATLAS Collaboration, G. Aad et al., *The ATLAS Simulation Infrastructure*, Eur. Phys. J. C **70** (2010) no. 3, 823–874, [arXiv:1005.4568](#) [[physics.ins-det](#)].
K. Assamagan et al., *The ATLAS Simulation Project*, Tech. Rep. ATL-SOFT-INT-2010-002, CERN, Geneva, February, 2010.
- [115] S. Agostinelli et al., *GEANT4: a simulation toolkit*, Nucl. Inst. Meth. **A506** (2003) no. 3, 250–303.
- [116] V. Kostyukhin, *VKalVrt - package for vertex reconstruction in ATLAS*, Tech. Rep. ATL-PHYS-2003-031, CERN, Geneva, August, 2003.
- [117] O. Fedin, *MCTruthClassifier*, <https://twiki.cern.ch/twiki/bin/view/AtlasProtected/MCTruthClassifier>.
- [118] T. Skwarnicki, *A Study of the Radiative Cascade Transitions between the Upsilon-Prime and Upsilon Resonances*. PhD thesis, Institute of Nuclear Physics, Cracow, Poland, 1986. DESY-F31-86-02.
J. Gaiser, *Charmonium Spectroscopy from Radiative Decays of the J/ψ and ψ'* . PhD thesis, Stanford University, Stanford, California, USA, 1982. SLAC-0255.
- [119] N. Amram, J. Baines, E. Etzion, V. Kartvelishvili, J. Kirk, D. Price, and J. Walder, *Measurement of the ratio $d\sigma(bb \rightarrow J/\psi)/d\sigma(pp \rightarrow J/\psi)$ with early ATLAS data*, Tech. Rep. ATL-COM-PHYS-2009-664, CERN, Geneva, December, 2009.
- [120] T. Adye et al., *RooUnfold: ROOT Unfolding Framework*, <http://hepunix.rl.ac.uk/~adye/software/unfold/RooUnfold.html>.
- [121] ATLAS Collaboration, *Luminosity Determination Using the ATLAS Detector*, Tech. Rep. ATLAS-CONF-2010-060, CERN, Geneva, July, 2010.

- [122] E. Schmidt, *Shower shape and TRT variable distributions for selected J/ψ electrons*, Private communication, September, 2010.
- [123] N. Kerschen, A. Schaffer, et al., *Plots for Electron performance of the ATLAS detector using the $J/\psi \rightarrow e^+e^-$ decays*, Tech. Rep. ATL-COM-PHYS-2010-518, CERN, Geneva, July, 2010.
<https://atlas.web.cern.ch/Atlas/GROUPS/PHYSICS/EGAMMA/PublicPlots/20100721/ATL-COM-PHYS-2010-518/index.html>.
- [124] M. Aharrouche et al., *Electron performance of the ATLAS detector using the $J/\psi \rightarrow e^+e^-$ decays*, Tech. Rep. ATL-PHYS-INT-2010-124, CERN, Geneva, November, 2010.
- [125] ATLAS Collaboration, *A first measurement of the differential cross section for the $J/\psi \rightarrow \mu\mu$ resonance and the non-prompt to prompt J/ψ cross-section ratio with pp collisions at $\sqrt{s}=7$ TeV in ATLAS*, Tech. Rep. ATLAS-CONF-2010-062, CERN, Geneva, July, 2010.
- [126] J. P. Lansberg, *On the mechanisms of heavy-quarkonium hadroproduction*, Eur. Phys. J. C **61** (2009) no. 4, 693–703, [arXiv:0811.4005 \[hep-ph\]](#).
- [127] C. S. Hill and J. R. Incandela, *Updated Measurement of the Top Quark Mass in the Lepton+Jets Channel using the Decay Length Technique*, http://www-cdf.fnal.gov/physics/new/top/2006/mass/ljets_lxy_mtop/lxy_mass_695_public.html.

APPENDIX A

Event weights and scaling

We want to define the event weights needed to correct the prompt J/ψ sample (as all branching ratios of forced decays are set to one in PYTHIA).

Let's start by defining w_i , the individual weights to be applied to each production type $i \in \{J/\psi, \chi_{c0}, \chi_{c1}, \chi_{c2}\}$. Let N_i^{bef} be the individual number of events before the filter is applied and $N_{tot}^{bef} = \sum_i N_i^{bef}$, the original content of the combined sample

before filter. The weights are defined such that, when they are applied to N_i^{bef} , the weighted sum of events gives back the original content of the sample, as shown in Eq. A.1.

$$\sum_i w_i \times N_i^{bef} = N_{tot}^{bef} \quad (\text{A.1})$$

Moreover, these event weights should be proportional to the individual branching ratio of the charmonium states produced in the hard interaction to decay to J/ψ , $BR_{i \rightarrow J/\psi \gamma}$, in order to correct for the fact that PYTHIA sets them to one, which we can write as

$$w_i = C \cdot BR_{i \rightarrow J/\psi}, \quad (\text{A.2})$$

where C is a proportionality constant. We can then rewrite Eq. A.1 as

$$C \sum_i BR_{i \rightarrow J/\psi} \times N_i^{bef} = N_{tot}^{bef}, \quad (\text{A.3})$$

$$C = \frac{N_{tot}^{bef}}{\sum_i BR_{i \rightarrow J/\psi} \times N_i^{bef}}. \quad (\text{A.4})$$

Using Eq. A.4 in Eq. A.2, we can rewrite w_i as

$$w_i = \frac{N_{tot}^{bef}}{\sum_j BR_{j \rightarrow J/\psi} \times N_j^{bef}} \times BR_{i \rightarrow J/\psi} = \frac{N_{tot}^{bef}}{N_{tot}^{norm}} \times BR_{i \rightarrow J/\psi} \quad (\text{A.5})$$

$$= \frac{BR_{i \rightarrow J/\psi}}{\sum_j BR_{j \rightarrow J/\psi} \times f_j^{bef}}, \quad (\text{A.6})$$

where j is the internal index of the sum, which represents the same quantity as i , i.e. the production type, f_j^{bef} is defined as N_j^{bef}/N_{tot}^{bef} and N_{tot}^{norm} is the total number of events in the combined sample after correcting for the branching ratios, defined by Eq. A.5.

Let's define now the scaling for event weights in the case where all four channels are generated together in a combined sample. Defining $w_i^{\mathcal{L}}$, the scaled event weights for production type i , \mathcal{L} , the luminosity we want to scale our sample to and \mathcal{L}^{gen} , the generated luminosity of the combined sample, we get

$$w_i^{\mathcal{L}} = w_i \times \frac{\mathcal{L}}{\mathcal{L}^{gen}}. \quad (\text{A.7})$$

We first define the corrected cross-section before the MultiLepton filter, σ_{norm}^{bef} , in terms of the generated cross-section σ^{gen} , the branching ratio of $J/\psi \rightarrow e^+e^-$, $BR_{J/\psi \rightarrow e^+e^-}$, and other previously defined quantities, as

$$\sigma_{norm}^{bef} = \sigma^{gen} \times BR_{J/\psi \rightarrow e^+e^-} \times \frac{N_{tot}^{norm}}{N_{tot}^{bef}} \quad (\text{A.8})$$

$$= \sigma^{gen} \times BR_{J/\psi \rightarrow e^+e^-} \times \sum_i BR_{i \rightarrow J/\psi} \times f_i^{bef}. \quad (\text{A.9})$$

We can now define \mathcal{L}^{gen} using N_{tot}^{bef} and σ_{norm}^{bef} , as

$$\mathcal{L}^{gen} = \frac{N_{tot}^{bef}}{\sigma_{norm}^{bef}}. \quad (\text{A.10})$$

Using Eq. A.10, we can rewrite Eq. A.7 as

$$w_i^{\mathcal{L}} = w_i \times \frac{\mathcal{L}}{N_{tot}^{bef}} \times \sigma_{norm}^{bef}. \quad (\text{A.11})$$

Using Eq. A.8 and the definition of w_i of Eq. A.5, we can rewrite Eq. A.11 as

$$\begin{aligned} w_i^{\mathcal{L}} &= \frac{N_{tot}^{bef}}{N_{tot}^{norm}} \times BR_{i \rightarrow J/\psi} \times \frac{\mathcal{L}}{N_{tot}^{bef}} \times \sigma^{gen} \times BR_{J/\psi \rightarrow e^+e^-} \times \frac{N_{tot}^{norm}}{N_{tot}^{bef}} \\ &= \frac{\mathcal{L}}{N_{tot}^{bef}} \times \sigma^{gen} \times BR_{i \rightarrow J/\psi} \times BR_{J/\psi \rightarrow e^+e^-}. \end{aligned} \quad (\text{A.12})$$

We obtained an expression for the scaled event weights. We will compare this expression to the scaling factors of the individual production types i .

Firstly, we need to define the individual cross-section after correction for the branching ratio, σ_i^{norm} , and the generated individual cross-section, σ_i^{gen} , as

$$\sigma_i^{norm} = \sigma_i^{gen} \times BR_{i \rightarrow J/\psi} \times BR_{J/\psi \rightarrow e^+e^-}. \quad (\text{A.13})$$

We also need to define \mathcal{L}_i^{gen} in terms of N_i^{bef} , the individual number of events before the filter and σ_i^{norm} , as

$$\mathcal{L}_i^{gen} = \frac{N_i^{bef}}{\sigma_i^{norm}}. \quad (\text{A.14})$$

Let's now define the individual scale factor to a luminosity \mathcal{L} , if each process was generated separately, as

$$s_i = \frac{\mathcal{L}}{\mathcal{L}_i^{gen}}. \quad (\text{A.15})$$

Using Eq. A.14, we can rewrite Eq. A.15 as

$$s_i = \frac{\mathcal{L}}{N_i^{bef}} \times \sigma_i^{norm}. \quad (\text{A.16})$$

Using Eq. A.13, we can rewrite Eq. A.16 as

$$s_i = \frac{\mathcal{L}}{N_i^{bef}} \times \sigma_i^{gen} \times BR_{i \rightarrow J/\psi} \times BR_{J/\psi \rightarrow e^+e^-}. \quad (\text{A.17})$$

Assuming that the samples were generated together, we have

$$\sum_i \sigma_i^{gen} = \sigma^{gen}, \quad (\text{A.18})$$

$$\sigma_i^{gen} = \frac{N_i^{bef}}{N_{tot}^{bef}} \times \sigma^{gen}, \quad (\text{A.19})$$

which we can use in Eq. A.17 to express s_i as

$$s_i = \frac{\mathcal{L}}{N_{tot}^{bef}} \times \sigma^{gen} \times BR_{i \rightarrow J/\psi} \times BR_{J/\psi \rightarrow e^+e^-}, \quad (\text{A.20})$$

which is the same as Eq. A.12. Using this technique, we cross-checked our method of computing event weights.

QED

APPENDIX B

Normalised cross-section derivation

We want to define σ_{norm}^{filter} , the normalised prompt J/ψ cross-section, based on Eq. A.9, but after applying the MultiLepton filter. With the knowledge of the way PYTHIA handles forced decays, we can write

$$\begin{aligned}\sigma_{norm}^{filter} &= \epsilon_{J/\psi} \sigma_{J/\psi \rightarrow e^+ e^-} + \sum_i \epsilon_{\chi_{ci}} \sigma_{\chi_{ci} \rightarrow J/\psi \gamma \rightarrow ee\gamma} \\ &= BR_{J/\psi \rightarrow e^+ e^-} \times \left[\epsilon_{J/\psi} \sigma_{J/\psi} + \sum_i BR_{\chi_{ci} \rightarrow J/\psi \gamma} \epsilon_{\chi_{ci}} \sigma_{\chi_{ci}} \right],\end{aligned}\quad (B.1)$$

where $i \in \{0,1,2\}$, $\epsilon_{J/\psi}$ and $\epsilon_{\chi_{ci}}$ are the individual filter efficiencies for each production type, and $\sigma_{J/\psi}$ and $\sigma_{\chi_{ci}}$ correspond to σ_i^{gen} defined previously in Eq. A.19. The values for the branching ratios used here are the PDG values [13].

Let, for numbers *after* the filter,

$$\begin{aligned}N_{J/\psi}^{after} &= \epsilon_{J/\psi} \sigma_{J/\psi} \mathcal{L}, \\ N_{\chi_{ci}}^{after} &= \epsilon_{\chi_{ci}} \sigma_{\chi_{ci}} \mathcal{L}, \\ N_{tot}^{after} &= \epsilon_{tot} \sigma_{tot} \mathcal{L},\end{aligned}$$

where \mathcal{L} , the equivalent luminosity when $BR_{\chi_{ci} \rightarrow J/\psi \gamma} = 1$, is used for all types of production since we assume here that they are generated together. Also, N_{tot}^{after} is the number of events for the combined sample after the filter is applied, and $N_{J/\psi}^{after}$ and $N_{\chi_{ci}}^{after}$ are the number of events after filter for the individual production channels. The

filter efficiency for the combined sample is represented by ϵ_{tot} and σ_{tot} is equivalent to σ^{gen} , previously defined in Eq. A.18.

Then, we can define $f_{J/\psi}^{after}$ and $f_{\chi_{ci}}^{after}$, the fractions of events after the filter, as

$$\begin{aligned} f_{J/\psi}^{after} &= \frac{N_{J/\psi}^{after}}{N_{tot}^{after}} = \frac{\epsilon_{J/\psi} \sigma_{J/\psi}}{\epsilon_{tot} \sigma_{tot}}, \\ f_{\chi_{ci}}^{after} &= \frac{N_{\chi_{ci}}^{after}}{N_{tot}^{after}} = \frac{\epsilon_{\chi_{ci}} \sigma_{\chi_{ci}}}{\epsilon_{tot} \sigma_{tot}}. \end{aligned}$$

Substituting in Eq. B.1, we get

$$\sigma_{norm}^{filter} = BR_{J/\psi \rightarrow e^+ e^-} \times \sigma_{tot} \times \epsilon_{tot} \left[f_{J/\psi}^{after} + \sum_i BR_{\chi_{ci} \rightarrow J/\psi \gamma} f_{\chi_{ci}}^{after} \right]. \quad (B.2)$$

The values needed for the normalised cross-section calculation for the prompt samples are listed in Table B.1, together with the final result.

Sample	$pp \rightarrow J/\psi \rightarrow e^+ e^-$ [CKIN(3)=3]	$pp \rightarrow J/\psi \rightarrow e^+ e^-$ [CKIN(3)=1]
σ_{tot} (nb)	190026	2245530
ϵ_{tot}	0.02715	0.00588
$f_{J/\psi}^{after}$ (%)	16.0	9.7
$f_{\chi_{c0}}^{after}$ (%)	20.9	32.4
$f_{\chi_{c1}}^{after}$ (%)	34.6	20.3
$f_{\chi_{c2}}^{after}$ (%)	28.5	37.6
σ_{norm}^{filter} (nb)	105.5	194.3

Table B.1: Generator level quantities used for the normalised cross-section calculation. The values are shown for both prompt J/ψ samples with different \hat{p}_\perp values, as indicated by the CKIN(3) PYTHIA parameter.

Using simple algebra, it is possible to derive the equivalent expression for σ_{norm}^{filter} using the fractions of events before the filter, f_i^{bef} , previously defined in Eq. A.6. To achieve this, let's rewrite Eq. B.2 as follows:

$$\begin{aligned}
\sigma_{norm}^{filter} &= BR_{J/\psi \rightarrow e^+e^-} \times \sigma_{tot} \times \epsilon_{tot} \times \frac{1}{N_{tot}^{after}} \left[N_{J/\psi}^{after} + \sum_i BR_{\chi_{ci} \rightarrow J/\psi \gamma} N_{\chi_{ci}}^{after} \right] \\
&= BR_{J/\psi \rightarrow e^+e^-} \times \sigma_{tot} \times \epsilon_{tot} \times \frac{1}{\epsilon_{tot} N_{tot}^{bef}} \left[\epsilon_{J/\psi} N_{J/\psi}^{bef} + \sum_i BR_{\chi_{ci} \rightarrow J/\psi \gamma} \epsilon_{\chi_{ci}} N_{\chi_{ci}}^{bef} \right] \\
&= BR_{J/\psi \rightarrow e^+e^-} \times \sigma_{tot} \times \frac{1}{N_{tot}^{bef}} \left[\epsilon_{J/\psi} N_{J/\psi}^{bef} + \sum_i BR_{\chi_{ci} \rightarrow J/\psi \gamma} \epsilon_{\chi_{ci}} N_{\chi_{ci}}^{bef} \right], \quad (B.3)
\end{aligned}$$

where N_{tot}^{bef} , $N_{J/\psi}^{bef}$ and $N_{\chi_{ci}}^{bef}$ are defined in Eq. A.1. Finally, we obtain the equivalent expression in Eq. B.4.

$$\sigma_{norm}^{filter} = BR_{J/\psi \rightarrow e^+e^-} \times \sigma_{tot} \times \left[\epsilon_{J/\psi} f_{J/\psi}^{bef} + \sum_i BR_{\chi_{ci} \rightarrow J/\psi \gamma} \epsilon_{\chi_{ci}} f_{\chi_{ci}}^{bef} \right] \quad (B.4)$$

We just proved that we have two equivalent choices:

- Either we use ϵ_{tot} together with the fractions *after* the filter
- Either we use *individual* ϵ together with the fractions *before* the filter

QED

APPENDIX C

Offline selection cuts

A summary of all cuts applied on reconstructed events is presented here. All events undergo preselection, which requires that:

- i) at least two cluster-seeded electrons are found in the event (electrons reconstructed only by the track-seeded algorithm and electrons found in the forward calorimeters, are not included),
- ii) the electromagnetic cluster of each of the electrons satisfies $0 \leq |\eta_{cluster}| \leq 1.37$ and $1.52 \leq |\eta_{cluster}| \leq 2.47$, and
- iii) has a transverse energy $E_T \geq 5$ GeV.

The selection used for the final analysis is then applied. The electrons should pass:

- iv) opposite-charge selection and common vertex refitting,
- v) $\chi^2 < 6$ on the vertex refit of the pair of tracks,
- vi) the electromagnetic clusters belonging to the two electrons are separated by $\Delta R_{cluster} = \sqrt{(\Delta\eta_{cluster})^2 + (\Delta\phi_{cluster})^2} > 0.1$ (to remove possible duplicates between nearby electromagnetic clusters - see §6.2.2),
- vii) the dielectron invariant mass is $2 \text{ GeV} \leq m_{ee} \leq 4 \text{ GeV}$,
- viii) both electrons pass the tight identification cuts,

- ix) the event passes the 2e5 trigger chain and the angular distance between the EF trigger object and the offline electron is $\Delta R \leq 0.03$ for both electrons in the pair,
- x) if more than one refitted electron pair is found, the one with the highest refitted p_T is kept.

Alternatively, for the various simulation studies, a simplified electron pair selection was used instead of the above. After the preselection cuts i)–iii) above, the events must have:

- xi) $\Delta R_{cluster} > 0.1$,
- xii) at least one electron of each charge,
- xiii) both electrons passing the identification cuts (loose, medium, medium_noiso, tight or tight_noiso),
- xiv) if more than one opposite-sign electron-pair combination is found, the combination with the highest p_T is kept.

The efficiency of the cuts used for the final analysis was also evaluated inside a truth acceptance for electrons, defined as:

- a) the generator level electron satisfies $E_T \geq 5$ GeV,
- b) it is produced within $|\eta| \leq 2.47$,
- c) it must be a generator stable particle (status=1), and
- d) it must not be a GEANT particle (barcode<100000), i.e. not coming from material interactions in the detector.

APPENDIX D

Transverse Decay Length

The transverse decay length L_{xy} is a measure of the displacement of a decay in the transverse plane, as indicated in Fig. D.1. It is defined in Eq. D.1, where \vec{x}_p is the position of the primary vertex, \vec{x}_s is the position of the secondary vertex, \vec{p}_T^{ee} is the refitted dielectron transverse momentum and $\theta_{\vec{x}_s - \vec{x}_p, \vec{p}_T^{ee}}$ is the angle between the primary to secondary vertex position vector and the direction of the refitted dielectron p_T .

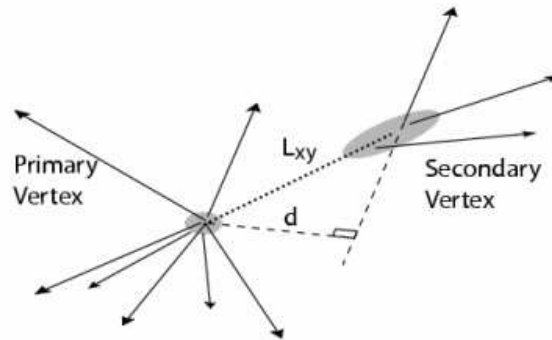


Figure D.1: Transverse decay length diagram [127].

$$\begin{aligned}
L_{xy} &= (\vec{x}_s - \vec{x}_p) \cdot \frac{\vec{p}_T^{ee}}{\|\vec{p}_T^{ee}\|} \\
&= \|\vec{x}_s - \vec{x}_p\| \cos \theta_{\vec{x}_s - \vec{x}_p, \vec{p}_T^{ee}}
\end{aligned} \tag{D.1}$$